Effect of temperature on sandstone permeability

Mineral-fluid interaction

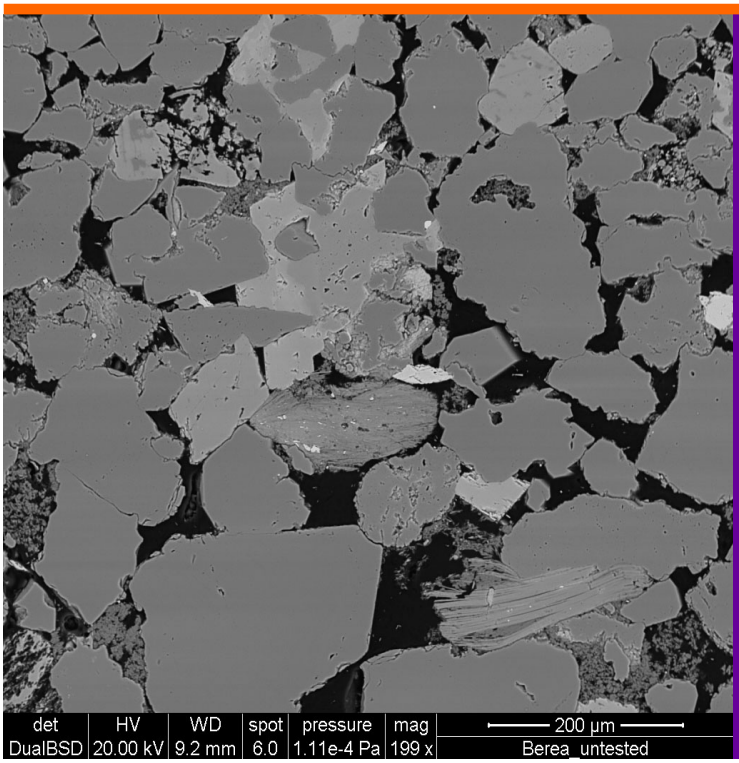

Esther Rosenbrand

PhD Thesis

Department of Civil Engineering

2014

DTU Civil Engineering Report R-313 (UK)
August 2014

DTU Civil Engineering
Department of Civil Engineering

Effect of temperature on sandstone permeability

Mineral-fluid interaction

Esther Rosenbrand

PhD Thesis

June 2014

Department of Civil Engineering

Technical University of Denmark

Preface

This thesis is submitted as a partial fulfilment of the requirements for a Danish PhD degree. The main supervisor is Professor Ida Lykke Fabricius at the Department of Civil Engineering of the Technical University of Denmark. The co-supervisor is Claus Kjøller, Head of the Core Laboratory of the Geological survey of Denmark and Greenland (GEUS). The project included a three-month external research stay at the University of Leeds, focussed on data mining, which was supervised by Professor Quentin Fisher from the School of Earth and Environmental Sciences. During a three-week stay at the Rheinisch-Westfälische Technische Hochschule (RWTH) Aachen data was acquired for image analysis based on electron microscopy and mineral mapping by using the QEMSCAN® system, in collaboration with Dr. Sven Sindern.

This PhD project is part of the Heat Storage in Hot Aquifers project, which investigates the possibility of heat storage in Danish geothermal aquifers. The HeHo project is a research collaboration among DTU, GEUS, the University of Vilnius and Dansk Fjernvarmes Geotermiselskab. Funding is provided by the Danish Council for Strategic Research. This PhD project addresses mechanisms by which hot brine injection could affect sandstone permeability.

This is a paper based thesis; manuscripts that are submitted for peer review and non-reviewed conference papers are included in Appendices B and C respectively. Different aspects of permeability in sandstones are addressed in one or more manuscripts. In order to present a coherent discussion of sandstone permeability in the thesis, a selection of content of the papers was re-grouped into five chapters addressing: sandstone permeability modelling by using Kozeny's equation; gas slip modelling based on Klinkenberg's procedure; the effect of immobile water on brine permeability; thermal expansion; and kaolinite fines migration. The thesis also contains supplementary material that was not used in the Manuscripts. A discussion of the application of Kozeny's equation to sandstone (Chapter 2) was added in order to place the results from the different manuscripts in a broader context. Supplementary data analysis was included in chapters 3 and 4, based on calculations that are included in Appendix A; some of these data are to be included in a further study of permeability in Gassum sandstone in the 'Crossover project', a collaboration between the HeHo project and the 'The geothermal energy potential in Denmark - reservoir properties, temperature distribution and models for utilization' project at GEUS. Chapter 3.5 is based on unfinished manuscript collaboration with Quentin Fisher, Carlos Grattoni and Nichola Eardley for which additional experiments are currently being performed at the University of Leeds.
The focus of this thesis is on data interpretation; therefore a chapter is included that addresses the different methods that were applied in one or more manuscripts.

Laboratory permeability data were measured by: Quentin Fisher and Carlos Grattoni as part of the PETGAS project at the University of Leeds; students of DTU: Christian Haugwitz, Peter Jacobsen, and Jacob Riis, in collaboration with Claus Kjøller at the GEUS Core Laboratory; Hanne Holmslykke, Marga Jørgensen, Hans

Lorentzen, and Claus Kjøller at the GEUS Core laboratory.
Unless otherwise indicated, images shown in this thesis were acquired by myself using a Quanta 200 (FEI) scanning electron microscope at DTU Civil engineering, or using a Quanta 650 (FEI) at the Leeds Electron Microscopy and Spectroscopy Centre, at the University of Leeds. Images in which mineralogy is mapped by the QEMSCAN® (FEI) system were acquired using a Quanta650 (FEI) scanning electron microscope and QemScan iDiscover (v.5.3) software at RWTH Aachen in collaboration with Sven Sindern and Roman Klinghardt.

Thanks are due to:

Ida Fabricius and Claus Kjøller for their guidance throughout the project; Quentin Fisher for good discussions during and following up on my stay in Leeds; Sven Sindern for pleasant collaboration during and after my visit to Aachen; and my other co-authors for good discussions and data collection: Carlos Grattoni, Christian Haugwitz, Peter Jacobsen, Frans Kets, Jacob Riis, and Hao Yuan.
Collaborators on the Crossover project, people who helped me with microscopy or with laboratory tests, and people who shared laboratory data or numerical codes: Hector Diaz, Nichola Eardley, Morten Hjuler, Hanne Holmslykke, Marga Jørgensen, Roman Klinghardt, Hans Lorentzen, Bjørn Maribo-Møgensen, Sing Nguyen, Mette Olivarius, Ebba Schnell, Ida Shafagh, Richard Walshaw, and Rikke Weibel.
All the colleagues in the long hallway of building 119 at DTU for a pleasant working environment these past three years. Reviewers from *Geothermics* for constructive reviews of submitted manuscripts.
Astrid and Gerard Rosenbrand for supporting me in more ways than I can say.

Dedicated to the memory of Anne Mijling

Dansk sammenfatning

Sæsonvarmelagring i forbindelse med geotermiske anlæg i dybtliggende sandsten er en mulighed i Danmark, men den derved forbundne temperaturstigning kan forårsage permeabilitetsreduktion og dermed fordyre metoden. Det er derfor nødvendigt at forstå mekanismen bag temperaturens indflydelse på permeabiliteten, og nærværende forskningsprojekt fokuserer således på sandstenspermeabilitet ud fra forskellige synsvinkler. Til det formål blev der analyseret data fra forskellige kilder: 1. En database med oplysninger om mere end 120 lavpermeable sandsten; 2. Gennemstrømningseksperimenter på Bereasandsten, som ofte anvendes som reference for reservoirsandsten; 3. Gennemstrøningseksperimenter på sandsten fra Gassumformationen og Bunterformationen, der begge er danske geoterme reservoirer. Elektronmikroskopi af polerede tyndslib blev brugt til at kvantificere sammenhængen mellem sandstenstekstur og permeabilitet.

Kozenys ligning fra 1927 sammenkæder permeabiliteten med porøsiteten og den specifikke overflade (som også kan udtrykke som den ækvivalente porestørrelse). Ligningen er baseret på en simpel fysisk model og gælder for et homogent porøst medium med ensartet porestørrelse, men da porestørrelsen i en sandsten kan variere fra nanometer til mikrometer, er det nødvendigt med flere antagelser for at kunne beskrive sandstenspermeabilitet ved hjælp af Kozenys ligning. Det kan gøres ved at definere en effektiv specifik overflade, og denne kan estimeres ved hjælp af billedanalyse elektronmikroskopibilleder eller ved hjælp af kernemagnetisk resonansspektrometri (NMR). Det viser sig, at i sandsten med lav porøsitet er det ofte de små porer, der betinger permeabiliteten. I disse sandsten er de store porer øjensynligt forbundet gennem de små, så at strømningshastigheden i de store porer begrænses. Her bliver den effektive specifikke overflade høj. I andre sandsten, hvor de store porer er direkte forbundet, er det disse porer der betinger permeabiliteten, mens de små porer bidrager meget lidt. Her bliver den effektive specifikke overflade lav.

Det er også muligt at definere en ækvivalent porestørrelse ved hjælp af Klinkenbergs procedure fra 1941. Den indebærer måling af gaspermeabilitet ved en serie forskellige poretryk og hermed, hvor meget ekstra strømning der kommer fordi strømningshastigheden for gas er større en nul ved porevæggen. En sammenligning mellem ækvivalent porestørrelse estimeret ud fra Klinkenbergs procedure og ud fra Kozenys ligning viser den forventede korrelation, men forskellen kan være op til en størrelsesorden. En af grundene til dette er, at i lavpermeable sandsten er permeabiliteten afhængig af differensspændingen mellem omslutningstryk og poretryk, og denne ændres dermed, når poretrykket ændres. Det giver en ekstra effekt ved Klinkenbergs procedure, og derfor blev porevægseffekten og effekten af omslutningstryk kombineret til et nyt udtryk.

Det ses ofte at permeabiliteten for saltvand er lavere end den Klinkenbergkorrigerede gaspermeabilitet, og det er muligt at en del af baggrunden er, at saltvandet interagerer med porevæggen, således at der opstår et immobilt væskelag på porevæggen. Denne effekt kan modelleres, bl.a. ved hjælp af NMR data, men det ser

ud til, at sådan en antagelse ikke er nok og at andre faktorer, der muligvis er relateret til lermineralernes morfologi spiller ind.

Temperaturstigning, og den dermed forbundne udvidelse af sandstenen, burde ud fra Kozenys ligning i sig selv kun have meget lille effekt på permeabiliteten, og i publicerede forsøg fandtes heller ingen målbar temperatureffekt, når porevæsken er inert. For kaolinholdige sandsten fandtes derimod, at hvis porevæsken er ferskvand eller saltvand, falder permeabiliteten, når temperaturen stiger. Dette kan skyldes at varmen betinger ændringer i mineralernes elektriske dobbeltlag, og dermed frastødning mellem lerpartikler og kvartskorn. Et permeabilitetsfald ses også ved reduktion af porevandssaliniteten. Der er tale om to forskellige effekter: Ved stigende temperatur stiger den absolutte værdi af mineralernes overfladeladning, mens ved faldende salinitet øges tykkelsen af det elektriske dobbeltlag.

Gennemstrømningsforsøg på Bereasandsten illustrerer forskellen på effekten af temperatur og effekten af salinitet: Mens en permeabilitetesreduktion på grund af reduktion af porevandssaliniteten var irreversibel ved 20^{o}C, var en permeabilitetesreduktion på grund af temperaturøgning til 80^{o}C reversibel. Ved 80^{o}C var en permeabilitetsøgning ved stigende gennemstrømningshastighed reversibel, mens den ikke var ved 20^{o}C. Dette tyder på at kaolinitpartikler mobiliseres ved forskellig mekanisme ved 20^{o}C og ved 80^{o}C. Mekanismerne blev diskuteres ved hælp af DLVO teori, der blev udviklet af Derjaguin and Landau i 1941 og Verwey and Overbeek i 1948. Det er således muligt at effekten ved 80^{o}C kan beskrives som ændringer i porevæskens reologi, mens effekten ved 20^{o}C indebærer omplacering kaolinitmineralerne.

Opløsning og udfældning af mineraler blev også observeret. I løbet af et eksperiment hvor NaCl opløsning i 150 døgn blev injiceret ved 80^{o}C, opløstes således øjensynligt siderit, hvorved Fe-ioner frigjortes. Disse blev derefter oxideret og fældede ud som jernhydroxid. Observationerne blev kvantificeret ved hjælp af billedanalyse af polerede tyndslib i elektronmikroskop. Her blev intensiteten af backscatter electroner sammenholdt med røntgenfluorescenssignalet ved hjælp af QEMSCAN® programmet. Analysen tyder på at udfældningen af jernhydroxid sker i de finkornede og lavporøse lag og dermed fremhæver sandstenens laminering. Effekten var dog for lille til at have væsentlig indflydelse på hverken den modellerede eller den målte permeabilitet, der kun var 20% lavere end den oprindelige.

Nærværende undersøgelse viser at sandstenens indhold af lermineraler og disses morfologi har betydelig indflydelse på: 1. Hvilken del af porøsiteten der kontrollerer permeabiliteten; 2. Forskellen på væske- og gaspermeabilitet; samt 3. I hvor høj grad temperaturen påvirker permeabiliteten. Injektion af varmt vand kan forårsage mobilisering af lerpartikler og opløsning af mineraler; men om det sker, afhænger af sandstenens mineralogi og porevæskens sammensætning. Man kan derfor ikke umiddelbart generalisere resultater fra én sandstensformation til en anden.

English summary

Hot water injection in geothermal sandstone aquifers is considered for seasonal energy storage in Denmark. However, an increase in the aquifer temperature might reduce permeability, and thereby increase production costs. An understanding of the factors that control permeability is required in order to address the effects of temperature on permeability. Therefore, different aspects of sandstone permeability are investigated in this research project. Data from a range of sources including: published literature; a database containing over 120 tight gas sandstone samples; new flow-through experiments on Berea sandstone, which is often used as a reference material to reservoir sandstones; and flow-through experiments on Danish Gassum Formation sandstone and Bunter Formation sandstone, were analysed. Polished thin sections were studied by using the electron microscope in order to relate permeability to sandstone texture.

The simple physically based Kozeny (1927) equation, relates permeability to porosity and specific surface per pore volume, or equivalent pore size, for a homogeneous porous medium with a uniform pore size. As pore sizes in sandstones can range from nanometres to micrometres, additional assumptions would be required in order to estimate sandstone permeability based on the Kozeny equation. An effective specific surface area per pore volume for permeability was estimated by using image analysis and pore size distributions as from nuclear magnetic resonance (NMR) transverse relaxation data. The smaller pores in the pore size distribution appear to control permeability in sandstones with a low clay-free intergranular porosity. Presumably in those sandstones larger intergranular pores are only connected through smaller pores, which therefore limit the flow rate in larger pores. In sandstones where larger intergranular pores do form a connected flow path, the higher permeability in these pores would have the dominant effect on the measured permeability, wherefore the effective specific surface reflects the specific surface of the framework grains.

A characteristic equivalent pore size can also be determined based on the Klinkenberg (1941) procedure, which accounts for effects on permeability of gas slip on the fluid-solid interface by means of several permeability measurements with different pore pressures. A comparison between the equivalent pore sizes as estimated using the Kozeny equation and the Klinkenberg procedure showed the expected correlation between the two measures, however, differences could be around one order of magnitude.

In tight gas sandstones, permeability is often sensitive to net stress, which might change due to the pore pressure change in the Klinkenberg procedure. Besides affecting the Klinkenberg procedure, the combined effect of slip and changes in permeability would affect production during pressure depletion in tight gas sandstone reservoirs; therefore effects of gas slip and net stress on permeability were combined in a model based on the Klinkenberg equation.

A lower permeability to brine than to gas is often observed, which might be due to interaction between the mineral surface and the pore fluid. By modelling a layer of immobile fluid on the fluid-mineral interface

permeability to brine was estimated, based on both the pore size distribution from NMR combined with the Kozeny equation and the Klinkenberg procedure. Both methods overestimated the measured brine permeability; this suggests that additional factors, possibly related to clay morphology, contributed to a lower brine permeability.

Thermal expansion would have a negligible effect on permeability as estimated based on the Kozeny equation. Accordingly, a literature survey indicated no effect of heating on permeability in experiments with an inert pore fluid; in tests with distilled water or brine, heating reduced permeability in sandstones containing kaolinite clay minerals.
Both heating and reduction of the salinity of the pore fluid can increase the electrical double layer repulsion between quartz grains and kaolinite particles in Berea sandstone, which could lead to kaolinite mobilisation and permeability reduction. Heating increases the magnitude of the mineral surface charge, whereas salinity reduction increases the range over which the surface charge acts. Flow-through experiments in Berea sandstone samples indicated differences between the effect of temperature and salinity on permeability. A permeability reduction at 20°C due to salinity reduction was not reversed by restoring the salinity; a permeability reduction due to heating to 80°C was reversible by restoring the temperature to 20°C. A reversible permeability increase with increasing flow rate was observed at 80°C, but not at 20°C. Therefore, it was suggested that mobilised kaolinite particles affect permeability by a different mechanism at 80°C than at 20°C; at 80°C the main effect might be due to an alteration of pore fluid rheology, whereas at 20°C particles might be filtered in pore constrictions. DLVO theory (Derjaguin and Landau (1941); Verwey and Overbeek (1948)) was used to compare effects of temperature and salinity on surface interaction forces.

Quantitative analysis of images, in which mineralogy was mapped based on backscatter electron intensity in combination with energy dispersive X-ray analysis by using the QEMSCAN® system, was used to compare a tested sample to an untested Berea sandstone sample. During the experiment, in which an 80°C NaCl solution was injected for 150 days, apparently siderite dissolutions released iron, which was oxidised and precipitated as iron hydroxides. Lamination appears to be enhanced by precipitation of iron hydroxides predominantly in finer grained, lower porosity, lamina. The effect of enhanced lamination, as estimated based on the specific interface to the pore from image analysis, was negligible; accordingly, the experimentally measured permeability at the end of the test was only 20% lower than at the start of the test.

This investigation indicates that clay morphology and abundance has a strong effect on: the fraction of the porosity that is effective for permeability, the difference between brine and gas permeability, and the effect of temperature. Hot water injection might induce clay particle mobilisation and mineral dissolution; however, these effects would depend on the mineralogy and pore fluid composition. Therefore, results from one formation cannot directly be generalised to other formations.

Notation

Latin Symbols

a empirical constant in the SDR, or Mean T_2, equation, L^2/s^2, m^2/s^2

b_{slip} Klinkenberg (1941) slip factor, Lt^2/m, 1/Pa

c Kozeny constant, -

c_0 shape factor in Kozeny's equation, -

c_{slip} proportionality factor in Klinkenberg's equation, -

$d_{s,mean}$ mean diameter of solids, L, m

e elementary charge, q, C

f_{NMR} fraction of porosity in NMR T_2 distribution, -

fw_{NMR} fraction of porosity in which water or brine is mobile in NMR T_2 distribution, -

f_{Hg} fraction of porosity filled in mercury injection, -

h separation between mineral surfaces, L, m

h_{RC} height of a rectangular channel, L, m

k permeability, L^2, mD

k_a apparent permeability with gas slip, L^2, mD

k_B Boltzmann constant, mL^2/t^2T, J/K

k_w permeability to water or brine, L^2, mD

l distance parallel to pressure gradient, L, m

l_{eff} effective distance travelled by fluid (in Kozeny (1927)), L, m

l_{pix} pixel length for square pixels, L, m

n_k net stress parameter for permeability, -

q specific discharge, flow rate, Q/A, L/t, m/s

r characteristic length scale, L, m

r_H hydraulic radius, $1/S_p$, L, m

r_p radius for cylindrical capillaries, or equivalent radius for pores ($r_p = 2/S_p$), L, m

$r_{p,slip}$ characteristic equivalent pore radius for gas slip, L, m

$r_{p,kozeny}$ equivalent pore radius for permeability in the Kozeny equation, L, m

$r_{p,NMR,max}$ maximum equivalent pore radius that is effective for permeability based on NMR, L, m

r_s equivalent radius of solids, L, m

v average flow velocity in capillary, or interstitial velocity in pores, ($q/\phi = Q/A\phi$), L/t, m/s

w width, L, m

z valence of an ion, -,

A cross sectional area, L^2, m^2

E_{EDL} electrical double layer interaction energy per square meter, L^2/t^2m, J/m^2

E_{vdW} van der Waals interaction energy per square meter, L^2/t^2m, J/m^2

E_{DLVO} net interaction energy per square meter, $E_{DLVO} = E_{EDL} + E_{vdW}$, L^2/t^2m, J/m^2

H Hamaker constant, mL^2/t^2, J

C concentration, n/L^3, mol/m^3

$C_{B\&K}$ shape parameter in model by Beskok & Karniadakis (1999), -

D density, m/L^3, kg/m^3

D_f fractal dimension, -

I ionic strength of electrolyte in mol per litre, n/L^3, mol/l

I_p specific pore interface per unit pore area, 1/L, m/mm^2

I_{qtz} specific quartz interface, L, m

K parameter relating 2D specific interface per pore area to 3D specific surface per pore volume, -

K_∞ permeability extrapolated to zero net stress, L^2, mD

M molar mass, m/n, g/mol

N_A Avogadro constant, 1/n, 1/mol

$\bar{P}$ mean pore pressure, m/Lt^2, Pa

ΔP pressure gradient (one dimensional), m/L^2t^2, Pa/m

P_c capillary pressure, m/Lt^2, Pa

Q volumetric flow rate, L^3/t, m^3/s

Q_M molar flow rate, n/t, mol/s

R ideal gas constant, $L^2m/(t^2Tn)$, J/molK

R_c correlation coefficient, (correlation between measurement and model), -

$S_{B\&K}$ shape parameter, 4 for cylinders and 6 for rectangles in unified slip flow model, -

S specific internal surface area per bulk volume, 1/L, m^2/cm^3

S_p specific surface area per pore volume, 1/L, m^2/cm^3

S_s specific surface area per solids volume, 1/L, m^2/cm^3

Sw_p specific surface area per pore volume for mobile water or brine, 1/L, m^2/cm^3

T absolute temperature, T, K

T_2 transverse relaxation time, t, s

$T_{2,gm}$ geometric mean transverse relaxation time, t, s

$T_{2,max}$ maximum transverse relaxation time that is considered effective for permeability, t, s

V_s volume of solids, L^3,m^3

V_b bulk (sample) volume , L^3,m^3

V_p volume of pores, L^3,m^3

V_{Hg} volume of mercury, L^3,m^3

Greek symbols

α empirical parameter in model by Beskok & Karniadakis (1999), -

α_T one dimensional coefficient of thermal expansion, 1/T, 1/K

$\alpha_{0B\&K}$ parameter characterizing free molecular flow in model by Beskok & Karniadakis (1999), -

$\alpha_{B\&K}$ function of Kn characterizing rarefaction in model by Beskok & Karniadakis (1999), -

β empirical parameter in model by Beskok & Karniadakis (1999), -

γ stress exponent for permeability, -

γ_{Hg} surface tension, m/t^2, N/m

ε permittivity of vacuum, q^2t^2/mL^3, F/m

ε_r static relative dielectric permittivity, -

ζ zeta potential, potential on the shear plane, mL^2/qt^2, V

θ contact angle, °

κ^{-1} Debye length, 1/L, 1/m

$\bar{\lambda}$ mean free path length of gas molecules, L, m

μ dynamic viscosity, m/tL, Pa.s

ρ surface relaxivity, L/t, m/s

σ_0 surface charge, or net charge density on the Stern plane, q/L^2, C/m^2

σ_c confining stress, m/Lt^2, Pa

σ_k' net stress for permeability ($\sigma_k' = \sigma_c - n_k\bar{P}$), m/Lt^2, Pa

τ thickness of immobile water layer, L, m

τ_{Stern} thickness of Stern layer, L, m

ϕ porosity, fraction, -

ϕ_c porosity relating to critical percolation threshold, fraction, -

ϕ_{mobile} mobile porosity, fraction, -

ψ_0 surface potential, or potential on Stern plane, mL^2/qt^2, V

Γ tortuosity

Subscripts

i counter

mono monovalent ions

ΔT after temperature increment by ΔT

T,0 prior to temperature increment in thermal expansion calculations.

Subscripts relating to measurement methods

BET as measured by nitrogen gas adsorption

kozeny as calculated based on Kozeny equation using porosity and permeability

NMR,max maximum T_2 or maximum equivalent pore size as estimated from NMR.

slip as estimated from Klinkenberg procedure.

Abbreviations

AFM atomic force microscopy

BSEM backscattered electron microscopy

EDS energy dispersive X-ray analysis

FIB focussed ion beam

LSA linear superposition approximation

μ-CT micro computed tomography

MRA minimum representative area

NMR nuclear magnetic resonance

REV representative elementary volume (3D equivalent of MRA)

SEM scanning electron microscopy

XRD X-ray diffraction

Content

1 Introduction

1.1 Motivation

Geothermal energy is used for district heating in Copenhagen and in Thisted (Lund et al., 2011). Both expansion of the existing plants and new geothermal plants at other sites are being considered in order to increase the supply of geothermal energy (Lund et al., 2011). Heat from other sources, such as waste incineration, could also be used for district heating. Whereas this heat is produced all year long, heat demand heat peaks during the winter, which requires seasonal heat storage.

The Heat Storage in Hot Aquifers project, HeHo, investigates the possibility of seasonally storing heat energy by means of heating geothermal brine prior to injection into the geothermal aquifer during the summer. This would increase the aquifer temperature above the natural temperature, which is approximately 44°C in Thisted and 74°C in Copenhagen (Lund et al., 2011), so that additional energy can be extracted during the winter.

Energy is required for injection and extraction of geothermal brine, and the pumping energy depends on the aquifer permeability, i.e., the conductivity of the rock to fluid flow. Permeability reduction increases pumping costs; therefore energy storage would be effective only if permeability is not significantly reduced due to heating.

1.2 Problem statement and scope

Permeability, as defined in Darcy's law, is a property of the rock; permeability would not depend on the properties of the fluid (Bear, 1972; Darcy, 1856). The physically based Kozeny (1927) equation relates permeability to porosity and specific surface area, or equivalent pore size, for a homogeneous rock with a uniform pore size. Sandstone permeability is often modelled by using the Kozeny equation (Berryman and Blair, 1987; Carman, 1937; Hossain et al., 2011; Pape et al., 2006; Walderhaug et al., 2012) [Manuscript I, II, III, IV]. However, due to the presence of clay minerals, sandstones can have a range of pore sizes; therefore additional assumptions are required to apply the Kozeny equation. Different methods of estimating the specific surface, or the equivalent pore size, that is effective for permeability are discussed in Chapter 2, based on literature and on Manuscripts II, III and IV.

Gas flow can be used to measure permeability (API, 1998). However, permeability to brine is often lower than permeability to gas in sandstones (Heid et al., 1950; Jones and Owens, 1980; Wei et al., 1986) [Manuscripts I,II,IV]. Gas slip can increase the gas flow rate at low pore pressures, and increase the apparent permeability to gas (Klinkenberg, 1941). The effect of gas slip is modelled by Klinkenberg (1941), as a function of both the gas properties and a characteristic pore size. Klinkenberg shows that a characteristic equivalent pore size for gas slip can be determined by measuring permeability at three or more different pore pressures. This can be used in order to estimate the true permeability, and the apparent permeability to a different gas or at a different pore pressure. The equivalent pore size that is effective for permeability in the Kozeny equation would presumably relate to the characteristic equivalent pore size for gas slip, however, a scatter is often observed (Florence et al., 2007; Funk et

al., 1989; Heid et al., 1950; Jones and Owens, 1980). Gas slip has a greater effect on apparent permeability in sandstones with smaller pores, such as tight sandstones. Therefore, gas slip is investigated in Chapter 3 by using data from both the PETGAS database, which contains petrophysical measurements on tight gas sandstones, and from sandstones with a higher porosity and permeability, which would be relevant for geothermal energy. Permeability is often sensitive to net stress in tight gas sandstones (Jones and Owens, 1980; Osorio et al., 1997; Ostensen, 1983). The stress sensitivity of the true permeability might cause errors when Klinkenberg's method is used. Furthermore, the effect of pore pressure on both true permeability and on gas slip would affect production from tight gas sandstone reservoirs; therefore the combined effect on apparent permeability is considered in Section 3.4.

A lower brine permeability can be observed even after correcting for gas slip (Heid et al., 1950; Jones and Owens, 1980; Wei et al., 1986) [Manuscripts I,II,IV] . Therefore, several authors suggest that a layer of immobile water on the mineral surface reduces the mobile pore volume (Andreassen and Fabricius, 2010; Faulkner and Rutter, 2003; Heid et al., 1950; Jones and Owens, 1980). Effects of an immobile water layer on permeability are estimated, based on both the Kozeny model [Manuscript IV] and the Klinkenberg model in Chapter 4. Similar to gas slip, the effect of immobile water would be greater in sandstones with smaller pores, therefore both tight gas sandstones and more permeable sandstone samples are considered.

Thermal expansion might affect permeability; this effect, as estimated based on the Kozeny equation in Chapter 5, can be considered negligible [Conference paper I; Manuscript I]. Accordingly, in an overview of published data, no effect of temperature on permeability is observed in tests with inert fluids, mineral oils or gas; however, some tests where hot distilled water or hot brine is injected show a significant permeability reduction due to heating [Conference paper I; Manuscript I]. This indicates that the effect of temperature on permeability relates to mineral-fluid interaction. Mechanisms by which hot water or brine injection might affect permeability include: alteration of the thickness of an immobile water layer on the mineral surface (Andreassen and Fabricius, 2010; Faulkner and Rutter, 2003); chemical reactions leading to dissolution and precipitation (Blair et al., 1984; Tenthorey et al., 1998); contamination of samples with particles that are generated by corrosion of the equipment (Milsch et al., 2009; Potter et al., 1981; Stottlemyre, 1981; Ungemach, 2003); and alteration of surface interaction forces among fine clay particles and sandstone quartz grains that could mobilise fines (Baudracco and Aoubouazza, 1995; Khilar and Fogler, 1984, 1987; Priisholm et al., 1987; Schembre and Kovscek, 2005) [Conference papers I, II, III; Manuscripts I, II, III].

Permeability reduction due to fines mobilisation is observed in Berea sandstone when the concentration of NaCl in the pore fluid is reduced (Grey and Rex, 1966; Khilar and Fogler, 1984, 1987; Mungan, 1965; Ochi and Vernoux, 1998; Schembre and Kovscek, 2005). Kaolinite is the dominant clay mineral in the Berea sandstone (Churcher, 1991; Khilar and Fogler, 1984). Reducing the NaCl concentration increases the electrical double layer (EDL) repulsion force between similarly charged kaolinite particles and quartz grains, which might mobilise

kaolinite particles. The DLVO (Derjaguin and Landau, 1941; Verwey and Overbeek, 1948) Theory is used by some authors to model the effect of salinity on surface interaction forces in Berea sandstone (e.g., Khilar and Fogler, 1984, 1987; Ochi and Vernoux, 1998; Schembre and Kovscek, 2005) [Conference papers II and III; Manuscript II]. Mobilised particles might reduce permeability when these are filtered in pore constrictions, and this effect would be irreversible when the NaCl concentration is restored (Khilar and Fogler, 1984) [Manuscript II]. Heating would also increase the EDL repulsion and mobilise particles (Khilar and Fogler, 1984, 1987; Schembre and Kovscek, 2005) [Conference papers II, III; Manuscript II]. However, the effect of temperature is found to be reversible with cooling by several authors (e.g., Baudracco and Aoubouazza, 1995; Cassé and Ramey Jr, 1979) [Manuscript I; II]. Differences between effects of temperature and NaCl concentration on permeability are investigated in Chapter 6 [Manuscripts I and II; Conference papers I, II, and III].

Methods that were used for data analysis are discussed in Chapter 7. This includes applications of quantitative image analysis, both to compare among sandstone formations, and to compare between an untested sandstone sample and a sample after injection of 80°C NaCl solution [Manuscript IV]. Chapter 8 summarises the main conclusions, and Chapter 9 rounds off with recommendations for further research.

2 Permeability

2.1 Definitions

2.1.1 Porosity

Sandstones are porous media, which consist of solids and pores, i.e., voids among the solids (Figure 1). The bulk volume, V_b, is the volume of pores, V_p, plus the volume of solids, V_s, Eq.(1). Porosity, ϕ, is the ratio of V_p to V_b (Eq.(2)). For sandstones, the solids include larger grains and cement that compose the framework, and smaller clay particles that are often present in the intergranular pores, i.e. the pores among the framework grains. Small, micro-, pores are also observed among clay particles (Desbois et al., 2011; Landrot et al., 2012).

$$V_b = V_p + V_s \tag{1}$$

$$\phi = \frac{V_p}{V_b} \tag{2}$$

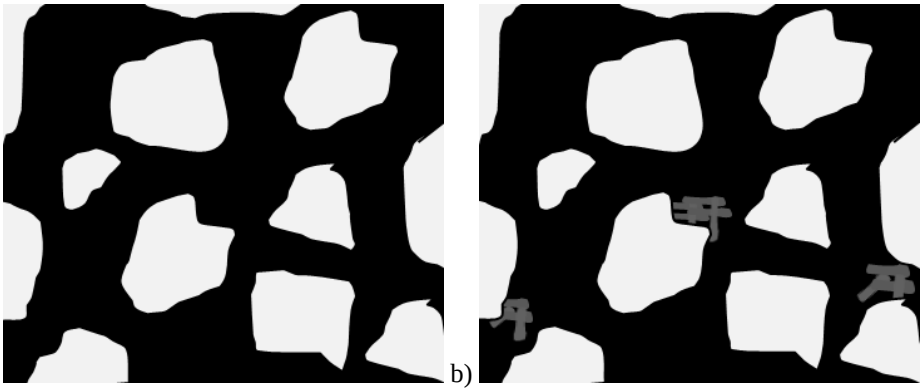

Figure 1: a) Schematic representation of sandstone consisting of framework grains (white) and pores (black). b) Schematic representation of sandstone containing clay particles (grey) in some intergranular pores (pores among framework grains). Smaller pores are also present among clay mineral particles.

2.1.2 Darcy's law

Darcy (1856) investigated vertical flow through water saturated sand columns and found that the volumetric flow rate depends on the cross sectional area of the column, the pressure gradient across the column, and the properties of the sand column. Flow rate also depends on fluid viscosity; thus for a general fluid, flow can be expressed by Eq.(3), which is known as Darcy's Law for laminar incompressible flow (Bear, 1972; Hubbert, 1957).

$$q = \frac{Q}{A} = \frac{k}{\mu}\Delta P \tag{3}$$

where, for one dimensional flow, ΔP is the pressure gradient, q is the specific discharge, henceforth referred to as the flow rate, Q is the volumetric flow rate, A is the cross-sectional area perpendicular to ΔP, μ is the dynamic viscosity of the fluid, and k is the permeability.

Darcy's law can be considered valid for a homogeneous incompressible fluid at flow rates where the Reynolds number for porous media (Eq.(4)) is less than one; inertia effects may cause additional energy dissipation at higher flow rates (Bear, 1972).

$$Re = \frac{Dqd_{s,\text{mean}}}{\mu} \tag{4}$$

where $d_{s,mean}$ is the mean diameter of the solids, and D is the fluid density.
There might also be a lower limit to the validity of Darcy's law (Bear, 1972). Some authors observed no flow of water or brine below a threshold ΔP, which might be due to mineral-fluid interaction (Bear, 1972; Byerlee, 1990; Swartzendruber, 1962). On the other hand, gas slip on the fluid-solid interface can result in an apparent permeability that is higher than the true permeability, and that depends on gas properties and pore pressure (Klinkenberg, 1941). Permeability to gas slip and to brine or water are discussed in chapters 3 and 4.

2.2 Cylindrical capillary model

Darcy's law can be derived by solving the Navier-Stokes equations for a geometrical model of the pore geometry (Bear, 1972). Possibly the simplest model is a collection of parallel cylindrical capillaries with a uniform radius r_p (Figure 2a).

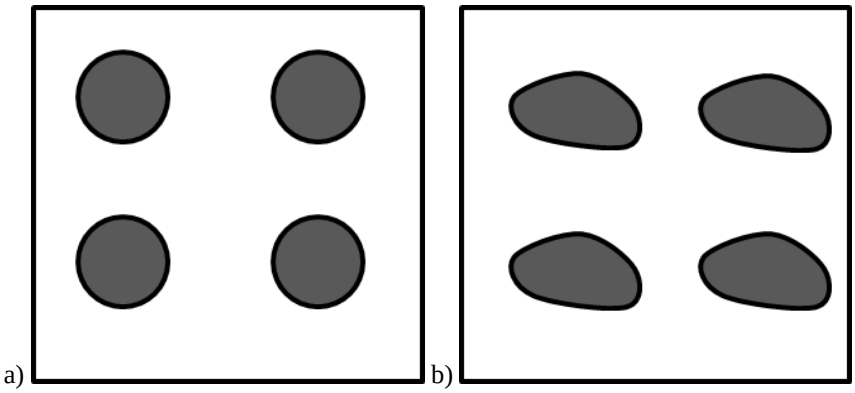

Figure 2: Model of a porous medium consisting of solids (white) and pores (grey). a) Pores are parallel cylindrical capillaries with equal radii. b) Pores are parallel capillaries with a general shape but equal size. Capillaries have a constant size in the third dimension.

The flow rate through a cube with a unit length containing n parallel cylindrical capillaries is given by Eq.(5) based on the Hagen-Poiseuille equation.

$$q = \frac{Q}{A} = \frac{n\pi r_p^{\,4}}{8}\frac{1}{\mu}\Delta P \tag{5}$$

The porosity is the volume of the cylindrical capillaries normalised by V_b, i.e., normalised by one for a unit length cube:

$$\phi = \frac{n\pi r_p^{\,2}}{V_b} = n\pi r_p^{\,2} \tag{6}$$

Permeability can therefore be expressed in terms of pore size and porosity by Eq.(7) (cf. Eq.(3), (5), and (6)).

$$k = \frac{1}{8} r_p^{\,2}\phi \tag{7}$$

2.3 Kozeny equation

Rather than assuming cylindrical capillaries, Kozeny (1927) solved the Navier-Stokes equations for parallel equal sized, smooth walled capillaries, with a general shape but a constant cross section (Figure 2b), yielding Eq.(8) (Kozeny, 1927).

$$q = \frac{Q}{A} = \frac{1}{\mu}\frac{c_0\phi^3}{S^2}\Delta P \tag{8}$$

where S is the specific surface, i.e., the solid-pore interface area normalised by V_b, and c_o is a shape parameter, which is 1/2 for cylindrical capillaries, and 2/3 for rectangular channels (Kozeny, 1927). The shape parameter c_0 is often replaced by a factor, c, which is referred to as the Kozeny constant (Bear, 1972; Mortensen et al., 1998). The Kozeny constant characterises not only the channel shape, but also pore geometry as discussed in Subsection 2.3.1.

The ratio of S to ϕ, S_p, (Eq.(9)), is inversely related to equivalent pore size, r_p, for smooth walled pores. For cylindrical capillaries, S_p is the inverse of the hydraulic radius, r_H, and half of the geometric radius, Eq.(10).

$$S_p = \frac{S}{\phi} \tag{9}$$

$$S_p = \frac{1}{r_H} = \frac{2}{r_p} \tag{10}$$

Permeability is expressed in terms of porosity, c, and $S_p^{\,2}$ in Eq.(11) (cf. Eq.(3), (8), and (9)), which is one form of the Kozeny equation. Both Eq.(7) and the Kozeny equation characterise permeability in terms of porosity and equivalent pore size squared.

$$k = \frac{c\phi}{S_p^2} \tag{11}$$

Permeability can also be expressed in terms of solids size r_s (Kozeny, 1927). For a unit cube consisting of n equal sized spheres, V_s is expressed by Eq.(12), and S by Eq.(13). The surface area per volume of solids, S_s, is related to S by Eq.(14) (cf. Eq.(1) and Eq.(2)), therefore S_p is related to r_s by Eq.(15) (Kozeny, 1927).

$$V_s = \frac{4}{3} n\pi r_s^3 \tag{12}$$

$$S = n4\pi r_s^2 \tag{13}$$

$$S_s = \frac{S}{(1-\phi)} \tag{14}$$

$$S_p = \frac{3}{r_s}\frac{(1-\phi)}{\phi} \tag{15}$$

Permeability can therefore be expressed in terms of r_s by Eq.(16) (Kozeny, 1927).

$$k = c\frac{\phi^3}{9(1-\phi)^2} r_s^2 \tag{16}$$

2.3.1 The Kozeny constant

Kozeny (1927) suggests that fluid flow paths would not be straight when fluid flows around solids. The effective distance travelled by the fluid in a tortuous, i.e. a winding, flow path, l_{eff}, would be greater than the distance l parallel to ΔP; therefore a reduced pressure gradient (cf. Eq.(17)) might be used to express flow as Eq.(18), whereby $c = c_0 l/l_{eff}$ (Kozeny, 1927).

$$\Delta P_{red} = \frac{l}{l_{eff}} \Delta P \tag{17}$$

$$q = c_0 \frac{l}{l_{eff}} \frac{\phi^3}{9(1-\phi)^2} r_s \Delta P \tag{18}$$

Carman (1937) points out that besides a lower flow velocity due to ΔP_{red}, the cross sectional area perpendicular to ΔP is also reduced by l/l_{eff}; therefore the flow rate parallel to ΔP would be reduced by $(l/l_{eff})^2$. This parameter can be referred to as tortuosity, Γ, and forms of the Kozeny equation in which $c = c_0\Gamma$ are often referred to as Kozeny-Carman equations (e.g., Bear, 1972; Berryman and Blair, 1987; Mavko and

Nur, 1997). By fitting Γ to laboratory measurements Carman (1937) suggests $\Gamma = 0.4$, which, combined with $c_0 = 1/2$ yields $c = 0.2$. Donaldson et al. (1975) model the permeability of glass bead packs and of crushed sand packs by using the Kozeny equation with $c = 0.2$ and S as measured by using nitrogen adsorption (the BET method, Brunauer et al. (1938).

Other properties, such as electrical resistivity, gas slip, or diffusion, are used in order to estimate Γ by some authors (e.g., Berryman and Blair, 1987; Boving and Grathwohl, 2001; Civan, 2002, 2010; Cornell and Katz, 1953; Dullien, 1975; Pape et al., 2006; Walsh and Brace, 1984). However, tortuosity for hydraulic flow, would not necessarily be the same as tortuosity for diffusion and electrical conduction (Bear, 1972; Pape et al., 2006). Whereas diffusion and electricity conduction have uniform velocity, i.e., piston-like displacement, fluid flow has a velocity profile with a zero velocity on the fluid-mineral interface. Therefore, if Γ is considered as purely a geometric length ratio, Γ would reflect tortuosity to diffusion or conduction. Due to local velocity differences, the average length that is travelled by a volume of fluid in a unit time might differ from the geometrical average length of the flow paths (Bear, 1972).

Rather than invoking a tortuous flow path, Mortensen et al. (1998) suggest a model where only a fraction ϕ contributes to flow. For a set of orthogonal equal sized regularly spaced interpenetrating capillaries (Figure 3a) pore pressure can be assumed to be equilibrated perpendicular to ΔP, so that the local pressure gradient in the cylindrical capillaries would equal the externally applied pressure gradient. Therefore flow would only be in the volume of the capillaries that is parallel to ΔP (Figure 3b) (Mortensen et al., 1998).

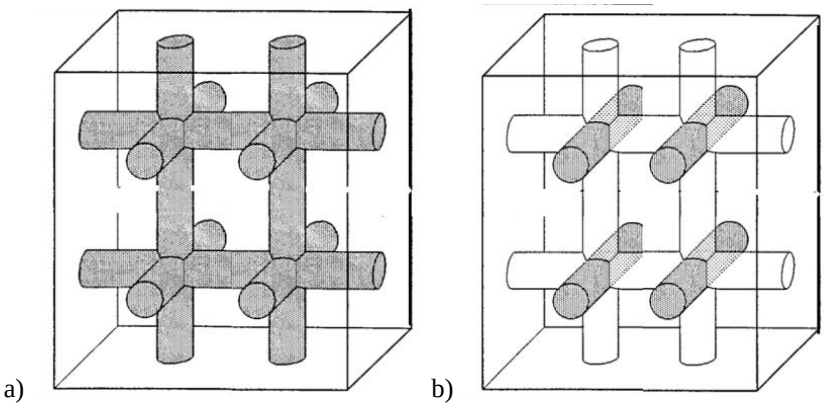

Figure 3: Porous medium in which pores are interpenetrating orthogonal equal sized capillaries. a) Entire porosity is shaded grey. b) Only porosity that is parallel to ΔP is shaded grey. (Modified from Mortensen et al. (1998)).

The Kozeny constant in the model by Mortensen et al. (1998) reflects the fraction of ϕ that conducts flow; accounting for the porosity in capillary intersections, c is expressed by Eq.(19) (Mortensen et al., 1998).

$$c = \left(4\cos\left(\frac{1}{3}\arccos\left(\phi\frac{64}{\pi^3} - 1 \right) + \frac{4}{3}\pi \right) + 4 \right)^{-1} \tag{19}$$

For ϕ tending towards zero, there are no intersections and c tends to 1/6, i.e., $c_0/3$. For ϕ tending to one, the entire porosity is parallel to flow and c tends to 0.5 (cf. Eq.(7)) (Mortensen et al., 1998). The value of c is 0.20 ± 0.02 for $2\% < \phi < 32\%$, comparable to the empirical $c_0\Gamma$ used in e.g., Carman (1937) and Donaldson (1975). Permeability of two chalk formations is modelled by using Eq.(19) and the specific surface area S as measured by nitrogen adsorption by Mortensen et al. (1998).

The Kozeny equation is simple and has a physical basis, and is therefore often used to model permeability in sandstones (e.g., Berryman and Blair, 1987; Carman, 1937; Hossain et al., 2011; Mortensen et al., 1998; Pape et al., 2006; Walderhaug et al., 2012). Pore geometry is simplified to express permeability in terms of c, ϕ, and S_p, and for homogeneous porous media with a uniform pore size, S_p can be determined by measurement of specific surface area or grain size (Kozeny, 1927). However, sandstones often have a pore size distribution; therefore different methods can be used to estimate the S_p that is effective for permeability.

2.4 The Kozeny equation in sandstone

2.4.1 Effective S_p versus total surface area

Permeability is underestimated by up to two orders of magnitude when S is measured by using nitrogen adsorption in samples of: Berea sandstone; sandstone from the Danish Gassum Formation; sandstone from Danish Bunter Formation; North Sea greensands; and sandstones from the onshore and offshore Rotliegend Formation (Donaldson et al., 1975; Solymar and Fabricius, 1999) [Manuscripts I;II; III and IV]. In these studies c is based on Eq.(19), or $c = c_0\Gamma = 0.2$ (Donaldson et al., 1975). The higher S_p that is estimated from ϕ and S from nitrogen adsorption, $S_{p,BET}$, might be affected by roughness of quartz framework grains that increases S without significantly affecting equivalent pore size and permeability (Berryman and Blair, 1987; Mortensen et al., 1998; Pape et al., 2006). Furthermore the presence of clay minerals could increase S.

Clay minerals have a high specific surface as compared to quartz grains and therefore make a disproportionately large contribution to $S_{p,BET}$ [Manuscript II;III;IV]. Nanometre or micrometre sized pores can be observed among clay aggregates in sandstones (Desbois et al., 2011; Landrot et al., 2012), however, the permeability in these micropores would be low due to the high S_p (cf. Eq.(11)). Therefore, when larger intergranular pores among framework grains form a connected flow path, these pores would make the dominant contribution to the total permeability (Solymar and Fabricius, 1999; Walderhaug et al., 2012) [Manuscript II, IV].

Berea sandstone is often studied as an analogue for reservoir sandstones, as this sandstone is considered to be relatively homogeneous and readily available (Churcher, 1991); some authors even consider Berea sandstone as an isotropic clean sandstone (Glover et al., 2006). Nonetheless, Berea sandstone would contain approximately 6 wt.%–8 wt.% clay minerals, predominantly kaolinite, and small amounts of illite and chlorite (< 1% illite, and < 1% chlorite (Baudracco and Aoubouazza, 1995; Churcher, 1991)). Figure 4a

shows an image of Berea sandstone where kaolinite particles can be observed concentrated in some pores and not in others (Schembre and Kovscek, 2005) [Manuscript II, III]. This suggests that intergranular pores would indeed form connected a flow path and control permeability. Accordingly the effective S_p of the Berea sandstone sample in Figure 4a is 1.5 m^2/cm^3, whereas the $S_{p,BET}$ is 19 m^2/cm^3 [Manuscript II].

By contrast Figure 4b shows a sample of kaolinite rich Rotliegend sandstone with an effective S_p of 34 m^2/cm^3 and an $S_{p,BET}$ of 37 m^2/cm^3 [PETGAS]. This suggests that the specific surface of kaolinite particles is effective for permeability. Only a small fraction of the intergranular porosity does not contain kaolinite particles, therefore larger clay-free pores might not form a connected flow path [Manuscript IV].

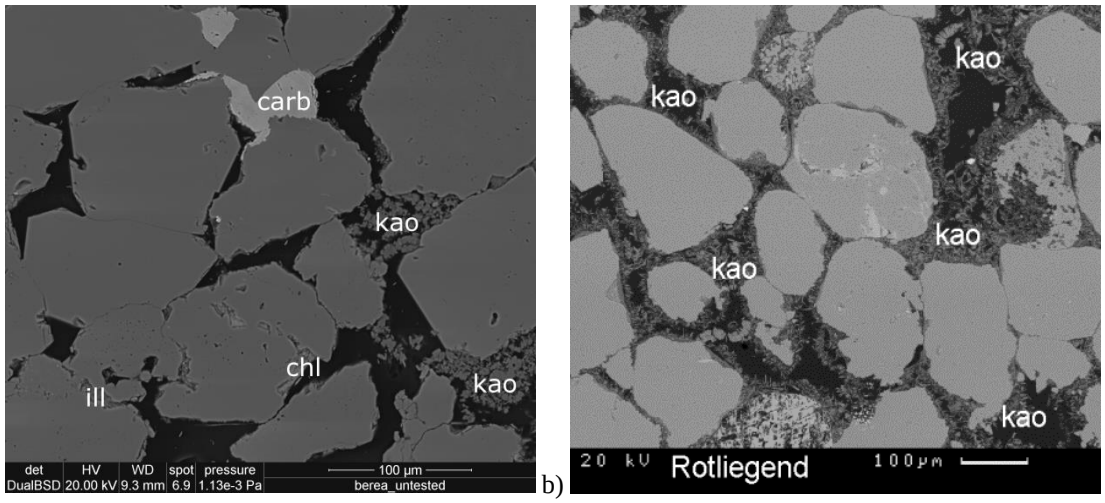

Figure 4: Backscatter electron microscopy, BSEM, images. a) Kaolinite particles are concentrated in some intergranular pores in a Berea sandstone sample. Some illite and chlorite minerals are also observed [Manuscript II]. b) Kaolinite particles are distributed throughout the intergranular pore volume in a Rotliegend sandstone sample [modified; BSEM image from PETGAS, University of Leeds]. Pores are black and grains are grey. (kao = kaolinite; ill=illite; chl=chlorite; carb=carbonate)

Redistribution of kaolinite particles due to fines mobilisation would increase the surface area of kaolinite that is effective to flow and reduce permeability in Berea sandstone. Fines migration in Berea sandstone is addressed in Chapter 6.

2.4.2 Effective S_p from image analysis

Image analysis can be used to estimate the effective S_p in sandstones where permeability is controlled by larger intergranular pores (Berryman and Blair, 1987; Blair et al., 1996; Borre et al., 1995; Solymar and Fabricius, 1999) [Manuscript III]. Those authors use a resolution that does not resolve surface roughness or micropores among clay minerals. The appropriate resolution depends on the effective S_p; some authors suggest a fixed ratio of pixel length, l_{pix}, to effective S_p can be used (Berryman and Blair, 1987). This could be compared to flow in cylindrical pipes, where the effect of surface roughness depends on the scale of asperities relative to the pipe diameter. Accordingly, the resolution used to quantify the effective S_p in images

of samples of Gassum Formation sandstone and Bunter Formation sandstone is too low to quantify the effective S_p for samples of Berea sandstone [Manuscript III]. The effective S_p of the latter is approximately twice as large as that of the former two samples (Figure 5). However, increasing resolution by a factor two still underestimates the effective S_p of the Berea sandstone samples. This does not support the suggestion of a fixed ratio of l_{pix} to effective S_p; hereby resolution might be considered as a fitting factor that can be used to compare among samples, rather than to predict permeability.

The S_p as determined by using image analysis is higher for the Gassum sandstone sample than for the Bunter sandstone sample in Figure 5, in accordance with the effective S_p of the respective samples. By contrast, $S_{p,BET}$ is higher in the Bunter sample, in accordance with a higher clay mineral content in this sample [Manuscript III]. The higher effective S_p of the Gassum sample is probably due to the smaller size of framework grains (Figure 5a) as compared to the size of the framework grains of the Bunter sandstone, (Figure 5b). Presumably, intergranular pores control permeability in both samples; therefore the effective S_p would relate to the specific surface of the framework grains. Image analysis resolves differences in grain size of the framework grains, rather than the specific surface of clay minerals, and thereby gives a better estimate of the effective S_p than $S_{p,BET}$ does.

a) 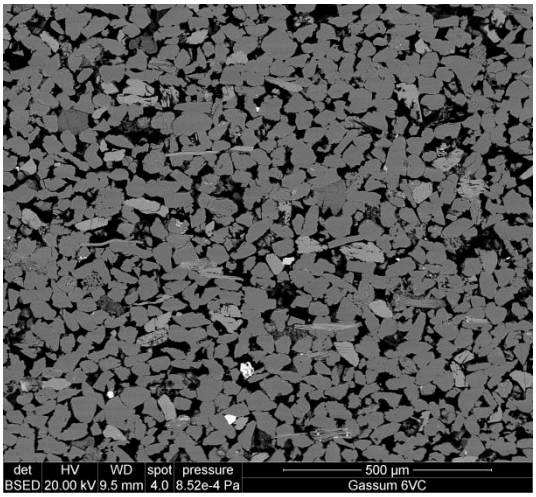

b) 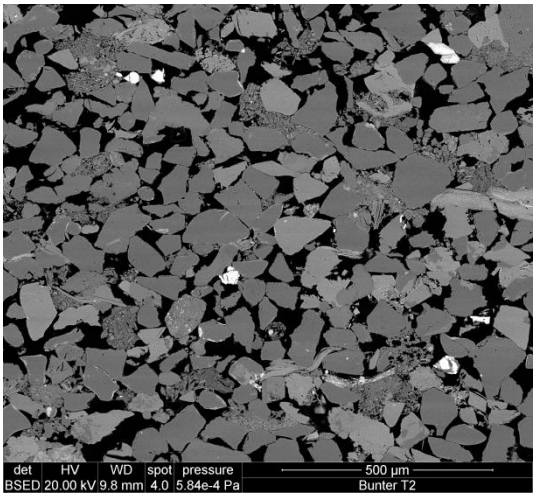

c) 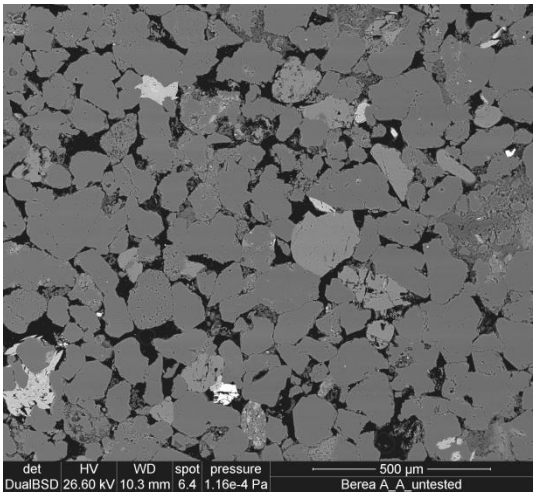

	porosity %	effective S_p for permeability m^2/cm^3
a: Gassum	28.6	0.69 (2)
b: Bunter	30.6	0.51 (2)
c: Berea	17.4	1.37 (7)

Figure 5: Backscatter electron microscopy, BSEM, images of: a) A Gassum Formation sandstone sample. b) A Bunter Formation sandstone sample. c) A Berea sandstone sample. Porosity is black, minerals are grey. [Porosity and permeability data are from Manuscript III].

Possibly, S_p can be characterised by a fractal relation; thereby $S_{p,R1}$, as measured at resolution R_1 is related to $S_{p,R2}$ as measured at resolution R_2 by Eq.(20) (Pape et al., 1999, 2006).

$$\frac{S_{p,R1}}{S_{p,R2}} = \left(\frac{R_2}{R_1} \right)^{D_f - 1} \tag{20}$$

where D_f is the fractal dimension. The empirical parameter D_f depends on texture and mineralogy (Giménez et al., 1997). Image analysis at different resolutions is applied to estimate D_f, in order to relate $S_{p,BET}$ to the effective S_p, by Pape et al. (1999, 2006). However, clay minerals would increase S to a greater extent at higher resolutions, i.e., D_f would depend on the range in which this is measured (Pape et al., 2006). Therefore, D_f as determined by using image analysis with a resolution range of the order of micrometres might differ from D_f when the resolution is approximately the size of one adsorbed nitrogen molecule for BET measurements, i.e. approximately 0.162 nm^2 (Sing, 2001).

An average grain size, r_s, of the framework grains is estimated by using image analysis by Walderhaug et al. (2012). Those authors use the Kozeny equation, with a constant c that is fit to data, to model permeability within a factor four for over 75% of 415 sandstone samples with clay contents less than 3 vol.%. from the Norwegian continental shelf. This method tends to overestimate permeability in samples with a higher clay content (Walderhaug et al., 2012). Presumably that is because r_s of the framework grains underestimates the effective S_p in samples where permeability is controlled by the smaller pores.

In order to relate the 2D specific pore interface per unit pore area, I_p, to the 3D S_p, or to estimate r_s, a conversion factor is required in Eq. (21)(Peters, 2009; Solymar and Fabricius, 1999; Weibel, 1989):

$$S_p = KI_p \tag{21}$$

where K is a constant. For perfect spheres $K = 4/\pi$, which is also used for sandstone by several authors (Peters, 2009; Solymar and Fabricius, 1999; Weibel, 1989). Crandell et al. (2012) compare pore sizes from 2D backscatter electron microscopy, BSEM, images to pore sizes that were estimated from 3D micro-computed tomography, μ-CT, and suggest, K = 2.11 for a sediment packed column. When K is considered to depend on pore geometry, this parameter might be considered as a fitting parameter.

Image based quantification of parameters that are relevant to experiments on core plugs requires that a minimum representative area, MRA, is analysed (Bear, 1972; Landrot et al., 2012; Solymar and Fabricius, 1999). An MRA can be estimated by quantifying an average property, such as ϕ or S_p, in an increasingly large interrogation area until the value stabilises (Bear, 1972). Figure 6a shows that the MRA of ϕ for a sample of Bunter sandstone would be between 20 mm^2 and 25 mm^2 [Manuscript III]. Lamination results in an apparent REV within a lamina, which changes as the area is increased to include multiple laminae; as observed in a sample of Berea sandstone in Figure 6b. This sample was altered by injection of 80°C NaCl solution [Manuscript II], however, lamination on a scale of millimetres is also observed in untested Berea sandstone samples by Knackstedt et al. (2001).

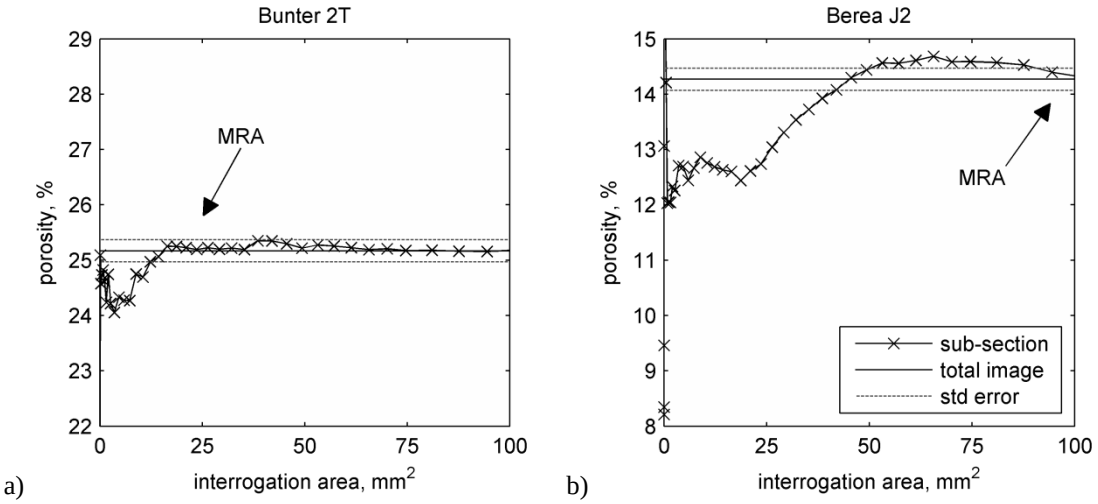

Figure 6: Porosity as a function of interrogation area in images of polished thin sections of sandstone samples; the minimum representative area, MRA, is the minimum size where porosity becomes constant as a function of interrogation area. a) The MRA of porosity for a sandstone sample from Bunter Formation is between 20 mm^2 and 25 mm^2. b) The MRA of porosity in a sample of Berea sandstone shows a plateau around 8 mm^2 due to lamination; whereas the MRA appears to stabilise at 100 mm^2, lamination on the plug scale might result in a higher MRA. [Manuscript III].

2.4.3 Effective S_p and percolation

Permeability of effectively clay-free samples of Fontainebleau sandstone is overestimated by using the Kozeny equation based on r_s and a constant c in samples where ϕ is less than 5%–10%; by contrast in Fontainebleau samples with 10% < ϕ < 30% permeability is modelled well by using this method (Bourbie and Zinszner, 1985; Mavko and Nur, 1997; Walderhaug et al., 2012). Authors of those studies suggest that percolation effects might play a role at low ϕ (Bourbie and Zinszner, 1985; Mavko and Nur, 1997; Walderhaug et al., 2012) .

Percolation theory relates to the probability of spatial connectivity among objects (Kirkpatrick, 1973). Porosity could be considered as a network of pores, where each pore is connected to one or to several other pores, so that a connected path exists. When pores are randomly removed, a point is reached at which there is no longer a path across the network, i.e., the network is no longer percolating (Hunt, 2009; Sahimi, 2011). The minimum porosity that is required in order to have a percolating network is the percolation threshold. Permeability of a network can be related to the porosity that exceeds the percolation threshold by a power law (Hunt, 2009). Therefore Mavko and Nur (1997) suggest a modification of the Kozeny equation, cf. Eq.(22).

$$k = c\frac{(\phi-\phi_c)^3}{(1-\phi+\phi_c)}r_s^2 \tag{22}$$

where ϕ_c is an empirical parameter that relates to the percolation threshold (Mavko and Nur, 1997). Values in the range 2.5% to 5% are fit to data of Fontainebleau sandstone, and to samples from different sandstone formations of the Norwegian continental shelf (Mavko and Nur, 1997; Walderhaug et al., 2012).

In samples with a low porosity, permeability might be controlled by flow in microfractures along grain boundaries, rather than by intergranular pores (Brower and Morrow, 1985; Morrow et al., 1983; Ostensen, 1983). Whereas the Kozeny equation is not restricted with regard to pore shape, r_s would relate to the S_p of intergranular pores rather than the S_p of microfractures. Figure 7 shows a Rotliegend sandstone sample where ϕ = 4.0%; both intergranular pores and fractures can be observed. When intergranular pores are only connected by microfractures the flow rate, and accordingly the effective S_p, would not reflect the S_p of the intergranular pores. Whereas Eq.(22) reflects that part of the porosity does not control permeability, this expression does not reflect that the effective S_p would not be characterised by r_s. Furthermore, introducing ϕ_c was found to only improve permeability fitting in samples with a low porosity by Walderhaug et al. (2012).

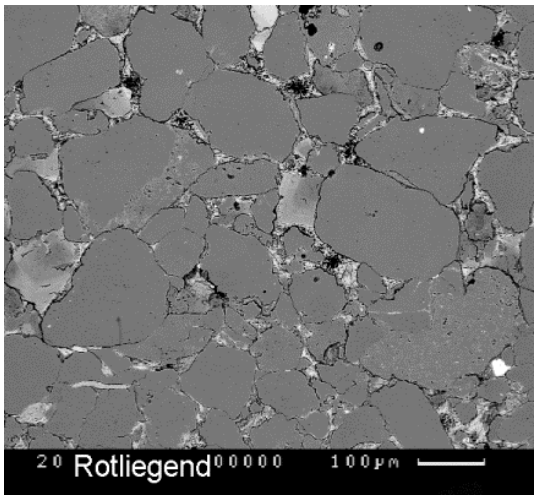

Figure 7: Backscatter electron microscopy, BSEM, image of a Rotliegend tight gas sandstone sample with 4.0% porosity. Porosity is black, minerals are grey. [PETGAS, University of Leeds].

Permeability is sometimes modelled by using pore network models, which are based on the analogy between permeability to fluid flow and resistance to electrical current (Dullien, 1975; Fatt, 1956; Sahimi, 2011). The porosity is represented as a pore network, consisting of pore bodies that are connected by pore throats. Each pore body is connected to two or more other pore bodies through a pore throat, and each pore throat is assigned a permeability. By solving a system of equations for the pressure distribution, the flow through the network, and the network permeability, can be calculated (Dullien, 1975; Sahimi, 1993). This method can be used to account for a pore size distribution, and for percolation effects. Characterisation of the network requires a number of parameters including: the number, the orientation, and the permeability of pore throats (Blunt et al., 2013; Rahmanian et al., 2013; Sahimi, 1993; Walderhaug et al., 2012). Image based methods, including 2D BSEM images and 3D μ-CT scans can be used to estimate these (Beckingham et al., 2013;

Blunt, 2001; Blunt et al., 2013). However, as the definition of pore bodies and pore throats can be ambiguous, network characterisation methods require verification. (Blunt et al., 2013; Kim et al., 2013; Lindquist et al., 2000; Walderhaug et al., 2012). Furthermore, image based characterisation depends on resolution; Beckingham et al. (2013) characterise the network properties by using images with l_{pix} = 1.8 μm and with l_{pix} = 3 μm–4 μm. At the higher resolution more smaller pore throats are identified, and more pore throats are assigned a smaller size, resulting in a network permeability of approximately 7 mD; at a lower resolution the permeability is approximately 450 mD (Beckingham et al., 2013).

Rather than simplifying pore geometry, permeability can also be calculated by using numerical methods, such as Lattice Boltzmann simulations, on a 3D representation of the porosity acquired directly from μ-CT (Blunt et al., 2013; Mostaghimi et al., 2013; Prodanović et al., 2007). This method would also be sensitive to the resolution used. For sandstones in which permeability is controlled by small pores (e.g., Figure 4a and Figure 7) a small voxel, volume element, size would be required in order to resolve the connecting pores. Indeed in a Rotliegend sample with ϕ = 9%, the volume of connected pores is only 1% when a voxel size of approximately 1 μm^3 is used by Landrot et al. (2012); the majority of the pores appear to be disconnected. Focussed ion beam, FIB, sectioning in combination with BSEM allows a characterisation of the porosity among clay minerals of the order of nanometres, which indicates that larger pores would be connected through micropores in a tight gas sandstone sample examined by Landrot et al. (2012). However, whereas in the image plane a nanometre scale resolution is achieved, due to the finite thickness of the FIB sections, the resolution in the third dimension would be lower. Furthermore, calculating the permeability in a representative elementary volume, REV the 3D equivalent of an MRA, at a high resolution increases computational costs. Currently 8000 voxels may be considered as a large volume (Blunt et al., 2013). With a voxel side of 10 nm, an 8000 voxel cube has a length of 20 μm; this is comparable to the framework grain size in some sandstones (e.g. Figure 7), which is presumably smaller than the REV.

2.4.4 Effective S_p from nuclear magnetic resonance

Nuclear magnetic resonance, NMR, transverse relaxation time can also be used to characterise S_p (Coates et al., 1999; Dastidar et al., 2006; Hossain et al., 2011; Kleinberg, 1996; Pape et al., 2006; Sen et al., 1990). In NMR, hydrogen nuclei in water saturated samples are aligned in a permanent magnetic field and flipped in a temporary magnetic field, and the consequent rate of decay of magnetisation is measured and converted to a transverse relaxation time, T_2, distribution (Coates et al., 1999; Kleinberg, 1996; Sen et al., 1990). The decay rate of magnetisation is higher near the water-solid interface than in the bulk water. So in the fast diffusion regime, in which the majority of hydrogen nuclei are relaxed at the fluid-solid interface by surface relaxation, the T_2, time reflects S_p as in Eq.(23) (Coates et al., 1999; Kleinberg, 1996; Sen et al., 1990).

$$T_2 = \frac{1}{\rho S_p} \tag{23}$$

where ρ is the surface relaxivity, which depends on the minerals present (Alam et al., 2014; Keating and Knight, 2007, 2010). If ρ is assumed uniform, ρ can be estimated by combining pore size distributions from mercury injection with the T_2 distribution from NMR (Coates et al., 1999; Dastidar et al., 2006; Mbia et al., 2014) [Section 7.8.2].

The SDR equation, or as the Mean T_2 equation, Eq.(24), can be used to estimate permeability from NMR logs (Coates et al., 1999).

$$k = aT_{2,gm}^2\phi^4 \tag{24}$$

where a is an empirical constant, $T_{2,gm}$ is the geometrically weighted mean T_2. This equation reflects the same proportionality between permeability and $1/S_p^2$ as the Kozeny equation (Hossain et al., 2011), but a different proportionality between k and ϕ.

NMR is also used to estimate S_p for the Kozeny equation by different authors. Whereas Pape et al. (2006) estimate and average S_p from $T_{2,gm}$; Hossain et al. (2011) account for the pore size distribution by calculating the permeability of each increment of the T_2 distribution (cf. Eq.(23), (11), and (19)):

$$k_i = c_i\rho^2\phi f_{NMR,i}T_{2,i}^2 \tag{25}$$

where $f_{NMR,i}$ is the fraction of the total porosity that has a specific $T_{2,i}$, and k_i is the permeability of $\phi f_{NMR,i}$. The sample permeability would be obtained by summation of the individual permeabilities (Hossain et al., 2011):

$$k = \sum_i k_i \tag{26}$$

This can be considered as a physically based approach to extend the Kozeny equation to model permeability of porous media with different pore sizes. By summing k_i rather than by summing $\phi S_{p,i}$ the contribution of pores is weighted by their contribution to flow, rather than by their contribution to the pore volume. Therefore larger pores with a higher k_i make a proportionally larger contribution to permeability than the same pore volume of smaller pores does.

Summation over all pores would model k in samples where all pores contribute to permeability. In samples of North Sea greensand, where clay minerals are concentrated in glauconite grains and intergranular porosity exceeds 15%, summation over the full T_2 range estimates the measured permeability (Hossain et al., 2011). By contrast, in samples where larger pores are only connected through smaller pores, the permeability of the

larger pores as estimated from the T_2 might not be effective for flow, as the flow rate would be limited by the smaller connecting pores. Therefore, the fraction of the pores that can be considered effective for permeability, is estimated by summation of k_i starting from the smallest $T_{2,i}$, i.e., the smallest equivalent pore size, up to the T_2 where the cumulative permeability equals the measured gas permeability in Manuscript IV.

Figure 8 shows the T_2 distribution and k_i of the fraction of pores that are considered effective for permeability for two samples of Rotliegend sandstone. Nearly the full pore volume would be effective in Sample 5B, which suggests that larger pores form a connected flow path. By contrast, in Sample 1A only the smaller pores appear to contribute to the measured permeability.

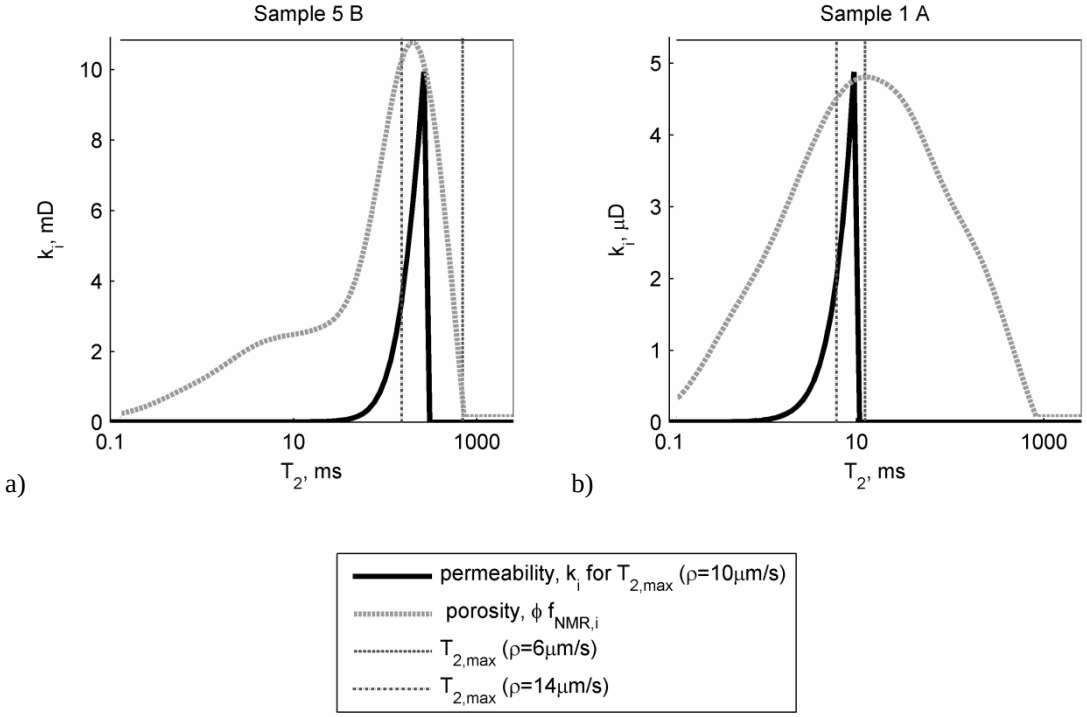

Figure 8: The dashed grey line shows the T_2 distribution from NMR; the height of the curve shows the porosity in the increment, $\phi f_{NMR,i}$. Permeability for each increment, k_i, (black line) is shown for increments that can be considered effective to permeability for a surface relaxivity, ρ = 10 µm/s. The fraction of porosity that is effective to permeability would be larger if ρ were smaller; vertical dashed lines shown the maximum T_2 that is effective for permeability, $T_{2,max}$, for ρ = 6 µm/s and for ρ = 14 µm/s. a) Most of the pore volume contributes to permeability in Rotliegend sandstone Sample 5B; total porosity, ϕ, ϕ = 17.9%. b) Only smaller pores contribute to permeability in Rotliegend sandstone Sample 1A, ϕ = 12.2%. [Manuscript IV].

The clay-free porosity from image analysis indicates in which samples larger pores would be effective for permeability; Sample 5B has a clay-free porosity of 13%, whereas sample 1A only has 1.0% clay-free porosity (Figure 9). [Manuscript IV].

A similar effect of clay minerals on permeability is modelled by using a simulated pore network model by Mehmani and Prodanović (2014). A network of larger, macropore bodies and macropore throats is generated based on a packing of spherical grains. Subsequently, some macropore throats are replaced by a second

network of smaller micropore bodies and micropore throats. Permeability decreases gradually as more macropore throats are replaced by micropore throats, and a sharp permeability reduction is observed when the macropores are no longer percolating, i.e., when macropores are only connected through micropores (Mehmani and Prodanović, 2014).

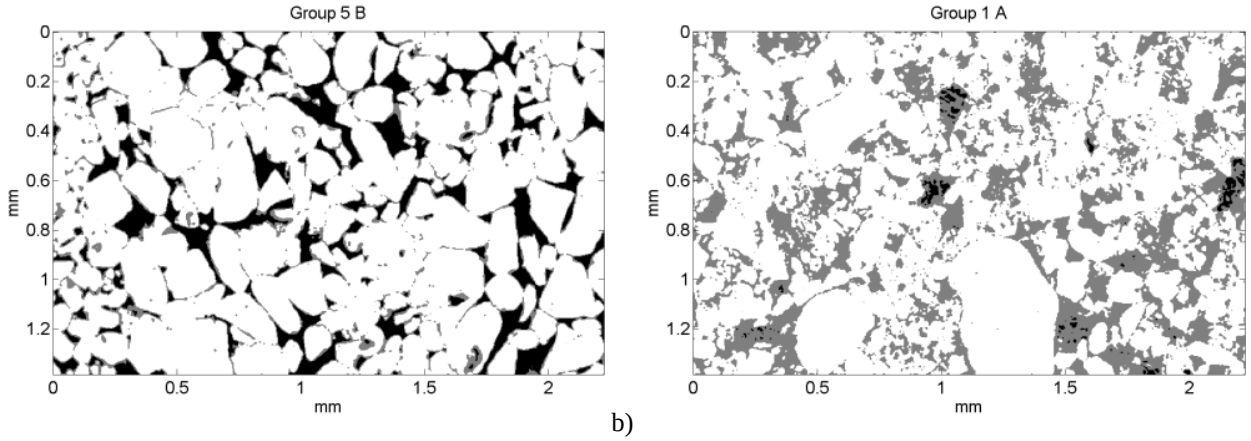

Figure 9: Segmented backscatter electron microscopy, BSEM, images, white pixels are grains, grey pixels contain clay minerals and porosity, and black pixels are clay-free porosity. Pixel length 3 μm/pixel. [Manuscript IV].

The maximum r_p that would be effective to permeability, $r_{p,NMR,max}$, is larger than the r_p estimated from the Kozeny equation $r_{p,kozeny}$ (cf. Eq.(27)). For 63 Rotliegend sandstone samples, which are analysed in Manuscript IV, $r_{p,NMR,max}$ is two to four times larger than $r_{p,kozeny}$ (Figure 10). This difference would be expected; Figure 8 shows that only a fraction of the total porosity makes a significant contribution to k (cf. Eq.(25) and Eq.(26)); by contrast, the full porosity is included in Eq.(27).

$$r_{p,kozeny} = \frac{2}{S_p} = 2\sqrt{\frac{k}{c\phi}} \tag{27}$$

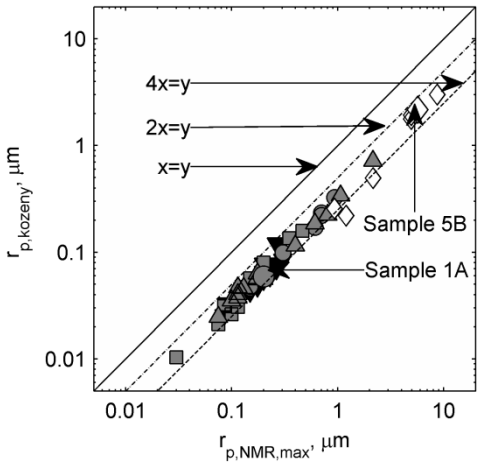

Figure 10: The maximum effective equivalent pore size based on permeability of each T_2 increment, $r_{p,NMR,max,}$ is between two and four times larger than the effective equivalent pore size as estimated from the total porosity and the measured permeability by using the Kozeny equation, $r_{p,kozeny.}$ [Data from PETGAS, University of Leeds].

3 Permeability to gas

3.1 Gas flow regime

The zero velocity boundary condition that is used to solve the Navier-Stokes equations in Chapter 2 would not necessarily apply for gas flow. During gas flow, driven by ΔP, gas molecules that have collided with the fluid-solid interface may lose their momentum parallel to ΔP, however, gas molecules close to the interface that have not collided with the interface would still have their momentum; therefore the average velocity parallel to ΔP of all molecules near the fluid-solid interface would be greater than zero (Cao et al., 2009; Klinkenberg, 1941).

The mean free path length, $\bar{\lambda}$, characterises the average distance that a gas molecule in the bulk gas travels before colliding with another gas molecule; $\bar{\lambda}$, depends on the nature of the gas, the temperature, T, and the mean pore pressure, $\bar{P}$, cf. Eq.(28) (Loeb, 1927).

$$\bar{\lambda} = \frac{\mu}{\bar{P}}\sqrt{\frac{RT\pi}{2M}} \tag{28}$$

where M is the molar mass of the gas and R is the gas constant.

Within distances of the order of $\bar{\lambda}$ from the fluid-solid interface, collisions between gas molecules and the interface are more frequent than collisions among gas molecules. This layer is known as the Knudsen layer, and the gas flow regime in a capillary can be characterised by the Knudsen number, Kn (Cao et al., 2009; Karniadakis et al., 2005):

$$Kn = \frac{\bar{\lambda}}{r} \tag{29}$$

where r is a characteristic length scale, which would be the radius, r_p, for cylindrical capillaries.

When Kn < 0.001, the effect of the Knudsen layer on the volumetric flow rate is insignificant; flow is in the continuum regime and can be characterised by the Navier-Stokes equations with a zero slip wall velocity. When 0.001 < Kn < 0.1, flow is in the slip regime; the Navier-Stokes equations are valid in the bulk flow, however, the volumetric flow rate is increased due to a non-zero wall velocity. When 0.1 < Kn < 10, flow is in the transition regime where the Navier-Stokes equations are no longer valid due to rarefaction effects (Cao et al., 2009). The gas can no longer be considered as a continuum and $\bar{\lambda}$ depends on Kn (Karniadakis et al., 2005). When Kn > 10, flow is in the free molecular regime (Cao et al., 2009).

3.2 Klinkenberg equation for gas slip

The effect of slip flow on permeability is modelled by Klinkenberg (1941) based on a slip flow model for cylindrical capillaries by Kundt and Warburg (1875). Half the gas molecules in the Knudsen layer are assumed to have lost all momentum parallel to ΔP due to collision with the fluid-solid interface, i.e. diffuse collisions as opposed to spectral collisions; the other half of the gas molecules in the Knudsen layer have the velocity of their last collision in the bulk flow. Therefore the average velocity in the Knudsen layer is half the velocity that molecules have at the location of the last collision with other gas molecules (Klinkenberg, 1941). By assuming that velocity increases linearly with distance from the interface, and that a proportionality factor c_{slip} characterises the average ratio between $\bar{\lambda}$ and the distance from the interface where the last collision among gas molecules occurs, the velocity on the wall is expressed by Eq.(30) (Klinkenberg, 1941; Kundt and Warburg, 1875).

$$v_{wall} = c_{slip}\bar{\lambda}\frac{dv}{dy} \tag{30}$$

where v is velocity in the cylindrical capillary, v_{wall} is the velocity on the wall, and y is the distance perpendicular to the wall. This is a first order slip condition, where v_{wall} depends linearly on the velocity gradient (Cao et al., 2009); this is an estimate, as the velocity gradient would probably decrease with increasing distance from the wall (Klinkenberg, 1941). Klinkenberg (1941) suggests that c_{slip} might be approximately one, but the parameter would depend on pore geometry and surface roughness.

As the volume of a given amount of gas depends on pressure, cf. the ideal gas law $\bar{P}V = nRT$, Klinkenberg (1941) derives the expressions for slip flow in terms of the mole flow rate, Q_M, rather than the volumetric flow rate, Q. Solving the Navier-Stokes equations for flow in a straight cylindrical capillary with a wall velocity cf. Eq.(30) yields Eq.(31) for Q_M (Klinkenberg, 1941).

$$Q_M = \frac{\pi r^4}{\mu 8}\bar{P}\left(1+\frac{4c_{slip}\bar{\lambda}}{r_p}\right)\Delta P \tag{31}$$

Klinkenberg (1941) models porosity as a network of straight orthogonal cylindrical capillaries, similar to Figure 3, however, without interpenetration of the capillaries. For an incompressible fluid and no slip, i.e. when Darcy's Law applies, flow would only be through 1/3rd of the capillaries; therefore the flow rate in a cube with unit length would be expressed by Eq.(32):

$$q = \frac{Q}{A} = \frac{1}{3}\frac{n\pi r_p^{\,4}}{8\mu}\Delta P \tag{32}$$

Thus permeability cf. Darcy's Law is expressed by Eq.(33) (Klinkenberg, 1941).

$$k = \frac{1}{3}\frac{n\pi r_p^{\,4}}{8} \tag{33}$$

By substitution of Eq.(33) in Eq.(31), the molar gas flow rate is expressed as Eq.(34) (Klinkenberg, 1941).

$$q_M = \frac{Q_M}{A} = \frac{k}{\mu}\overline{P}\left(1 + \frac{4c\overline{\lambda}}{r_p}\right)\Delta P \tag{34}$$

where k is cf. Eq.(33). Eq.(34) can be rewritten in a form similar to the Darcy law by introducing an apparent permeability, k_a (Klinkenberg, 1941):

$$q_M = \frac{Q_M}{A} = \frac{k_a}{\mu}\overline{P}\Delta P \tag{35}$$

where k_a is given by Eq.(36) (Klinkenberg, 1941).

$$k_a = k\left(1 + \frac{4c_{slip}\overline{\lambda}}{r_p}\right) \tag{36}$$

Considering that $\bar{\lambda}$ is inversely proportional to $\bar{P}$ (cf. Eq.(28)), Eq.(36) can be expressed in terms of a slip factor b_{slip}, which is constant as a function of $\bar{P}$ if μ is assumed constant with $\bar{P}$ (Klinkenberg, 1941):

$$k_a = k\left(1 + \frac{b_{slip}}{\overline{P}}\right) \tag{37}$$

where b_{slip} is expressed by Eq.(38):

$$b_{slip} = \frac{4c_{slip}\overline{\lambda}\,\overline{P}}{r_{p,slip}} \tag{38}$$

where $r_{p,slip}$ is the characteristic equivalent pore radius for slip flow.

Permeability and b_{slip}, can be determined by measuring k_a at different $\bar{P}$, which is known as the Klinkenberg procedure (API, 1998). In a plot of k_a versus $1/\bar{P}$, a Klinkenberg plot, k is the y-intercept, and the gradient is $b_{slip}k$ (Figure 11). Whereas b_{slip} depends on both the properties of the rock and on the properties of the gas (cf. Eq.(38) and Eq.(28)), $r_{p,slip}$ would relate only to the rock properties and can be used to estimate permeability to different gasses, at different $\bar{P}$, and at different T (Klinkenberg 1941).

3.2.1 Extension of the Klinkenberg equation

For sandstones with a small r_p, such as tight gas sandstones, flow might be in the transition regime, where alternative gas flow models are required (Ertekin et al., 1986; Florence et al., 2007; Rahmanian et al., 2013). A unified slip flow model is derived by Beskok and Karniadakis (1999), which these authors suggest is valid over the entire range of Kn. The model is based on a second order slip boundary condition; the velocity at the wall is dependent on the first and the second derivatives of velocity (Cao et al., 2009). As in the Klinkenberg model, collisions of gas molecules with the wall are diffuse. In order to account for rarefaction effects, a term, $\alpha_{B\&K}$, is included, which is a function of Kn. The volumetric flow rate is given by Eq.(39) for cylindrical capillaries and by Eq.(40) for rectangular channels (Beskok and Karniadakis, 1999).

$$Q = \frac{\pi r^4}{8\mu}\left(1+\alpha_{B\&K}Kn\right)\left(1+\frac{4Kn}{1+Kn}\right)\Delta P \tag{39}$$

$$Q = \frac{C_{B\&K} w h_{RC}^{\ 3}}{12\mu}\left(1+\alpha_{B\&K}Kn\right)\left(1+\frac{6Kn}{1+Kn}\right)\Delta P \tag{40}$$

where $C_{B\&K}$ is a constant that depends on the ratio of channel width, w, to channel height, h_{RC}, and the rarefaction parameter $\alpha_{B\&K}$, is expressed by Eq.(41) (Beskok and Karniadakis, 1999).

$$\alpha_{B\&K} = \alpha_{0,B\&K}\frac{2}{\pi}\tan^{-1}\left(\alpha Kn^{\beta}\right) \tag{41}$$

where $\alpha_{0,B\&K}$ characterises flow in the free molecular flow regime ($\alpha_{0,B\&K} = 64/15\pi$ for cylindrical capillaries, $\alpha_{0,B\&K} = 1.527$ for rectangular channels where $w/h_{RC} = 4$), and α and β are empirical parameters ($\alpha = 4$ and $\beta = 0.4$ for cylindrical capillaries; $\alpha = 2.5$ and $\beta = 0.5$ for rectangular channels where $w/h_{RC} = 4$) (Beskok and Karniadakis, 1999).

Using the same derivation as Klinkenberg (1941), Florence et al. (2007) derive permeability when the gas flow rate is expressed cf. Eq.(39) resulting in Eq.(42). Considering that flow in microfractures may be characterised by rectangular channels with a high ratio of w/h_{RC} rather than by cylindrical capillaries, the same derivation is used here to express flow in rectangular channels in Eq.(43).

$$k_a = k\left(1+\alpha_{B\&K}Kn\right)\left(1+\frac{4Kn}{1+Kn}\right) \tag{42}$$

$$k_a = k\left(1+\alpha_{B\&K}Kn\right)\left(1+\frac{6Kn}{1+Kn}\right) \tag{43}$$

Therefore when the unified slip model is used, b_{slip} would be expressed by Eq.(44) (cf. Eq.(42), (43), and Eq.(37)).

$$b_{slip} = \bar{P}\left[\left(1+\alpha_{B\&K}Kn\right)\left(1+\frac{S_{B\&K}Kn}{1+Kn}\right)-1\right] \tag{44}$$

where $S_{B\&K}$ is 4 for cylindrical capillaries and 6 for rectangular channels.

3.2.2 Klinkenberg procedure to determine permeability and $r_{p,slip}$

The effect of using different gas flow models, and of using a model for cylindrical rather than for rectangular capillaries, is shown in the Klinkenberg plot (Figure 11a), and in a plot of b_{slip} as a function of characteristic pore size (Figure 11b); Kn < 0.03 therefore both gas flow equations may be used. For thin rectangular channels, Kn = $\bar{\lambda}/h_{RC}$. For a specific h_{RC} or $r_{p,slip}$ there would be more slip, a higher k_a, for the rectangular channel model, which is also reflected by a larger b_{slip} in Figure 11b. Presumably, this partly due to using h_{RC} rather than $h_{RC}/2$. The difference between the two gas flow models for cylindrical capillaries is smaller than the difference between cylindrical capillaries and rectangular capillaries, and the difference between models increases with increasing $1/\bar{P}$, i.e., with increasing Kn. Several authors use the derivation by Florence et al. (2007), Eq.(42), to model flow in tight gas sandstones or in shale, as this model is expected to provide a better estimate of gas flow at high Kn (e.g., Civan, 2010; Freeman et al., 2011; Xu and Yu, 2008; Ziarani and Aguilera, 2012).

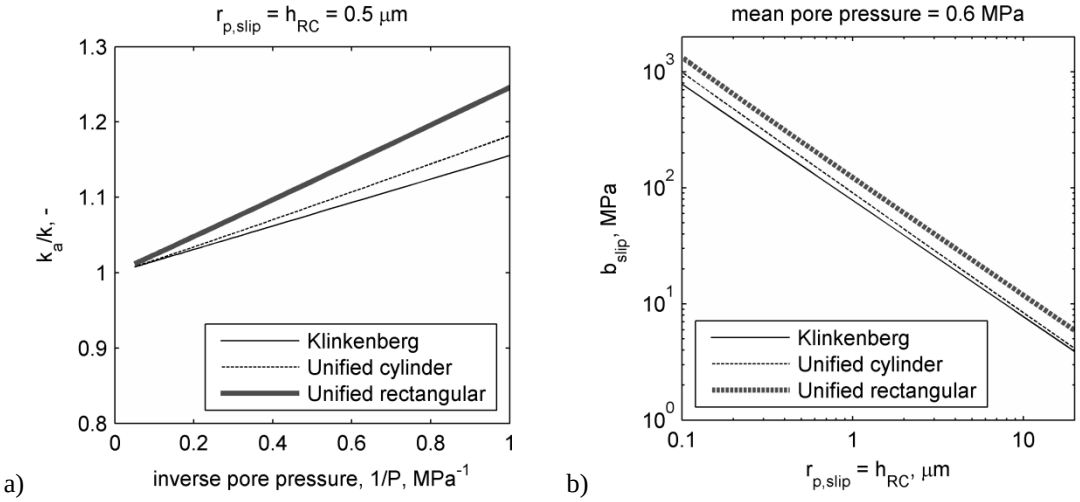

Figure 11: a) Klinkenberg plot showing the apparent permeability normalised by permeability, k_a/k, as a function of inverse mean pore pressure, $1/\bar{P}$. At the y-intercept $\bar{P} \rightarrow \infty$ so that $k_a = k$; the gradient of the lines is kb_{slip}. b) Slip factor, b_{slip} as a function of characteristic equivalent pore radius for slip, $r_{p,slip,}$ or channel height, h_{RC} as calculated for different gas flow models. Results are for helium gas at 25°C; rectangular channels have w/h_{RC} = 4.

3.3 Relating effective $r_{p,slip}$ to effective S_p

As equivalent pore size relates both to gas slip and to permeability, several authors suggest correlations between b_{slip} or $r_{p,slip}$ and k, ϕ and k, or $(k/\phi)^{1/2}$ (Civan, 2010; Florence et al., 2007; Heid et al., 1950; Jones and Owens, 1980; Sampath and Keighin, 1982). Whereas those authors include fitting factors, if $r_{p,kozeny}$ is estimated by using Kozeny's equation with c cf. Eq.(19), the same geometrical simplifications are made as in the Klinkenberg model, i.e., straight parallel capillaries with a uniform pore size. The Kozeny constant, c, is divided out in Eq.(37) as k_a is expressed in terms of k. Therefore, no additional parameters would be required in order to relate $r_{p,slip}$ to $r_{p,kozeny}$.

In Appendix A-I: Gas Slip, $r_{p,slip}$ are calculated based data from Klinkenberg procedures for samples of Rotliegend sandstone, Berea sandstone, Gassum sandstone and Bunter sandstone. Flow was in the transition regime for both experiments on samples from Rotliegend Group 6, and for experiments on sample Gassum Aa. For the remaining samples, flow was in the slip regime. For the latter, $r_{p,slip}$ as estimated unified slip model is up to 20% larger than $r_{p,slip}$ estimated based on the Klinkenberg slip model.

Figure 12 shows a correlation between $r_{p,kozeny}$ (Eq.(27)), and $r_{p,slip}$, based on the unified slip model for cylindrical pores (Eq.(42)). The two equivalent pore sizes are within a factor five from each other for samples of: Rotliegend sandstones from three localities, Berea sandstone, and for Gassum Formation sandstone from three localities; for Bunter Formation sandstone from one locality $5r_{p,slip} < r_{p,kozeny}$.

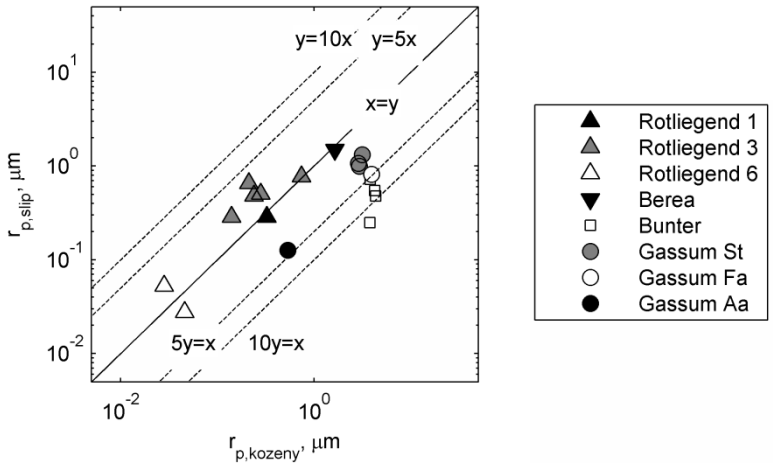

Figure 12: The characteristic equivalent pore radius for slip, $r_{p,slip}$, is calculated by using the unified flow model for cylindrical capillaries. The effective radius for permeability, $r_{p,kozeny,}$ is calculated from porosity and permeability by using the Kozeny equation. [Rotliegend sandstone samples are from PETGAS, University of Leeds; other samples are from the Geological Survey of Denmark and Greenland (GEUS) Core Laboratory. Refer to Appendix A-I for data and calculations].

Differences between r_p as estimated from permeability and from gas slip might be partly due to model assumptions, i.e., the simplification of the pore geometry to smooth walled straight tubes. Effects of surface roughness on flow in the Kozeny model would depend on the scale of the roughness relative to the effective

S_p (Berryman and Blair, 1987; Pape et al., 2006); on the other hand, effects of surface roughness on slip would depend on the ratio of the scale of the roughness relative to $\bar{\lambda}$ (Cao et al., 2006; Cao, 2007). Furthermore, the gas slip model is based on diffuse collisions between gas molecules and pore walls; if gas molecules retain some momentum, the velocity on the interface would be higher, i.e., there would be more slip for a specific $r_{p,slip}$. Therefore, models based on diffuse collisions gives a lower bound estimate for $r_{p,slip}$ from a specific b_{slip}. Nonetheless, the reasonable correlation in Figure 12, and the absence of a systematic difference between $r_{p,slip}$ and $r_{p,kozeny}$, indicates that both models give a similar approximation of equivalent pore size that is effective to flow; without introducing additional fitting parameters.

Experimental artefacts might also contribute to scatter in Figure 12 (Heid et al., 1950; McPhee and Arthur, 1991). Heterogeneity on the plug scale might possibly cause the onset of inertial energy losses at lower flow velocities, when the Reynolds number would suggest that flow is laminar (Al-Rumhy and Kalam, 1996; Noman and Archer, 1987). Inertia effects would be greater at higher $\bar{P}$, which would result in a downward deviation from the straight line in the Klinkenberg plot at high $\bar{P}$ (McPhee and Arthur, 1991). A straight line that is fit to such data would have a higher gradient i.e. a higher b_{slip} that indicates a smaller $r_{p,slip}$. Indeed, Funk et al. (1989) observe a high b_{slip} relative to ϕ and k in carbonate samples that have some distinctly larger pores. A patchy distribution of anhydrite or gypsum is observed in BSEM images of side trims of Bunter sandstone samples from the same locality as the samples in Figure 12 [Manuscript III]. Therefore, inertia might affect tests on the Bunter sandstone samples and contribute to the lower ratio of $r_{p,slip}$ to $r_{p,kozeny}$. Only three measurements are made during the Klinkenberg procedures on those samples, therefore it is difficult to distinguish whether k_a deviate from a straight line.

Data on Klinkenberg plots containing four data points by Rushing et al. (2003)[1], would suggest that k_a at the highest $\bar{P}$ is less than estimated by a straight line in those tests. Those samples are tight gas sandstones where k could be sensitive to changes in stress; to avoid changing net stress during the Klinkenberg procedure, Rushing et al. (2003) increase confining stress by the same increments as $\bar{P}$. However, the increase in confining stress might possibly reduce k, and thereby k_a, which could contribute to a downward deviation on the Klinkenberg plot at higher $\bar{P}$.

3.4 Klinkenberg procedure and net stress change

The permeability of tight sandstones is often sensitive to the stress and pore pressure at which measurements are made (Brower and Morrow, 1985; Byrnes, 1997; Jones and Owens, 1980; Keighin and Sampath, 1982; Rushing et al., 2003; Warpinski and Teufel, 1992). Permeability can be expressed as a function of the net stress for permeability i.e., $k = F(\sigma_k')$, where net stress for permeability, σ_k', can be expressed by a linear

[1] Figures 5 and 6 of that publication for samples with 0% water saturation.

combination of mean pore pressure and confining stress, σ_c (Al-Wardy and Zimmerman, 2004; Li et al., 2009; Warpinski and Teufel, 1992; Zoback and Byerlee, 1975):

$$\sigma_k' = \sigma_c - n_k \bar{P} \tag{45}$$

where n_k is the net stress parameter for permeability. In order to maintain a constant σ_k' during the Klinkenberg tests, the change in $\bar{P}$ should be compensated by a change in σ_c (Keighin and Sampath, 1982; McPhee and Arthur, 1991; Rushing et al., 2003).

The value of n_k is often not known; Berryman (1992) derives $\phi < n_k < 1$ for a homogeneous, single mineral, porous medium. For tight sandstones, some authors report n_k of approximately one (Warpinski and Teufel, 1992), whereas other authors report n_k of four to six (Al-Wardy and Zimmerman, 2004; Zoback and Byerlee, 1975). The latter authors suggested that changes in $\bar{P}$ might compact clay minerals in intergranular pores, whereas changes in σ_c only affect stiffer framework grains. However, samples in those investigations are allowed to equilibrate only from a few minutes up to two hours after changes in $\bar{P}$ or σ_c, therefore the high n_k might reflect non-equilibration of the pressure in those experiments.

Some authors suggest that a high stress sensitivity of k in tight sandstones indicates that k is controlled by microfractures along the grain boundaries, rather than by intergranular pores (Brower and Morrow, 1985; Ostensen, 1983). Closing of microfractures would reduce the stress sensitivity of k with increasing σ_k', which is in accordance with laboratory measurements of the stress sensitivity of permeability in some sandstones (Osorio et al., 1997; Ostensen, 1983). Such a trend can be approximated by a simple power law relation (Keaney et al., 2004):

$$k = K_\infty \left(\sigma_c - n_k \bar{P} \right)^{-\gamma} \tag{46}$$

where K_∞ is the permeability extrapolated to zero net stress, and γ is the stress exponent for permeability. Figure 13 indicates that Eq.(46) approximates the stress sensitivity of a Rotliegend tight gas sandstone sample.

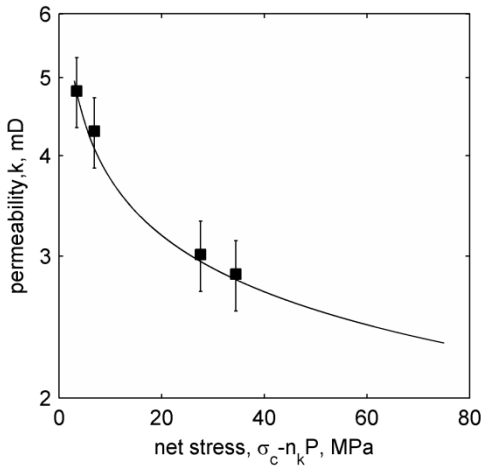

Figure 13: Permeability of Rotliegend sandstone Sample 3.4, as fit by a power law. The x-axis shows the net stress for permeability, σ_k', as the difference between confining stress, σ_c, and pore pressure, $\bar{P}$, for a net stress parameter for permeability, $n_k = 1$. Parameters fit to the power law: permeability extrapolated to zero net stress, $K_\infty = 6.5$ mD; stress exponent for permeability, $\gamma = 0.23$; correlation coefficient between data and model, $R_c = 0.997$). [Data from PETGAS, University of Leeds].

The effect of changing σ_k' on k_a during a Klinkenberg procedure is modelled by combining the expression for k_a as a function of $\bar{P}$ (Eq.(42)) with the expression for k as a function of σ_k' (Eq.(46)) to obtain Eq.(47).

$$k_a = K_\infty \left(\sigma_c - n_k \bar{P}\right)^{-\gamma} \left(\left(1+\alpha_{B\&K} Kn\right)\left(1+\frac{S_{B\&K} Kn}{1+Kn}\right)\right) \tag{47}$$

Some authors increase σ_c by the same amount as $\bar{P}$ during the Klinkenberg procedure (Rushing et al., 2003; Sampath and Keighin, 1982). However, Figure 14 shows that this would only result in a straight Klinkenberg plot if $n_k = 1$. If $n_k < 1$, k is reduced due to the increase in σ_k'; if $n_k > 1$, k increases (Figure 14a). A change in σ_k' has a greater effect on k_a at high $\bar{P}$, when the effect of slip is small due to a small Kn, or at low σ_k' when changes in σ_k' have a larger effect on k due to the power law relation.

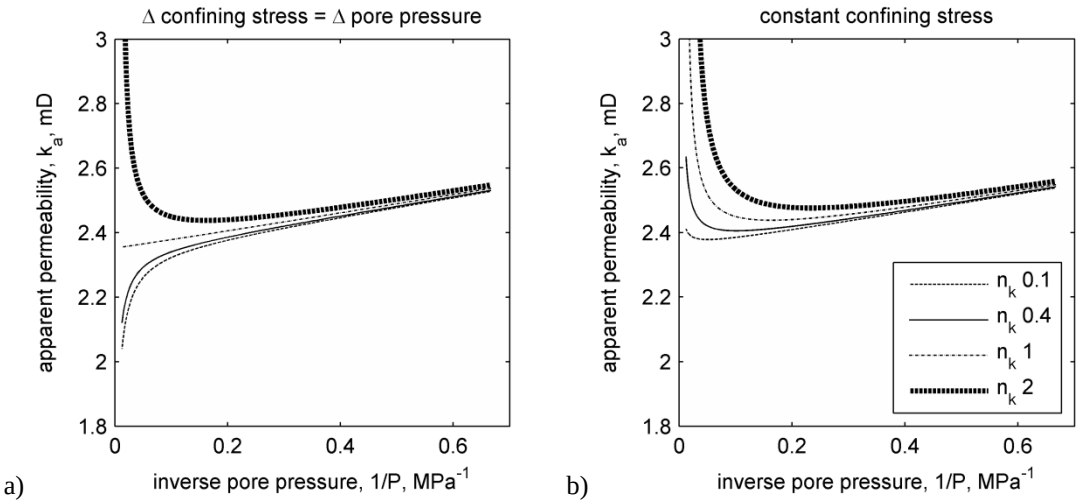

Figure 14: Apparent permeability, k_a, as a function of inverse mean pore pressure, $1/\bar{P}$, in a Klinkenberg plot. a) Confining stress, σ_c, is increased by the same amount as $\bar{P}$. b) Constant σ_c. Parameters: permeability extrapolated to zero net stress, K_∞ = 6.5 mD; stress exponent for permeability, γ = 0.23; characteristic equivalent pore radius for gas slip, $r_{p,slip}$ = 0.75 μm (based on Rotliegend sandstone Sample 3.4).

The changes in σ_k' during a Klinkenberg procedure can be reduced by using a limited range of $\bar{P}$; however, the range must be sufficient to observe a significant difference in k_a. For the tests in Figure 12, σ_c is maintained constant; therefore a change in σ_k' would cause an upward deviation of k_a (Figure 14b); which might reduce b_{slip} and overestimate $r_{p,slip}$ cf. Eq.(44). Therefore, changes in σ_k' would not account for the small ratio of $r_{p,slip}$ to $r_{p,kozeny}$ that is observed in the Bunter sandstone samples (Figure 12). No upward deviations from the Klinkenberg plots are observed in the tests used for Figure 12, and the correlation coefficient between the straight line fit and the data, R_c, exceeds 0.96 for most samples [Refer to Appendix A-I for data and calculations].

Changing $\bar{P}$ intentionally over a wide range (6 MPa to 30 MPa) at constant σ_c causes artefacts in the Klinkenberg procedure as shown in Figure 15a. At lower $\bar{P}$, increasing $\bar{P}$ reduces slip and thereby reduces k_a in accordance with the Klinkenberg model; however, around $\bar{P}$ > 20 MPa the increase in k with increasing $\bar{P}$ offsets the reduction of gas slip with increasing $\bar{P}$ whereby k_a increases.

The combined effects of gas slip and changes in permeability are relevant for production forecasting in gas reservoirs. The data in Figure 15a are shown as a function of σ_k' in Figure 15b, where the absolute permeability is estimated by using the $r_{p,slip}$ as determined from the straight portion of the Klinkenberg plot. During pressure depletion, the reduction in k due to increasing σ_k' might be offset by an increase in flow rate due to gas slip, as observed in Figure 15b.

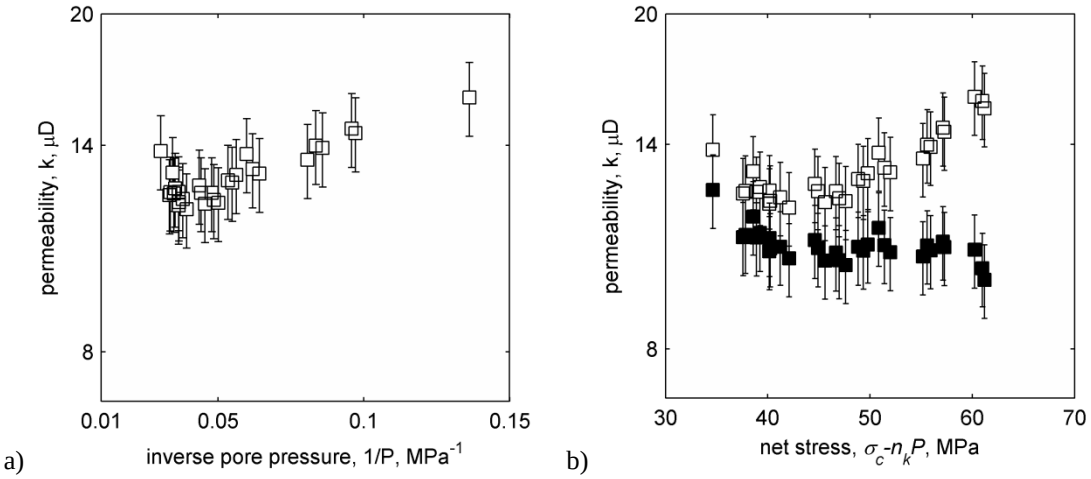

Figure 15: a) At constant confining stress, σ_c, apparent permeability (white symbols) falls with increasing pore pressure, $\bar{P}$, at low $\bar{P}$ due to the reduction of gas slip; at high $\bar{P}$ the apparent permeability, k_a, increases, presumably due to an increase in permeability, k, as the net stress for permeability, σ_k', is reduced by increasing $\bar{P}$ at constant confining stress, σ_c. b) The same k_a and k (black symbols) plotted as a function of σ_s' where the effective stress parameter for permeability, n_k = 1. [Shown is Rotliegend sandstone Sample 6.23; PETGAS, University of Leeds].

4 Permeability to water or brine

4.1 Immobile water layer thickness

The permeability that is measured by using flow with water or brine is often lower than the slip corrected gas permeability in sandstones (Heid et al., 1950; Jones and Owens, 1980; Solymar et al., 2003; Wei et al., 1986). Different factors can contribute to this difference including clay mobilisation, clay swelling, and reduction of the mobile porosity by a layer of immobile fluid on the fluid-solid interface (Andreassen and Fabricius, 2010; Bear, 1972; Faulkner and Rutter, 2000, 2003; Heid et al., 1950; Jones and Owens, 1980; Rutter, 1983; Wei et al., 1986). The effect of a layer of immobile fluid on permeability may be estimated both based on an increase in the effective S_p (Andreassen and Fabricius, 2010), and based on a reduction in the characteristic equivalent pore size which can be found for gas slip (Jones and Owens, 1980), if the thickness of immobile fluid, τ, is known. However, as different mechanisms may contribute to an immobile fluid layer, τ is uncertain.

The crystal lattice of clay minerals might induce a structuring of water molecules in layers adjacent to the water-clay mineral interface (Behnsen and Faulkner, 2011; Grim, 1953; Rutter, 1983). Different structures are suggested, with τ ranging from 0.8 nm to 4 nm (Grim, 1953, and references therein). The permeability of clay-rich fault rocks, and of different clay mineral powders, including kaolinite, illite, and chlorite is indeed lower when this is measured by using water than when this is measured by using gas (Behnsen and Faulkner, 2011; Faulkner and Rutter, 2003). Thermal energy of water molecules would counteract the structuring effect of the surface and reduce τ (Grim, 1953). This might account for the increase in the permeability of clay-rich fault rock to water that is observed by Faulkner and Rutter (2003) when they heat samples from room temperature to 80°C.

Adsorption of water on individual clay platelets might cause expansion of clay aggregates in the pores of sandstones and reduce the mobile intergranular pore volume, even for non-swelling clays like kaolinite (Behnsen and Faulkner, 2011). Expansion of dry kaolinite powders when these are moistened is observed by Rutter (1983), even in tests where kaolinite is compressed by a load 100 MPa. Rutter (1983) estimates that an adsorbed water layer with a thickness of 1nm–2 nm on the individual kaolinite particles could account for the measured expansion.

An immobile water layer might also be present on other mineral surfaces, such as quartz. Interaction between broken bonds on the mineral surface and water molecules or ions results in a layer that can be considered bound to the surface (Elimelech, 2010; Grahame, 1953; Khilar and Fogler, 1984; Lorne et al., 1999; Stern, 1924). The thickness of this bound layer, also referred to as the Stern layer in Chapter 6, can range from 0.5 nm–2.5 nm as estimated based on the surface interaction forces that are measured between mica surfaces

(Israelachvili and Adams, 1978). Additionally, surface roughness may immobilise water up to some distance beyond the Stern plane; to distances of 0.2 nm–2 nm (Ishido and Mizutani, 1981; Lorne et al., 1999). Measurement of water and brine flow in cylindrical glass capillaries with radii up to 1 μm even suggest that τ might be as large as 8 nm (Zheleznyi et al., 1972).

The forces that are exerted on the water layer may affect τ; a minimum ΔP or $\underline{Q}$ below which brine does not flow is observed by several authors in tests on clay-bearing sandstones or in clay-rich fault rocks (Bear, 1972; Byerlee, 1990; Swartzendruber, 1962). This would suggest that measurement of surface forces, or of flow through capillaries, would not necessarily represent immobile water layer thicknesses in laboratory experiments on sandstones. Therefore, in order to estimate τ that would account for measured gas and brine permeabilities, the effect of τ on permeability is modelled based on $r_{p,slip}$ in Section 4.2, and based on $r_{p,NMR,max}$ in Manuscript IV and in Section 4.3.

4.2 Brine permeability estimated from $r_{p,slip}$

As opposed to gas slip, where the velocity on the fluid-solid interface is greater than zero, τ reduces the effective equivalent pore size resulting in a water or brine permeability k_w that is smaller than the true permeability k. The volumetric flow rate in a cylindrical capillary with an immobile layer of thickness, τ, can be expressed as:

$$Q = \frac{\pi}{8\mu}\left(r_p - \tau\right)^4 \Delta P \tag{48}$$

In a model of orthogonal equal sized cylindrical capillaries with 1/3rd conducting fluid flow, the same model as used in Klinkenberg's derivation, the volume flux with immobile fluid for a unit cube is expressed by Eq.(49).

$$Q = \frac{1}{3}\frac{n\pi\left(r_p - \tau\right)^4}{8\mu}\Delta P \tag{49}$$

So that k_w is given by Eq.(50) (cf. Eq.(49) and Eq.(3)), and the ratio of k_w to k can be expressed in terms of only r_p and τ in Eq.(51) (cf. Eq.(50) and Eq.(33)):

$$k_w = \frac{1}{3}\frac{n\pi\left(r_p - \tau\right)^4}{\mu} \tag{50}$$

$$\frac{k_w}{k} = \frac{\frac{1}{3}\frac{n\pi\left(r_p - \tau\right)^4}{\mu}}{\frac{1}{3}\frac{n\pi {r_p}^4}{\mu}} = \frac{\left(r_p - \tau\right)^4}{{r_p}^4} \tag{51}$$

Permeability data from PETGAS, University of Leeds, and from the GEUS Core Laboratory, are used to estimate τ that would account for measured k and k_w in Appendix A-II.

4.3 Brine permeability estimated from S_p

A layer of immobile water on the fluid-solid interface would reduce the mobile porosity by a volume τS (Andreassen and Fabricius, 2010). For the S_p distribution from NMR, the mobile brine porosity, $\phi fw_{nmr,i}$, in a T_2 increment is given by the total porosity in the increment, $\phi f_{nmr,i}$, minus the immobile water, τS_i, on the fluid-solid interface cf. Eq.(52) [Manuscript IV]:

$$\phi fw_{NMR,i} = \phi f_{NMR,i} - \tau S_i \tag{52}$$

where $fw_{NMR,i}$ is the fraction of the total porosity in which brine is mobile. Substitution of Eq.(23) and Eq.(9) yields Eq.(53).

$$\phi fw_{NMR,i} = \phi f_{NMR,i} - \frac{\tau\phi}{\rho T_{2,i}} \tag{53}$$

The internal specific surface area, S, is not affected by τ; therefore the specific surface per volume of mobile water, $Sw_{p,i}$ is:

$$Sw_{p,i} = \frac{S_i}{\phi fw_{NMR,i}} = \frac{S_i}{\phi f_{NMR,i}} \frac{f_{NMR,i}}{fw_{NMR,i}} = S_{p,i} \frac{f_{NMR,i}}{fw_{NMR,i}} \tag{54}$$

Whereby the permeability to brine of each pore size increment, $k_{w,i}$, is expressed in Eq.(55) [Manuscript IV]:

$$k_{w,i} = \rho^2 c_{w,i} \phi fw_{NMR,i} T_{2,i}^2 \left(\frac{fw_{NMR,i}}{f_{NMR,i}} \right)^2 \tag{55}$$

The τ that would account for the measured k_w is estimated by assuming that the same pore sizes that are effective for k are also effective for k_w, so that the maximum effective equivalent pore size is $r_{p,NMR,max}$ (as found in Subsection 2.4.4). Figure 16 shows the total ϕ distribution, the distribution of ϕ that would be mobile to brine, and the k and k_w distributions for two samples of Rotliegend sandstone (these are the same samples as in Figure 8 and in Figure 9 in Subsection 2.4.4).

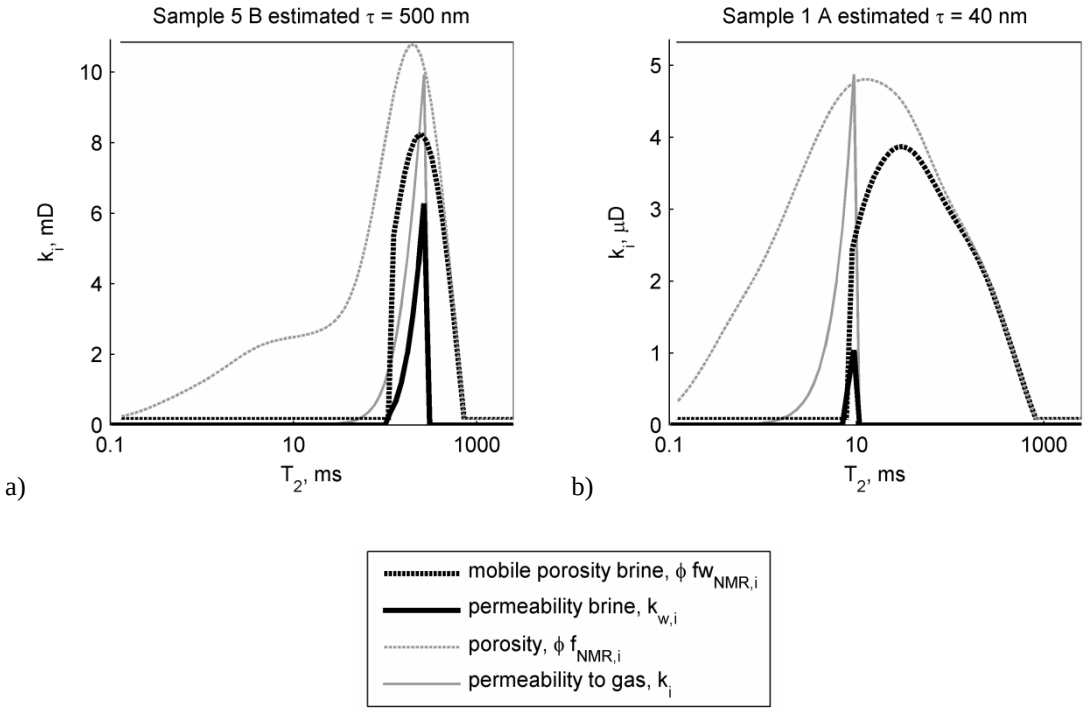

Figure 16: Permeability, k_i,(grey solid line) and permeability as measured by using brine, $k_{w,i}$, (black solid line) up to the maximum T_2 that is effective for gas permeability, $T_{2,max}$. The estimated immobile layer thickness, τ, is the thickness that would be required to account for the measured k_w. The mobile brine porosity of each increment, $\phi fw_{NMR,i}$ (black dashed line) is the total porosity of the increment $\phi f_{NMR,i}$ (grey dashed line) reduced immobile water on the solid surface, $\tau S_{p,i}$. Mobile porosity to brine is zero in pores that have an equivalent pore size smaller than τ/2 [Manuscript IV].

4.4 Estimated immobile water layer thickness

Figure 17a shows the estimated τ as a function of $r_{p,slip}$ [data in Appendix A-II]; Figure 17b shows the estimated τ as a function of $r_{p,NMR,max}$ for 63 Rotliegend sandstone samples [Manuscript IV]. With the exception of sample Gassum Aa, the τ estimated by using $r_{p,slip}$ fall on a higher trend than the τ estimated by using $r_{p,NMR,max}$. This might simply be the result of plotting $r_{p,slip}$ and $r_{pNMR,max}$ on the x-axis, the former would represent an average characteristic pore size, whereas latter represents a maximum characteristic pore size. Both NMR and Klinkenberg data are measured in only four samples for which $r_{p,NMR,max} > r_{p,slip}$ (Table C2.2); there is no consistent difference between τ estimated using the two methods for the same sample.

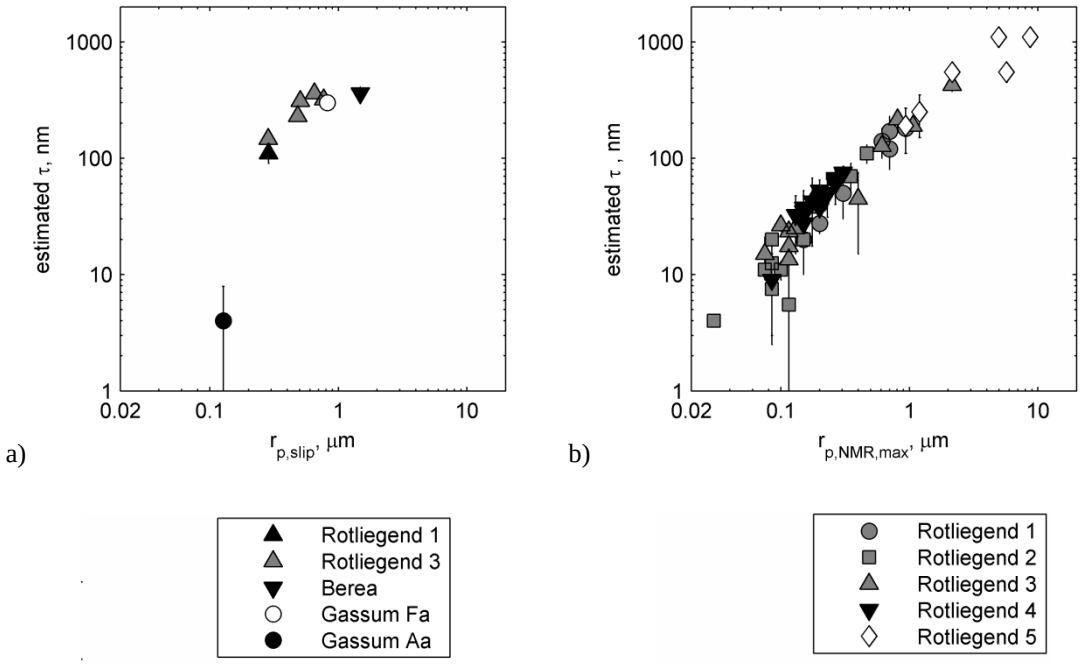

Figure 17: Thickness of immobile water, τ, that would account for the difference between the permeability and the permeability as measured by using brine. a) Based on the characteristic equivalent pore radius to gas slip, $r_{p,slip.}$ b) Based on the pore size distribution from NMR, where the maximum radius that is effective to gas flow, $r_{p,NMR,max}$, is also the maximum radius effective to brine flow. [Data for Rotliegend sandstone samples are from PETGAS, University of Leeds; data for other samples are from the Geological Survey of Denmark and Greenland (GEUS) Core Laboratory. Refer to Appendices A-I and A-II for data and calculations].

The estimated τ range from 4 nm–1200 nm; this is up to two orders of magnitude larger than the τ suggested in Section 4.1, which range from 0.2 nm–8 nm. Whereas τ might depend on the shear stress, layers of 1200 nm thickness appear unlikely.

The permeability reduction due to immobile water for $\tau < 10$ nm would be insignificant for the samples in Figure 17a; as the measured k_w would equal k. This is observed in sample Gassum Aa, which has the smallest $r_{p,slip}$ in Figure 17a. With a 10% uncertainty in the permeability measurements k_w is within the error margin of k, and $\tau = 4$ nm ± 4 nm. For samples with larger $r_{p,slip}$ the effect of τ on k_w would be smaller. Accordingly tests on a synthetic opal A plug, with an effective S_p of 0.3 m^2/cm^3, showed no significant difference between k and k_w (GEUS Core Laboratory).

When k_w is modelled based on the S_p distribution by using Eq.(55), the ratio of k_w to k would be smallest in samples where permeability is controlled by smaller pores, as shown in Figure 18a. However a wide scatter can be observed for the measured k_w/k of the Rotliegend sandstone samples as a function of $r_{p,NMR,max}$ (Figure 18b). By using $\tau = 10$ nm, k_w/k is underestimated in some samples (Figure 18c), which would indicate that $\tau < 10$ nm, in accordance with values of the order of ångströms to nanometres that are suggested in Section 4.1. However, for the majority of the samples k_w/k is overestimated; τ would be in the range of 100 nm–1200 nm (Figure 17b). This suggests that additional factors contribute to a lower k_w in those samples.

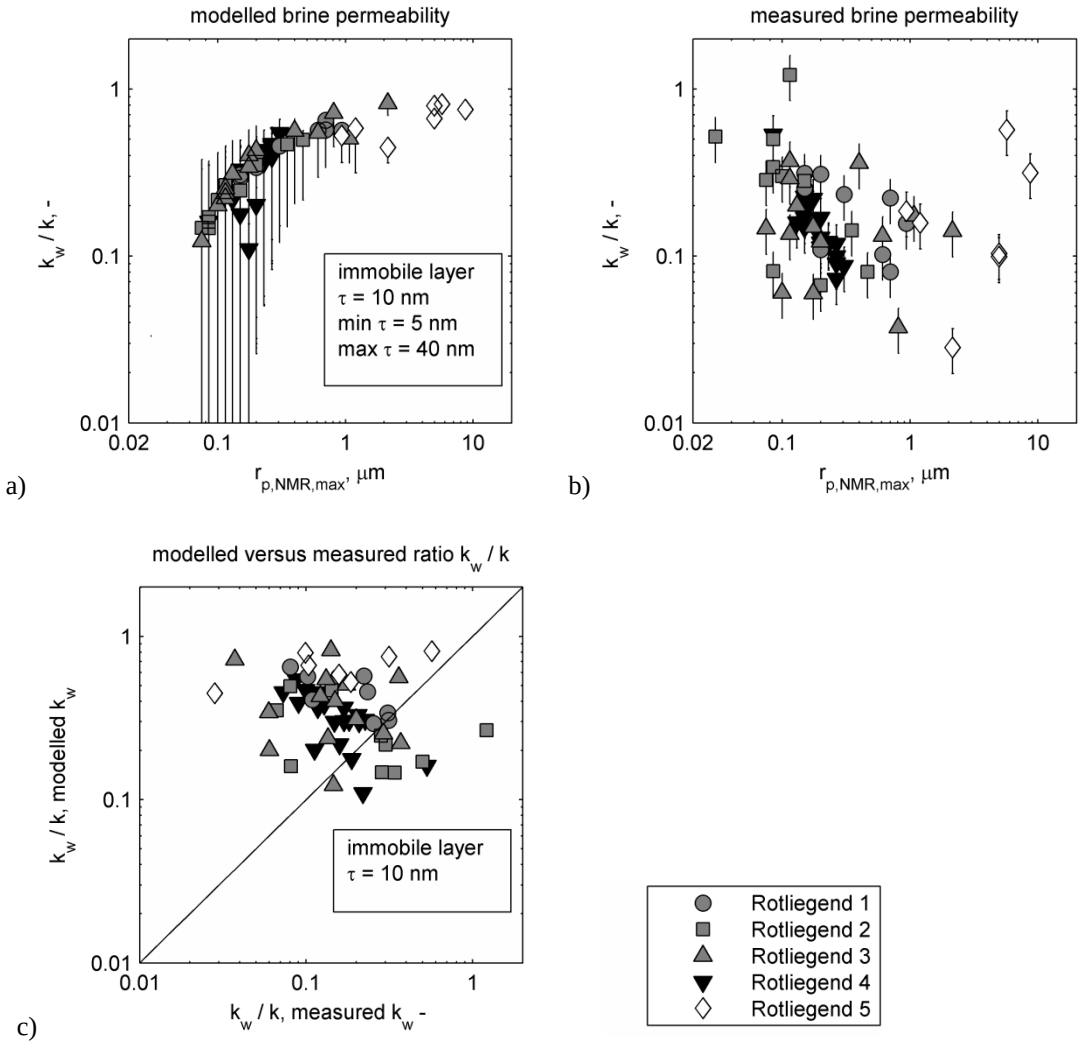

Figure 18: An immobile water layer thickness, τ = 10 nm is used to model brine permeability, k_w. a) Ratio of modelled k_w over permeability to gas, k, as a function of the maximum pore size, $r_{p,NMR,max}$, that is effective to gas permeability. b) Ratio measured k_w/k as a function of $r_{p,NMR,max.}$ c) The modelled k_w/k over predicts k_w in the majority of the sandstone samples. Error bars for τ = 5 nm and τ = 40 nm; error bars tending towards zero in a) indicate that with a 40 nm immobile layer k_w = 0 mD. [data PETGAS, University of Leeds].

4.5 Effect of clay minerals on brine permeability

Illite minerals in sandstone can often be observed: as delicate fibres that protrude perpendicular to the grain surface into the pore space; as irregularly shaped flakes that line framework grains; in mixed layers with smectite (Desbois et al., 2011; Luffel et al., 1993; Wilson et al., 2014; Wilson and Pittman, 1977). Illite fibres can partially collapse on the grain surface during sample drying (Luffel et al., 1993). Accordingly, in air dried sandstone samples, several authors observe both fibrous illite protruding into the pore bodies and tangential illite, which might be collapsed fibres (Desbois et al., 2011; Wilson et al., 2014). Figure 19 shows these two forms of illite in a Rotliegend sandstone sample [PETGAS data].

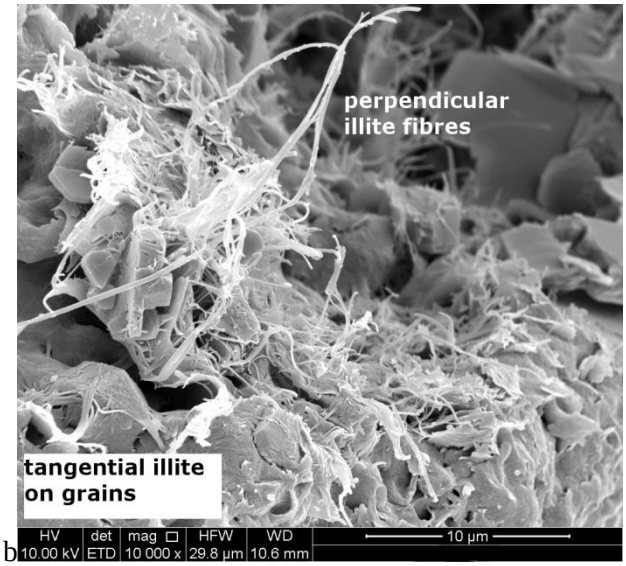

b

Figure 19: Scanning electron microscopy, SEM, image of illite in a sample from Rotliegend sandstone (Group 3 in Manuscript IV). Both tangential illite on the grain surface and illite fibres perpendicular to grains are observed. [Manuscript IV].

Luffel et al. (1993) suggest that the collapse of illite fibres onto the grain surface would be partially reversible when samples are subsequently saturated again. Therefore collapse of illite fibres could decrease the effective S_p in gas saturated samples as compared to brine saturated samples.

All 63 Rotliegend sandstone samples in Manuscript IV, and the additional Rotliegend samples that are used for Klinkenberg tests, contain more than 3 wt.% illite or mica according to X-ray diffraction, XRD. Samples of Gassum sandstone, Bunter sandstone and Berea sandstone also contain illite or mica according to image analysis in combination with energy dispersive X-ray analysis, EDS [Manuscript III]. However, for the Rotliegend samples, the ratio of k_w to k does not correlate to the illite/mica content per unit pore volume. Presumably the effect of drying depends on the morphology of illite or mica, as well as on the amount of illite or mica present.

Kaolinite minerals in sandstones are often observed as stacks of flat particles, known as kaolinite booklets (Wilson and Pittman, 1977). Expansion of kaolinite booklets due to adsorbed water might possibly reduce mobile intergranular porosity (Behnsen and Faulkner, 2011; Rutter, 1983). In Section 4.3 (and Manuscript IV), the effect of τ is estimated by assuming that pores with $r_p = 2/S_p < 2\tau$ would be filled with immobile water and therefore have zero mobile porosity. The immobilised volume of water is therefore limited by S_p, i.e., expansion of smaller pores at the expense of larger pores would cause a greater permeability reduction than estimated in Figure 18a.

Kaolinite booklets are observed in Rotliegend samples of groups 1 and 3 (Figure 20), and in samples of Gassum sandstone and Berea sandstone (Figure 21). Whereas a high kaolinite content is observed in sample Gassum Aa (Figure 21a), this is the only sample where the measured k_w is approximately equal to k. The

effect of expanding kaolinite booklets on permeability appears negligible in that sample. Presumably, this is not due to a lack of space for kaolinite to expand, as kaolinite booklets do not completely fill the intergranular pores (Figure 21). Therefore it is uncertain whether this mechanism has a significant effect on k_w.

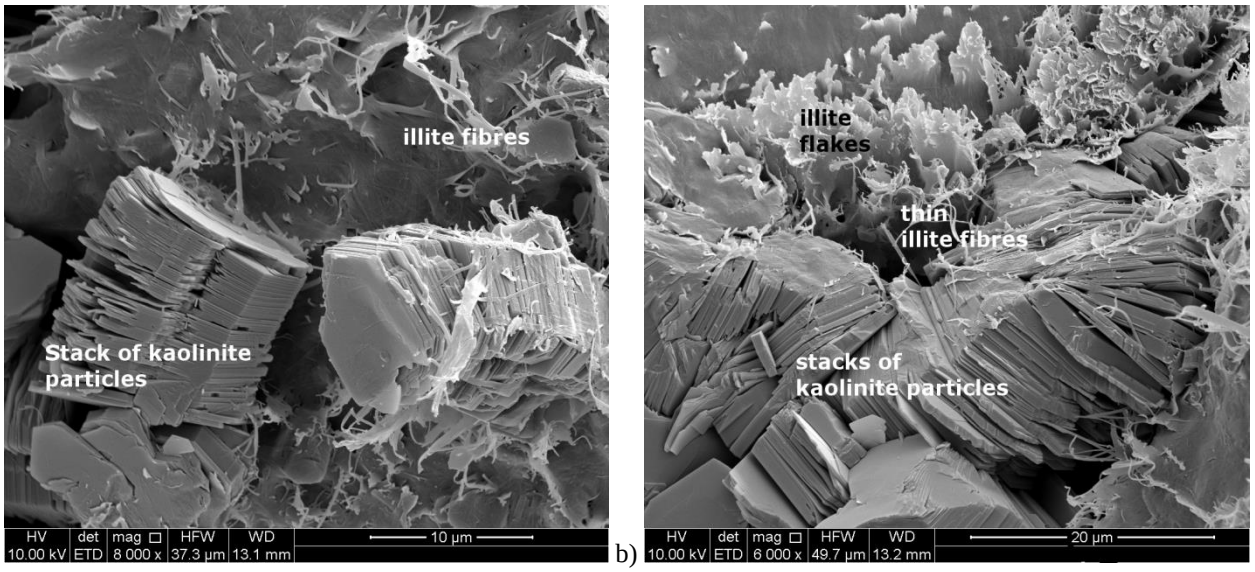

Figure 20: Scanning electron microscopy (SEM) images of kaolinite stacks in the pores of Rotliegend sandstone samples from the same locality. Both thin illite fibres a), and illite flakes b) are observed.

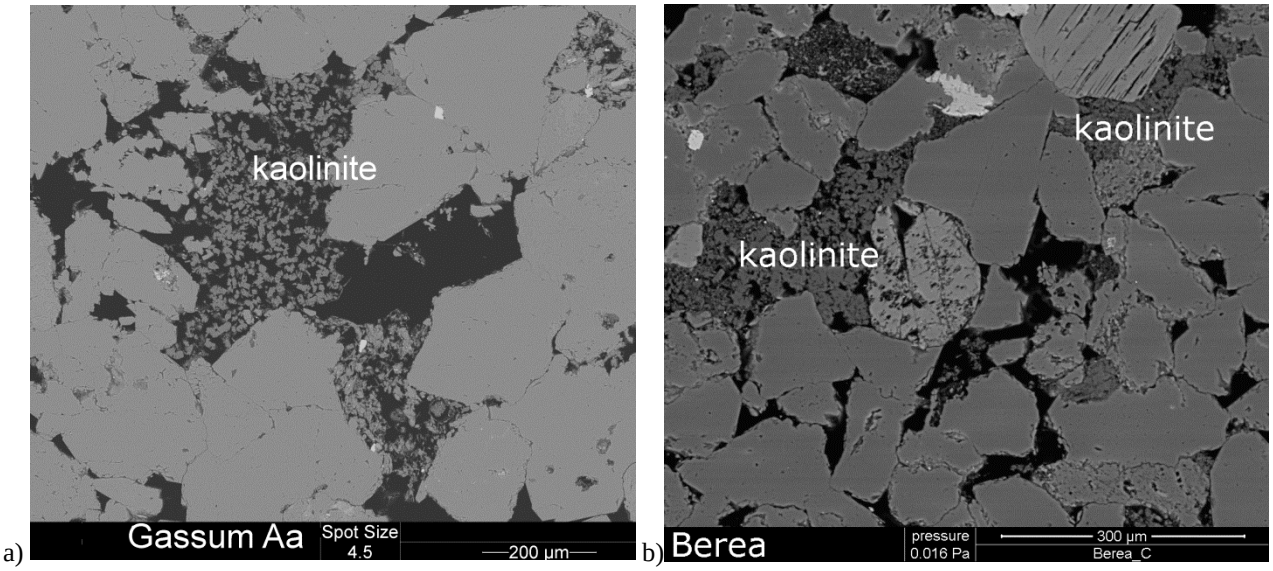

Figure 21: Backscatter electron microscopy (BSEM) images of kaolinite in sandstone samples. a) Kaolinite booklets do not fill intergranular pores in sample Gassum Aa. [BSEM image by R. Weibel, Geological Survey of Denmark and Greenland, GEUS]. b) Kaolinite can be observed in some intergranular pores in a Berea sandstone sample.

5 Permeability reduction due to thermal expansion

Heating may affect permeability by causing thermal expansion (Baudracco and Aoubouazza, 1995; Somerton, 1992) [Manuscript I]. The effect of thermal expansion on porosity depends on the expansion of the solids and of the bulk volume. Expansion of the solids depends on the specific mineral thermal expansion coefficient, whereas expansion of the bulk volume also depends on the level of confining stress.

A first approximation of the effect of temperature on porosity is made in Manuscript I. Assuming a homogeneous sandstone and isotropic expansion, so that volumetric expansion is three times the linear expansion, the bulk volume after changing temperature by ΔT, $V_{b,\Delta T}$, is given by Eq.(56), and the solids volume after ΔT, $V_{s,\Delta T}$, is given by Eq.(57):

$$V_{\mathrm{b},\Delta T} = V_{\mathrm{b,T0}}(1+3\alpha_{T,b}\Delta T) \tag{56}$$

$$V_{\mathrm{s},\Delta T} = V_{\mathrm{s,T0}}(1+3\alpha_{T,s}\Delta T) \tag{57}$$

where α_T is the one-dimensional thermal expansion coefficient, $V_{b,T0}$ is the original bulk volume, and $V_{s,T0}$ is the original solid volume. In terms of the original porosity ϕ_{T0} and the original bulk volume, $V_{b,T0}$ the solid volume after ΔT is given by Eq.(58):

$$V_{\mathrm{s},\Delta T} = (1-\phi_{T0})V_{\mathrm{b,T0}}(1+3\alpha_{T,s}\Delta T) \tag{58}$$

The porosity after ΔT, $\phi_{\Delta T}$, is given by Eq.(59):

$$\phi_{\Delta T} = \frac{V_{\mathrm{p},\Delta T}}{V_{\mathrm{b},\Delta T}} = \frac{V_{\mathrm{b},\Delta T} - V_{\mathrm{s},\Delta T}}{V_{\mathrm{b},\Delta T}} = \frac{V_{\mathrm{b,T0}}\left(1+3\alpha_T\Delta T\right) - (1-\phi_{T0})V_{\mathrm{b,T0}}(1+3\alpha_{T,s}\Delta T)}{V_{\mathrm{b,T0}}(1+3\alpha_{T,b}\Delta T)} \tag{59}$$

where $V_{p,\Delta T}$ is the pore volume after ΔT; Eq.(59) simplifies to Eq.(60):

$$\phi_{\Delta T} = 1 - \frac{\left(1-\phi_{T0}\right)\left(1+3\alpha_{T,s}\Delta T\right)}{1+3\alpha_{T,b}\Delta T} \tag{60}$$

The effect of thermal expansion on permeability is estimated by using the effective S_p for permeability from the Kozeny equation (cf. Eq.(11) and Eq.(19)). The effective specific surface of the solids S_s is related to the effective S_p by Eq.(61):

$$S_s = \frac{S_p\phi}{1-\phi} \tag{61}$$

In a confined sample, i.e., $\alpha_{T,b} = 0$, thermal expansion of the solids would reduce porosity cf. Eq.(60); the effect of a change in porosity on S_p is estimated by using Eq.(62)

$$S_{\mathrm{p},\Delta T} = \frac{S_s(1-\phi_{\Delta T})}{\phi_{\Delta T}} \tag{62}$$

Isotropic expansion of spheres would reduce $S_{s,}$ which would partly offset the effect of a porosity reduction on S_p in Eq.(62). Grain shape and anisotropic expansion would affect changes in S_s, therefore assuming a constant S_s would estimate the maximum permeability reduction that could be attributed to thermal expansion.

A compilation of published data, where permeability is measured at two or more different temperatures, is analysed in Manuscript I. The temperatures at which permeability is measured range from 15°C–180°C. Data are normalised to effective S_p for comparison among samples, and to estimate effects of thermal expansion and bound water. Tests with an inert fluid show no significant effect of temperature on the effective S_p (Figure 22a). This indicates that porosity reduction due to thermal expansion has a negligible effect on permeability, in these tests where the confining stress levels are below 14 MPa. This is in accordance with the maximum change in S_p estimated Cf. Eq.(62), also shown in Figure 22.

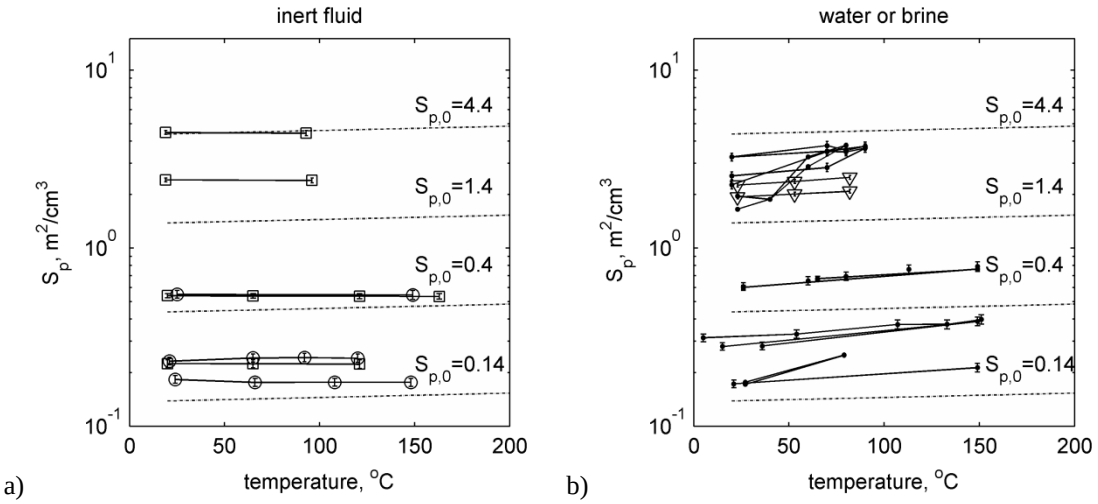

Figure 22: Effect of temperature on effective specific surface per unit pore volume, S_p, of sandstone samples. Dotted lines indicated modelled maximum increase in S_p that might be due to thermal expansion for samples with 10% porosity and different permeability, k, i.e. different effective S_p. a) Tests in which mineral oil (circles) or nitrogen gas (squares) are used to measure k indicate no change in S_p, or a change that is less than the estimated maximum effect of thermal expansion. b) Tests where the change in S_p exceeds the estimated maximum effect of thermal expansion are tests where permeability is measured by using distilled water (dots) or brine (triangles). Tests where the temperature is restored show a partial or complete reversibility of the effect of temperature on effective S_p [Modified from Manuscript I].

With aqueous solutions the effective S_p is increased by heating in some tests, but not in other tests (Figure 22). There is no reduction in effective S_p that would reflect a reduction in the immobile water layer thickness due to heating. Heating increases the effective S_p in six sandstone formations (Figure 22b); these formations

all contain kaolinite. Sandstone formations that do not contain kaolinite show no effect of temperature. Furthermore, no effect of temperature is observed in samples of kaolinite-bearing Berea sandstone that are pre-treated by heating above the temperature where kaolinite starts to dehydrate, between 400°C and 800°C (Grim, 1953); whereas heating does increase the effective S_p in untreated Berea sandstone samples in investigations by the same authors (Cassé and Ramey Jr, 1979; Schembre and Kovscek, 2004).

This suggests that kaolinite mobilisation causes the observed reduction in the effective S_p. Samples are heated and subsequently cooled to the original temperature in 12 tests, which shows that the change in S_p is partially or entirely reversible with cooling (Figure 22b).

Both increasing the temperature, and reducing the NaCl concentration of the pore fluid, could mobilise kaolinite particles in Berea sandstone; as these changes increase electrostatic repulsion forces between the like charged kaolinite and quartz surfaces (Khilar and Fogler, 1984, 1987; Schembre and Kovscek, 2005). However, the reversibility of the temperature effect observed in Figure 22b contrasts with permeability reduction that is observed in tests where the NaCl concentration is reduced and restored. As the reversibility of permeability changes would be relevant for geothermal energy storage, when temperature varies seasonally, effects of temperature and salinity on fines migration are investigated in Chapter 6 [Manuscript II and Conference papers II and III].

6 Permeability reduction due to kaolinite mobilisation

This Chapter addresses the effect of kaolinite mobilisation on permeability in Berea sandstone. Kaolinite-bearing Berea sandstone is often used as a reference for reservoir rocks; and, accordingly several authors use Berea sandstone samples to study effects of temperature, flow rate, and NaCl concentration on fines migration (e.g. Baudracco and Aoubouazza, 1995; Gray and Rex, 1966; Khilar and Fogler, 1984, 1987; Kia et al., 1987; Mungan, 1965; Ochi and Vernoux, 1998; Schembre and Kovscek, 2005).

6.1 Kaolinite in Berea sandstone

Kaolinite is the dominant clay mineral in the Berea sandstone (Churcher, 1991; Khilar and Fogler, 1987). Kaolinite particles are typically flat pseudo-hexagonal particles with diameters ranging from 0.5 μm to 20 μm and thicknesses ranging from 0.1 μm to 1 μm (Grim, 1953; Gupta and Miller, 2010; Wilson and Pittman, 1977). Kaolinite belongs to the kaolin mineral group, which also contains dickite; dickite tends to form thicker particles (Grim, 1953; Wilson and Pittman, 1977). The term kaolinite is often used to refer to both kaolinite and dickite, as both minerals may be present in the same sample and they can be interlayered (Wilson and Pittman, 1977). Within the same intergranular pores of Berea sandstone, kaolinite particles can be observed with a range of sizes, and they can be present both as kaolinite booklets and as individual platelets (Figure 23).

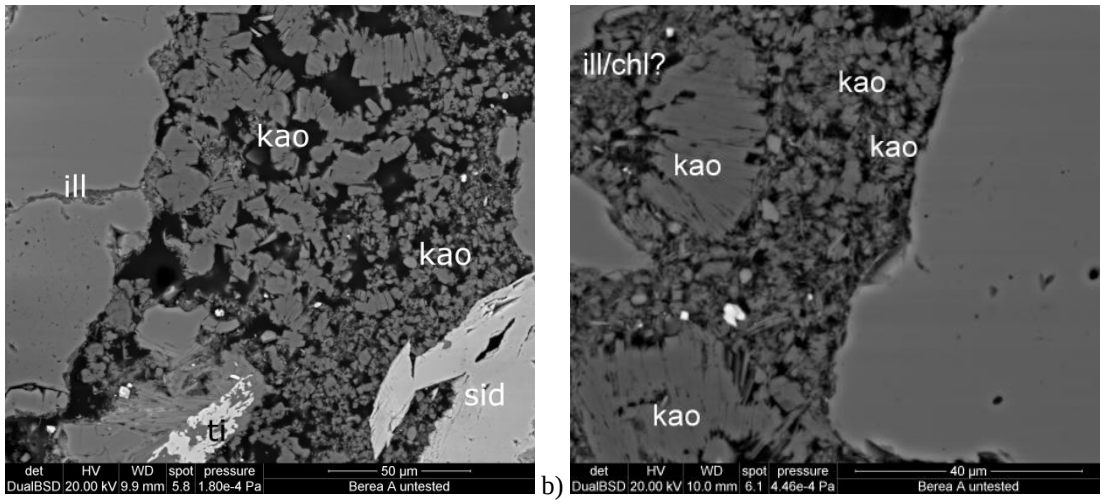

Figure 23: Backscatter electron microscopy, BSEM, images of kaolinite booklets and kaolinite plates in the pores of one Berea sandstone sample. A range of particle sizes can be observed even within the same pore. [Figure b) is from Manuscript II] (kao = kaolinite; ill/chl? = illite or chlorite; ti= titanium minerals; sid = siderite).

6.2 Permeability reduction mechanisms

The effect of mobile particles on permeability in porous media can be investigated by using filtration experiments (Bedrikovetsky et al., 2011; McDowell-Boyer et al., 1986; Pandya et al., 1998; Sen and Khilar, 2006; Wong and Mettananda, 2010; Yuan and Shapiro, 2011). Hereby, a homogeneous particle suspension is injected into a sample, and the permeability reduction is related to the amount of particles that are retained,

or filtered, in the sample. Conceptual models for particle retention include: deposition of particles on the framework grains; straining of larger particles in pore constrictions; and bridge formation, whereby multiple small particles obstruct, or jam, pore constrictions (Bedrikovetsky et al., 2011; McDowell-Boyer et al., 1986; Sen and Khilar, 2006).

Deposition of particles on framework grains would occur when retaining forces exceed mobilising forces (Bedrikovetsky et al., 2011). Hydrodynamic forces are mobilising, the gravitational force is retaining, and electrostatic surface interaction forces may be mobilising or retaining, depending on whether there is a net attraction or repulsion between charged surfaces of the particles and the framework grains (Bedrikovetsky et al., 2011; Sen and Khilar, 2006). Particle retention by deposition is presumably negligible when kaolinite particles are mobilised within the sample; as mobilisation would occur only when mobilising forces exceed retaining forces. Therefore, the permeability reduction due to kaolinite mobilisation might be attributed to straining or to bridging as suggested by e.g., Khilar and Fogler (1984) and by Kia et al. (1987). However, whereas these mechanisms may account for the permeability reduction when the NaCl concentration is reduced, which is not reversible when the NaCl concentration is restored, the reversible permeability reductions due to heating and cooling as observed in Chapter 5 suggest that particles might not be filtered in the heated samples. This suggests that other mechanisms might contribute to the effect of temperature on permeability [Manuscript II]. Particle mobilisation within sandstone samples differs from injection of a particle suspension in several ways, which might affect the permeability changes.

The viscosity of the injected particle suspension is known in filtration experiments. By contrast, fines that are mobilised within the pores would affect the viscosity of the pore fluid. This is not accounted for when permeability is calculated by using Darcy's law (Eq.(3)) and the viscosity of the injection fluid. An increase in fluid viscosity would therefore appear as a permeability reduction.

A stable homogeneous particle suspension is injected in filtration experiments; by contrast, kaolinite is distributed heterogeneously in the pores of Berea sandstone (Figure 4) (Schembre and Kovscek, 2005). Mobilisation presumably results in higher concentrations of suspended kaolinite particles in some pores than in other pores; therefore electrostatic interaction forces among kaolinite particles would play a larger role than in filtration experiments with the same average concentration of suspended particles. Furthermore, kaolinite particles have a heterogeneous surface charge density, which affects electrostatic interaction forces among particles (Gupta and Miller, 2010; Gupta et al., 2011; Schofield and Samson, 1954; Wang and Siu, 2006; Zbik and Frost, 2009). Microporous kaolinite aggregates, could form due to interaction among differently charged sides of kaolinite particles (Schofield and Samson, 1952).

Porous networks of kaolinite particles that are suspended in low salinity solutions[2] are observed in cryo-SEM images (Gupta et al., 2011; Zbik and Frost, 2009). Those images are acquired by vitrifying a suspension of kaolinite, and performing scanning electron microscopy, SEM, at -90°C on a fresh fracture surface. (Gupta et al., 2011). Interactions among kaolinite particles might also prevent particles or aggregates from settling. Zbik and Frost (2009) observe a gel, i.e., a 3D porous network of particles (Olphen, 1977), that remains suspended at the bottom of a container of a kaolinite suspension that is allowed to settle in 0.01 M NaCl solution at pH 9. If such a gel, or microporous kaolinite aggregates, were to form in kaolinite-bearing pores, this would reduce the mobile porosity. On a macroscopic scale, interactions among kaolinite particles in low salinity suspensions results in a yield stress below which the suspensions do not flow (Johnson et al., 1998; Mpofu et al., 2003; Olphen, 1977). Indeed, Wong and Mettananda (2010) could not inject a kaolinite suspension for filtration tests, therefore they used a suspension of colloids with a homogeneous surface charge density instead.

Figure 24 illustrates different mechanisms by which kaolinite might affect permeability. Prior to mobilisation, kaolinite booklets presumably reside on the quartz grain surface due to gravitational forces (Figure 24a). If electrostatic repulsion forces are increased by heating, or by reducing the concentration of NaCl solution, kaolinite particles may be mobilised (Figure 24b); and presumably suspended particles affect the viscosity of the pore fluid and thereby the apparent permeability. If the pressure gradient is sufficient to transport kaolinite particles, particles might be transported to a pore constriction that is smaller than the particle size, where they are retained by straining (Figure 24c). If the concentration of transported particles is high, particles arriving simultaneously at a larger pore constriction might be filtered by bridging (Figure 24d). On the other hand, the electrostatic repulsion force between quartz and kaolinite, which presumably mobilised the kaolinite particles, might limit filtration. If suspended particles form microporous kaolinite aggregates or a kaolinite gel, the pressure gradient may be too low to shear this. Kaolinite aggregates might increase the effective S_p or reduce the mobile porosity and thereby reduce permeability (Figure 24e). These mechanisms would not be mutually exclusive; due to the range of kaolinite particle sizes, the heterogeneous distribution of kaolinite in the pores, and pore scale variation of the flow rate, different mechanisms might prevail in different pores.

[2] Solutions: 0.001 M KCl at pH 9 in (Gupta et al., 2011); 0.01 M NaCl at pH 8 (Zbik and Frost, 2009).

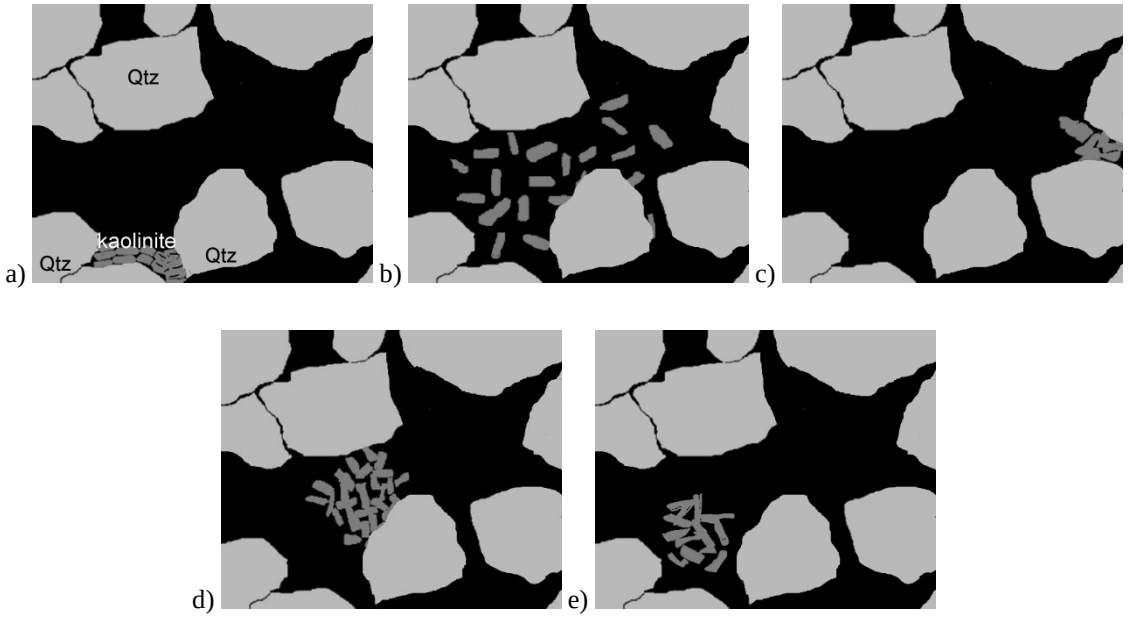

Figure 24: Schematic representation of kaolinite particles (dark grey) in intergranular pores (black) among quartz framework grains (light grey). a) Kaolinite particles concentrated in stacks on the grain surface prior to mobilisation. b) After an increase in electrostatic repulsive forces mobilises kaolinite particles, particles are suspended in the pore fluid. c) Kaolinite particles, which are filtered by straining in pore constrictions that are smaller than the kaolinite particles. d) Kaolinite particles, which are filtered by bridging, i.e., a high concentration of kaolinite particles arriving at a larger pore constriction simultaneously. e) A microporous kaolinite aggregate, gel, that reduces the intergranular pore volume. Not to scale.

According to the DLVO (Derjaguin and Landau, 1941; Verwey and Overbeek, 1948) theory, the net interaction energy is the sum of the electrical double layer (EDL) interaction energy and the van der Waals interaction energy. The DLVO theory is used to model: interactions between colloids and pore walls, in order to model colloid filtration (Bedrikovetsky and Caruso, 2014; Bedrikovetsky et al., 2011, 2012; Hahn and O'Melia, 2004; Sen and Khilar, 2006; Yuan and Shapiro, 2011); interactions among suspended kaolinite particles, in order to model rheological properties of kaolinite suspensions (Gupta et al., 2011; Johnson et al., 1998; Mpofu et al., 2003); and interactions between kaolinite and quartz grains, in order to model kaolinite mobilisation in sandstones (Khilar and Fogler, 1984; Kia et al., 1987; Schembre and Kovscek, 2005). In order to investigate effects of temperature and salinity on permeability reduction by mobilised kaolinite, interaction both among kaolinite particles and between kaolinite particles and quartz grains are estimated by using DLVO theory in this Chapter [based on Manuscript II and Conference papers II and III]. The surface charge density of the minerals affects the interaction forces. However, published surface charge density data for kaolinite show a range of values. Furthermore, there is only limited data regarding the effect of temperature on the surface charge of kaolinite and quartz. Therefore the nature of the surface charge density is discussed in Section 6.3; and the effect of this parameter on the results of DLVO calculations is addressed in Section 6.7 [Conference paper III].

6.3 Surface charge on kaolinite and quartz

The net surface charge density on quartz and on kaolinite depends on interaction between water molecules and broken bonds on the fluid-mineral interface (Grim, 1953; Lorne et al., 1999; Schofield and Samson, 1954). Possibly isomorphic substitution in the kaolinite lattice also contributes to the kaolinite surface charge (Huertas et al., 1998; Lorne et al., 1999; Schofield and Samson, 1954; Wang and Siu, 2006; Wilson et al., 2014).

Quartz (SiO_2) consists of silica tetrahedra that consist of one silicium atom bonded to four oxygen atoms (Figure 25a). Each oxygen atom is shared between two tetrahedra forming a 3D lattice (Gautier et al., 2001). Tetrahedra on the surface of quartz grains have broken bonds, which interact with water forming silanol groups that can gain or lose protons, H^+ (Eq.(63)) (Lorne et al., 1999).

$$\begin{aligned} Si-OH &\rightleftharpoons Si-O^- + H^+ \\ Si-OH + H^+ &\rightleftharpoons Si-OH_2^+ \end{aligned} \tag{63}$$

The net surface charge of quartz grains results from charges on the individual silanol groups. With a pH greater than 3, the net charge is negative; the net charge becomes more negative when pH increases, as more silanol groups dissociate, i.e., lose H^+ (Lorne et al., 1999). Increasing the temperature in the range from 20°C–80°C also makes the net surface charge of quartz more negative (Brady, 1992; House and Orr, 1992; Rodríguez and Araujo, 2006).

Kaolinite particles have a different charge on the two faces and on the edges, due to the mineral lattice (Grim, 1953; Gupta and Miller, 2010; Gupta et al., 2011). The kaolinite mineral ($Al_2Si_2O_5(OH)_4$) consists of a series of layers; each layer is made up of a silica tetrahedral sheet bonded to an alumina octahedral sheet (Figure 25). Silica tetrahedra are arranged in a hexagonal pattern in the silica sheet (Figure 25b); three oxygens of each tetrahedron are shared with three other tetrahedra, and the fourth oxygen is shared with two alumina octahedra in the alumina sheet (Figure 25c). In the alumina sheet, an aluminium atom is bonded to four hydroxyl (OH) groups and to two oxygens from the tetrahedral sheet. Layers are joined by hydrogen bonds between adjacent silica and alumina sheets (Grim, 1953). Kaolinite particles would therefore only have broken bonds on the particle edges, and not on the faces. The charge on the silanol and aluminol groups on the particle edges depends on protonation, and thereby on temperature and on pH, similar to the silanol groups on the quartz surface (Brady et al., 1996; Gupta and Miller, 2010; Huertas et al., 1999; Rand and Melton, 1977; Wang and Siu, 2006).

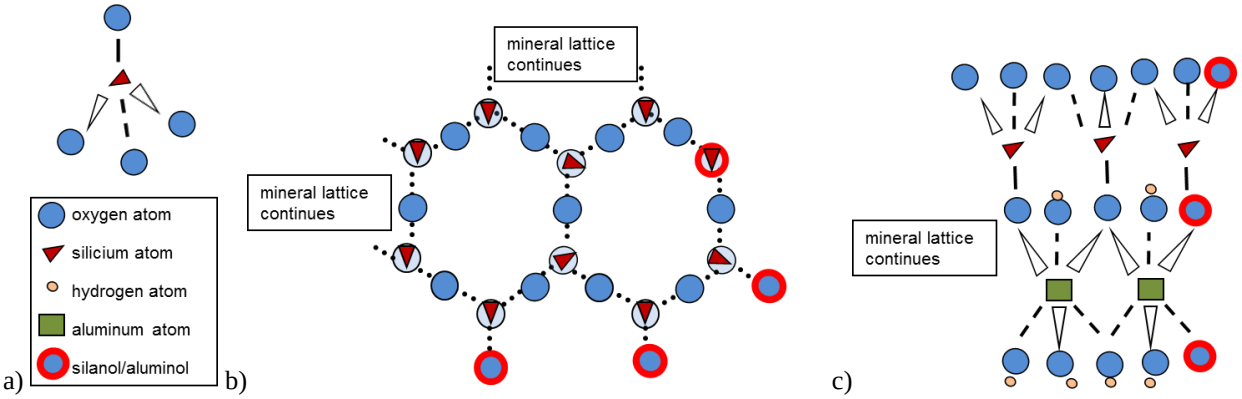

Figure 25: a) Silicon tetrahedron, a silicium atom is bonded to four oxygen atoms. b) Top view of kaolinite silica tetrahedral face; silica tetrahedra are arranged in a hexagonal pattern. Each tetrahedron shares three oxygen atoms with other tetrahedra, and the fourth oxygen atom is shared with two alumina octahedra in the alumina sheet. Broken bonds, i.e., silanol sites, are only present on the edges of a kaolinite particle. c) Side view of a kaolinite layer consisting of an alumina octahedral sheet (lower half) bonded to a silica tetrahedral sheet (upper half); Broken bonds, i.e., silanol and aluminol sites, are only present on the edges of a kaolinite particle. Not to scale. [Modified from Conference paper II; kaolinite structure kaolinite after Grim (1953)].

There exists some uncertainty regarding the magnitude and the reactivity of the charge on the kaolinite faces, as these do not contain broken bonds (Brady et al., 1996; Huertas et al., 1998; Wang and Siu, 2006). Some authors suggest that the surface charge on both faces is negative due to isomorphic substitution of silicium and aluminium by trivalent and divalent ions (Rand and Melton, 1977; Schofield and Samson, 1954). This charge would be independent of temperature and of pH. Other authors suggest that hydroxyl groups on the alumina face do react with water (Huertas et al., 1999; Wang and Siu, 2006). Steps can be observed on kaolinite faces of kaolinite particles (Figure 26); thereby faces might also have broken bonds (Brady et al., 1996; Zbik and Frost, 2009).

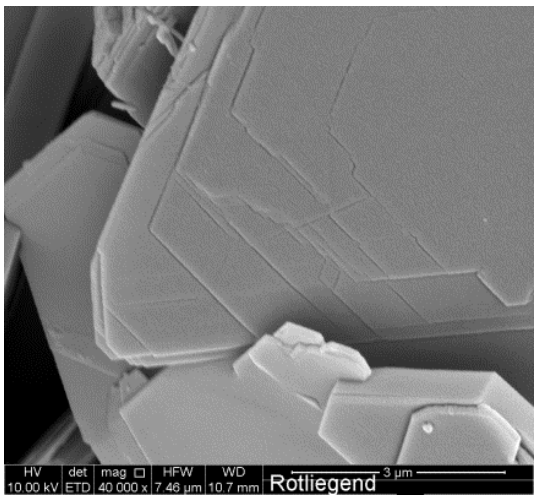

Figure 26: Scanning electron microscopy (SEM) image of the face of a kaolinite particle in a sample of Rotliegend sandstone. Lines indicate that stacked layers do not have the same size, which results in steps on the particle face.

Potentiometric titration can be used in order to quantify the average charge on kaolinite particles; however, distinction among the charge on the two faces and on the edges based on this method can be considered uncertain (Brady et al., 1996). Therefore, Gupta and Miller (2010) use atomic force microscopy, AFM, to determine the surface charge on the silica and alumina faces separately. They find that the charge on both faces depends on pH, which suggests that groups on the faces do react with water whereby their charge presumably also depends on temperature; Gupta and Miller (2010) do not observe steps on the faces.

Berea sandstone saturated with water or with NaCl solution has a pH 8–9, due to buffering by carbonate minerals (Kia et al., 1987). At this pH the surface charge on both faces and on the edges of kaolinite would be negative, with a higher charge density on the edges than on the faces (Gupta and Miller, 2010; Gupta et al., 2011).

Due to the different charge densities on different sides of kaolinite particles, the average charge density on a kaolinite particle, and the effect of temperature on the average charge density, would depend on the particle shape and size. With a higher charge density on the edges than on the faces, thicker particles would have a more negative average charge density than thinner particles (Figure 27).

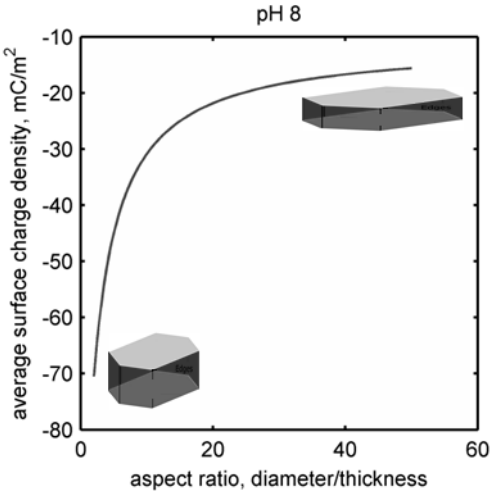

Figure 27: Average surface charge density of a kaolinite particle as a function of aspect ratio at pH 8. Surface charge densities are based on data from Gupta et al. (2011) at pH 8: alumina face -11 mC/m^2; silica face -11 mC/m^2; edges -134 mC/m^2.

6.4 Electrical double layer

The surface charge attracts oppositely charged ions and repels like charged ions, resulting in an electrical double layer (EDL) (Israelachvili, 2011; Lyklema et al., 1995). A simple Stern model (1924), consisting of a Stern layer and a diffuse layer, can be used to characterise the EDL interactions between charged surfaces (Israelachvili, 2011). The Stern layer contains ions and water molecules that are bound to the surface groups. This layer would have a finite thickness, and the surface charge can be considered to act from the Stern plane, which separates the Stern layer and the diffuse layer (Grahame, 1947, 1953; Lyklema et al., 1995).

The charge in the diffuse layer is equal and opposite to the surface charge on the Stern plane. The potential distribution in the diffuse layer is described by Gouy-Chapman theory which treats ions in as point charges (Chapman, (1913); Gouy, (1909) in Lyklema et al. (1995)). The Debye length, κ^{-1}, characterises the distance over which the potential in the diffuse layer falls by a factor 1/e (e is the natural logarithm) Eq.(64).

$$\kappa^{-1} = \frac{\varepsilon_0 \varepsilon_r k_B T}{2 N_A e^2 I} \tag{64}$$

where ε_0 is the permittivity of a vacuum, ε is the static relative permittivity of the bulk solution, which is a function of temperature and salinity[3] (Maribo-Mogensen et al., 2013; Michelsen and Mollerup, 2004), k_B is the Boltzmann constant, N_A is the Avogadro constant, e is the elementary charge, and I is the ionic strength of the solution given by:

$$I = \frac{1}{2} \sum_i C_i z_i^2 \tag{65}$$

where C_i is the concentration of the i^{th} species of ions, and z_i is the valence of the ions, and the summation is over all ion species in the solution.

The Grahame equation (Grahame, 1947, 1953) relates the net surface charge density on the Stern plane, σ_0, to the surface potential at the Stern plane, ψ_0, by Eq.(66) (Israelachvili, 2011):

$$\sigma_0 = \sqrt{8000 N_A \varepsilon_0 \varepsilon_R k_B T C_{mono}} \sinh\left(\frac{e\psi_0}{2k_B T}\right) \tag{66}$$

where C_{mono} is the concentration of monovalent ions in the bulk solution.

The zeta potential, ζ, is the potential on the shear plane, the interface between mobile and immobile ions when the bulk solution moves relative to the mineral surface. Some authors suggest that the shear plane would be at a greater distance from the surface than the Stern plane, whereby $|\zeta| < |\psi_0|$ (e.g., Ishido and Mizutani, 1981; Lorne et al., 1999). Nonetheless, as ζ can be measured by using electrophoresis, ζ is considered equivalent to ψ_0 in order to estimate DLVO interactions by several authors (e.g., Johnson et al., 1998; Khilar and Fogler, 1984, 1987; Mpofu et al., 2003; Schembre and Kovscek, 2005).

The concentration of monovalent, K^+ and Na^+, ions appears not to significantly affect σ_0 for kaolinite (Huertas et al., 1998; Tertre et al., 2006). The effect of salinity and temperature on ψ_0 for a constant σ_0 is

[3] In this thesis and the appended manuscripts ε_r is calculated as a function of salinity and temperature using Matlab 2012b (the MathWorks) code provided by Bjørn Maribo-Mogensen (Maribo-Mogensen et al., 2013).

estimated by inverting Eq.(66), to illustrate the effects of temperature and salinity in Figure 28. A reduction of the NaCl concentration from 0.2 M to 0.02 M is observed to reduce permeability in tests on Berea sandstone at 20°C [Manuscript II]. This salinity reduction would have a larger effect on both ψ_0 (cf. Eq.(66)) and on κ^{-1} (cf. Eq.(64)) than heating from 20°C to 80°C would.

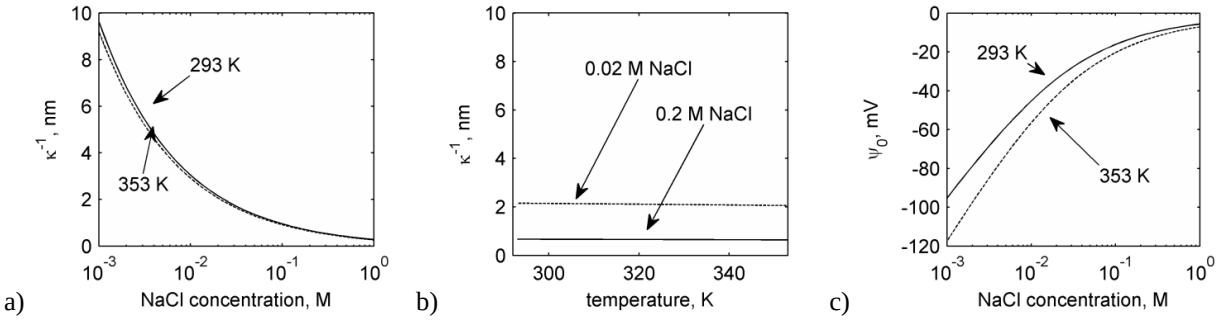

Figure 28: a) Debye length, κ^{-1}, as a function of NaCl concentration at 293 K and at 353 K. b) κ^{-1} as a function of temperature in 0.1 M and 0.2 M NaCl solutions. c) Surface potential, ψ_0, as a function of NaCl concentration at 293 K and at 353 K for a constant average surface charge density, σ_0 = -12 mC/m^2. [a and c from Conference paper III].

As the effect of temperature on the average σ_0 of kaolinite depends on particle size and shape, the effect of temperature on σ_0 is investigated by combining observed permeability changes with DLVO modelling in Section 6.7.

6.5 Electrical double layer interaction energy

Interaction between similarly charged double layers causes a repulsive EDL interaction energy. The interaction energy due to the overlapping double layers can be calculated by solving the Poisson-Boltzmann equations (Gregory, 1975; Israelachvili, 2011). This requires numerical methods, however, analytical solutions based on simplifications can give results that closely approximate the exact solution (Gregory, 1975).

Boundary conditions must be assumed for both numerical and analytical solutions. A constant σ_0 might apply when σ_0 is due isomorphic substitution; however, a σ_0 due to protonation would be affected by an approaching EDL (Elimelech, 2010). Therefore a constant ψ_0 is used to interpret AFM measurements in order to determine the kaolinite surface charge by Gupta and Miller (2010). A constant ψ_0 would apply when the surface charges are in equilibrium with the overlapping double layers. Whereas equilibrium might establish during AFM measurements, collisions among particles would involve more rapidly approaching surfaces; in which case an intermediate between a constant σ_0 and a constant ψ_0 condition might apply (Frens and Overbeek, 1972; Gregory, 1975). The linear superposition approximation, LSA, estimates an intermediate condition; the potential halfway between two approaching surfaces is the summation of the potential that would be observed at this distance from each individual surface (Elimelech, 2010; Gregory, 1975). An analytical solution, based on the LSA, for the EDL interaction energy per square meter, E_{EDL}, between parallel plates is derived by Gregory (1975):

$$E_{EDL} = \frac{64000 N_A C}{\kappa} \tanh\left(\frac{e\psi_{0,1}}{4k_bT}\right) \tanh\left(\frac{e\psi_{0,2}}{4k_bT}\right) \exp\left(-\kappa(h-\tau_{Stern})\right) \quad (67)$$

where the two surfaces can have different charges i.e., $\psi_{0,1} \neq \psi_{0,2}$, h is the separation between mineral surfaces, and τ_{Stern} is the thickness of the Stern layer, which accounts for ψ_0 acting from the Stern plane rather than from the mineral surface.

Figure 29 shows E_{EDL} as a function of separation between negatively charged parallel plates cf. Eq.(67). A positive E_{EDL} indicates repulsion; heating from 20°C to 80°C would increase E_{EDL} less than reducing salinity from 0.2 M NaCl to 0.02 M NaCl would, if σ_0 is not affected by heating.

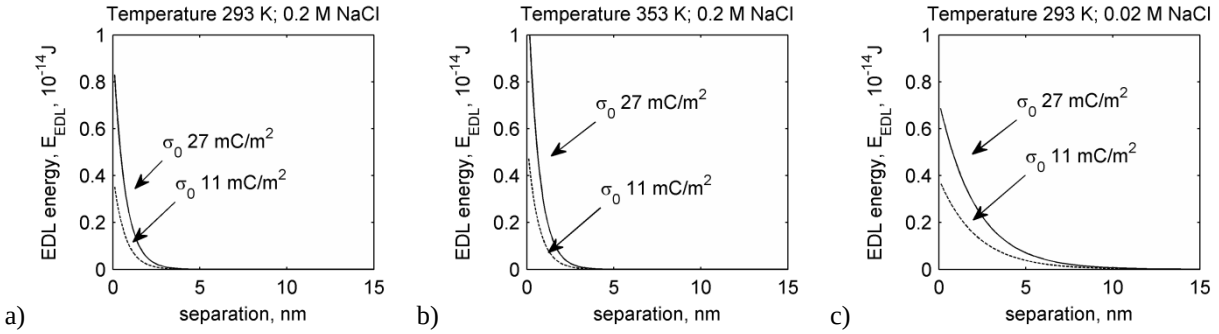

Figure 29: Electrical double layer interaction energy, E_{EDL}, between parallel plates with equal surface charge densities, σ_0, as a function of separation between mineral surfaces for an interacting area of 4 μm^2. a) At 293 K and 0.2 M NaCl solution. b) At 353 K and 0.2 M NaCl solution. c) At 293 K and 0.02 M NaCl solution.

6.6 Van der Waals interaction

The van der Waals interaction energy, E_{vdW}, between atoms arises from interaction between their electron clouds, which can result in a temporary polarisation and an attractive force (Israelachvili, 2011). On the scale of particles and surfaces, E_{vdW} is characterised by the geometry of the interacting particles and by the Hamaker constant, H, which depends on the material of the surfaces and the medium across which they interact (Israelachvili, 2011; Visser, 1972). The interaction energy between parallel plates energy per square meter can be expressed by Eq.(68) (Israelachvili, 2011).

$$E_{vdW} = -\frac{H}{12\pi h^2} \quad (68)$$

The value of H can be calculated from the dynamic dielectric constants of the interacting by media using the Lifshitz Theory, or from measured interaction forces; the latter is based on interpretation by using the DLVO theory (Israelachvili, 2011; Visser, 1972). Several authors use H values in the range from 1.6×10^{-20} J to 4.4×10^{-20} J, for interaction in aqueous solutions both between kaolinite and quartz and among kaolinite particles (Gupta et al., 2011; Khilar and Fogler, 1984; Kia et al., 1987; Schembre and Kovscek, 2005). Limited experimental data do not show a clear effect of temperature on H (Visser, 1972); and several authors

suggest that H would not be affected by salinity (Israelachvili and Adams, 1978; Israelachvili, 2011; Khilar and Fogler, 1984; Schembre and Kovscek, 2005).

The Born repulsion term is sometimes added to the DLVO terms, E_{EDL} and E_{vdW}, in order to account for repulsion on the atomic scale (Elimelech, 2010; Khilar and Fogler, 1987; Schembre and Kovscek, 2005). If E_{vdW} exceeds E_{EDL}, the net interaction energy tends towards minus infinity as separation tends to zero. The high repulsion at sub-nanometre separations in the Born term results in a net energy minimum at a finite separation where particles can be considered bound (Elimelech, 2010; Schembre and Kovscek, 2005). However, the closest approach between mineral surfaces would also be limited by the finite size of ions adsorbed to the surface (Elimelech, 2010; Israelachvili, 2011; Khilar and Fogler, 1984). Furthermore, the LSA assumption in Eq.(67) would not be valid for separations of h-τ_{Stern} smaller than κ^{-1}, whereby net interaction energies estimated for separations less than one or two nanometres would already be uncertain (Elimelech, 2010; Israelachvili, 2011). Therefore, in Section 6.7 only E_{EDL} and E_{vdW} are considered, and the net interaction energy, $E_{DLVO} = E_{EDL} + E_{vdW}$, is only evaluated up to a minimum separation of $2\tau_{Stern}$, where the distance between Stern planes is zero.

6.7 Effects of temperature and salinity on DLVO interaction and on permeability

This Section combines permeability test data on Berea sandstone[4] [Manuscript I and II] with estimates of surface interaction forces based on the DLVO theory, to investigate effects of temperature and NaCl concentration on permeability reduction by kaolinite mobilisation [Conference paper III, Manuscript II]. As kaolinite particles typically occur as flat platelets, the interaction energy both between kaolinite and quartz and among kaolinite particles is estimated based on the expressions for planar surfaces in the previous Sections.

Stern layer thicknesses in the order of 0.3 nm–2.5 nm are suggested in literature (Elimelech, 2010; Israelachvili and Adams, 1978; Khilar and Fogler, 1984); as a first approximation, $\tau_{Stern} = 0.5$ nm.

The $\psi_{0,i}$ in Eq.(67) are calculated from $\sigma_{0,i}$ by inverting Eq.(66), in order to account for effects of salinity and temperature as in Section 6.4. The van der Waals forces are assumed to be constant with temperature and salinity.

6.7.1 Permeability prior to particle mobilisation

In Berea sandstone samples saturated with 0.5 M–2.0 M NaCl solution at room temperature, kaolinite might be located on the quartz grain surface (Figure 24a) (Khilar and Fogler, 1984, 1987; Ochi and Vernoux, 1998; Schembre and Kovscek, 2005). Thereby the specific surface of kaolinite would have a small effect on permeability. As discussed in Section 2.4.1 when intergranular pores form a connected flow path the effective S_p would reflect the specific surface of the framework grains [Manuscript II, IV].

[4] Test data from literature and from new experiments performed by Christian Haugwitz, Peter Jacobsen and Jacob Riis (DTU students) in collaboration with Claus Kjøller (GEUS).

6.7.2 Effect of salinity

At room temperature, reduction of the concentration of NaCl solution below a threshold value, or the switch from flow with NaCl solution to flow with distilled water can reduce permeability in samples of Berea sandstone by over 90% (Grey and Rex, 1966; Khilar and Fogler, 1984; Mungan, 1965; Ochi and Vernoux, 1998) [Manuscript II]. This reduction is irreversible in tests where the salinity is subsequently restored, however, reversing the flow direction can partially restore permeability (Khilar and Fogler, 1984), [Manuscript II] (Figure 30).

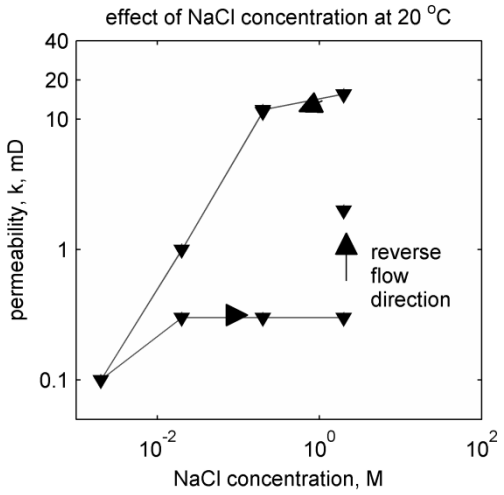

Figure 30: At 20°C the permeability of a sample of Berea sandstone falls sharply when the NaCl concentration is reduced below 0.2 M and the effect is largely irreversible when NaCl concentration is subsequently restored. Reversing the flow direction partially restores permeability. [Modified from Manuscript II].

Reducing the NaCl concentration increases both κ^{-1} and the magnitude of ψ_0, and consequently the repulsive E_{EDL} between kaolinite and quartz increases (Figure 28a and c; Figure 29). Figure 31 shows E_{DVLO} as a function of separation between surfaces that have average $\sigma_{0,1}$ and $\sigma_{0,2}$ representing kaolinite and quartz. With 2.0 M NaCl solution, E_{DLVO} tends towards negative infinity as h tends to zero, indicating attraction between kaolinite particles and quartz grains. The maximum E_{DLVO} appears to switch from attraction (negative interaction energy) to repulsion (positive interaction energy) between 0.2 M NaCl solution and 0.02 M NaCl solution. A net repulsion energy might cause kaolinite mobilisation, accounting for observed permeability reductions as shown in Figure 30.

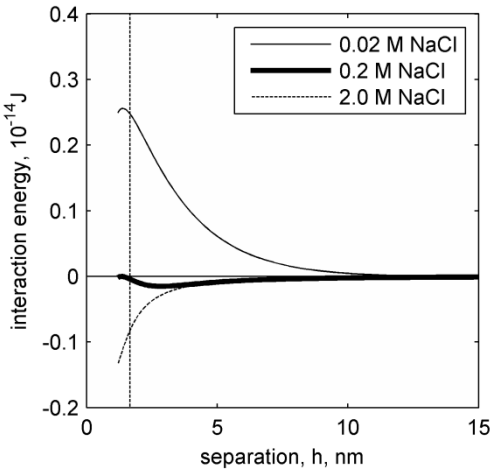

Figure 31: Net interaction energy as a function of the separation between parallel planar kaolinite and quartz surfaces. Negative interaction energy indicates attraction. Interaction energy is scaled by an interaction area of 4 μm^2; surface charge densities are: 11 mC/m^2 for kaolinite, 27 mC/m^2 for quartz. The Stern layer thickness, τ_{Stern} = 0.5 nm. Vertical dashed line indicates a separation equal to the Debye length between Stern planes, i.e., $h = 2\tau+\kappa^{-1}$, in 0.2 M NaCl solution. Below this separation, expressions for the electrical double layer interaction energy are more uncertain[Modified from Conference Paper III].

Several authors attribute permeability reduction due to salinity reduction to filtration of mobilised particles, by means of straining of larger particles or bridging by multiple particles (Figure 24c and d) (Khilar and Fogler, 1984, 1987; Kia et al., 1987; Mungan, 1965; Ochi and Vernoux, 1998). As the size of kaolinite particles varies (Figure 23b), both mechanisms might occur in the same sample if all particles are mobilised. Some authors suggest that due to their greater mass larger particles would not be mobilised (Bedrikovetsky et al., 2011; Khilar and Fogler, 1987). This would be due to a proportionally higher gravitational retaining force on larger particles; the gravitational force increases with volume, proportional to r^3 for spherical particles, whereas the DLVO forces are scaled by surface area, r^2 for spheres. For kaolinite particles the effect of size on the net DLVO forces, would depend on whether size affects the particle aspect ratio, which affects the average σ_0 (Figure 27).

Kaolinite filtration could increase the effective S_p if flow paths through larger intergranular pores are only connected through smaller pores among filtered kaolinite particles. Thereby, the specific surface area of kaolinite would be effective to permeability. Accordingly, the effective S_p after reducing the NaCl concentration from 2.0 M to 0.002 M at 20°C reduced permeability (Figure 30), is approximately equal to $S_{p,BET}$ [Manuscript II].

Particles that are filtered by straining or bridging would not be remobilised by restoring salinity, which reduces E_{EDL}; straining could be considered irreversible, even when the flow direction is reversed (Khilar and Fogler, 1984; Mohan et al., 1999). However, reversing the flow direction after the NaCl concentration is restored could remove bridged particles, which might possibly re-aggregate in booklets or re-attach to the

quartz grains as E_{DLVO} is attractive (Figure 31) (Khilar and Fogler, 1984). Therefore the permeability changes observed in Figure 30 might reflect kaolinite mobilisation and filtration by bridging as suggested by Khilar and Fogler (1984).

6.7.2.1 Sensitivity to surface charge density

As the average ψ_0, or ζ, depends on kaolinite particle shape and size (Figure 27), the effect of ψ_0 on E_{DLVO} is investigated in this Subsection [Conference paper III]. The ζ data at pH 8–9 from several publications are used to estimate σ_0 of kaolinite particles by using Eq.(66); this indicates a range from 11 mC/m^2 to 22 mC/m^2 (Johnson et al., 1998; Rodríguez and Araujo, 2006; Zbik and Frost, 2009). The edge σ_0 is suggested to be approximately three times higher than σ_0 on the faces by Brady et al. (1996); whereas data by Gupta et al. (2011) indicate that the edge σ_o would be a factor five to ten times higher than the face σ_0 at pH 8. Differences may be due to assumptions made regarding the size and shape of the kaolinite particles in the interpretation of potentiometric titration data by Brady et al (1996); and to assumptions regarding the boundary conditions and the magnitude of E_{vdW} in interpretation of AFM data by Gupta et al. (2011). Quartz σ_0 are likewise estimated from ζ data; values indicate a range from 22 mC/m^2 to 32 mC/m^2 at pH 8 (House and Orr, 1992; Rodríguez and Araujo, 2006). Thus the average σ_0 on kaolinite particles appears to be less negative than the σ_0 of quartz.

The E_{DLVO} for a specific h is calculated for a range of ψ_0. Interaction energies for σ_0 that could represent kaolinite faces or the average σ_0 on a kaolinite particle are scaled by an interaction area of 4 nm^2, whereas interactions for σ_0 that represent kaolinite edges are scaled by 0.2 nm^2, to account for the smaller edge area.

Figure 32 shows an attractive E_{DLVO} between kaolinite and quartz in 0.2 M NaCl solution and a net repulsion in 0.02 M NaCl solution, for the range of σ_0 that could characterise the faces or the average charge on kaolinite particles. The E_{DLVO} is repulsive between quartz and kaolinite edges even in 0.2 M NaCl solution. This suggests that in order to estimate kaolinite mobilisation, the average σ_0 on the kaolinite particle would be relevant; and indeed ζ is used to model kaolinite mobilisation by several authors (e.g., Khilar and Fogler, 1984; Kia et al., 1987; Ochi and Vernoux, 1998; Schembre and Kovscek, 2005).
Due to the smaller surface area of the edges, the interaction energy for the interactions between the edges of kaolinite and quartz is smaller in magnitude than the interaction energy between kaolinite faces and quartz. This difference is comparable to the difference between pressure and force.

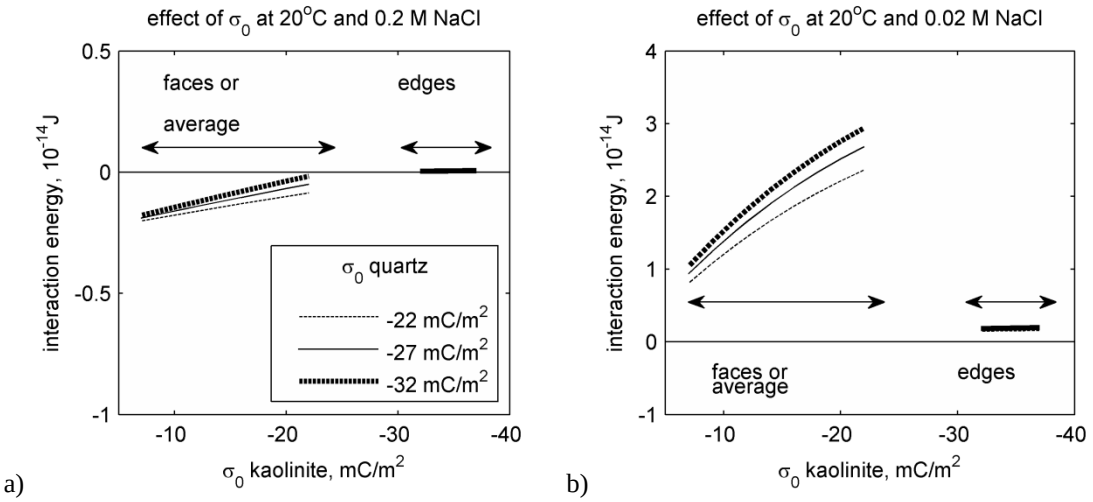

Figure 32: a) In 0.2 M NaCl solution, the net interaction energy at 2 nm separation between Stern planes is attractive (negative) for a range of surface charge densities, σ_o, that might represent the charge kaolinite faces or on an the average kaolinite particle; whereas the net interaction energy between surfaces with a σ_0, which could represent kaolinite edges, and quartz is repulsive (positive). b) In 0.02 M NaCl solution there is a net repulsion between quartz and kaolinite for the range of surface charge densities for kaolinite faces as well as for kaolinite edges. Interaction areas are scaled by 4 μm^2 for faces of kaolinite particles or for the average kaolinite particle and by 0.2 μm^2 for edges of kaolinite particles. [Modified from Conference paper III].

6.7.2.2 Ion Exchange

The permeability is not reduced in tests where the concentration of $CaCl_2$ is reduced (Grey and Rex, 1966; Khilar and Fogler, 1987). This may be due to the adsorption of divalent Ca^{2+} ions to the kaolinite surface, yielding a positive ζ (Chassagne et al., 2009; Khilar and Fogler, 1987; Kia et al., 1987) [Manuscript II and III]. With opposite charges on kaolinite and quartz, E_{EDL} is attractive; therefore mobilisation would not occur when salinity is reduced. In samples that are initially saturated with distilled water, the measured permeability is comparable to the permeability with a high salinity solution (Khilar and Fogler, 1984; Mungan, 1965) [Manuscript I]. Divalent ions that are naturally present in carbonate cement in the Berea sandstone could be adsorbed to the kaolinite surface so that E_{EDL} is attractive; saturating the sample with NaCl solution would replace divalent ions by Na^+ and reverse the sign of the kaolinite ζ (Grey and Rex, 1966; Khilar and Fogler, 1984; Mungan, 1965). Therefore the effect of salt concentration that is observed in laboratory tests with NaCl solution might not be representative for effects that occur in a geothermal reservoir, where the brine would presumably contain different ions.

6.7.3 Effect of temperature

Permeability reduction due to increasing temperature from room temperature to 80°C–90°C is observed in Berea sandstone samples saturated with distilled water, with NaCl solution, and with $CaCl_2$ solution (Baudracco and Aoubouazza, 1995; Cassé and Ramey Jr, 1979; Schembre and Kovscek, 2005). In contrast to the effect of NaCl concentration, the effect of temperature appears to be largely reversible with cooling (Baudracco and Aoubouazza, 1995; Cassé and Ramey Jr, 1979) [Manuscript I and II].

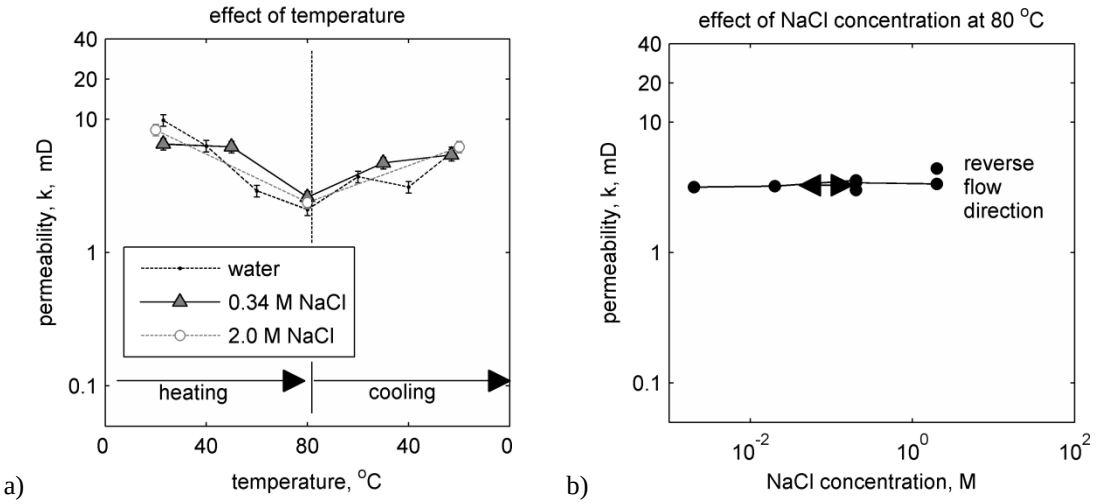

Figure 33: a) Permeability, *k*, reduction due to heating from 20°C to 80°C is largely reversible when temperature is restored; the effect is observed in different tests, with distilled water and with different NaCl concentrations. Interstitial velocity, *v*, for the data in this Figure $v = Q/A\phi$, v = 4 µm/s–7 µm/s. b) Reducing and increasing NaCl concentration at 80°C has no effect on permeability and reversing the flow direction has an insignificant effect; in this Figure v = 70 µm/s–95 µm/s . [Data in a) from Manuscript I and Manuscript II; figures Modified from Manuscript II].

The effect of temperature on permeability might be due to kaolinite mobilisation, as heating can increase the repulsive E_{EDL} between kaolinite and quartz (Khilar and Fogler, 1984; Schembre and Kovscek, 2005). Heating would only slightly increase the repulsive E_{EDL} if σ_0 of the minerals were constant with temperature (Figure 29b). In samples with a 0.2 M NaCl solution the increase might possibly be sufficient to yield a net repulsion energy (Figure 34a), however, heating also reduces permeability in tests with a 2.0 M NaCl solution (Figure 33a). Figure 34b indicates that even a doubling of σ_0 would not cause a repulsive E_{DLVO}; however, a fourfold increase of σ_0 would result in a net repulsion for separations less than 2 nm.

The ζ of kaolinite and of quartz from electrophoresis tests by Rodriguez and Araujo (2006) indicate that σ_0 becomes approximately twice as negative, when the temperature is increased from 20°C to 45°C. Based on potentiometric titration data, Brady et al. (1996) determined that the σ_0 of kaolinite becomes approximately twice as negative when the temperature is increased from 25°C to 70°C. These results indicate that indeed heating can result in the σ_0 of kaolinite and of quartz becoming substantially more negative, which might lead to kaolinite mobilisation.

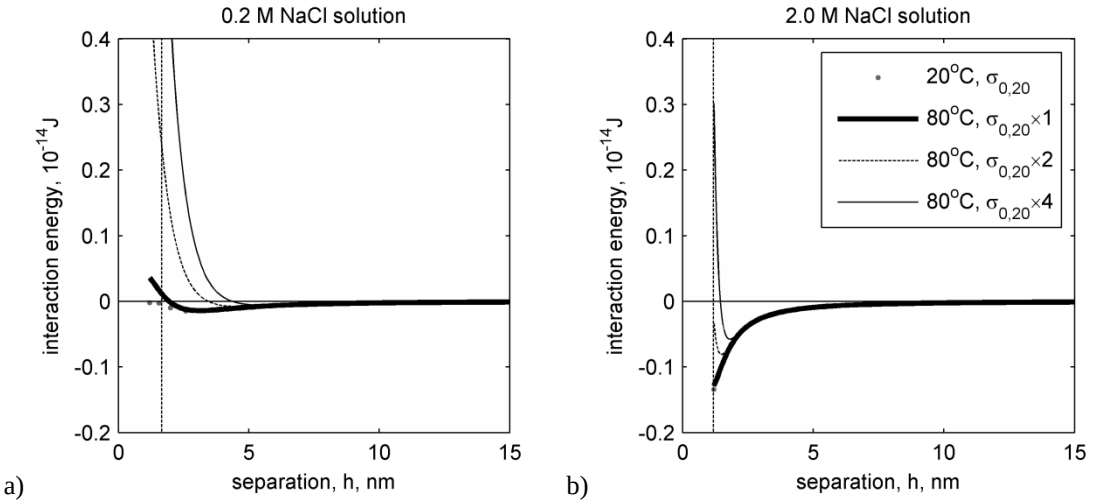

Figure 34: Interaction energy as a function of the separation, *h*, between parallel kaolinite and quartz surfaces.
a) Heating with 0.2 M NaCl solution causes a small net repulsion (positive interaction energy) at short separations if σ_0 is constant (thick dotted line is 20°C, thick solid black line is 80°C with the same surface charge, σ_0, as at 20°C).
b) With 2.0 M NaCl solution heating only causes a net repulsion at short separations if σ_o increases by a factor four. An energy minimum at 2 nm–3 nm separation can be observed. Interaction energy is scaled by an interaction area of 4 μm^2; surface charge densities at 20°C, $\sigma_{0,20}$, are: 11 mC/m^2 for kaolinite, and 27 mC/ m^2 for quartz. Vertical dashed line indicates a separation equal to the Debye length between Stern planes, i.e., $h = 2\tau+\kappa^{-1}$, below which EDL expression is more uncertain. [Modified from Conference paper III].

At separations of 2 nm–5 nm E_{DLVO} shows an attractive minimum for a twofold and for a fourfold increase of $\sigma_{0,20}$ due to heating with 2.0 M NaCl solution (Figure 34b). This is referred to as the second energy minimum, to distinguish it from the first energy minimum that can be observed at smaller separations when $E_{vdW} > E_{EDL}$ and the Born term is included (Hahn and O'Melia, 2004). As the Born term is not included in Figure 34b, no first energy minimum is observed.

Some authors suggest that particles could be attached in the second energy minimum, where they would be more susceptible to hydrodynamic forces than particles that are attached closer to the mineral surface (Hahn and O'Melia, 2004; Yuan and Shapiro, 2011). Salinity reduction at 80°C does not affect permeability during the test in Manuscript II (Figure 33b). This indicates that particles are not attached in a second energy minimum at 80°C, as the second energy minimum would be eliminated by reducing salinity (Figure 34a).

The lack of an effect of reducing salinity at 80°C suggests that particles are already mobilised by heating, even in 2.0 M NaCl solution (Figure 33b). By contrast, Khilar and Fogler (1984) find that salinity reduction reduces permeability in samples of Berea sandstone at 60°C. However, they do not comment on permeability reduction due to heating, which indicates that kaolinite is not mobilised by heating to 60°C in that test. Indeed, Figure 33 indicates that that permeability falls more steeply between 50°C and 80°C than between 20°C and 50°C with 0.34 M NaCl solution; and other authors also observe that the permeability reduction occurs only when a threshold temperature is exceeded (Baudracco and Aoubouazza, 1995)[Manuscript I]. The results by Khilar and Fogler (1984) suggest that if heating did not mobilise kaolinite particles, a subsequent salinity reduction would.

The reversibility of the heat-induced permeability reduction suggests that mobilised particles might not be filtered in pore constrictions. A higher repulsive E_{EDL} between quartz and kaolinite at 80°C due to an increase in σ_0 of both minerals might prevent filtration. Suspended kaolinite particles presumably would affect the rheology of the pore fluid; and possibly interaction among different sides of the particles results in microporous aggregates or in a gel that reduce the intergranular porosity as suggested in Section 6.2 (Figure 24e). The effect of temperature on σ_0 is presumably reversible, whereby cooling might cause kaolinite to re-aggregate as compact booklets or to re-attach to the quartz surface, restoring permeability.

Figure 35 indicates that an increase in the kaolinite σ_0 by a factor four would also yield repulsion among all sides of kaolinite particles; this would suggest that particles remain dispersed in a suspension, rather than that they form aggregates. Nonetheless, the yield stress of kaolinite suspensions, the microporous kaolinite networks, and the kaolinite gel, that are discussed in Section 6.2, are also observed in suspensions with a pH 8–10.5 and monovalent salt concentrations of 0.01 M or less, i.e., when E_{DLVO} is presumably repulsive (Gupta et al., 2011; Zbik and Frost, 2009). Some authors suggest that additional forces, e.g., attractive hydrophobic forces, might possibly affect kaolinite interactions at pH 8–9 (Gupta et al., 2011; Zbik and Horn, 2003; Zbik and Frost, 2009). Thereby, E_{DLVO} would not predict interaction among suspended kaolinite particles in the pore fluid.

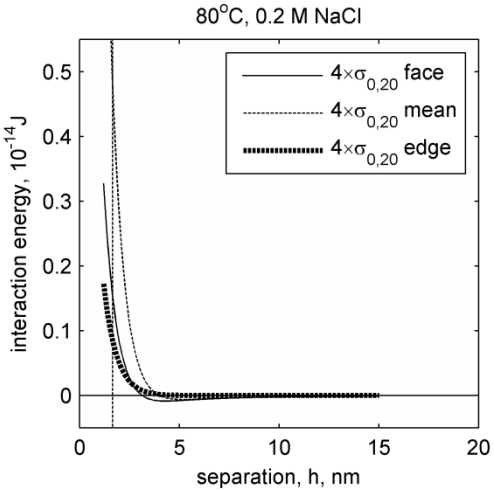

Figure 35: Interaction energy between parallel kaolinite surfaces as a function of separation, *h*. Negative interaction energy indicates attraction. Interaction energy is scaled by an interaction area of 4 μm^2 for interaction between kaolinite faces or for the average kaolinite particles, and by an interaction area of 0.2 μm^2 for interaction between edges. Surface charge densities at 20°C, $\sigma_{0,20}$, are: 7 mC/m^2 for kaolinite faces; 12 mC/m^2 for average on kaolinite particles; 37 mC/m^2 for kaolinite edges. Vertical dashed line indicates a separation equal to the Debye length between Stern planes, i.e., $h = 2\tau+\kappa^{-1}$, below which EDL expression is more uncertain. [Modified from Conference paper III].

6.7.4 Effect of flow rate

At room temperature, hydrodynamic forces may also mobilise particles (Bedrikovetsky et al., 2011, 2012; Khilar and Fogler, 1987; Ochi and Vernoux, 1998; Sen and Khilar, 2006). Ochi and Vernoux observe a

threshold flow rate, below which permeability does not depend on flow rate and above which permeability is reduced, presumably by filtration of mobilised particles. The flow rates used in Manuscript II at 20°C are over one order of magnitude smaller than threshold flow rates for Berea sandstone samples found by Ochi and Vernoux (1998). Accordingly, flow rate has no effect on permeability prior to reducing the NaCl concentration (Figure 36a) indicating that particles are not mobilised by hydrodynamic forces. After permeability is reduced by reducing the NaCl concentration, flow rate also has no effect on permeability (Figure 36a). If mobilised particles are filtered, flow rate apparently does not remobilise filtered particles.

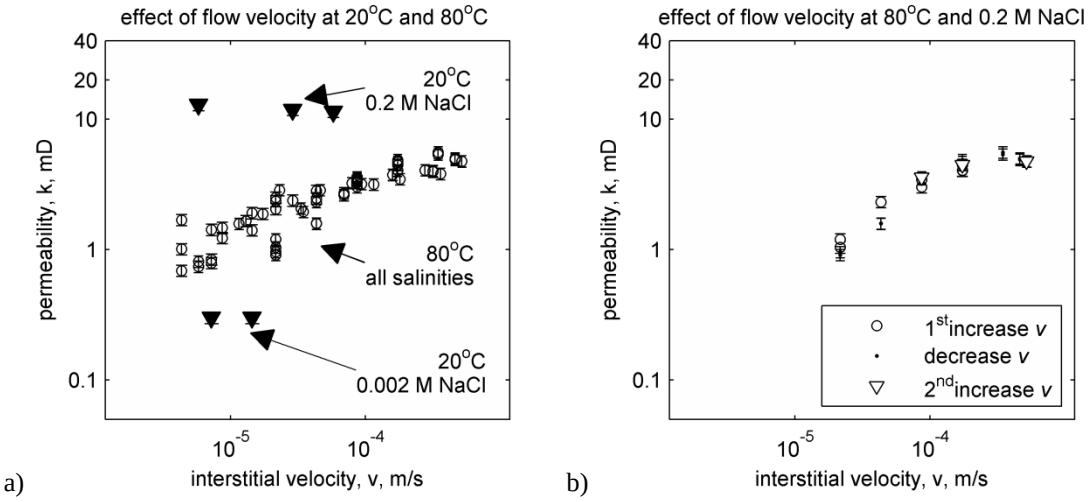

Figure 36: a) Increasing the interstitial velocity, *v*, has no significant effect on permeability, *k*, of a Berea sandstone sample at 20°C (black triangles). Salinity reduction reduces *k*, however, no effect of *v* is observed before or after the salinity reduction. At 80°C, in tests on a different Berea sandstone sample from the same block (white circles), *k* increases with increasing *v*. At 80°C, *k* is independent of salinity. b) At 80°C, the effect of *v* is reversible when the flow velocity was increased, reduced, and increased again. [Modified from Manuscript II].

By contrast, at 80°C after permeability reduction by heating, permeability increases with increasing flow rate, and no hysteresis is observed in cycles where the flow rate is increased and reduced (Figure 36b). Such an effect might be observed when a suspension of interacting kaolinite particles or kaolinite aggregates that only shear above a yield stress is present in some pores (Figure 24b and e). When below the yield stress, this would reduce the mobile pore volume and reduce permeability; above the yield stress, shearing of the suspension or suspended aggregates might increase the free pore volume and partially restore permeability. The magnitude of the shear forces during experiments in Manuscript II is of the order of magnitude of the yield stress of dense kaolinite suspensions that is observed at pH 10.5 in 0.001 M KNO_3 solution by Mpofu et al. (2003). The reversibility of the effect of flow rate suggests that kaolinite is not removed from the pores. Accordingly, the kaolinite content of this tested sample after the test is not significantly lower than the kaolinite content of an untested sample of Berea sandstone from the same block, as determined from quantitative image analysis [Manuscript III].

Estimating the effect of temperature and salinity on the interaction forces using the DLVO theory involves a number of uncertainties including: the value of σ_0 of the minerals, and in particular of kaolinite as the average σ_0 depends on particle shape and size; the effect of temperature on σ_0; the estimation of boundary conditions and interaction geometry for the DLVO equations; the effect of temperature on the Hamaker constant; the extent to which additional, non-DLVO forces characterise interaction among suspended kaolinite particles. Therefore, calculations in this Chapter are only considered as a qualitative estimate of effects of salinity and temperature on the DLVO interaction forces, E_{EDL} and E_{vdW}.
Nonetheless, the effect of heating on surface charge density that would be required to account for particle mobilisation, is of the same order of magnitude as the effect of temperature that is observed in electrokinetic experiments and potentiometric titrations in literature. The effect of the higher surface charge density on the interaction between kaolinite and quartz might indeed limit filtration at elevated temperatures. Furthermore, interaction among kaolinite particles would be less repulsive than between kaolinite and quartz, due to the heterogeneous surface charge on kaolinite particles, and due to the lower average surface charge density on kaolinite than on quartz. Accordingly, literature on kaolinite suspensions indicates that interactions among kaolinite particles substantially affect the viscosity of the suspension.

The mechanisms of permeability reduction that are discussed in this Chapter, filtration and effects of suspended particles on pore fluid rheology, would not be mutually exclusive. Indeed, when the concentration of mobilised kaolinite particles is high, particles would presumably have a significant effect on rheology and there would be more interactions among kaolinite particles; when the concentration of mobilised particles is lower, particles might be entrained by the pore fluid and transported. The effects of temperature and salinity that are observed in permeability experiments do indicate that different meachnisms dominate in the two situations. The reversibility of permeability changes due to heating, and the different effects of flow rate at 20°C and at 80°C that are observed in laboratory experiments, could be relevant for geothermal energy production and seasonal heat storage in kaolinite-bearing sandstones. At 80°C, permeability might be increased by increasing the flow rate, and this would reduce pumping costs. Furthermore, a permeability increase due to cold water re-injection during winter might improve the acquifer permeability.

7 Approach to investigation

The focus of the PhD project lies on data analysis and interpretation; this Chapter gives an overview of methods of data interpretation that were used. For details of experimental procedures that were performed by others, I refer to the appended manuscripts.

7.1 Literature analysis: effect of temperature on permeability

To investigate the effects of temperature, data from 17 publications, comprising 13 sandstone Formations, in which permeability is measured at two or more temperatures, using mineral oil, nitrogen gas or aqueous solutions, is systematically investigated [Conference paper I, Manuscript I]. In order to compare among formations with different porosity and permeability, the reported permeabilities are normalised to the effective S_p by using the Kozeny equation (Eq.(11), Eq.(19)). The Kozeny equation is also used to model effects of thermal expansion. Results are discussed in in Chapter 5.

7.2 Flow-through experiments

Flow-through experiments on Berea sandstone plugs were performed by DTU students[5] and Claus Kjøller at the GEUS Core Laboratory in order to assess the practical aspects of permeability experiments at elevated temperature [Manuscript I]. Experiments using a synthetic opal plug were used to verify the absence of corrosion in the setup[6]. Effects of temperature, flow rate, and salinity on permeability in samples of Berea sandstone were investigated in additional tests, one of which lasted approximately 150 days[7] [Manuscript II]. This sample was subsequently used for quantitative image analysis [Section 7.5].

7.3 Specific surface area from nitrogen adsorption

The specific surface area of samples of Gassum Formation sandstone, Bunter Formation sandstone and Berea sandstone is measured by using nitrogen adsorption (BET method, Brunauer et al. (1938)). Measurements are made using a Mircomeritics Gemini 2735 surface area analyser[8]. In order to have a sufficient surface area, 2 g or more of coarsely ground samples are used, giving a total surface area > 2.5 m^2. Samples are degassed in nitrogen at 70°C for four hours prior to measurement, as the presence of adsorbed water might interfere with gas adsorption (Clausen and Fabricius, 2000; Sing, 2001). Adsorption is measured at four relative pressures between 0.05 and 0.24 in order to remain below the pressure range where capillary condensation might occur (Sing, 2001).

The specific surface area from nitrogen adsorption, in combination with grain density and helium porosity, is used to calculate $S_{p,BET}$, [Manuscript I, II, III, IV]. The effective S_p for permeability is compared with $S_{p,BET}$ in chapters 2 and 6.

[5] Christian Haugwitz, Peter Sally Munch Jacobsen, and Jacob Fabricius Riis.
[6] C. Haugwitz, P.S.M. Jacobsen, and C. Kjøller
[7] J.F. Riis and C. Kjøller
[8] Department of Environmental Engineering, DTU

7.4 Qualitative electron microscopy analysis

Electron microscopy is used throughout the investigation in order to relate mineralogy and texture to permeability. Polished thin sections of Berea sandstone samples, both prior to and after flow-through experiments, sandstone samples from the Gassum Formation, and sandstone samples from the Bunter formation are analysed by using a combination of BSEM and EDS, using a Quanta 200 (FEI) scanning electron microscope[9]. SEM is used to study kaolinite and illite morphology in selected samples of Rotliegend sandstone, by using a Quanta 650 (FEI)[10].

Qualitative observations are used to support the discussion of permeability in Chapters 2, 3, 4, and 6.

7.5 Quantitative image analysis combined with mineral mapping

Chemical alteration may result from prolonged hot water injection or hot water storage (Milsch et al., 2009; Schepers and Milsch, 2013; Tenthorey et al., 1998) [Manuscript I, II, and III]. Therefore, applications of quantitative analysis of images in which mineralogy is mapped by using the QEMSCAN® system (FEI) are investigated in Manuscript III. The objective is quantification of: mineral content, reactive surface areas of different minerals, lamination of mineralogy and porosity, and chemical alteration resulting from hot water injection. An untested sample of Berea sandstone is compared to a sample in which 80°C NaCl solution is injected for 150 days [same sample as in Manuscript II[11]]; and a comparison is made among untested sandstone samples from Gassum formation and Bunter formation and Berea sandstone [Manuscript III]. The methods used, and the results that demonstrate the relevance of these methods for geothermal energy storage, are discussed in the following Subsections.

7.5.1 Mineral identification

The QEMSCAN® system (FEI) is used to map mineralogy by using BSE intensity in combination with EDS. This results in images with a large interrogation area, 100 mm^2, and a resolution of l_{pix} = 1.8 μm, in a reasonable time. A second mapping of the same area is made using only BSEM with l_{pix} = 0.83 μm, a higher resolution is not used for mineral mapping, due to the interaction volume of the electron beam for the generation of fluorescence light in EDS.

Pore space and solids are distinguished based on a BSE intensity threshold. With l_{pix} = 1.8 μm, pixels containing both pores and minerals would have a lower BSE intensity than pixels containing only minerals (Peters, 2009). Reducing the intensity threshold increases the solids area at the cost of pore area; in particular the area of clay minerals that have small pores among clay particles, is sensitive to the BSE threshold. A low threshold is used to study the distribution of clay minerals; accordingly image porosity is lower than porosity as measured by using helium porosimetry [Manuscript III]. The difference between image porosity and the helium porosity can be accounted for by assuming an unresolved porosity among clay minerals of

[9] At the Department of Civil Engineering, DTU.
[10] At the Leeds Electron Microscopy and Spectroscopy Centre, at the University of Leeds.
[11] Tests performed by Jacob Riis (DTU) and Claus Kjøller (GEUS)

approximately 50%; this is comparable to estimates for porosity of clay mineral aggregates in sandstones ranging from 40%–70% by other authors (e.g., Hurst and Nadeau, 1995; Vernik, 1994).

Different minerals are identified based on EDS spectra; mineral compositions are defined in the species identification protocol (SIP) of the QEMSCAN® iDiscover (v.5.3) software (Ayling et al., 2012; Pirrie et al., 2004). The *oil and gas v3.7* SIP (by FEI) is used as a basis SIP for this study. Individual pixels may contain EDS spectra from a combination of minerals, e.g., for fine-grained clay minerals, or on the interface between different minerals. The original SIP contains some interface categories that account for commonly occurring interfaces in the formations that were used to define that SIP; additional interface categories are defined for interfaces that are common in the formations in this study. Furthermore, categories are included in order to account for iron oxide/hydroxide precipitates that formed in the tested Berea sandstone sample.
The mineral definitions are arranged hierarchically in the SIP; accordingly, a pixel is assigned to the first definition that matches the EDS spectrum. Therefore, modifications are also made in the order of minerals in the SIP in order to improve classification.
After a first identification of all pixels, some pixels are regrouped. Interface pixels are assigned to one mineral phase, i.e., a pixel that is identified as 25% kaolinite 75% quartz is assigned to the quartz phase. Several minerals are grouped for further analysis: illite and muscovite (IM); chlorite group minerals, mixed layer chlorite-smectite and biotite (CMB); dolomite and ankerite (DA); gypsum and anhydrite (GA); iron oxide/hydroxide (Fe); and titanium oxides (Ti); and feldspar minerals (F).

7.5.2 Pre-processing

Unidentified single pixels remain on interfaces between minerals for which no interface group is defined. These pixels are assigned to the phase that they border in a pre-processing step. No smoothing is applied, as with l_{pix} = 1.8 μm isolated pixels could be due to small particles. Examples are mixtures of illite and kaolinite particles, and kaolinite particles that are located in between the cleavage planes of mica grains (Figure 37).

Mineral identification based on the SIP is compared to manual analysis of BSEM images in combination with EDS, and to the bulk mineralogy from XRD for samples of Gassum and Bunter Formation sandstones (Weibel et al., 2010), and Berea sandstone (Baudracco and Aoubouazza, 1995; Churcher, 1991).
The kaolinite content of the untested Berea sample is only 2.9 vol.%, i.e., 3.3 wt.%[12], and the illite/mica content corresponds to 3.2 wt.%. By contrast, other authors observe 5 wt.%–6 wt.% kaolinite and only 1 wt.% illite (Baudracco and Aoubouazza, 1995; Churcher, 1991). Whereas variation among samples might contribute to this difference, qualitative analysis of BSEM images also indicates that the sample that kaolinite is more abundant than illite in the scanned samples. The amount of kaolinite might be underestimated in the QEMSCAN images when pixels contain a mixture of illite and kaolinite, or when

[12] $V_{kaolinite}/V_b$ = 2.9 %; $V_{kaolinite}/Vs = V_{kaolinite}/(1-\phi)\ V_b$; $mass_{kaolinite}/mass_s = V_{kaolinite}/Vs\ density_{kaolinite}/density_{solids.}$

pixels are on an interface between kaolinite and mica (Figure 37). Such pixels are assigned to illite/mica due to the presence of potassium in illite.

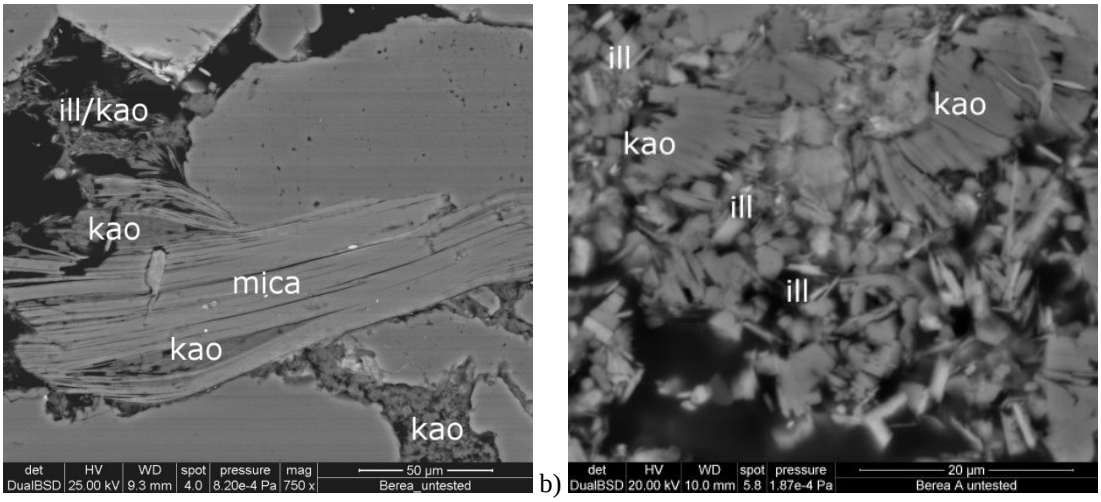

Figure 37: Backscatter electron microscopy, BSEM, images of an untested Berea sandstone sample: a) Kaolinite (kao) particles are located in between the cleavage planes of a mica grain. b) A mixture of fine illite particles (ill) and kaolinite particles where some plates have a thickness less than 1.8 µm.

Image analysis is performed on images that are exported from the QEMSCAN® software in which pores and different minerals or mineral groups have distinct, grey-scale, colours. Codes for image analysis are written in Matlab 2012b (MathWorks, USA).

7.5.3 Minimum representative area

The MRA of mineral phases and of porosity are quantified, as described in Subsection 2.4.2. The MRA exceeds the total interrogation area for gypsum/anhydrite in samples of Bunter sandstone. This is due to a patchy distribution of this phase, which is also observed by Weibel et al. (2010). This indicates that the G/A content of an untested side trim would not be representative for the G/A content in a corresponding plug sample; therefore effects of hot water injection cannot be quantified based on comparison of the G/A content in a side trim and in the tested plug. For other mineral phases and for porosity in the untested samples, the interrogation area does exceed the MRA. An error margin to account for variation on the millimetre scale is estimated from the standard deviation among the mineral content of four 25 mm^2 subsections for each 100 mm^2 image.

7.5.4 Specific interface

The specific interface of a phase is quantified by duplicating the image and shifting the duplicate by one pixel in a specified direction. Subtracting the shifted image from the original image results in an image where only interface pixels are nonzero. This is comparable to image differentiation; however, this is computationally more efficient, which is relevant for the large grey-scale images in this study (5760 pixels × 5760 pixels). Multiplication by a mask of the phase whose interface is to be determined results in an image

with only pixels that contain an interface of this phase in the direction that the image was shifted. This is done by shifting in all four directions to identify the four possible edges for each pixel. Pixels on a diagonal interface, are assigned a length $l_{pix}\sqrt{2}$ rather than $2l_{pix}$ after Borre et al. (1995).

The reactive surface area from images would require calibration in order to apply this in chemical models, as specific interface, mineral content, and porosity depend on the resolution and on the BSE threshold for porosity. Furthermore, due to micropores among clay particles, interfaces of other mineral phases to clay phases could also be considered as interfaces to the pore area, i.e., as reactive interfaces.

For permeability estimation, the specific pore interface, I_p, is estimated at a constant ratio of l_{pix} to effective S_p for permeability as in (Berryman and Blair, 1987)[Subsection 2.4.2]. The parameter K, to estimate 3D S_p from 2D I_p, (Eq.(21)), is fit to the data. The same K fits the Gassum and the Bunter sandstone samples; this K overestimates permeability in the Berea sandstone samples by approximately 50%. Nonetheless, the ranking of permeabilities as estimated from images with a constant K and ratio of l_{pix} to S_p does correspond to the measured permeabilities of the three samples [Manuscript III].

7.5.5 Heterogeneity: lamination and patches

Heterogeneity is quantified by calculating mineral content of subsections of the images. Lamination is investigated in rectangular subsections parallel to the lamination, which have different widths and span the length of the image; widths are in the range 90 μm–630 μm. A patchy distribution of minerals is investigated by using square subsections with the same area as the rectangular subsections.

The specific interface of quartz scaled by the quartz area is an estimate of the effective grain size. This estimate corresponds to a visible lamination in the quartz grain size, and a lamination in porosity in the tested sample of Berea sandstone (Figure 38b and Figure 39b). Lamination is less pronounced in images of the untested Berea sandstone plug from the same block (Figure 38a and Figure 39a). As grain size lamination would be a sedimentary feature, rather than due to hot water injection experiments, this indicates that the degree of lamination varies over a larger area than the 100 mm^2 interrogation areas used. Nonetheless, the quartz content and porosity of the two samples are approximately equal, and the MRA of porosity and quartz in the untested sample are smaller than 100 mm^2 [Manuscript III].

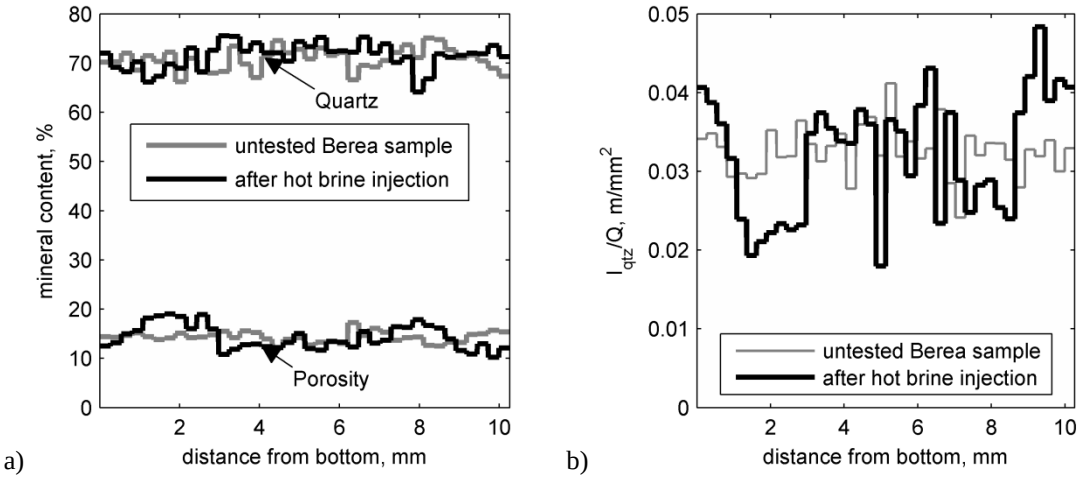

Figure 38: a) Porosity and quartz content of horizontal subsections (width 270 µm, length 10300 µm) are shown as a function of distance from the bottom of the image. b) Specific interface of quartz, I_{qtz}, scaled by quartz area, Q, for the same subsections. [Modified from Manuscript III].

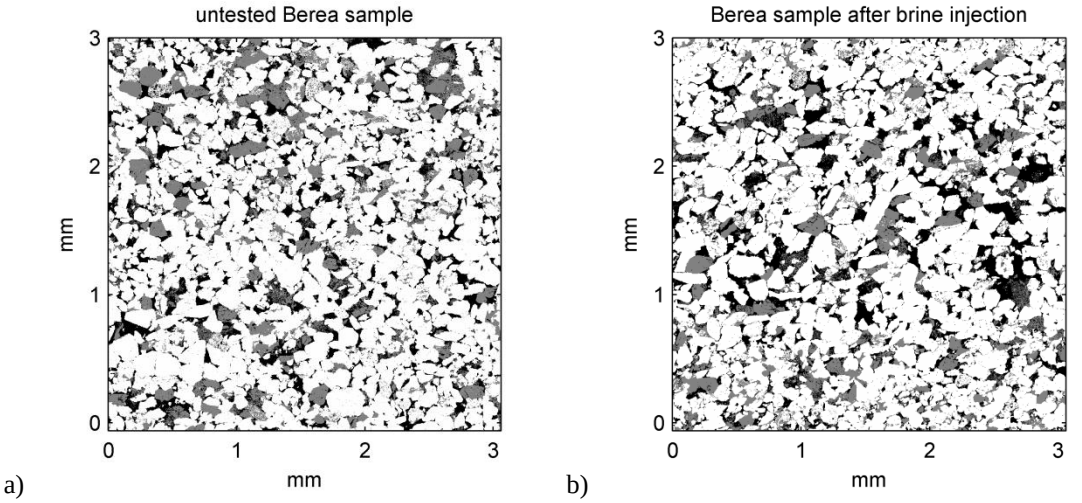

Figure 39: Segmented images showing quartz (white), pores (black), and other minerals (grey) in: a) The untested Berea sandstone sample; b) The Berea sandstone sample after 150 days of 80°C NaCl solution injection. Horizontal lamination of the quartz grain size can be observed in the tested sample. These images represent lamination in the first 3 mm in Figure 38 and Figure 40. Pixel length l_{pix} = 1.8 µm. [Modified from Manuscript III].

A lower siderite content and a higher iron oxide/hydroxide content in the tested Berea sandstone sample indicate that iron is released by dissolution of siderite, which oxidised and precipitated during the tests [Manuscript II, III]. Lamination of the iron oxide/hydroxide content indicates that iron oxide/hydroxide precipitates predominantly in the finer grained low porosity lamina (Figure 40a). In the untested sample, a lamination of siderite can be observed; however, this does not correspond to the grain size or porosity lamination (Figure 40b). This suggests that hot water injection enhanced the existing lamination.

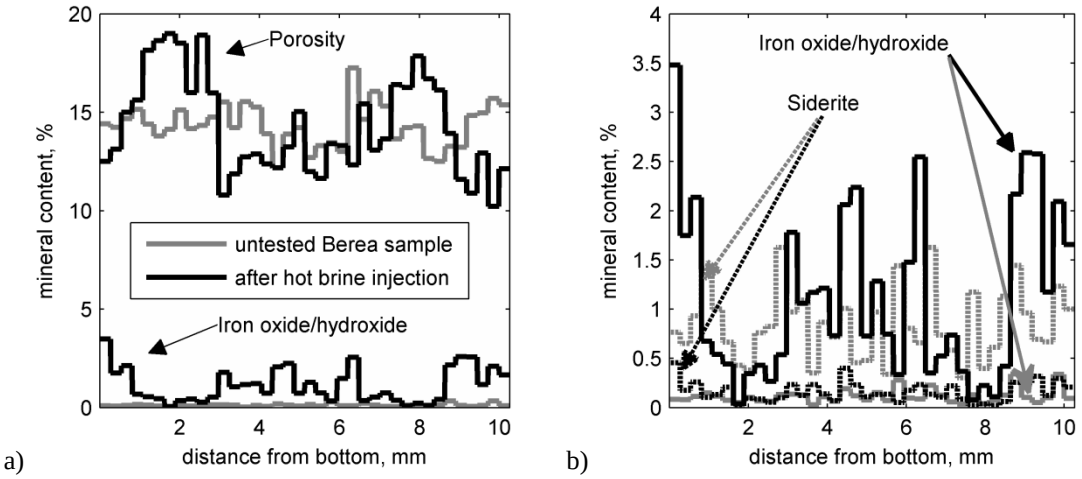

Figure 40: a) The fluctuations in the porosity and in the iron oxide/hydroxide content are shown as a function of distance from the bottom of the image for horizontal subsections (width 270 μm, length 10300 μm). b) Fluctuations in siderite (dashed lines) and iron oxide/hydroxide content (solid lines) for same lamina. In the untested sample the iron oxide/hydroxide content is smaller than the siderite content, whereas the opposite is observed in the sample after hot brine injection. [Modified from Manuscript III].

The effect of lamination on permeability is estimated by calculating permeability from I_p in subsections parallel to the lamination and comparing the harmonic, geometric and arithmetic averages. Permeability estimated by different means is not significantly different, and permeability in the tested Berea sample is similar to the permeability in the less laminated, untested, Berea sample. Measured permeability is only 20% lower at the end of the 150 day experiment than at the start; these results indicate that the enhancement of lamination did not significantly affect permeability in this sample [Manuscript II and III].

7.5.6 Multivariate analysis

Principal component analysis (PCA) is used to analyse correlations among minerals, to distinguish among the subsections of images from the different untested sandstone formations, and to distinguish among subsections from the tested and the untested Berea sandstone samples. The PCA is done by singular value decomposition of the data matrix. The data matrix consists of a row for each subsection, whose columns contain the content of the different mineral phases and porosity. Data are centred in order to reduce the square error (Miranda et al., 2008). The variation in volumetrically minor phases, such as clay minerals, carbonate minerals, and iron hydroxides, is accounted for by normalising the data. Subsections from different formations are distinct in a plot of the first and second principal components; subsections from the untested and the tested Berea sandstone samples can be reasonably distinguished (Figure 41).

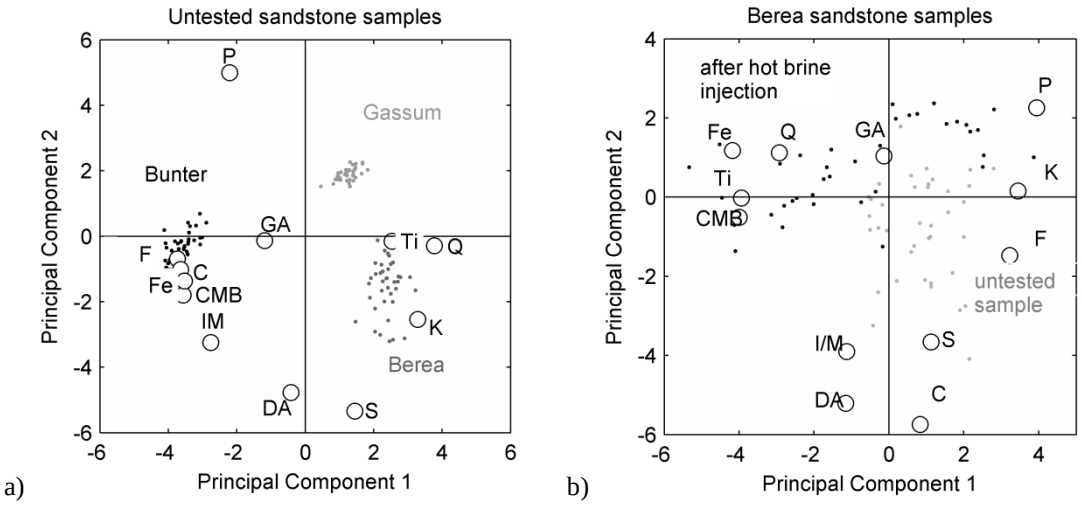

Figure 41: The first two principal components show the loading on the minerals scaled by 10 (white circles) and the principal component scores of horizontal subsections (dots) (width 270 µm, length 10300 µm). a) Subsections from the three formations plot in distinct groups. b) Subsections from a sample of untested Berea sandstone (grey) from a sample of Berea sandstone after injection of 80°C NaCl solution for 150 days (black) generally fall into separate groups. (P=porosity; Q=quartz; F=feldspar; K=kaolin; IM=illite/muscovite; CMB=chlorite/mixed layer illite-muscovite/biotite; C=calcite; S=siderite; DA=dolomite/ankerite; Fe= Fe_2O_3/FeOOH; Ti=Titanium oxides; GA=gypsum/anhydrite.) [Modified from Manuscript III].

7.5.7 Clay minerals and potential fines mobilisation

Kaolinite and also illite particles might reduce permeability by fines migration (Wilson et al., 2014). Kaolinite is only present in Berea and Gassum sandstone samples [Manuscript III]. Whereas this Gassum sandstone sample only contains 1.2 vol.% kaolinite, samples of Gassum formation from different localities can contain higher kaolinite contents (Weibel et al., 2010); therefore kaolinite mobilisation might affect permeability during hot water injection in this Formation.

Samples from all three formations contain in excess of 2 vol.% illite or mica; however, no distinction is made between illite and mica based only on elemental analysis in QEMSCAN®. Whereas small illite or kaolinite particles in intergranular pores might be mobilised, larger mica grains can be observed in the Gassum and Bunter samples that are presumably not mobile (Figure 42). Due to the large pixel size l_{pix} = 1.8 µm, the specific interface of the clay minerals scaled by clay mineral area does not characterise the size of clay particles, but rather the size of clay particle aggregates. Therefore, this could not be used to quantitatively distinguish between illite and mica, and chlorite and biotite, in Gassum and Bunter sandstone samples.

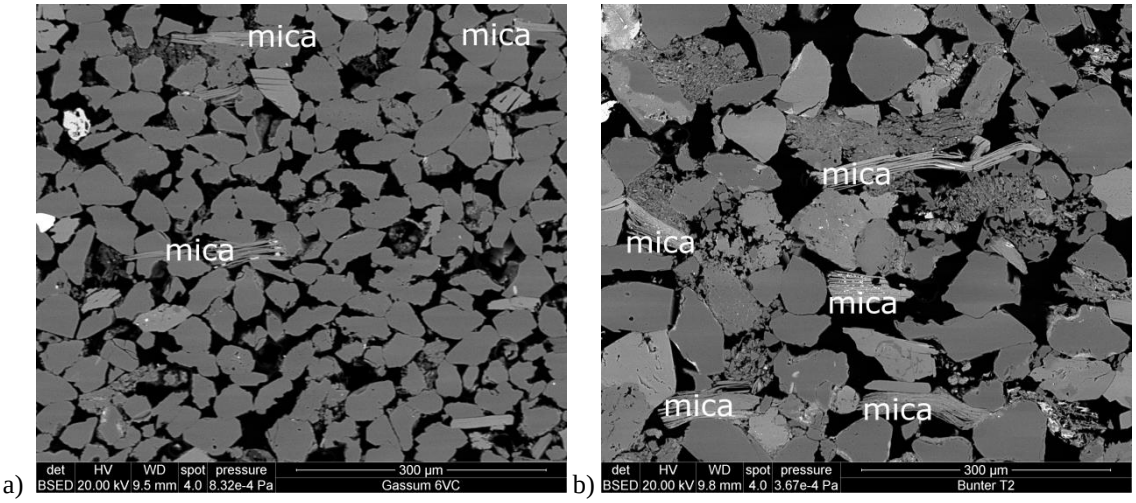

Figure 42: Backscatter electron microscopy, BSEM, image showing mica grains. a) Gassum Formation sandstone. b) Bunter Formation sandstone.

The difference between the kaolinite, and also the illite, contents of the untested Berea sample and of the tested Berea sample is below the estimated error margin, and there is no significant difference between the interfaces of kaolinite to other minerals in the two samples [Manuscript III]. This suggests that kaolinite was neither transported out of the sample nor permanently redistributed during hot water injection.
Heating did reduce the permeability, which suggests that kaolinite particles were mobilised during the experiment. However, the effect of temperature was also largely reversible with cooling, which might indicate that particles re-aggregated, which might be the reason that there is no observable alteration in images of the tested sample.
As l_{pix} = 1.8 µm is larger than the smallest kaolinite particles, and changes in the distribution of smaller particles might not be observed in QEMSCAN® images. However, higher resolution BSEM images also indicate no qualitative alteration in the kaolinite distribution.

7.6 Klinkenberg procedure

Data from the Klinkenberg procedure on: Berea sandstone samples, sandstone samples from Gassum Formation from three localities, and sandstone samples from Bunter Formation from one locality, as measured at the GEUS Core Laboratory; and Klinkenberg test data for Rotliegend sandstone samples from 3 localities from PETGAS, University of Leeds, is used to estimate characteristic equivalent pore size and the effects of immobile water on permeability. Results are discussed in chapters 3 and 4, experimental data and calculations are included in Appendix A.

7.7 DLVO modelling

DLVO theory is used in order to estimate effects of temperature and salinity on electrostatic interaction energy in relation to fines migration (Chapter 6) [Conference papers II, III, Manuscript II].

7.8 Database analysis

The PETGAS database of the University of Leeds contains petrophysical measurements on tight gas sandstones; this data is used to discuss permeability in chapters 2, 3, and 4, and for a systematic database analysis in Manuscript IV. For the latter, samples for which: gas and brine permeability, NMR, mercury injection, helium porosity, grain density, mineralogy as quantified using XRD, and BSEM images with a l_{pix} = 3 μm/pixel are available are used. Samples with an abnormally low grain density, as compared to their mineralogy, are discarded, as this might indicate disconnected porosity or poor sample cleaning. BSEM images are examined to verify the absence of drilling mud, and to qualitatively check mineralogy from XRD. Results from this investigation are discussed in chapters 2 and 4.

In addition to the data used in Manuscript IV, specific surface area from nitrogen adsorption is available for 43 out of the 63 samples. This data is referred to in subsections 2.4.1 and 7.8.2. Those measurements were made on samples that were oven-dried over night at 60°C, but not degassed.

7.8.1 Principal component analysis of mineralogy

Samples are grouped based on PCA of the mineralogy. In order to include porosity in the characterisation, the mass fraction of each mineral from XRD is converted to the volume fraction based on estimates of mineral density from literature [Manuscript IV]. The same PCA method as in Section 7.5.6 is used.

7.8.2 Estimation surface relaxivity

An average ρ is used to estimate the S_p distribution from the T_2 distribution cf. Eq.(23). The value of ρ is estimated from S from mercury injection and S from NMR. The Washburn (1921) equation Eq.(69) relates capillary pressure P_c to equivalent pore radius:

$$r_p = -\frac{2\gamma_{Hg}\cos(\theta)}{P_c} \tag{69}$$

where γ_{Hg} is the surface tension, and θ is the contact angle. Surface area can be estimated by integration of the differential mercury injection curve cf. Eq.(70) (Giesche, 2006; Rootare and Prenzlow, 1967).

$$S = -\frac{1}{V_B\gamma_{Hg}\cos(\theta)}\int P_c dV_{Hg} \tag{70}$$

where V_{Hg} is the volume of mercury injected. Eq.(70) can be derived from Eq.(69) for cylindrical capillaries where $S_p = 2/r_p$. For stepwise injection of mercury, where $f_{Hg,i}$ is the fraction of the porosity that is filled by mercury for the i^{th} pore pressure increment $P_{c,i}$, S is expressed by Eq.(71).

$$S = -\frac{\phi}{\gamma_{Hg}\cos(\theta)}\sum P_{c,i} f_{Hg,i} \tag{71}$$

Surface area is estimated from NMR by summation of $S_{p,i,NMR}$ weighted by the fraction of porosity f_{NMR} that has this $S_{p,i,NMR}$. Thus, when $S_{p,i,NMR}$, is estimated from $T_{2,i}$ cf. Eq.(23), for a uniform ρ, S is:

$$S = \frac{\phi}{\rho} \sum \frac{f_{NMR,i}}{T_{2,i}} \tag{72}$$

Assuming 100% mercury saturation, ρ is:

$$\rho = \frac{-\gamma_{Hg} \cos(\theta) \sum \frac{f_{NMR,i}}{T_{2,i}}}{\sum P_{c,i} f_{Hg,i}} \tag{73}$$

A mean value of ρ = 10 μm/s with a standard deviation of 4 μm/s is obtained for the 63 samples of Rotliegend sandstone [Manuscript IV]. Values of ρ reported for quartz and kaolinite are only 2 μm/s–5 μm/s in NaCl solution (Alam et al., 2014). However, iron-bearing minerals can increase ρ, and values of ρ > 18 μm/s are reported for quartz covered with goethite in a mixture containing only 1 wt.% iron, and for mixtures of siderite and quartz (Keating and Knight, 2007, 2010). Results in those studies indicate that ρ is affected by the mass of iron, and by the structural relation in which iron is present. All 63 samples contain iron-bearing minerals, which could account for the estimated values of ρ.

Experimental artefacts might affect estimates of ρ based on S. Incomplete saturation with mercury would yield a lower S from mercury injection, resulting in an overestimation of ρ cf. Eq.(72). On the other hand, if larger pores are accessed only through smaller pores during mercury injection, this would yield a higher S, and accordingly an underestimation of ρ.
Some authors estimate ρ by comparing the mode of the differential mercury injection curve with the mode of the NMR T_2 distribution, and report values in a range 6 μm/s–50 μm/s (Coates et al., 1999; Dastidar et al., 2006). This method yields values in a range of 1 μm/s–300 μm/s for the 63 Rotliegend samples. Other authors overlay the cumulative mercury injection curve and the cumulative NMR T_2 curve to estimate ρ (e.g. Mbia et al., 2014). However, the shapes of these curves may differ, whereby only sections of the curves for some samples can be overlaid. If the sections corresponding to the smaller pores are overlaid, the results for the Rotliegend samples are comparable to estimates of ρ based on S.

The specific surface area as measured by nitrogen adsorption, for 43 samples, is also used to estimate ρ cf. Eq.(72) yielding ρ = 18 μm/s ± 22 μm/s. A higher ρ could be due to a smaller surface area measured by nitrogen adsorption; values of ρ = 60 μm/s–40 μm/s are obtained for some samples. These values suggest that S is underestimated by nitrogen adsorption. This could be due to interference of water films on the mineral surface, as samples were only oven-dried, and not degassed, prior to measurements. Discarding three

outliers with ρ > 35 μm/s yields ρ = 13 μm/s ± 6 μm/s for the remaining 60 samples, which is comparable to ρ = 10 μm/s ± 4 μm/s.

The value of ρ affects k_i (cf. Eq.(25)), and thereby the fraction of the porosity that is required for the sum of k_i to equal the measured permeability, which is considered as the fraction of porosity that is effective for permeability [Subsection 2.4.4; sections 4.3 and 4.4; Manuscript IV], and the maximum T_2 time that contributes to permeability, $T_{2,max}$. The effect of ρ on the maximum equivalent pore size that is effective for permeability, $r_{p,NMR,max}$, is offset by the effect of ρ on the S_p calculated from $T_{2,max}$ cf. Eq.(23).
Figure 43 shows the effect of ρ on the estimated effective fraction of porosity and on $r_{p,NMR,max}$ for the two samples shown in Chapter 2 and Chapter 4 (Figure 8, Figure 9, and Figure 12). For ρ < 6 μm/s summation of k_i over the entire pore volume underestimates the measured permeability for some samples, including Sample 5B (Figure 43a). The stepwise decline of fraction of effective porosity (Figure 43a), and the saw tooth trend of $r_{p,NMR,max}$ in Figure 43b reflect the discretisation of the T_2 bins, i.e., for several values of ρ the maximum T_2 is constant.

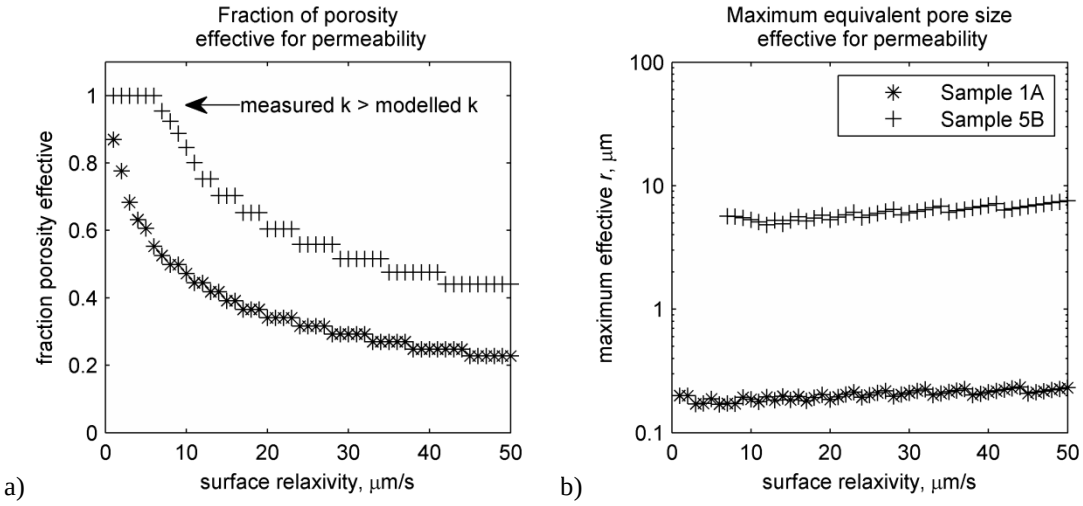

Figure 43: a) The fraction of porosity effective for permeability is the fraction of porosity that is required for the modelled permeability, k, to match the measured k. The effective porosity decreases as a function of surface relaxivity, ρ, because the modelled permeability of each pore size increment is larger with a higher ρ; thus fewer pore size increments are required to match the measured k. b) The maximum equivalent pore size that is effective for permeability, $r_{p,NMR,max}$, as estimated from the maximum T_2 time that is effective for permeability, $T_{2,max}$, is relatively constant with ρ as the smaller $T_{2,max}$ with higher ρ is partly offset by a higher r estimated from T_2 with higher ρ. In Sample 5B the measured permeability exceeds the modelled permeability for the entire pore volume for ρ < 6 μm/s.

7.8.3 Texture analysis

BSEM images with l_{pix} = 3 μm are used to estimate the distribution of clay minerals in the intergranular pore volume. This resolution is too low to resolve pores among clay minerals, therefore pixels that contain both clay particles and porosity have a lower BSE intensity, and accordingly a lower grey level, than pixels that contain only clay minerals, and a higher grey level than pixels with only porosity. By using a double threshold, the images can therefore be segmented into: grains, pores and clay minerals, and pores without

clay minerals (resulting in Figure 9 in Section 2.4.4). Sample-specific thresholds are estimated based on a histogram of pixel grey levels; histograms are not equalised, as the histograms shape depends on mineralogy (Figure 44).

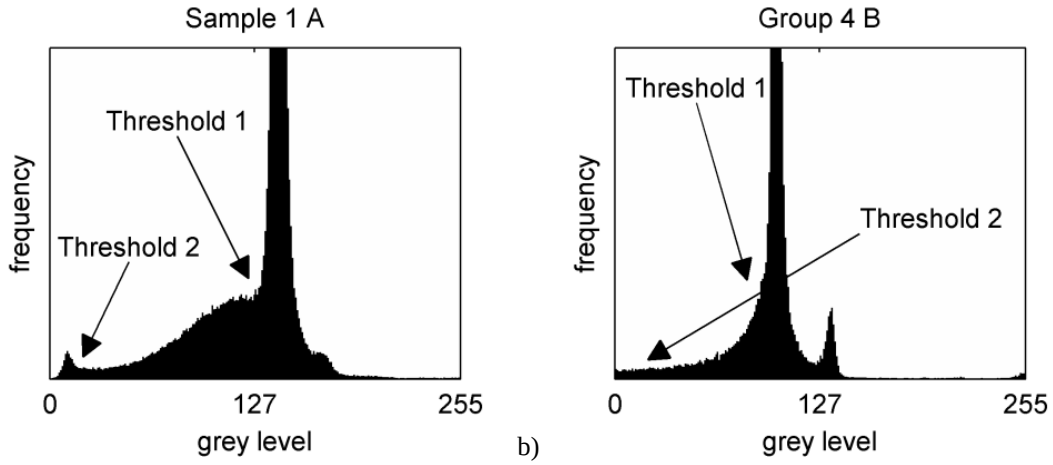

Figure 44: Histograms of grey level, where grey level reflects the backscattered electron, BSE, intensity. Threshold 1 separates solid grains, with a higher intensity, from clay minerals and pore volume. Threshold 2 separates pixels that contain both minerals and porosity from clay-free porosity. a) The distinct peak smaller than Threshold 2 indicates the presence of clay-free porosity. b) The distinct peak for high grey levels is due to the presence of minerals with a relatively high density. [Figure a is from Manuscript IV].

8 Conclusions

Both the physical basis and the simplicity of the Kozeny equation contribute to the continued application of this equation to model permeability (e.g., Berryman and Blair, 1987; Carman, 1937; Hossain et al., 2011; Mortensen et al., 1998; Pape et al., 2006; Walderhaug et al., 2012). However, the Kozeny equation relates permeability to porosity and specific surface area per pore volume, S_p, for materials with a uniform equivalent pore size. Therefore, in sandstones that have a pore size distribution, additional assumptions or empirical fitting parameters are required in order to estimate the S_p that can be considered effective for permeability, i.e., the S_p that, in combination with porosity, would estimate permeability.

When permeability is controlled by intergranular pores, the effective S_p may be estimated from the specific interface length per pore area, I_p, from images that are acquired at an appropriate resolution (Berryman and Blair, 1987; Solymar and Fabricius, 1999) [Manuscript II and III]. As I_p depends on resolution and on porosity threshold, and furthermore, as a parameter, K, is required in order to convert from 2D I_p to 3D S_p, calibration to data would be required. Image-based estimates of S_p were used for comparison of permeability among samples; for sandstones from three formations, Berea sandstone, Gassum Formation, and Bunter Formation, permeability was estimated within a 50% margin, by using one value of K and a constant ratio of resolution to effective S_p for samples from the three formations [Manuscript III].

By summation of permeability in increments of the pore size distribution Hossain et al. (2011), apply the Kozeny equation to model permeability in samples with a range of pore sizes. The NMR T_2 time distribution can be converted to an S_p distribution if the surface relaxivity, ρ, of the sample is known; the permeability in each S_p increment is then estimated by using Kozeny's equation. Additional data, from mercury injection, and the specific surface area from nitrogen adsorption, were used to estimate ρ [Manuscript IV and Chapter 7]. Summation of permeability increments up to the measured permeability was used to estimate which pores are effective for permeability in 63 samples of Rotliegend sandstone [Manuscript IV].

In samples where summation over the entire pore volume yielded the measured permeability, the fraction of porosity containing the largest pores controlled the total permeability, i.e., the permeability in the smaller pore sizes was negligible as compared to the total permeability. This was observed in samples with a high clay-free porosity. On the other hand, in samples with a low porosity, and in samples where clay particles were distributed throughout the intergranular pores yielding a low clay-free porosity, permeability was estimated by summation over only a fraction of porosity which contained the smaller pores. This suggests that larger pores were only connected through smaller pores in those samples; whereby smaller pores would limit the flow rate in larger pores. As the range of pores that contribute to permeability was sample dependent, image analysis was used to indicate samples in which larger pores would control permeability [Manuscript IV].

The Klinkenberg (1941) equation for gas slip is based on similar geometrical assumptions as the Kozeny equation, when the Kozeny constant is calculated as in Mortensen et al. (1998), i.e., for a 3D network of

straight, orthogonal, equal spaced, intersecting, equal sized capillaries. Accordingly, a positive correlation was observed between the effective equivalent pore size for permeability and the characteristic equivalent pore size for gas slip. Whereas no systematic difference was observed, there was an order of magnitude difference between the two measures for some samples. Factors that might contribute to this difference include: a different effect of heterogeneity on permeability than on gas slip; a different effect of surface roughness on permeability than on gas slip; and experimental error during the Klinkenberg procedure.
A reduction in pore pressure can increase gas slip, and simultaneously reduce the permeability by increasing the net stress. The net effect on the apparent permeability to gas would be relevant to both the Klinkenberg procedure and to production from tight gas sandstone reservoirs; this was modelled by combining expressions for slip flow and for the stress sensitivity of permeability.

Permeability to brine was modelled by including a layer of immobile water in permeability modelling by using the Kozeny model with the S_p distribution from NMR [Manuscript IV], and by using Klinkenberg model and the characteristic equivalent pore size for gas slip. However, the measured brine permeability could not be estimated by assuming the same thickness of immobile water in different samples. The thickness of immobile water as estimated from the measured brine permeability by using these methods ranged from 4 nm–1200 nm. This large range indicates that other factors, possibly the presence of illite and kaolinite minerals, contributed to a lower permeability to gas than to brine in some samples [Manuscript IV]. This introduces uncertainty when the permeability of a geothermal aquifer to brine is estimation based on gas permeametry.

Thermal expansion as modelled based on the Kozeny equation would have a negligible effect on permeability; and accordingly, results from a literature survey indicated no effect of temperature in flow-through experiments with inert fluids at confining stress levels below 14 MPa and temperatures ranging from 20°C–150°C [Manuscript I]. Heating was found to reduce permeability in tests with distilled water or brine in kaolinite-bearing sandstones, which suggests that heating might mobilise kaolinite particles [Manuscripts I and II].

Permeability reduction was observed when the NaCl concentration was reduced at 20°C in a sample of Berea sandstone [Manuscript II]; permeability reduction due to reduction of the NaCl concentration is often attributed to kaolinite mobilisation and filtration (Khilar and Fogler, 1984; Kia et al., 1987). Heating to 80°C also reduced permeability in other tests on comparable Berea sandstone samples; subsequent reduction of the NaCl concentration did not affect permeability, which indicates that kaolinite was indeed mobilised by heating. Both heating and salinity reduction increase the electrostatic repulsion forces between quartz and kaolinite, which might and mobilise kaolinite particles (Schembre and Kovscek, 2005).
Whereas restoring the NaCl concentration did not significantly improve permeability in the test at 20°C, the permeability reduction due to heating was largely reversible with cooling. At 80°C, permeability depended

on the flow rate, increasing the flow rate increased permeability reversibly; by contrast, no flow rate dependency was observed in the test where the NaCl concentration was reduced at 20°C [Manuscript II]. These differences suggest that mobilised kaolinite had a different effect on permeability at 80°C than at 20°C. A higher electrostatic repulsion between kaolinite and quartz surfaces at 80°C than at 20°C might possibly prevent filtration in heated samples. Interactions among mobilised particles might affect the pore fluid viscosity locally; this could appear as a permeability reduction when permeability is calculated by using Darcy's law and the viscosity of the injection fluid.

DLVO theory was used to compare the effects of salinity and temperature on the net interaction energy between kaolinite and quartz and among kaolinite particles [Conference papers II and III, Manuscript II]. An increase in surface charge density due to heating would be required in order obtain a net repulsive interaction that might mobilise kaolinite and account for the observed permeability reduction. Published measurements of surface potential or surface charge, indeed indicate that heating increases the surface charge of kaolinite and quartz substantially (Brady et al., 1996; Rodríguez and Araujo, 2006). The higher surface charge densities might limit filtration of kaolinite particles. There would be less repulsion among kaolinite particles than between kaolinite and quartz, which presumably would favour interactions among kaolinite particles over filtration of kaolinite particles.

Differences between the effects of temperature and salinity could be relevant for geothermal heat storage in kaolinite bearing aquifers, as these suggest that: cooling of the reservoir during winter might improve permeability; increasing the flow rate might offset permeability reduction due to heating; salinity changes might have less effect in hot aquifers than in laboratory tests at room temperature.

Quantitative analysis of images in which mineralogy was mapped by using the QEMSCAN® system, was used to generate statistics on mineralogy, reactive surface area and millimetre scale heterogeneity [Manuscript III]. Minimum representative areas were different for different phases within the same sample. Patchy cementation in samples of Bunter Formation sandstone resulted in a representative area that exceeded the 100 mm^2 interrogation area that was used in this study.

Principal component analysis of subsections of images could be used to distinguish among subsections of images from Gassum Formation sandstone, Bunter Formation sandstone and Berea sandstone; a reasonable distinction could also be made between subsections of an image of untested Berea sandstone and an image of tested Berea sandstone, after 150 days of injection of 80°C NaCl solution.

Lamination, of mineral abundance, of porosity, and of pore-mineral specific interface, was more pronounced in the tested Berea sandstone sample than in the untested sample. A loss of siderite and a corresponding gain in iron oxide/hydroxide appears to have enhanced existing lamination in the tested sample, by precipitation of iron oxide/hydroxide predominantly in finer grained, lower porosity, lamina. Both experimentally measured permeability and estimates of permeability based on image analysis indicated that the enhanced lamination only caused a minor permeability reduction.

9 Recommendations for further investigation

This investigation addressed temperature effects on sandstone permeability, based on laboratory flow-through experiments that were conducted at low confining stress levels. Several authors suggest that heating could increase rock compressibility (e.g., Faulkner and Rutter, 2003; Stottlemyre, 1981); mechanical tests would be required in order to assess changes in compressibility and the effects of this on permeability.

Kaolinite is observed in samples of Gassum Formation sandstone from different localities. To avoid permeability reduction by hot water injection, localities with a low kaolinite content would be preferred. If hot water injection is planned in localities with a high kaolinite content, effects of flow rate and temperature on permeability might be investigated by means of additional flow-through experiments tests, using the *in situ* pore fluid composition and the range of flow rates that would be expected in the aquifer.

Quantitative image analysis was used to estimate mineralogy and reactive surface area; this data can be used for geochemical modelling of effects of hot water injection. Calibration is required, due to the effects of resolution and a porosity threshold on interface length in images; this could involve calibrating: image porosity with helium porosity; image mineralogy with mineralogy from quantitative X-ray diffraction; and specific interface length per pore area with specific surface area from nitrogen adsorption. Furthermore, interfaces of other minerals to clay minerals in images could be considered as reactive interfaces, due to porosity among clay particles.

Interrogation areas larger than the 100 mm^2 that were used in this study might be required for quantification of minerals with a patchy distribution, or for laminated samples. Nonetheless, the content of gypsum/anhydrite in Bunter sandstone samples that is observed in side trims could differ significantly from the content in adjacent plug samples. Non-destructive methods of quantifying the content of these minerals in the plugs prior to testing would be needed in order to quantify changes due to hot water storage. For other minerals, such as siderite in Berea sandstone, alteration could be estimated by comparing adjacent tested and untested plug samples.

10 References

Alam, M.M., Katika, K., Fabricius, I.L., 2014. Effect of salinity and specific ions on amount of bound water on quartz, calcite and kaolinite, as observed by NMR transverse relaxation time (T2), in: 76th EAGE Conference & Exhibition. Amsterdam RAI, The Netherlands.

Al-Rumhy, M.H., Kalam, M.Z., 1996. Relationship of Core-Scale Heterogeneity With Non-Darcy Flow Coefficients. SPE Form. Eval. 11, 108–113. doi:10.2118/25649-PA

Al-Wardy, W., Zimmerman, R.W., 2004. Effective stress law for the permeability of clay-rich sandstones. J. Geophys. Res. Solid Earth 109, B04203. doi:10.1029/2003JB002836

Andreassen, K., Fabricius, I.L., 2010. Biot critical frequency applied to description of failure and yield of highly porous chalk with different pore fluids. GEOPHYSICS 75, E205–E213. doi:10.1190/1.3504188

API, 1998. Recommended Practices for Core Analysis, API RP 40.

Ayling, B., Rose, P., Petty, S., Zemach, E., Drakos, P., 2012. QEMSCAN® Quantitative evaluation of minerals by scanning electron microscopy: capability and application to fracture characterization in geothermal systems., in: Thirty-Eighth Workshop on Geothermal Reservoir Engineering Stanford University. 11, p. 11.

Baudracco, J., Aoubouazza, M., 1995. Permeability variations in Berea and Vosges sandstone submitted to cyclic temperature percolation of saline fluids. Geothermics 24, 661–677. doi:10.1016/0375-6505(95)00027-5

Bear, J., 1972. Dynamics of fluids in porous media. American Elsevier, 764 pp.

Beckingham, L.E., Peters, C.A., Um, W., Jones, K.W., Lindquist, W.B., 2013. 2D and 3D imaging resolution trade-offs in quantifying pore throats for prediction of permeability. Adv. Water Resour. 62, 1–12. doi:10.1016/j.advwatres.2013.08.010

Bedrikovetsky, P., Caruso, N., 2014. Analytical Model for Fines Migration During Water Injection. Transp. Porous Media 101, 161–189. doi:10.1007/s11242-013-0238-7

Bedrikovetsky, P., Siqueira, F.D., Furtado, C.A., Souza, A.L.S., 2011. Modified particle detachment model for colloidal transport in porous media. Transp. Porous Media 86, 353–383. doi:10.1007/s1142-010-9626-4

Bedrikovetsky, P., Zeinijahromi, A., Siqueira, F.D., Furtado, C. a., Souza, A.L.S., 2012. Particle Detachment Under Velocity Alternation During Suspension Transport in Porous Media. Transp. Porous Media 91, 173–197. doi:10.1007/s11242-011-9839-1

Behnsen, J., Faulkner, D.R., 2011. Water and argon permeability of phyllosilicate powders under medium to high pressure. J. Geophys. Res. Solid Earth 116, - B12203. doi:10.1029/2011JB008600

Berryman, J.G., 1992. Effective stress for transport properties of inhomogeneous porous rock. J. Geophys. Res. Solid Earth 97, 17409–17424. doi:10.1029/92JB01593

Berryman, J.G., Blair, S.C., 1987. Kozeny–Carman relations and image processing methods for estimating Darcy's constant. J. Appl. Phys. 62, 2221–2228. doi:http://dx.doi.org/10.1063/1.339497

Beskok, A., Karniadakis, G.M., 1999. Report: a model for flows in channels, pipes, and ducts at micro and nano scales. Microscale Thermophys. Eng. 3, 43–77. doi:10.1080/108939599199864

Blair, S.C., Berge, P.A., Berryman, J.G., 1996. Using two-point correlation functions to characterize microgeometry and estimate permeabilities of sandstones and porous glass. J. Geophys. Res. 101, 375,20320–20359.

Blair, S.C., Deutsch, W.J., Kannberg, L.D., 1984. Laboratory Permeability Measurements In Support Of An Aquifer Thermal Energy Storage Site In Minnesota, in: The 25th US Symposium on Rock Mechanics (USRMS). 296–303, pp. 296–303.

Blunt, M.J., 2001. Flow in porous media pore-network models and multiphase flow. Curr. Opin. Colloid Interface Sci. 6, 197–207.

Blunt, M.J., Bijeljic, B., Dong, H., Gharbi, O., Iglauer, S., Mostaghimi, P., Paluszny, A., Pentland, C., 2013. Pore-scale imaging and modelling. Adv. Water Resour. 51, 197–216. doi:10.1016/j.advwatres.2012.03.003

Borre, M., Lind, I.L., Mortensen, J., 1995. Specific surface as a measure of burial diagenesis of chalk. Zentralblatt für Geol. und Paläontologie 1071–1078.

Bourbie, T., Zinszner, B., 1985. Hydraulic and acoustic properties as a function of porosity in Fontainebleau Sandstone. J. Geophys. Res. Solid Earth 90, 11524–11532. doi:10.1029/JB090iB13p11524

Boving, T.B., Grathwohl, P., 2001. Tracer diffusion coefficients in sedimentary rocks: correlation to porosity and hydraulic conductivity. J. Contam. Hydrol. 53, 85–100. doi:10.1016/S0169-7722(01)00138-3

Brady, P. V, 1992. Silica surface chemistry at elevated temperatures. Geochim. Cosmochim. Acta 56, 2941–2946. doi:10.1016/0016-7037(92)90371-O

Brady, P. V, Cygan, R.T., Nagy, K.L., 1996. Molecular Controls on Kaolinite Surface Charge. J. Colloid Interface Sci. 183, 356–364. doi:10.1006/jcis.1996.0557

Brower, K.R., Morrow, N.R., 1985. Fluid Flow in Cracks as Related to Low-Permeability Gas Sands. SPEJ 25, 191–201. doi:10.2118/11623-PA

Brunauer, S., Emmett, P.H., Teller, E., 1938. Adsorption of Gases in Multimolecular Layers. J. Am. Chem. Soc. 60, 309–319. doi:10.1021/ja01269a023

Byerlee, J., 1990. Friction, overpressure and fault normal compression. Geophys. Res. Lett. 17, 2109–2112. doi:10.1029/GL017i012p02109

Byrnes, A.P., 1997. Reservoir characteristics of low-permeability sandstones in the Rocky Mountains. Mt. Geol. 43, 37–51.

Cao, B., Sun, J., Chen, M., Guo, Z., 2006. Effect of surface roughness on gas flow in microchannels by molecular dynamics simulation. Int. J. Eng. Sci. 44, 927–937. doi:http://dx.doi.org/10.1016/j.ijengsci.2006.06.005

Cao, B., Sun, J., Chen, M., Guo, Z., 2009. Molecular Momentum Transport at Fluid-Solid Interfaces in MEMS/NEMS: A Review. Int. J. Mol. Sci. 10, 4638–4706. doi:10.3390/ijms10114638

Cao, B.-Y., 2007. Non-Maxwell slippage induced by surface roughness for microscale gas flow: a molecular dynamics simulation. Mol. Phys. 105, 1403–1410. doi:10.1080/00268970701361322

Carman, P.C., 1937. Fluid flow through granular beds. Trans. Instn Chem. Engrs. 15, 150–166. doi:10.1016/S0263-8762(97)80003-2

Cassé, F.J., Ramey Jr, H.J., 1979. The Effect of Temperature and Confining Pressure on Single-Phase Flow in Consolidated Rocks (includes associated paper 9087). J. Pet. Technol. 31, 1051–1059. doi:10.2118/5877-PA

Chapman, D.L., 1913. A contribution to the theory of electrocapillarity. Philos. Mag. 25, 475–481. doi:10.1080/14786440408634187

Chassagne, C., Mietta, F., Winterwerp, J.C., 2009. Electrokinetic study of kaolinite suspensions. J. Colloid Interface Sci. 336, 352–9. doi:10.1016/j.jcis.2009.02.052

Churcher, P.L., 1991. Rock Properties of Berea Sandstone, Baker Dolomite, and Indiana Limestone, in: SPE International Symposium on Oilfield Chemistry. Anaheim, California, 431–466, pp. 431–466. doi:10.2118/21044-MS

Civan, F., 2002. Relating Permeability To Pore Connectivity Using A Power-law Flow Unit Equation. Petrophysics 43.

Civan, F., 2010. Effective Correlation of Apparent Gas Permeability in Tight Porous Media. Transp. Porous Media 82, 375–384. doi:10.1007/s11242-009-9432-z

Clausen, L., Fabricius, I.L., 2000. BET measurements: Outgassing of minerals. J. Colloid Interface Sci. 227, 7–15. doi:10.1006/jcis.2000.6880

Coates, G.R., Xiao, L., Prammer, M.G., 1999. NMR Logging Principles and Applications. Halliburton Energy Services, Houston, 234 pp.

Cornell, D., Katz, D.L., 1953. Flow of Gases through Consolidated Porous Media. Ind. Eng. Chem. 45, 2145–2152. doi:10.1021/ie50526a021

Crandell, L.E., Peters, C.A., Um, W., Jones, K.W., Lindquist, W.B., 2012. Changes in the pore network structure of Hanford sediment after reaction with caustic tank wastes. J. Contam. Hydrol. 131, 89–99. doi:10.1016/j.jconhyd.2012.02.002

Darcy, H., 1856. Les fontaines publiques de la ville de Dijon: exposition et application. Victor Dalmont, Paris, 647 pp.

Dastidar, R., Sondergeld, C.H., Rai, C.S., 2006. NMR Desaturation and Surface Relaxivity Measurements on Clastics Rocks, in: SPE EUROPEC/EAGE Annual Conference and Exhibition. Vienna, Austria, 7, p. 7.

Derjaguin, B. V, Landau, L.D., 1941. Theory of the stability of strongly charged lyophobic sols and the adhesion of strongly charged particles in solutions of electrolytes. Acta Physicochim. USSR 14, 633–662. doi:10.1016/0079-6816(93)90013-L

Desbois, G., Urai, J.L., Kukla, P.A., Konstanty, J., Baerle, C., 2011. High-resolution 3D fabric and porosity model in a tight gas sandstone reservoir:A new approach to investigate microstructures from mm- to nm-scale combining argon beam cross-sectioning and SEM imaging. J. Pet. Sci. Eng. 78, 243–257. doi:10.1016/j.petrol.2011.06.004

Donaldson, C.E., Kendall, F.R., Baker B., A., Manning F., S., 1975. Surface-Area Measurement of Geologic Materials. Soc. Pet. Eng. J. 15, 111–116. doi:10.2118/4987-PA

Dullien, F.A.., 1975. Invited Review Single Phase Flow Through Porous Media and Pore Structure. Chem. Eng. J. 10, 1–34.

Elimelech, M., 2010. Particle deposition and aggregation : measurement, modelling and simulation. Butterworth-Heinemann, Woburn, Mass, 441 pp.

Ertekin, T., King, G.A., Schwerer, F.C., 1986. Dynamic Gas Slippage: A Unique Dual-Mechanism Approach to the Flow of Gas in Tight Formations. SPE Form. Eval. 1, 43–52. doi:10.2118/12045-PA

Fatt, I., 1956. The network model of porous media. AIME Pet. Trans. 207, 141–181.

Faulkner, D.R., Rutter, E.H., 2000. Comparisons of water and argon permeability in natural clay-bearing fault gouge under high pressure at 20°C. J. Geophys. Res. Solid Earth 105, 16415–16426. doi:10.1029/2000JB900134

Faulkner, D.R., Rutter, E.H., 2003. The effect of temperature, the nature of the pore fluid, and subyield differential stress on the permeability of phyllosilicate-rich fault gouge. J. Geophys. Res. Solid Earth 108, - 2227. doi:10.1029/2001JB001581

Florence, F.A., Rushing, J., Newsham, K.E., Blasingame, T.A., 2007. Improved Permeability Prediction Relations for Low Permeability Sands, in: Rocky Mountain Oil & Gas Technology Symposium. SPE, Denver, Colorado, U.S.A. doi:10.2118/107954-MS

Freeman, C.M., Moridis, G.J., Blasingame, T.A., 2011. A Numerical Study of Microscale Flow Behavior in Tight Gas and Shale Gas Reservoir Systems. Transp. Porous Media 90, 253–268. doi:10.1007/s11242-011-9761-6

Frens, G., Overbeek, J.T., 1972. Repeptization and Theory of Electrocratic Colloids. J. Colloid Interface Sci. 38, 376–387. doi:10.1016/0021-9797(72)90253-6

Funk, J.J., Choinski, C.M., Saxman, B.B., Callender, A.C., 1989. Characterization of Carbonate Porosity Using Petrophysical Properties and Image Analysis, in: Middle East Oil Show. 1989 Copyright 1989, Society of Petroleum Engineers, Inc., Bahrain. doi:10.2118/17943-MS

Gautier, J.-M., Oelkers, E., Schott, J., 2001. Are quartz dissolution rates proportional to BET surface areas? Geochim. Cosmochim. Acta 65, 1059–1070. doi:10.1016/S0016-7037(00)00570-6

Giesche, H., 2006. Mercury porosimetry: a general (practical) overview. Part. Part. Syst. Charact. 23, 9–19. doi:10.1002/ppsc.200601009

Giménez, D., Perfect, E., Rawls, W.J., Pachepsky, Y., 1997. Fractal models for predicting soil hydraulic properties: a review. Eng. Geol. 48, 161–183. doi:10.1016/S0013-7952(97)00038-0

Glover, P., Zadjali, I., Frew, K., 2006. Permeability prediction from MICP and NMR data using an electrokinetic approach. GEOPHYSICS 71, F49–F60. doi:10.1190/1.2216930

Gouy, M., 1909. Sur la constitution de la charge électrique à la surface d'un électrolyte. Comptes rendus l'Academie des Sci. 149, 654–657. doi:10.1051/jphystap:019100090045700

Grahame, D.C., 1947. The Electrical Double Layer and the Theory of Electrocapillarity. - Chem. Rev. 41, 441–501. doi:10.1021/cr60130a002

Grahame, D.C., 1953. Diffuse Double Layer Theory for Electrolytes of Unsymmetrical Valence Types. J. Chem. Phys. 21, 1054–1060. doi:10.1063/1.1699109

Gray, D.H., Rex, R.W., 1966. Formation Damage in Sandstones caused by Clay Dispersion and Migration. Clays Clay Miner. 14, 355–366. doi:10.1346/CCMN.1966.0140131

Gregory, J., 1975. Interaction of unequal double layers at constant charge. J. Colloid Interface Sci. 51, 44–51. doi:10.1016/0021-9797(75)90081-8

Grim, R.E., 1953. Clay Mineralogy. McGraw-Hill Book Company inc., New York, 384 pp.

Gupta, V., Hampton, M.A., Stokes, J.R., Nguyen, A. V, Miller, J.D., 2011. Particle interactions in kaolinite suspensions and corresponding aggregate structures. J. Colloid Interface Sci. 359, 95–103. doi:10.1016/j.jcis.2011.03.043

Gupta, V., Miller, J.D., 2010. Surface force measurements at the basal planes of ordered kaolinite particles. J. Colloid Interface Sci. 344, 362–371. doi:10.1016/j.jcis.2010.01.012

Hahn, M.W., O'Melia, C.R., 2004. Deposition and Reentrainment of Brownian Particles in Porous Media under Unfavorable Chemical Conditions: Some Concepts and Applications. Environ. Sci. Technol. 38, 210–220. doi:10.1021/es030416n

Heid, J.G., McMahon, J.J., Nielsen, R.F., Yuster, S.T., 1950. Study of the Permeability of Rocks to Homogeneous Fluids, in: Drilling and Production Practice. American Petroleum Institute.

Hossain, Z., Grattoni, C.A., Solymar, M., Fabricius, I.L., 2011. Petrophysical properties of greensand as predicted from NMR measurements. Pet. Geosci. 17, 111–125. doi:10.1144/1354-079309-038

House, W.A., Orr, D.R., 1992. Investigation of the Ph-Dependence of the Kinetics of Quartz Dissolution at 25-Degrees-C. J. Chem. Soc. Trans. 88, 233–241. doi:10.1039/ft9928800233

Hubbert, M.K., 1957. Darcy's Law and the Field Equations of the Flow of Underground Fluids. Int. Assoc. Sci. Hydrol. Bull. 2, 23–59. doi:10.1080/02626665709493062

Huertas, F.J., Chou, L., Wollast, R., 1998. Mechanism of kaolinite dissolution at room temperature and pressure: Part 1. Surface speciation. Geochim. Cosmochim. Acta 62, 417–431. doi:10.1016/S0016-7037(97)00366-9

Huertas, F.J., Chou, L., Wollast, R., 1999. Mechanism of kaolinite dissolution at room temperature and pressure Part II: kinetic study. Geochim. Cosmochim. Acta 63, 3261–3275. doi:10.1016/S0016-7037(99)00249-5

Hunt, A.G.., 2009. Percolation theory for flow in porous media. Springer, 319 pp.

Hurst, A., Nadeau, P.H., 1995. Clay microporosity in reservoir sandstones: an application of quantitative electron microscopy in petrophysical evaluation. AAPG Bull. Assoc. Pet. Geol. 79, 563–573.

Ishido, T., Mizutani, H., 1981. Experimental and theoretical basis of electrokinetic phenomena in rock-water systems and its applications to geophysics. J. Geophys. Res. Solid Earth 86, 1763–1775. doi:10.1029/JB086iB03p01763

Israelachvili, J.N., 2011. Intermolecular and surface forces. Elsevier/Academic Press, Amsterdam, the Netherlands, 674 pp.

Israelachvili, J.N., Adams, G.E., 1978. Measurement of forces between 2 mica surfaces in aqueous electrolyte solutions in range 0-100 nm. J. Chem. Soc. Faraday Trans. 74, 975.

Johnson, S.B., Russell, A.S., Scales, P.J., 1998. Volume fraction effects in shear rheology and electroacoustic studies of concentrated alumina and kaolin suspensions. Colloids Surfaces A Physicochem. Eng. Asp. 141, 119–130. doi:10.1016/S0927-7757(98)00208-8

Jones, F.O., Owens, W.W., 1980. A Laboratory Study of Low-Permeability Gas Sands. SPE J. Pet. Technol. 32, 193–199. doi:10.2118/7551-PA

Karniadakis, G., Beskok, A., Aluru, N.R., 2005. Microflows and nanoflows : fundamentals and simulation. Springer, New York, NY, 817 pp.

Keaney, G.M., Meredith, P., Murrell, S., Barker, J., 2004. Determination Of The Effective Stress Laws For Permeability And Specific Storage In A Low Porosity Sandstone, in: North America Rock Mechanics Symposium. American Rock Mechanics Association, Houston, Texas.

Keating, K., Knight, R., 2007. A laboratory study to determine the effect of iron oxides on proton NMR measurements. Geophysics 72, E27–E32. doi:10.1190/1.2399445

Keating, K., Knight, R., 2010. A laboratory study of the effect of Fe (II)-bearing minerals on nuclear magnetic resonance (NMR) relaxation measurements. Geophysics 75, F71–F82.

Keighin, W.C., Sampath, K., 1982. Evaluation of Pore Geometry of Some Low-Permeability Sandstones-Uinta Basin. J. Pet. Technol. 34, 65–70. doi:10.2118/9251-PA

Khilar, K.C., Fogler, H.S., 1984. The existence of a critical salt concentration for particle release. J. Colloid Interface Sci. 101, 214–224. doi:10.1016/0021-9797(84)90021-3

Khilar, K.C., Fogler, H.S., 1987. Colloidally induced fines migration in porous media. Rev. Chem. Eng. 4, 41–108. doi:10.1016/0920-4105(90)90011-Q

Kia, S.F., Fogler, H.S., Reed, M.G., 1987. Effect of pH on colloidally induced fines migration. J. Colloid Interface Sci. 118, 158–168. doi:10.1016/0021-9797(87)90444-9

Kim, J.-W., Kim, D., Lindquist, W.B., 2013. A re-examination of throats. Water Resour. Res. 49, 7615–7626. doi:10.1002/2013WR014254

Kirkpatrick, S., 1973. Percolation and conduction. Rev. Mod. Phys. 45, 574–588.

Kleinberg, R.L., 1996. Utility of NMR T2 distributions, connection with capillary pressure, clay effect, and determination of the surface relaxivity parameter ρ2. Proc. Third Int. Meet. Recent Adv. MR Appl. to Porous Media 14, 761–767. doi:http://dx.doi.org.globalproxy.cvt.dk/10.1016/S0730-725X(96)00161-0

Klinkenberg, L.J., 1941. The Permeability Of Porous Media To Liquids And Gases, in: Dril. Prod. Prac. API, Tulsa, Oklahoma.

Knackstedt, M.A., Sheppard, A.P., Sahimi, M., 2001. Pore network modelling of two-phase flow in porous rock: the effect of correlated heterogeneity. Adv. Water Resour. 24, 257–277. doi:10.1016/S0309-1708(00)00057-9

Kozeny, J., 1927. Über kapillare Leitung des Wassers im Boden. Sitzungsberichte der Akad. der Wissenschaften Wien, Math. Klasse 136, 271–306.

Kundt, A., Warburg, E., 1875. Ueber Reibung und Waermeleitung verduennter Gase. Poggendorfs Ann. Phsik. 155, 337–366,525–551.

Landrot, G., Ajo-Franklin, J.B., Yang, L., Cabrini, S., Steefel, C.I., 2012. Measurement of accessible reactive surface area in a sandstone, with application to CO2 mineralization. Chem. Geol. 318-319, 113–125. doi:10.1016/j.chemgeo.2012.05.010

Li, M., Bernabe, Y., Xiao, W.-I., Chen, Z.-Y., Liu, Z.-Q., 2009. Effective pressure law for permeability of E-bei sandstones. J. Geophys. Res. Earth 114, B07205–B07205. doi:10.1029/2009JB006373

Lindquist, W.B., Venkatarangan, A., Dunsmuir, J., Wong, T.-F., 2000. Pore and throat size distributions measured from synchrotron X-ray tomographic images of Fontainebleau sandstones. J. Geophys. Res. 105, 21527–21527. doi:0148-0228/00/200JB900208$09.00

Loeb, L.B., 1927. Kinetic theory of gases. McGraw-Hill, New York, NY, 555 pp.

Lorne, B., Perrier, F., Avouac, J.P., 1999. Streaming potential measurements: 1. Properties of the electrical double layer from crushed rock samples. J.geophys.Res 104, 17857–17877. doi:10.1029/1999JB900156

Luffel, D., Herrington, K., Walls, J., 1993. Effect of Drying on Travis Peak Cores Containing Fibrous Illite. SPE Adv. Technol. Ser. 1, 188–194.

Lund, J.W., Freeston, D.H., Boyd, T.L., 2011. Direct utilization of geothermal energy 2010 worldwide review. Geothermics 40, 159–180. doi:http://dx.doi.org/10.1016/j.geothermics.2011.07.004

Lyklema, J.J., de Keizer, A., Bijsterbosch, B.H., Fleer, G.J., Cohen Stuart, M.A., 1995. Electric double layers, in: Fundamentals of Interface and Colloid Science, Solid-Liquid Interfaces. Academic Press, 232, p. 232. doi:10.1016/S1874-5679(06)80006-1

Maribo-Mogensen, B., Kontogeorgis, G.M., Thomsen, K., 2013. Modeling of Dielectric Properties of Aqueous Salt Solutions with an Equation of State. J. Phys. Chem. B 117, 10523–10533. doi:10.1021/jp403375t

Mavko, Nur, A., 1997. Short Note The effect of a percolation threshold in the Kozeny-Carman relation. Geophysics 62, 1480–1482.

Mbia, E.N., Fabricius, I.L., Krogsbøll, A., Frykman, P., Dalhoff, F., 2014. Permeability, compressibility and porosity of Jurassic shale from the Norwegian-Danish Basin. J. Pet. Geosci. (In press).

McDowell-Boyer, L.M., Hunt, J.R., Sitar, N., 1986. Particle Transport Through Porous Media. Water Resour. Res. 22, 1901–1921.

McPhee, C.A., Arthur, K.G., 1991. Klinkenberg permeability measurements: Problems and practical solutions, in: Reviewed Proceedings of the Second Society of Core Analysts European Core Analysis Symposium, London, UK, 20-22 May 1991. Taylor & Francis US.

Mehmani, A., Prodanović, M., 2014. The effect of microporosity on transport properties in porous media. Adv. Water Resour. 63, 104–119. doi:10.1016/j.advwatres.2013.10.009

Michelsen, M.L., Mollerup, J.M., 2004. Thermodynamic Models: Fundamentals & Computational Aspects. Tie-Line Publications, Holte, Danmark, 330 pp.

Milsch, H., Seibt, A., Spangenberg, E., 2009. Long-term Petrophysical Investigations on Geothermal Reservoir Rocks at Simulated In Situ Conditions. Transp. Porous Media 77, 59–78. doi:10.1007/s11242-008-9261-5

Miranda, A., Borgne, Y.-A., Bontempi, G., 2008. New Routes from Minimal Approximation Error to Principal Components. Neural Process. Lett. 27, 197–207. doi:10.1007/s11063-007-9069-2

Mohan, K.K., Reed, M.G., Fogler, H.S., 1999. Formation damage in smectitic sandstones by high ionic strength brines. Colloids Surfaces A-Physicochemical Eng. Asp. 154, 249–257. doi:10.1016/S0927-7757(98)00338-0

Morrow, N.R., Brower, K.R., Kilmer, N.H., 1983. Relationship Of Pore Structure To Fluid Behavior In Low Permeability Gas Sands First Annual Report. 82 pp.

Mortensen, J., Engstrøm, F., Lind, I.L., 1998. The Relation Among Porosity, Permeability, and Specific Surface of Chalk From the Gorm Field, Danish North Sea. SPE Reserv. Eval. Eng. 1, 245–251. doi:10.2118/31062-PA

Mostaghimi, P., Blunt, M.J., Bijeljic, B., 2013. Computations of Absolute Permeability on Micro-CT Images. Math. Geosci. 45, 103–125. doi:10.1007/s11004-012-9431-4

Mpofu, P., Addai-Mensah, J., Ralston, J., 2003. Influence of hydrolyzable metal ions on the interfacial chemistry, particle interactions, and dewatering behavior of kaolinite dispersions. J. Colloid Interface Sci. 261, 349–359. doi:10.1016/S0021-9797(03)00113-9

Mungan, M., 1965. Permeability Reduction Through Changes in pH and Salinity. SPE J. Pet. Technol. 17, 1449–1453. doi:10.2118/1283-PA

Noman, R., Archer, J.S., 1987. The Effect of Pore Structure on Non-Darcy Gas Flow in Some Low-Permeability Reservoir Rocks, in: Low Permeability Reservoirs Symposium. Society of Petroleum Engineers, Denver, Colorado. doi:10.2118/16400-MS

Ochi, J., Vernoux, J.F., 1998. Permeability decrease in sandstone reservoirs by fluid injection: Hydrodynamic and chemical effects. J. Hydrol. 208, 237–248. doi:10.1016/S0022-1694(98)00169-3

Olphen, H., 1977. An introduction to clay colloid chemistry. For clay technologists, geologists, and soil scientists. 2.ed. Wiley, New York,NY, 318 pp.

Osorio, J.G., Chen, H.-Y., Teufel, L.W., 1997. Numerical Simulation of Coupled Fluid-Flow/Geomechanical Behavior of Tight Gas Reservoirs with Stress Sensitive Permeability, in: Fifth Latin American and Caribbean Petroleum Engineering Conference and Exhibition. Society of Petroleum Engineers. doi:10.2118/39055-MS

Ostensen, W.R., 1983. Microcrack Permeability in Tight Gas Sandstone. Soc. Pet. Eng. J. 23, 919–927. doi:10.2118/10924-PA

Pandya, V.B., Bhuniya, S., Khilar, K.C., 1998. Existence of a critical particle concentration in plugging of a packed bed. AIChE J. 44, 978–981. doi:10.1002/aic.690440424

Pape, H., Clauser, C., Iffland, J., 1999. Permeability prediction based on fractal pore-space geometry. Geophysics 64, 1447–1460. doi:10.1190/1.1444649

Pape, H., Tillich, J.E., Holz, M., 2006. Pore geometry of sandstone derived from pulsed field gradient NMR. J. Appl. Geophys. 58, 232–252. doi:10.1016/j.jappgeo.2005.07.002

Peters, C.A., 2009. Accessibilities of reactive minerals in consolidated sedimentary rock: An imaging study of three sandstones. Chem. Geol. 265, 198–208. doi:10.1016/j.chemgeo.2008.11.014

Pirrie, D., Butcher, A.R., Power, M.R., Gottlieb, P., Miller, G.L., 2004. Rapid quantitative mineral and phase analysis using automated scanning electron microscopy (QemSCAN); potential applications in forensic geoscience. Spec. Publ. Geol. Soc. London 232, 123–136.

Potter, J.M., Dibble, W.E., Nur, A., 1981. Effects of temperature and solution composition on the permeability of St. Peters sandstone-Role of iron (III). J. Pet. Technol. 33, 905–907.

Priisholm, S., Nielsen, B.L., Haslund, O., 1987. Fines Migration Blocking and Clay Swelling of Potential Geothermal Sandstone Reservoirs Denmark. SPE Form. Eval. 2, 168–178. doi:10.2118/15199-PA

Prodanović, M., Lindquist, W.B., Seright, R.S., 2007. 3D image-based characterization of fluid displacement in a Berea core. Adv. Water Resour. 30, 214–226. doi:10.1016/j.advwatres.2005.05.015

Rahmanian, M., Aguilera, R., Kantzas, A., 2013. A New Unified Diffusion--Viscous-Flow Model Based on Pore-Level Studies of Tight Gas Formations. SPE J. 18, pp. 38–pp. 38–49. doi:10.2118/149223-PA

Rand, B., Melton, I.E., 1977. Particle interactions in aqueous kaolinite suspensions. J. Colloid Interface Sci. 60, 308–320. doi:10.1016/0021-9797(77)90290-9

Rodríguez, K., Araujo, M., 2006. Temperature and pressure effects on zeta potential values of reservoir minerals. J. Colloid Interface Sci. 300, 788–794. doi:10.1016/j.jcis.2006.04.030

Rootare, H.M., Prenzlow, C.F., 1967. Surface areas from mercury porosimeter measurements. J. Phys. Chem. 71, 2733–2736.

Rushing, J.A., Newsham, K.E., Van Fraassen, K.C., 2003. Measurement of the Two-Phase Gas Slippage Phenomenon and Its Effect on Gas Relative Permeability in Tight Gas Sands, in: SPE Annual Technical Conference and Exhibition. SPE. doi:10.2118/84297-MS

Rutter, E.H., 1983. Pressure solution in nature, theory and experiment. J. Geol. Soc. London. 140, 725–740. doi:10.1144/gsjgs.140.5.0725

Sahimi, M., 1993. Flow Phenomena in Rocks - from Continuum Models to Fractals, Percolation, Cellular-Automata, and Simulated Annealing. Rev. Mod. Phys. 65, 1393–1534. doi:10.1103/RevModPhys.65.1393

Sahimi, M., 2011. Flow and Transport in Porous Media and Fractured Rock. From Classical Models to Modern Approaches. 709 pp.

Sampath, K., Keighin, W.C., 1982. Factors Affecting Gas Slippage in Tight Sandstones of Cretaceous Age in the Uinta Basin. J. Pet. Technol. 34, 2715–2720. doi:10.2118/9872-PA

Schembre, J.M., Kovscek, A.R., 2004. Thermally Induced Fines Mobilization: Its Relationship to Wettability and Formation Damage, in: SPE International Thermal Operations and Heavy Oil Symposium and Western Regional Meeting. Bakersfield, California. doi:10.2118/86937-MS

Schembre, J.M., Kovscek, A.R., 2005. Mechanism of Formation Damage at Elevated Temperature. J. Energy Resour. Technol. 127, 171–180. doi:10.1115/1.1924398

Schepers, A., Milsch, H., 2013. Dissolution-precipitation reactions in hydrothermal experiments with quartz-feldspar aggregates. Contrib. to Mineral. Petrol. 165, 83–101. doi:10.1007/s00410-012-0793-x

Schofield, R.K., Samson, H.R., 1952. THE DEFLOCCULATION OF KAOLINITE SUSPENSIONS AND THE ACCOMPANYING CHANGE-OVER FROM POSITIVE TO NEGATIVE CHLORIDE ADSORPTION. Commonwealth Scientific & Industrial Research Organisation, Melbourne, 45, p. 45.

Schofield, R.K., Samson, H.R., 1954. Flocculation of Kaolinite due to the Attraction of Oppositely Charged Crystal Faces. Discuss. Faraday Soc. 18, 135–145. doi:10.1039/DF9541800135

Sen, P.N., Straley, C., Kenyon, W.E., Whittingham, M.S., 1990. Surface to volume ratio, charge density, nuclear magnetic relaxation, and permeability in clay-bearing sandstones. Geophysics 55, 61–69. doi:10.1190/1.1442772

Sen, T.K., Khilar, K.C., 2006. Review on subsurface colloids and colloid-associated contaminant transport in saturated porous media. Adv. Colloid Interface Sci. 119, 71–96. doi:10.1016/j.cis.2005.09.001

Sing, K., 2001. The use of nitrogen adsorption for the characterisation of porous materials. Colloids Surfaces A Physicochem. Eng. Asp. 187, 3–9. doi:10.1016/S0927-7757(01)00612-4

Solymar, M., Fabricius, I.L., 1999. Image analysis and estimation of porosity and permeability of Arnager Greensand, Upper Cretaceous, Denmark. Phys. Chem. Earth, Part A Solid Earth Geod. 24, 587–591. doi:10.1016/S1464-1895(99)00084-8

Solymar, M., Fabricius, I.L., Middleton, M., 2003. Flow characterization of glauconitic sandstones by integrated Dynamic Neutron Radiography and image analysis of backscattered electron micrographs. Pet. Geosci. 9, 175–183. doi:10.1144/1354-079302-517

Somerton, W.H., 1992. Thermal properties and temperature-related behavior of rock/fluid systems. Elsevier, Amsterdam, 257 pp.

Stern, H.O., 1924. Zur Theorie der Elektrolytischen Doppelschicht. S. f. Electrochem. 30, 508.

Stottlemyre, J.A., 1981. An Investigation Of Temperature Sensitivity Of Ottawa Sand And Massillon Sandstone Intrinsic Permeabilities. University of Washington, 168.

Swartzendruber, D., 1962. Non-Darcy flow behavior in liquid-saturated porous media. J. Geophys. Res. 67, 5205–5213. doi:10.1029/JZ067i013p05205

Tenthorey, E., Scholz, C.H., Aharonov, E., Léger, A., 1998. Precipitation sealing and diagenesis: 1. Experimental results. J. Geophys. Res. Solid Earth 103, 23951–23967. doi:10.1029/98JB02229

Tertre, E., Castet, S., Berger, G., Loubet, M., Giffaut, E., 2006. Surface chemistry of kaolinite and Na-montmorillonite in aqueous electrolyte solutions at 25 and 60 degrees C: Experimental and modeling study. Geochim. Cosmochim. Acta 70, 4579–4599. doi:10.1016/j.gca.2006.07.017

Ungemach, P., 2003. Reinjection of cooled geothermal brines into sandstone reservoirs. Geothermics 32, 743–761. doi:10.1016/S0375-6505(03)00074-9

Vernik, L., 1994. Predicting lithology and transport properties from acoustic velocities based on petrophysical classification of siliciclastics. Geophysics 59, 420–427. doi:doi: 10.1190/1.1443604

Verwey, E.J.W., Overbeek, J.T.G., 1948. Theory of the stability of lyophobic colloids, Elsevier. Elsevier, New York.

Visser, J., 1972. On Hamaker constants: A comparison between Hamaker constants and Lifshitz-van der Waals constants. Adv. Colloid Interface Sci. 3, 331–363. doi:10.1016/0001-8686(72)85001-2

Walderhaug, O., Eliassen, A., Aase, N.E., 2012. Prediction of Permeability In Quartz-Rich Sandstones: Examples from the Norwegian Continental Shelf and the Fontainebleau Sandstone. J. Sediment. Res. 82, 899–912. doi:10.2110/jsr.2012.79

Walsh, J.B., Brace, W.F., 1984. The effect of pressure on porosity and the transport properties of rock. J. Geophys. Res. Solid Earth 89, 9425–9431. doi:10.1029/JB089iB11p09425

Wang, Y.-H., Siu, W.-K., 2006. Structure characteristics and mechanical properties of kaolinite soils. I. Surface charges and structural characterizations. Can. Geotech. J. 43, 587–600. doi:10.1139/t06-026

Warpinski, N.R., Teufel, L.W., 1992. Determination of the Effective-Stress Law for Permeability and Deformation in Low-Permeability Rocks. SPE Form. Eval. 7, 123–131. doi:10.2118/20572-PA

Washburn, E.W., 1921. The Dynamics of Capillary Flow. Phys. Rev. 17, 273–283. doi:10.1103/PhysRev.17.273

Wei, K.K., Morrow, N.R., Brower, K.R., 1986. Effect of Fluid, Confining Pressure,and Temperature on Absolute Permeabilities of Low Permeability Sandstones. SPE Form. Eval. 1, 413–423. doi:10.2118/13093-PA

Weibel, E.R., 1989. Measuring through the microscope: development and evolution of stereological methods. J. Microsc. 155, 393–403.

Weibel, R.H., Olivarius, M., Nielsen, L.H., Abramovitz, T., Kjøller, C., 2010. Petrography and diagenesis of the Triassic and Jurassic sandstones, eastern part of the Norwegian-Danish Basin., Danmark og Grønlands Geologiske Undersøgelse Rapport. 88 pp.

Wilson, L., Wilson, M.J., Green, J., Patey, I., 2014. The Influence of Clay Mineralogy on Formation Damage in North Sea Reservoir Sandstones: A Review with Illustrative Examples. Earth-Science Rev. doi:10.1016/j.earscirev.2014.03.005

Wilson, M.D., Pittman, E.D., 1977. Authigenic clays in sandstones; recognition and influence on reservoir properties and paleoenvironmental analysis. J. Sediment. Res. 47, 3–31. doi:10.1306/212F70E5-2B24-11D7-8648000102C1865D

Wong, R.C.K., Mettananda, D.C.A., 2010. Permeability Reduction in Qishn Sandstone Specimens due to Particle Suspension Injection. Transp. Porous Media 81, 105–122. doi:10.1007/s11242-009-9387-0

Xu, P., Yu, B., 2008. Developing a new form of permeability and Kozeny–Carman constant for homogeneous porous media by means of fractal geometry. Adv. Water Resour. 31, 74–81. doi:10.1016/j.advwatres.2007.06.003

Yuan, H., Shapiro, A.A., 2011. A mathematical model for non-monotonic deposition profiles in deep bed filtration systems. Chem. Eng. J. 166, 105–115. doi:http://dx.doi.org/10.1016/j.cej.2010.10.036

Zbik, M., Horn, R.G., 2003. Hydrophobic attraction may contribute to aqueous flocculation of clays. Colloids Surfaces A Physicochem. Eng. Asp. 222, 323–328.

Zbik, M.S., Frost, R.L., 2009. Micro-structure differences in kaolinite suspensions. J. Colloid Interface Sci. 339, 110–116. doi:10.1016/j.jcis.2009.07.038

Zheleznyi, B. V, Zorin, Z.M., Sobolev, W.D., Churaev, N. V, 1972. Experimental study of properties of water in thin films and fine capillaries. Bull. Int. Assoc. Eng. Geol. 5, 57–61. doi:10.1007/BF02634653

Ziarani, A.S., Aguilera, R., 2012. Knudsens Permeability Correction for Tight Porous Media. Transp. Porous Media 91, 239–260. doi:10.1007/s11242-011-9842-6

Zoback, M.D., Byerlee, J.D., 1975. Permeability and Effective Stress. Aapg Bull. Assoc. Pet. Geol. 59, 154–158.

Appendices

Appendix A: Additional calculations

- A-I: Gas slip
- A-II: Immobile water layer thickness

Appendix B: Journal Manuscripts

- Manuscript I: The effect of hot water injection on sandstone permeability
- Manuscript II: Different effects of temperature and salinity on permeability reduction by fines migration in Berea sandstone
- Manuscript III: Quantitative image analysis of sandstone mineralogy with application to hot water storage in geothermal aquifers
- Manuscript IV: Permeability in Rotliegend Gas Sandstones to gas and brine as predicted from NMR, mercury injection and image analysis

Appendix C: Conference Papers

- Conference paper I: Effect Of Hot Water Injection On Sandstone Permeability: An Analysis Of Experimental Literature
- Conference paper II: Thermally induced permeability reduction due to particle migration in sandstones: the effect of temperature on kaolinite mobilisation and aggregation
- Conference paper III: Kaolinite Mobilisation in Sandstone: Pore Plugging vs. Suspended Particles

Appendix A: Additional calculations

- A-I: Gas slip
- A-II: Immobile water layer thickness

A-I: Gas slip

Data:

The Klinkenberg procedure was performed on sandstone samples from Gassum Formation and from Bunter formation at the Geological Survey of Denmark and Greenland (GEUS) Core Laboratory. Apparent permeability, k_a, was measured by using flow of nitrogen gas at three mean pore pressures, $\bar{P}$. Porosity was measured using helium porosimetry, and grain density was determined from a combination of Archimedes' test using mercury and the helium porosity. Confining pressure was 2.8 MPa.

The Klinkenberg procedure was also performed on Rotliegend sandstone samples from the PETGAS project. These tests were performed using helium gas flow at four or more $\bar{P}$. Samples from Group 6 were tested using a pulse-decay technique (Jones, 1997), whereas the other samples in Table C1.1 were tested using steady state permeametry.

Apparent permeability measurements from the Klinkenberg tests were plotted as a function of $1/\bar{P}$ in a Klinkenberg plot and fit using a straight line. The permeability, k, is the y-intercept and the slope is kb_{slip}. The correlation coefficient, R_c, for the fit indicates the goodness of the fit; API (1998) recommends R_c > 0.997 for three data points and R_c > 0.95 for four data points. However, as R_c < 0.997 for all measurements on Bunter sandstone, Gassum sandstone and Berea sandstone, data with R_c > 0.96 for three data points were used. For samples from groups 1 and 3 the confining stress was 10.3 MPa; for samples in group 6 confining stress was 68 MPa.

The pressure gradient across the samples was low during tests on some samples in the PETGAS dataset. Therefore the uncertainty on k_a is high. As the difference among k_a was small the uncertainty on the gradient of the Klinkenberg plot was high. Therefore these data were not included to estimate the characteristic equivalent pore size for gas slip, $r_{p,slip}$, despite R_c > 0.95 for four data points.

Calculations

The mean free path length, $\bar{\lambda}$, was estimated from the mean $\bar{P}$ applied during the Klinkenberg procedure, by assuming a constant gas viscosity, μ, in Eq.(A1) (Loeb, 1927).

$$\bar{\lambda} = \frac{\mu}{\bar{P}}\sqrt{\frac{RT\pi}{2M}} \tag{A1}$$

where M is the molar mass of the gas, R is the gas constant, and T is the absolute temperature.

The characteristic equivalent pore size for gas slip was calculated by using Eq (A2) (Klinkenberg, 1941)

$$r_{p,slip} = \frac{4c_{slip}\bar{\lambda}\bar{P}}{b_{slip}} \tag{A2}$$

where c_{slip} = 1 (Klinkenberg, 1941).

In order to calculate $r_{p,slip}$ using the uniform slip model, the generalised reduced gradient solver was used (Fylstra et al., 1998) to solve Eq.(A3) for Kn, and $r_{p,slip}$ was calculated from Kn by using Eq.(A4).

$$0 = \left[\left(1+\left(\alpha_{0,B\&K}\frac{2}{\pi}\tan^{-1}\left(\alpha_1 Kn^{\beta}\right)\right)Kn\right)\left(1+\frac{4Kn}{1+Kn}\right)-1\right]-\frac{b}{\bar{P}} \tag{A3}$$

$\alpha_{0,B\&K}$ = 1.358 for cylindrical capillaries, α_1 = 4 and β = 0.4 (Beskok and Karniadakis, 1999).

$$Kn = \frac{\lambda}{r} \tag{A4}$$

Knudsen numbers for tests on Rotliegend 6.01 and 6.23 were 1.3 and 2.5 indicating that gas flow was in the transition regime therefore the Klinkenberg slip model would not be valid. The tests on sample Gassum Aa had Kn = 0.13 indicating that flow was on the boundary of the slip and transition flow regime. For other samples flow was in the slip regime during the Klinkenberg tests, i.e., Kn < 0.1.

Kozeny's constant, c was calculated by using Eq.(A5) (Mortensen et al., 1998) and $r_{p,kozeny}$ was calculated by using Eq.(A6) (Kozeny, 1927).

$$c = \left(4\cos\left(\frac{1}{3}\arccos\left(\phi\frac{64}{\pi^3}-1\right)+\frac{4}{3}\pi\right)+4\right)^{-1} \tag{A5}$$

$$r_{p,kozeny} = 2\sqrt{\frac{k}{c\phi}} \tag{A6}$$

Results:

Table A1.1: Porosity, ϕ, and data from Klinkenberg procedure: correlation coefficient of Klinkenberg plot, R_c; permeability corrected for gas slip k; slip factor, b_{slip}. Calculated: Kozeny factor, c; effective equivalent pore size based on Kozeny's Equation, $r_{p,kozeny}$; characteristic equivalent pore size for gas slip $r_{p,slip}$ from Klinkenberg's slip model; and $r_{p,slip}$ from the unified slip model.

Sample	ϕ[a]	R_c[b]	k[c]	b_{slip}[c]	c	$r_{p,kozeny}$	$r_{p,slip}$ **klink-enberg**[d]	$r_{p,slip}$ **unified slip model**[d]
	%		**mD**	**MPa**		**µm**	**µm**	**µm**
Gassum Fa	17.8	0.963	141 (6)	0.037 (2)	0.20	3.95 (9)	0.70 (3)	0.82 (2)
Gassum Aa	11.6	0.975	1.61 (6)	0.256 (11)	0.19	0.536 (13)	0.101 (4)	0.127 (2)
Berea A1	17.0	0.990	23.3 (9)	0.0201 (8)	0.20	1.64 (3)	1.29 (5)	1.48 (3)
Rotliegend 3.3	10.9	0.997	0.105 (4)	0.296 (11)	0.19	0.141 (3)	0.259 (11)	0.285 (11)
Rotliegend 3.4	13.2	0.992	3.61 (14)	0.106 (4)	0.20	0.75 (2)	0.72 (3)	0.77 (3)
Rotliegend 3.9	12.7	0.999	0.357 (14)	0.173 (7)	0.20	0.24 (6)	0.440 (18)	0.48 (2)
Rotliegend 3.11	13.9	0.960	0.312 (12)	0.126 (5)	0.20	0.213 (5)	0.61 (3)	0.65 (3)
Rotliegend 3.12	17.5	1.000	0.71 (2)	0.164 (7)	0.20	0.281 (6)	0.47 (2)	0.51 (2)
Rotliegend 1.33	28.7	0.995	1.67 (7)	0.295 (11)	0.22	0.326 (7)	0.256 (8)	0.286 (11)
Bunter 4001HC	30.4	0.986	320 (13)	0.0632 (3)	0.22	4.35 (9)	0.41 (2)	0.48 (2)
Bunter 4002HC	28.1	0.980	220 (9)	0.124 (5)	0.22	3.79 (8)	0.209 (8)	0.249 (9)
Bunter 4010VA	30.1	0.988	245.4 (9.8)	0.041 (1)	0.22	3.83 (8)	0.63 (3)	0.71 (3)
Bunter 4012VC	30.2	0.989	300 (12)	0.0553 (2)	0.22	4.23 (9)	0.47 (2)	0.54 (2)
Gassum St 6VB	28.1	0.984	154 (6)	0.0221 (9)	0.22	3.16 (7)	1.17 (5)	1.32 (5)
Gassum St VB	28.1	0.988	127 (5)	0.0277 (11)	0.22	2.88 (6)	0.94 (4)	1.06 (4)
Gassum St86Va	28.7	0.993	137 (5)	0.0297 (12)	0.22	2.94 (6)	0.88 (4)	1.00 (4)
Rotliegend 6.01	14.0	0.981	0.0056 (8)	2.1 (0.3)	0.20	0.028 (2)	0.038 (7)	0.053 (7)
Rotliegend 6.23	10.7	0.976	0.012 (2)	3.9 (0.6)	0.19	0.046 (4)	0.019 (3)	0.027 (4)

[a] estimated error 0.1 porosity %.
[b] nr data points: 3 in Gassum, Berea and Bunter sandstone samples; 4 Rotliegend 1 and 3 samples; 6 for Rotliegend 6 samples.
[c] percentage error on permeability for 68% level of confidence was 4% for k > 1 mD; 10 % for 1 >k >0.1 mD (GEUS Core Laboratory). For k < 0.01 mD 15% error was estimated. The same percentage errors were used for b_{slip}.
[d] error is estimated by calculating $r_{p,slip}$ for the upper and lower limits of $b_{,slip}$.

Rotliegend data part of PETGAS database, University of Leeds, measured using helium gas flow. Other sandstone formations measured by Geological Survey of Denmark and Greenland GEUS using nitrogen gas flow. Except Rotliegend 6.01 and 6.23 all samples are measured using steady state permeametry, samples 6.01 and 6.23 were measured using a pulse decay technique.

A-II: Immobile water layer thickness

Data:

Permeability to brine was measured on samples of sandstone from Gassum Formation and on samples of Berea sandstone at the GEUS Core Laboratory. Synthetic brine with a composition based on the expected composition of the pore fluid of the Gassum sandstone Formation was used in order to prevent fines migration or chemical reactions. The brine was composed of 4.4 M NaCl and minor contributions of Ca, Mg, K, Sr, Br, SO42- and HCO3- and had an ionic strength of 5.0 M. Saturation was verified using Archimedes' test. A confining pressure of 2.8 MPa was applied, as in the gas permeability measurements.
Despite de-airing the brine prior to injection, alteration of ankerite, iron bearing carbonate cement, resulted in precipitation of rims of iron oxides or iron hydroxides on the ankerite cement in Gassum sandstone samples.

Permeability to brine of Rotliegend sandstone samples in the PETGAS project was measured with 3.45 M NaCl solution. Saturation was verified by using NMR. A confining pressure of 10.3 MPa was applied, as in the gas permeability measurements.

Calculations:

The immobile water thickness, τ, was calculated by using Eq.(A7) and data from the Klinkenberg procedure (Appendix A-I).

$$\tau = r - \left(\frac{k_w}{k}\right)^{1/4} r_{p,slip} \qquad \text{(A7)}$$

Results:

Table CA.1: Measured permeability to brine, k_w, and immobile water layer thickness, τ, as estimated cf. Eq.(A7).

Sandstone sample	**k_w[a] mD**	**τ[b] nm**
Gassum Fa	22 (2)	300 (20)
Gassum Aa	1.41 (14)	4 (4)
Berea A1	7.6 (8)	360 (50)
Rotliegend 3.3	0.0060 (12)	146 (13)
Rotliegend 3.4	0.43 (9)	320 (40)
Rotliegend 3.9	0.026 (5)	230 (20)
Rotliegend 3.11	0.012 (2)	360 (30)
Rotliegend 3.12	0.017 (3)	310 (20)
Rotliegend 1.33	0.26 (5)	110 (20)

[a] estimated error, 20% Rotliegend samples, 10% other sandstone samples.
[b] error based on maximum and minimum τ calculated with error bounds for k_w, $r_{p,slip}$, and k.
Gassum and Berea data are part of Crossover project measured at GEUS Core Laboratory using a brine with 5.0 M ionic strength. Rotliegend data part of PETGAS database measured using 3.45 M NaCl solution.

Table A2.2: Characteristic equivalent pore size for gas slip, $r_{p,slip,}$ was estimated from b_{slip} by using the unified gas slip model in Appendix A-I; maximum effective equivalent pore size, $r_{p,NMR,max,}$ was estimated from gas permeability and NMR [Manuscript IV]. Immobile water layer thickness, τ, was calculated based on measured permeability and $r_{p,slip,}$ and also by assuming that the pores smaller than or equal to $r_{p,NMR,max}$ also contribute to brine flow in Manuscript IV.

Sample	**$r_{p,slip}$[a] from unified slip model µm**	**τ[b] from unified slip model nm**	**$r_{p,NMR,max}$ from NMR pore size distribution µm**	**τ[c] from NMR pore size distribution nm**
Rotliegend 3.4	0.77 (3)	320 (40)	2.2 (2)	420 (30)
Rotliegend 3.9	0.48 (2)	230 (20)	0.61 (4)	130 (20)
Rotliegend 3.12	0.51 (2)	310 (20)	0.81 (6)	210 (20)
Rotliegend 1.33	0.286 (11)	110 (20)	0.93 (7)	160 (20)

[a] error is estimated by calculating $r_{p,slip}$ for the upper and lower limits of b_{slip}.
[b] error based on maximum and minimum τ calculated with error bounds for k_w, $r_{p,slip}$ and k.
[c] error margins in brackets indicate result range for ρ 6-14 µm/s.

Appendix B: Journal Manuscripts

- Manuscript I: The effect of hot water injection on sandstone permeability
  Co-authors: Haugwitz, C; Jacobsen, PSM; Kjøller, C; Fabricius, IL
  Geothermics, 50, 155-166, 2014

- Manuscript II: Different effects of temperature and salinity on permeability reduction by fines migration in Berea sandstone
  Co-authors: Kjøller, C; Riis, JF; Kets, F; Fabricius, IL
  Geothermics, 53, 225-235, 2015

- Manuscript III: Quantitative image analysis of sandstone mineralogy with application to hot water storage in geothermal aquifers
  Co-authors: Sindern, S; Fabricius, IL
  Submitted to Geothermics on 17 April 2014;

- Manuscript IV: Permeability in Rotliegend Gas Sandstones to gas and brine as predicted from NMR, mercury injection and image analysis
  Co-authors: Fabricius, IL; Fisher, QJ; Grattoni, CA
  Under review at Journal of Marine and Petroleum Geology

Geothermics 50 (2014) 155–166

Contents lists available at ScienceDirect

Geothermics

journal homepage: www.elsevier.com/locate/geothermics

The effect of hot water injection on sandstone permeability

Esther Rosenbrand[a,*], Christian Haugwitz[a], Peter Sally Munch Jacobsen[a], Claus Kjøller[b], Ida Lykke Fabricius[a]

[a] Technical University of Denmark, Department of Civil Engineering, Brovej 118, DK-2800 Kongens Lyngby, Denmark
[b] Geological Survey of Denmark and Greenland, Øster Voldgade 10, DK-1350 Copenhagen, Denmark

ARTICLE INFO

Article history:
Received 26 October 2012
Accepted 18 September 2013
Available online 31 October 2013

Keywords:
Sandstone
Permeability
Temperature dependency
Kaolinite mobilisation

ABSTRACT

Seasonal energy storage can be achieved by hot water injection in geothermal sandstone aquifers. We present an analysis of literature data in combination with new short-term flow through permeability experiments in order to address physical and physico-chemical mechanisms that can alter permeability when sandstones are heated from 20 °C to 70–200 °C. The pore surface area per unit pore volume was used to normalise permeability data, so that the temperature effect on samples with different pore size could be compared. In sandstones containing the clay mineral kaolinite, heating reduced permeability, suggesting that the observed permeability reduction was due to kaolinite mobilisation. The effect was partly reversible.

1. Introduction

Geothermal sandstone aquifers with temperatures below 75 °C provide renewable energy for district heating in Denmark (Lund et al., 2011); so in order to increase the thermal energy available during the winter, seasonal storage of surplus heat from renewable sources is considered. This would involve that during summer, produced geothermal waters are heated prior to re-injection so that the temperature of the reservoir is increased. The advantage of this kind of heat storage is that the combination of a relatively high in situ temperature and a low aquifer flow rate will minimise heat loss to the environment. A concern with regard to the feasibility of this method is the effect of increasing the temperature on the aquifer permeability. At operating temperatures exceeding 100 °C, corrosion of experimental equipment has been found to cause a progressive permeability decline by building up a filter cake at the inlet of the sample (Potter et al., 1981; Milsch et al., 2009). However, increasing the temperature may reduce permeability by other mechanisms as well, including: thermal expansion (Somerton, 1992), increased compressibility (Stottlemyre, 1981), mineral dissolution/precipitation (Tenthorey et al., 1998), changes of the electrical double layer (EDL) thickness that affect the effective porosity (Andreassen and Fabricius, 2010), or particle mobilisation due to changes in the surface charge of the minerals (Schembre and Kovscek, 2005). Several authors suggest that released particles reduce permeability by plugging pore throats (Mungan, 1965; Stottlemyre, 1981; Blair et al., 1984; Khilar and Fogler, 1984; Somerton, 1992; Ochi and Vernoux, 1998; Schembre and Kovscek, 2005).

Porosity reduction due to thermal expansion depends on the level of confining stress. When the sample cannot expand, the porosity is reduced by expansion of the grains into the pore space, whereas in a sample that is free to expand, both the grains and the sample expand. When the expansion of the sample equals that of the solids, the porosity is not reduced.

Heating also affects the stability of mineral phases and chemical reaction rates. This can lead to dissolution and precipitation that alter the permeability. Dissolution of silica can also lead to an apparent decrease in permeability if this increases the viscosity of the pore fluid (Stottlemyre, 1981). The amount of mineral dissolution and precipitation depend amongst other things on the stress state, the nature of the pore fluid, the minerals present and the duration of the experiment (Tenthorey et al., 1998). Investigating the effect of mineral dissolution and precipitation requires long term tests in which pore fluid composition is monitored as well as permeability (Tenthorey et al., 1998; Milsch et al., 2009). Immediate effects of heating can be due to changes in the electric double layer (EDL) at the mineral pore water interface. An electrical double layer forms on the minerals due to interaction between charged sites on the mineral surface and water molecules. The EDL is composed of a net surface charge, and a diffuse ion-bearing layer, with a net equal and opposite charge (Lorne et al., 1999). The thickness of the diffuse layer depends on the concentration of ions in the pore fluid and is characterised by the inverse Debye parameter, κ^{-1} (Lyklema et al.,

* Corresponding author. Tel.: +45 4525 5085.
E-mail addresses: esro@byg.dtu.dk, estherrosenbrand@gmail.com (E. Rosenbrand), christian.haugwitz@gmail.com (C. Haugwitz), pede_jacobsen@hotmail.com (P.S.M. Jacobsen), clkj@geus.dk (C. Kjøller), ilfa@byg.dtu.dk (I.L. Fabricius).

0375-6505/$ – see front matter © 2013 Elsevier Ltd. All rights reserved.
http://dx.doi.org/10.1016/j.geothermics.2013.09.006

Nomenclature

e	elementary charge (q, C)
I	ionic strength of electrolyte (n/L^3, mol/l)
k	absolute permeability, L^2, in text and figures: m^2; in tables: mD
k_B	Boltzmann's constant (mL^2/t^{2}T, J/K)
N_A	Avogadro's constant (n^{-1}, mol^{-1})
S	specific surface area (grain surface area to total rock volume) (L^2/L^3, m^2/cm^3)
S_s	specific surface area per unit solids volume (grain surface area to solids volume) (L^2/L^3, m^2/cm^3)
S_p	specific surface area per unit pore volume (grain surface area to pore volume) (L^2/L^3, m^2/cm^3)
T	absolute temperature (K)
V_s	volume of solids (m^3)
α	linear thermal expansion coefficient (K^{-1})
ε_o	permittivity of vacuum (q^{2}t^2/mL^3, F/m)
ε_r	relative dielectric permittivity
κ^{-1}	inverse Debye parameter (L, m)
ϕ	porosity

1995). The ions and water molecules that are close to the surface are immobilised, so an increased EDL thickness could reduce the effective pore volume (Andreassen and Fabricius, 2010).

Temperature induced changes in the EDL or the surface charge can have another effect in kaolinite bearing sandstone. These changes can increase the repulsive electrical double layer force between similarly charged diffuse layers, which can mobilise kaolinite particles resulting in permeability reduction (Khilar and Fogler, 1984; Schembre and Kovscek, 2005). High flow rates can also mobilise particles and cause permeability reduction, when a critical flow rate is exceeded (Ochi and Vernoux, 1998).

An overview of existing data (Rosenbrand and Fabricius, 2012) shows that in numerous laboratory investigations heating from room temperature to 70–200 °C reduces permeability; however, there are also reported cases where heating has no effect. In 11 of the 25 published investigations, the kaolinite bearing Berea sandstone was used. In the present paper, we include new experiments on Berea sandstone that show a permeability reduction due to heating, as is also observed in the literature data. Short-term tests, where the permeability is measured as soon as the temperature has stabilised, allow comparison of physical and physico-chemical effects between samples. In order to normalise the permeability data representing highly variable pore size, we use Kozeny's (1927) equation to estimate the surface area per unit pore volume, S_p. We rule out contamination for our tests, which thereby support the hypothesis that heating affects kaolinite mobilisation.

2. Theory

2.1. Specific surface

The specific surface, S, is defined as the internal surface area/rock volume ratio. According to Kozeny (1927), S relates permeability, k, to porosity, ϕ, of a homogenous sedimentary rock:

$$k = \frac{c\phi^3}{S^2} \tag{1}$$

The factor c accounts for the geometry of the porous medium. In a homogeneous medium it can be expressed as a direct function of porosity (Mortensen et al., 1998).

$$c = \left(4\cos\left(\frac{1}{3}\arccos\left(\phi\frac{8^2}{\pi^3} - 1\right) + \frac{4}{3}\pi\right) + 4\right)^{-1} \tag{2}$$

It should be noted that when S is measured by nitrogen adsorption (BET, Brunauer et al., 1938) only chalk and artificial sand made from glass beads have been found to be homogeneous enough to follow Kozeny's equation directly (Donaldson et al., 1975; Mortensen et al., 1998). For most natural sandstones, specific surface from BET will be higher than S calculated from porosity and permeability.

The ratio S_p (Eq. (3)), expresses the internal surface area per unit of pore volume. This is inversely related to the pore radius and thereby allows comparison of porosity and permeability changes between lithologies with different pore size.

$$S_p = \frac{S}{\phi} = \sqrt{\frac{c\phi}{k}} \tag{3}$$

S_p can be expressed as a function of the internal surface area per unit volume of solids S_s (Eqs. (4) and (5)) (Fabricius et al., 2007).

$$S_p = \frac{(1-\phi)S_s}{\phi} \tag{4}$$

$$S_s = \frac{S}{1-\phi} \tag{5}$$

2.2. Porosity

From Eq. (1) it follows that permeability may be directly influenced by porosity reduction. A porosity reduction due to heating without a phase change of the minerals depends on the expansion of the solid volume (i.e. the grains only) and of the sample bulk volume (i.e. grains and pore volume). The volume expansion of the solids depends on the specific mineral thermal expansion coefficient, whereas the expansion of the bulk volume also depends on the level of the confining stress. Heating results in thermal strain, which is characterised by the one-dimensional coefficient of thermal expansion α. We estimated the porosity $\phi_{\Delta T}$ after applying a temperature change ΔT in terms of the original bulk volume $V_{B,0}$ and the original porosity ϕ_0 from the expanded bulk, $V_{B,\Delta T}$, and expanded solid, $V_{s,\Delta T}$, volumes, assuming isotropic expansion so that the volumetric expansion is three times the linear expansion.

$$V_{B,\Delta T} = V_{B,0}(1 + 3\alpha_{bulk}\Delta T) \tag{6}$$

$$V_{s,\Delta T} = V_{s,0}(1 + 3\alpha_{solid}\Delta T) \tag{7}$$

Expressing the original solid volume in terms of the original porosity and the bulk volume, Eq. (7) becomes:

$$V_{s,\Delta T} = (1-\phi_o)V_{B,0}(1 + 3\alpha_{solid}\Delta T) \tag{8}$$

The porosity after a temperature change, ΔT, is then given by Eq. (9) where $V_{P,\Delta T}$ is the pore volume after ΔT.

$$\begin{aligned}\phi_{\Delta T} &= \frac{V_{P,\Delta T}}{V_{B,\Delta T}} = \frac{V_{B,\Delta T} - V_{S,\Delta T}}{V_{B,\Delta T}} \\ &= \frac{V_{B,0}(1 + 3\alpha_{bulk}\Delta T) - (1-\phi_0)V_{B,0}(1 + 3\alpha_{solid}\Delta T)}{V_{B,0}(1 + 3\alpha_{bulk}\Delta T)}\end{aligned} \tag{9}$$

This simplifies to Eq. (10).

$$\phi_{\Delta T} = 1 - \frac{(1-\phi_0)(1 + 3\alpha_{solid}\Delta T)}{1 + 3\alpha_{bulk}\Delta T} \tag{10}$$

2.3. Electrical double layer

The formation of an EDL on the mineral surface may reduce the mobility of the fluid in the EDL, and reduce the effective pore volume in which water can flow (Andreassen and Fabricius, 2010). The thickness of the diffuse layer is characterised by the inverse Debye parameter, κ^{-1} (Eq. (11)), which predicts the distance over which

Table 1
Porosity and permeability measured prior to and after heating experiments. Samples PC1 and PC2 are heated and cooled first with pure Milli-Q™ filtered water and subsequently with 0.34 M aqueous NaCl solution. Specific surface area is measured using N_2 adsorption (BET method) and reported in area per volume of solids.

Sample code	ϕ before test	ϕ after test	Gas permeability before test (mD)	Gas permeability after test (mD)	Klinkenberg permeability before test (mD)	Klinkenberg permeability after test (mD)	Specific surface area, S_s(m^2/cm^3)
PC1	0.181 ± 0.001	0.185 ± 0.001	63 ± 3	42 ± 3	58 ± 2	38 ± 2	3.05 ± 0.02
PC2	0.183 ± 0.001	0.184 ± 0.001	57 ± 3	43 ± 3	52 ± 2	39 ± 2	2.99 ± 0.02

the surface potential is reduced by a factor 1/e (e is the base of the natural logarithm) (Lyklema et al., 1995).

$$\kappa^{-1} = \sqrt{\frac{\varepsilon_0 \varepsilon_r k_B T}{2e^2 N_A I}} \tag{11}$$

where k_B is the Boltzmann constant, ε_0 is the vacuum permittivity, ε_r is the relative static permittivity of the solution, N_A is Avogadro's constant, e is the electron charge, I is the ionic strength of the solution and T is absolute temperature.

Eq. (11) suggests that heating increases κ^{-1} and would therefore reduce the effective pore volume (Andreassen and Fabricius, 2010). This applies only when ε_r is assumed constant, however, because a temperature rise causes a more than proportional reduction in the relative static permittivity of water, κ^{-1} is reduced as a consequence of heating.

A change in κ^{-1} also affects kaolinite particle mobilisation (Khilar and Fogler, 1984; Schembre and Kovscek, 2005). The interaction between double layers of two negatively charged surfaces results in a repulsive EDL force (Israelachvili, 2011). The EDL repulsion force is countered by the attractive van der Waals force, and the net force can be calculated using the DLVO theory (Derjaguin and Landau, 1941, 1993; Verwey and Overbeek, 1948). Schembre and Kovscek (2005) suggest that the surface charge on both kaolinite and quartz becomes more negative with increasing temperature, and that this increases the EDL repulsion force. In line with this, measurements of the zeta potential of the minerals show that this is more negative at 70 °C than at 20 °C (Ramachandran and Somasundaran, 1986). The zeta potential is the potential at the interface between the immobile and the mobile fluid in the EDL, and can be used to estimate the surface charge (Elimelech et al., 1995). Heating may mobilise kaolinite if the effect of temperature on the surface charge outweighs the reduction of the double layer thickness.

3. Materials and method

3.1. Experiments

Duplicate tests were performed on Berea sandstone plugs, PC1 and PC2, from the Cleveland Quarries (Amherst, OH). Both plugs had a 38 mm diameter and 63 mm length. He-porosity, N_2-gas permeability and Klinkenberg permeability (American Petroleum Institute, 1998) were measured before and after the tests, and specific surface area by N_2 adsorption (BET, Brunauer et al., 1938) was measured before the experiments (Table 1). Fluid permeability experiments were carried out using Milli-Q™ filtered water and 0.34 M NaCl brine. The brine was prepared from Milli-Q™ filtered water and 99.5% pure NaCl. All solutions were de-gassed in a vacuum chamber before application in the experiments.

Fig. 1 shows a backscatter electron microscopy (BSEM) image of the Berea sandstone used and elemental analysis was performed using energy dispersive X-ray spectroscopy (EDS). The samples consist predominantly of quartz grains with pore filling kaolinite as the dominant clay mineral, as also reported by Somerton et al. (1974). We also observed the presence of feldspar grains, carbonate cement and of other clay minerals that could be illite or chlorite. The kaolinite clay particles are concentrated locally in some pores and not in others as also noted by Schembre and Kovscek (2005).

An illustration of the experimental apparatus is shown in Fig. 2. The samples were placed in a Viton sleeve inside a Hassler type core holder and a confining stress of 2.8 MPa was applied. The temperature was controlled by placing the core holder inside an oven. A constant fluid flow rate was ensured by a high precision Pharmacia P500 piston pump, and the inlet pressure was measured using a Druck PDCR 910 transducer connected to a Druck DPI 280 pressure indicator at the inlet of the sample. The outlet pressure was atmospheric. Stainless steel tubing was used, and corrosion tests with NaCl brine at 80 °C using sintered glass beads in the core holder showed no corrosion in this setup.

The saturation state of the samples was verified using the Archimedes test. The details of the test protocol are given in Table 2. The samples were first tested with Milli-Q™ filtered water and subsequently with 0.34 M NaCl solution. The temperature was increased in steps and allowed to stabilise for 24 h prior to measurements. At each temperature step the permeability was measured with two flow rates. Permeability was calculated using viscosity corrections for temperature and salinity using the CREWES Fluid Properties Calculator. The value of S_p was estimated using He-porosity and Klinkenberg permeability (cf. Eqs. (2) and (3)). Table 2 shows S_p for all flow rates. The permeability change between 23 °C and 80 °C is included with the literature data in Table A.1.

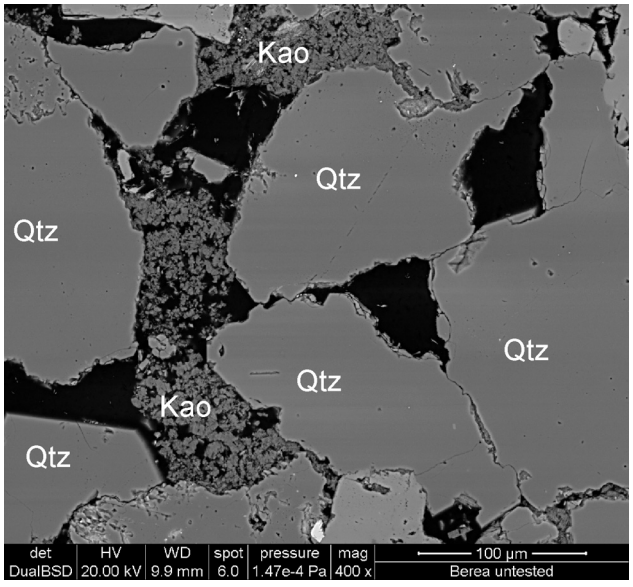

Fig. 1. Backscatter electron microscope (BSEM) image of Berea sandstone. Black areas constitute pore space, quartz (Qtz) grains make up the majority of the sample. Kaolinite particles (Kao) are observed concentrated in some pores and not in others.

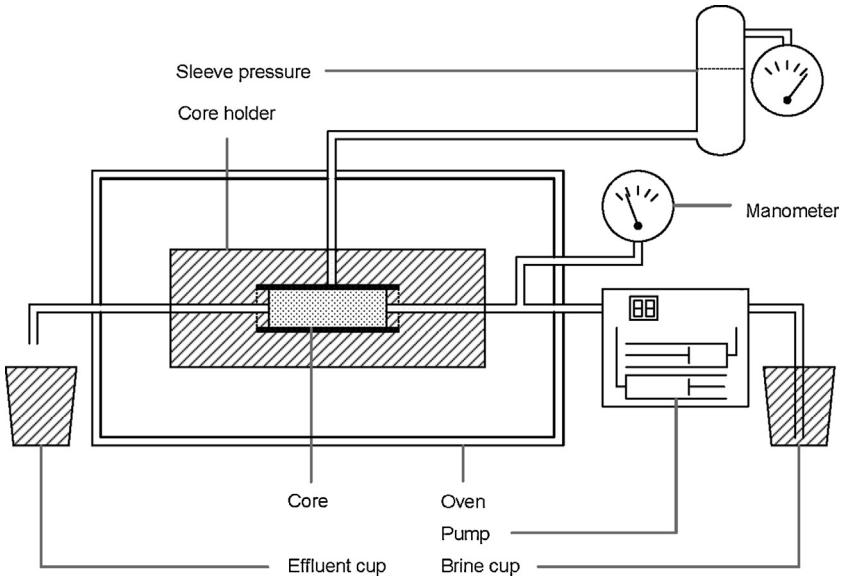

Fig. 2. Experimental setup: the core is placed in the core holder inside the oven. Water is injected at constant flow rate and the inlet pressure is measured outside the oven. The outlet pressure is atmospheric.

3.2. Literature data

Porosity and permeability data reported in tables or shown in graphs in the cited publications are listed in Table A.1. Each sandstone sample was assigned a different Arabic number for publications addressing several sandstones. Firing, i.e. heating the dry sample, causes loss of the structural water of kaolinite, which transforms mineralogically between 400 °C and 800 °C (Grim, 1953), and may also alter the surface charge of the quartz grains (Sharma and Yen, 1984). Sandstones that were fired prior to testing were therefore considered as different lithologies in this study. When multiple fluids were tested in the same sandstone, the tests for each fluid are indicated by Roman numerals, i.e., No. 1i, 1ii.

Not all investigators reported the mineralogy of the tested samples (cf. Table A.1). Thus to support the information in Table A.1 mineralogical descriptions of the sandstones in question were taken from other studies (cf. Table A.2). The duration of a test is important in order to address chemical changes (Tenthorey et al., 1998); however, this was not reported by all investigators. The investigations where the permeability is measured as soon as the temperature and pressure in the samples have stabilised are indicated as 'short-term' tests in the last column of Table A.1.

Data from tests where the permeability was reported both at room temperature and at elevated temperature were used to compute S_p for further analysis. These were all short-term tests. Porosity was not reported in all studies. Hence, for tests on Berea or Boise sandstones where the permeability was not reported, the porosity values based on data from related investigations were assumed. For less well studied sandstones or investigations where only the relative change in permeability was reported, the qualitative results were included in the discussion. Emphasis was placed on data from the more thoroughly documented tests that can be compared on a normalised basis using S_p.

3.3. Data processing

We estimated S_p from the porosity and permeability data in Table A.1 by using Eqs. (2) and (3). In the majority of the experiments, the porosity was only measured at room temperature. The lower bound for the porosity at elevated temperature was estimated by using Eq. (10) for a zero strain case, i.e., $\alpha_{bulk} = 0\,K^{-1}$, and $\alpha_{solid} = 18 \times 10^{-6}\,K^{-1}$, the linear thermal expansion coefficient of quartz perpendicular to the *c*-axis (Fjaer et al., 2008). Equal expansion of the grains and the bulk volume, i.e. constant porosity with temperature, yields the upper bound for the porosity. We approximated the maximal increase in S_p due to thermal expansion of the solids by using Eq. (4). S_s was estimated for a given combination of porosity and permeability by using Eqs. (1), (2) and (5),

Table 2
Experimental procedure for samples PC1 and PC2. Samples are saturated with pure Milli-Q™ filtered water and permeability is measured at 23 °C at two flow rates before changing the temperature to the next temperature step. Specific surface with respect to pore volume, S_p, is calculated from helium porosity and the measured permeability.

Fluid	Temperature (°C)	Flow rates (mL/h)	PC1 S_p (m^2/cm^3)	PC2 S_p (m^2/cm^3)
Milli-Q™ filtered water	23	20; 40	1.9; 1.9	1.7; 1.7
	40	20; 40	2.4; 2.4	2.3; 1.9
	60	10; 20	4.3; 3.5	3.8; 3.3
	80	10; 20	5.1; 4.2	4.5; 3.8
	60	10; 20	3.5; 3.2	3.6; 2.9
	40	10; 20	3.8; 3.5	2.3; 1.9
	23	10; 20	2.6; 2.6	2.7; 2.0
0.34 M NaCl	23	10; 20	2.4; 2.4	2.1; 2.0
	50	10; 20	2.5; 2.4	2.3; 2.2
	80	10; 20	4.7; 3.7	4.5; 3.6
	50	10; 20	3.1; 2.8	2.9; 2.8
	23	10; 20	2.7; 2.6	2.6; 1.9

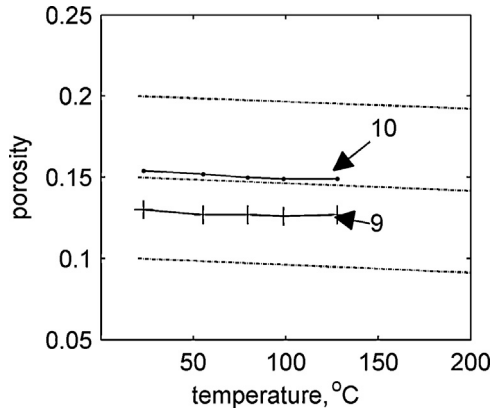

Fig. 3. In a confined sample, porosity declines as a function of temperature due to thermal expansion. Dashed lines represent the predicted reduction for a quartzitic sample, data points represent 85 wt% quartz samples from Jing et al. (1992). Numbers correspond to tests in Table A.1.

and S_s was assumed to be constant with temperature, although in principle thermal expansion can be expected to reduce S_s. This is because isotropic expansion of a spherical grain with radius r increases the surface area by a factor proportional to r^2 whereas volume increases proportional to r^3, so that $S_s = S/V_s$ is proportional to $1/r$. The effect of expansion on S_s for sandstone grains is affected by grain shape, surface roughness, and anisotropy of the thermal expansion coefficient. By choosing a constant S_s we thus made a conservative estimate and can interpret an increase in S_p exceeding the estimate of the maximum porosity reduction due to thermal expansion as an indication that additional mechanisms contributed to permeability reduction.

4. Results

4.1. Thermal expansion and change in S_p

Fig. 3 shows the estimated maximum effect on porosity due to thermal expansion for a confined quartzitic sample (dashed lines). Data for two sandstones with 85 wt% quartz (No. 9 and 10; Table A.1) at 14 MPa confining stress do not contradict the estimated trends. The corresponding estimated effect of thermal

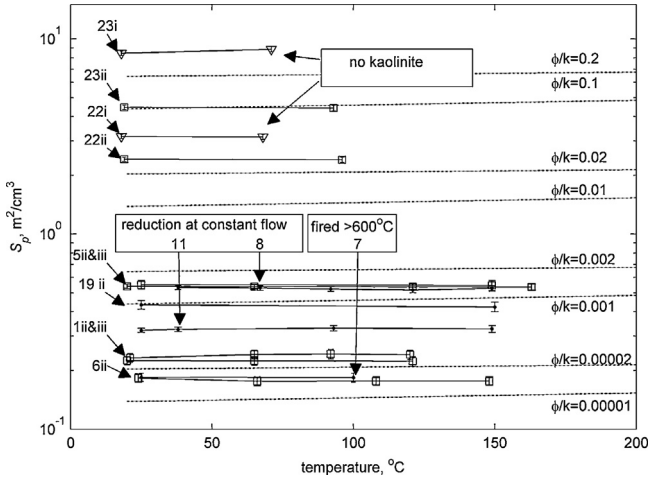

Fig. 4. Specific surface with respect to pore volume, S_p, as a function of temperature for tests where permeability is constant with temperature. Dashed lines: predicted increase due to thermal expansion. Dots: tests with distilled water; triangles: tests with brine; squares: tests with inert fluid (mineral oil or N_2 gas). Numbers correspond to tests in Table A.1. Porosity-permeability ratio ϕ/k is given in units of %/mD.

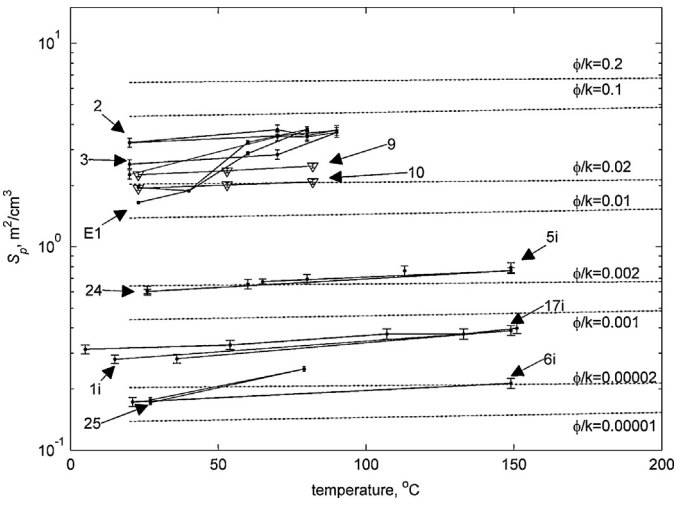

Fig. 5. Specific surface with respect to pore volume, S_p, as a function of temperature for tests where permeability is reduced and S_p consequently increased at elevated temperature. Dashed lines: predicted increase in S_p due to thermal expansion. Dots: tests with distilled water; triangles: tests with NaCl brine with a concentration greater than 0.3 M. No. E1 represents data from experiments in this study. Tests where samples are heated and subsequently cooled (No. 1i, 2, 3, 6, 24, 25, E1) show that the increase in S_p is largely reversible with cooling. Samples No. 2, 3 and E1 are also tested with brine (ref. Fig. 6a–c). Numbers correspond to tests in Table A.1. Porosity-permeability ratio ϕ/k is given in units of %/mD.

expansion on S_p is shown by dashed lines in Figs. 4–6. Sample numbers in the figures and the following sections refer to the sample numbers in Table A.1. We separated tests where S_p changed less than predicted by the maximum porosity reduction (Fig. 4), and tests where the S_p changed more than this (Fig. 5). Samples No. 2, 3, and E1, were tested successively with distilled water and with brine, and the effect of temperature was different for the different tests. For clarity only the tests with distilled water are shown in Fig. 5, and for these three studies the tests with distilled water, NaCl, and $CaCl_2$ solution are shown in Fig. 6. Heating increased S_p in 15 tests on the Berea, Boise, Massillon, Millstone Grit, Vosges and Upper Coal Measures samples. In 12 of these tests, on Berea, Boise, Massillon, and Vosges samples, the samples were subsequently cooled, which reduced S_p. In seven tests the effect of temperature was found to be practically reversible (No 1, 2i and iii, 3ii, 24, 25, E1ii).

4.2. Change in compressibility

Chemical and physico-chemical reactions can be neglected in tests with inert fluids, so that porosity reduction due to thermal expansion or an increase in compressibility of the minerals would be the only permeability reducing mechanism. Tests with inert fluids showed no change in permeability (Fig. 4).

4.3. Corrosion of the equipment

Corrosion produced colloid particles that reduced permeability in tests No. 12i, 14i and 19i, as indicated by discoloration at the inlet of the core (No. 12i and 14i), or observation of metal oxide and hydroxide particles in the effluent (No. 19i). Modification of the equipment prevented corrosion, suggesting the corrosion products were not generated by fluid-mineral interaction. We verified the absence of corrosion in our tests (No. E1) by a subsequent test with a sintered glass sample.

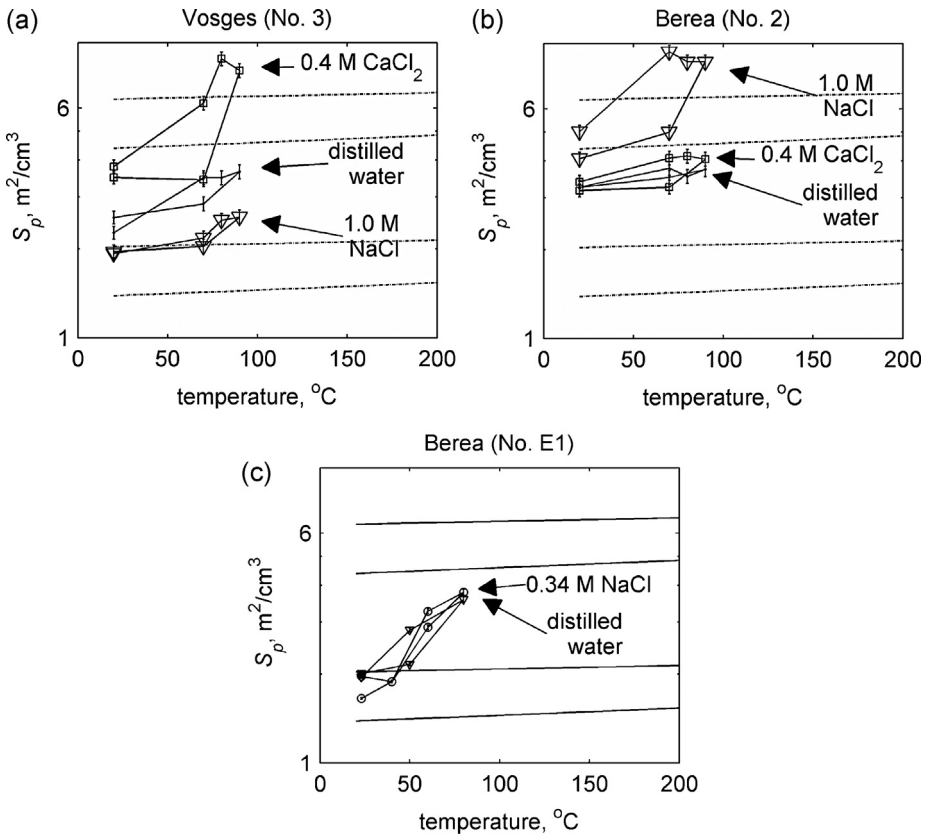

Fig. 6. Specific surface with respect to pore volume, S_p, as a function of temperature for tests on samples No. 2 (a) and No. 3 (b); with distilled water (tiny dots), 1.0 M NaCl (triangles), and 0.4 M $CaCl_2$ (squares). Tests on sample No. E1 (c) with distilled water (tiny dots) and 0.34 M NaCl (triangles).

4.4. Dissolution

Silica was detected in the effluent in tests No. 4, 12, 18 and 19, for samples of Ironton-Galesville, Rotliegend, Berea and Massillon sandstones. Permeability reduction at constant temperature, as indicated by an increase in S_p, was observed in No. 4 (Ironton-Galesville) but not in No. 12ii (Rotliegend sandstone). Heating to 150 °C and subsequent cooling had no effect on S_p in No. 19ii (Massillon sandstone). However, a permeability reduction was observed when the temperature was increased to 156 °C in No. 18 (Berea sandstone); the change was fully reversible with cooling at 3.5 MPa confining stress (No.18i), but only 75% of the original permeability was recovered with 6.9 MPa confining stress (No.18ii) (Somerton, 1992).

4.5. Change in EDL thickness

Heating reduces κ^{-1} (cf. Eq. (11)), which could increase porosity and decrease S_p cf. Eq. (3). A decrease in S_p with temperature was not observed in any test. In distilled water, κ^{-1} is larger than in brine, but we found no effect of this; Fig. 6a–c does not show a consistently larger S_p with distilled water than with brine for two Berea sandstone samples and one Vosges sandstone sample.

4.6. Kaolinite mobilisation

The sandstones in which heating increased S_p (Figs. 5 and 6) all contain kaolinite. Kaolinite was not reported by Jing et al. (1992) for the Millstone grit sandstone sample (No. 9); however, kaolinite was observed in this sandstone by Jerret and Hampson (2007). There are only two sandstones that were not reported to contain kaolinite: Cige sandstone and Old Man Mountain sandstone (No. 22 and 23) and these showed no effect of heating (Fig. 4).

No temperature effect was found in a Boise sandstone sample (No. 7) that was fired above 600 °C, whereas heating did increase S_p in Boise sandstone samples that were not fired above 600 °C (No. 6i and 25). Likewise S_p was increased when the temperature was raised in Berea sandstone samples (No. 2, 16, 19, 24, E1), that were not fired above 600 °C, but not in a Berea sandstone sample that had been fired (No. 15). In two samples from sandstones that do contain kaolinite (Berea sandstone No. 8 and Fontainebleau sandstone No. 11) where temperature had no effect, kaolinite mobilisation reduced permeability, i.e. increased S_p, at room temperature. In one Massillon sandstone sample, kaolinite was observed in the effluent (No. 19ii), but no permeability reduction was observed, whereas in another investigation of the Massillon sandstone (No. 1i) heating increased S_p.

Baudracco and Aoubouazza (1995) found that the effect of temperature was different on Berea sandstone or Vosges sandstone samples with distilled water, 1.0 M NaCl and with 0.4 M $CaCl_2$ (Fig. 6a and b, No. 2 and 3). Both sandstones contain kaolinite but illite is the dominant clay mineral in the Vosges sandstone, which also contains smectite, a swelling clay mineral (Baudracco and Aoubouazza, 1995). We found a comparable effect of temperature in the Berea sandstone with 0.34 M NaCl and with distilled water (Fig. 6c No. E1).

5. Discussion

5.1. Thermal expansion and change in S_p

Even without expansion of the bulk volume, heating from 20 to 150 °C should only reduce porosity from, e.g. 0.10 to 0.094 in a

low-porosity sandstone (Fig. 3). Thermal expansion has a greater effect at low porosity due to the larger volume of solids expanding into the smaller pore volume, and samples in Table A.1 have porosities greater than 0.10. Thermal expansion data of the Berea and Boise sandstones (70% and 40% quartz content respectively) indicate that the two sandstones have the same bulk thermal expansion coefficient, which is close to that of quartz perpendicular to the *c*-axis, for temperatures below 200 °C (Somerton and Selim, 1961;Somerton et al., 1981). Thus it is unlikely that thermal expansion can explain the observed increases in S_p with temperature.

5.2. Compressibility change

Compressibility changes cannot be assessed from the permeability experiments, this requires rock mechanical testing, but it should be noted that samples with an inert fluid suffered no change in permeability (Fig. 4). So if compressibility was reduced due to heating, this had an insignificant effect for the confining stresses used for tests in Table A.1.

5.3. Corrosion of the equipment

The contamination from the equipment in No. 19i was detected by analysis of the effluent, although this was not apparent from a discoloration at the inlet of the sample (Stottlemyre, 1981). This suggests that colloid contamination cannot be ruled out for the other tests, with the exception of No. E1 where we established that no contamination occurred by testing a sintered glass sample. However, contamination was less probable to cause the changes observed in tests No. 5i and 6i (Fig. 5) as there was no effect of temperature in test No. 7 (Fig. 4) under the same conditions. The same reasoning applies to tests No. 15 and 16 (Table A.1).

5.4. Dissolution

Chemical changes cannot be assessed from permeability changes. Silica was observed in the effluent without a concurrent change in S_p when the temperature was increased in one test on the Massillon sandstone (No. 19ii). The increase in pore fluid viscosity due to silica dissolution was considered negligible for that test (Stottlemyre, 1981). During 26 days of flow at 150 °C in a sample of Rotliegend sandstone, silica was observed in the effluent, but the permeability was reported to remain constant (No. 12, Milsch et al., 2009).

It has been suggested that dissolution releases fines that subsequently block pore throats (Mungan, 1965; Stottlemyre, 1981; Blair et al., 1984; Somerton, 1992), and this may account for the permeability reduction observed in the friable Ironton-Galesville sandstone (No. 4, Blair et al., 1984). Both the silica concentration and the release of particles depend on the dissolution rate, the reactive surface area, and the flow rate. Therefore, the effect of chemical reactions observed in one sandstone for specific test conditions cannot be extrapolated to other tests. Dissolution or precipitation may cause progressive alteration of the sample mineralogy and pore geometry over time, and these effects may not be apparent in the short-term experiments shown in Figs. 4–6. Results from study No. 18 suggest that silica dissolution may contribute to the permeability reduction at higher confining stresses, causing a larger permeability reduction and a lower permeability recovery (Somerton, 1992). The reversibility of the heating effect in seven tests in Figs. 5 and 6 indicates that a different mechanism caused the permeability reduction observed in those samples.

5.5. Change in the EDL thickness

We observed no changes in S_p that support the hypothesis that changes in κ^{-1} due to heating affect the volume of immobile water in the EDL for the samples in Table A.1.

5.6. Kaolinite particle mobilisation

Heating makes the surface charge on kaolinite and quartz more negative, which increases the EDL repulsion force between kaolinite and quartz, which again may lead to kaolinite mobilisation and supposed pore plugging (Schembre and Kovscek, 2005). The EDL repulsion force is also increased by reducing the salinity of the pore fluid, and this caused an irreversible permeability reduction at room temperature in tests by Khilar and Fogler (1984). The reduction of S_p that was observed when the temperature was reduced to the original value in tests No. 1–3, 6i, 18i, 24, 25 and E1 appears contradictory to the hypothesis of particles plugging pores. Because the effect of temperature on the surface charge can be presumed to be reversible, cooling reduces the EDL repulsion force so that particles may re-attach to the grain surface.

6. Conclusion

The use of specific surface of pores, S_p, to normalise data permits comparison of temperature effects on permeability in sandstones with different pore size. S_p was also used to distinguish between results where the permeability alteration can be due to thermal expansion and those where other mechanisms can have contributed to alter the permeability. Our analysis accounts for short-term effects of temperature on (1) thermal expansion, (2) electrical double layer (EDL) thickness, and (3) particle mobilisation due to physico-chemical interactions. (1) Tests with an inert fluid show no significant effect of temperature. This indicates that thermal expansion has a negligible effect. (2) We found no indication that a change in the volume of fluid immobilised by the EDL has a significant effect on S_p. (3) With aqueous solutions Berea sandstone showed permeability reduction due to heating, and permeability recovery due to cooling. This effect was also found for Boise sandstone, Massillon sandstone, and Vosges sandstone, but not for all studied sandstones. The sandstones where permeability was reduced due to heating contain dispersed kaolinite, and pre-treatment by heating above the temperature where kaolinite starts to dehydrate was found to prevent permeability reduction. This indicates that kaolinite mobilisation caused the observed permeability changes. It is noteworthy that the permeability reduction due to proposed kaolinite mobilisation was reversible at least in the short term.

Acknowledgements

This research was funded by the Danish Council for Strategic Research as part of the HeHo project grant. Thanks are due to Jacob Fabricius Riis for his illustration of the experimental setup.We appreciate constructive reviews by Dr. Harald Milsch and by an anonymous reviewer that improved the manuscript.

Appendix A. Summary of permeability test data

This section contains Tables A.1 and A.2.

Table A.1
Overview of the literature data (adapted from Rosenbrand and Fabricius, 2012) and new experimental results. Error margins for permeability measurements are those reported in the publication or estimated from scatter in the reported data. Where neither is available, an error margin of 10%, indicated in italic, is assumed. Short-term tests are tests where permeability is measured as soon as temperature and pressure in the sample are stabilised. Refer to Table A.2 for the mineralogical composition for studies where this is not reported (ϕ is porosity; k is permeability).

No.	Reference	Stratigraphic unit Mineralogy	ϕ	Fluid	k at room temperature (mD)	Maximum temperature (°C)/permeability k (mD)	k after cooling (mD)	Comments
1	Aruna (1976)	Massillon Sandstone Fired 300 °C. Grains: quartz Clay minerals: N.R. Cement: iron oxide; silica	0.22	i) Distilled water ii) Mineral oil iii) Nitrogen gas	i) 585 ii) 866 iii) 923 (±*10%*)	i) 149 °C/369 mD ii) 120 °C/792 mD ii) 121 °C/923 mD	i) 593 ii) 824 iii) N.R.	i) Confining pressure 19.7 MPa ii) Confining pressure 13.7 MPa iii) Klinkenberg procedure. Short-term.
2	Baudracco and Aoubouazza (1995)	Berea Sandstone Grains: mainly quartz; feldspar; plagioclase Clay minerals: total 8%: 6% kaolinite, 1% illite, 1% chlorite Cement: silica	0.20	i) Distilled water ii) 1.0 M NaCl iii) 0.4 M $CaCl_2$	i) 3.9 ii) 1.6 iii) 3.6 (±*10%*)	i) 90 °C/2.9 mD ii) 90 °C/0.5 mD iii) 90 °C/2.5 mD	i) 3.7 ii) 2.5 iii) 4.1	Confining pressure 0.2 MPa Tests were done on the same sample with water, $CaCl_2$ and NaCl solution Short-term
3	Baudracco and Aoubouazza (1995)	Vosges Sandstone Grains: quartz; feldspar Clay minerals: 4%: 2% illite; 1% kaolinite; 0.5% chlorite; 0.5% smectite	0.20	i) Distilled water ii) 1.0 M NaCl iii) 0.4 M $CaCl_2$	i) 7.6 ii) 10.7 iii) 2.8 (±*10%*)	i) 90 °C/3.0 mD ii) 90 °C/6.0 mD iii) 90 °C/0.6 mD	i) 6.12 ii) 10.4 iii) 3.3	Confining pressure 0.2 MPa Tests were done on the same sample with water, $CaCl_2$ and NaCl solution Short-term
4	Blair et al. (1984)	Ironton-Galesville Sandstone Grains: quartz Cement: dolomite	N.R.	Synthetic brine	N.R.	150 °C/gradual permeability reduction over time to 20% of original	N.R.	Confining pressure 6.2 MPa Sample loses mechanical strength Silicium and calcium in the effluent Sample was heated incrementally and flow is stopped for 2 days at increments: 60 °C, 100 °C, 160 °C. Duration approx. 7 days
5	Cassé and Ramey (1979)	Berea Sandstone Fired 450 °C N.R.	N.R. 0.19[a]	i) Distilled water ii) Mineral oil iii) N_2 gas	i) 98 ii) 130 iii) 134 (±5%)	i) 148 °C/81 mD ii) 148 °C/130 mD iii) 163 °C/134 mD	N.R.	Confining pressure 13.8 MPa For water the effect of temperature is greater for higher confining pressure Short-term
6	Cassé and Ramey (1979)	Boise Sandstone Fired 450 °C N.R.	N.R. 0.28[a]	i) Distilled water ii) Mineral oil	i) 2063 ii) 1930 (±5%)	i) 148 °C/1340 mD ii) 149 °C/2240 mD	i) 1651 ii) N.R.	i) Confining pressure 25.5 MPa ii) Confining pressure 3.4 MPa Repeated cycles of heating with distilled water cause hysteresis Short-term
7	Cassé and Ramey (1979)	Boise Sandstone Fired 760 °C N.R.	N.R. 0.28[a]	Distilled water	1852 (±5%)	149 °C/1852 mD	N.R.	Confining pressure13.8 MPa Short-term

Table A.1 (*Continued*)

No.	Reference	Stratigraphic unit Mineralogy	ϕ	Fluid	k at room temperature (mD)	Maximum temperature (°C)/permeability k (mD)	k after cooling (mD)	Comments
8	Gobran et al. (1987)	Berea Sandstone N.R.	N.R. 0.19[a]	Distilled water	138 (±5%)	149 °C/138 mD	N.R.	Confining pressure 13.8 MPa Permeability is reduced initially. Heating has no additional effect Short-term
9	Jing (1990); Jing et al. (1992)	Millstone Grit Series Sandstone Grains: 85% quartz; 10% feldspar; 5% mica	0.13	0.86 M NaCl.	5 (±5%)	93 °C/3.8 mD	N.R.	Confining pressure 13.8 MPa Short-term
10	Jing (1990); Jing et al. (1992)	Upper Coal Measures Sandstone Grains: 85% quartz; 5% feldspar; 5% mica Clay minerals: 5% N.R.	0.17	0.86 M NaCl	8.2 (±5%)	93 °C/6.6 mD	N.R.	Confining pressure 13.8 MPa Short-term
11	McKay and Brigham (1984)	Fontainebleau Sandstone Grains: Quartz Clay minerals: kaolinite	0.11	Distilled water	260 (±5%)	149 °C/200 mD	N.R.	Confining pressure 13.8 MPa Permeability reduced during flow at constant temperature, heating does not cause significant additional effect Short-term
12	Milsch et al. (2009)	Rotliegend Sandstone Grains: quartz 80%; feldspar <10%; <10% rock fragments Clay minerals: illite; chlorite Cement: quartz dominates; rarely carbonitic or albitic	0.11	i) Synthetic formation brine with contamination ii) Synthetic formation brine without contami-nation	N.R.	i)150°C/0.33-0.01 mD ii) 150 °C/2.00 mD (±0.36)	N.R.	Confining pressure 50 MPa Permeability is approximately constant over 26 days of flow in ii In an initial test (i) corrosion occurred. In subsequent tests this was avoided Long-term
13	Piwinskii and Netherton (1977)	Kayenta Sandstone N.R.	N.R.	Synthetic brine containing 140 ppm silica unfiltered.	N.R.	100 °C/50 mD declines to Approx. 1 mD	N.R.	Permeability decreases as function of flow volume. Tests are performed with and without filters, without filters a filter cake builds up on the sample inlet Short-term
14	Potter et al. (1981)	St. Peters Sandstone Grains: quartz.	N.R.	i) Distilled water with contamination ii) Distilled water.	i) N.R. ii) N.R.	i) 100 °C/554 mD initial. Reduction at constant temperature ii) No reduction	N.R.	i) Contamination from the equipment causes a gradual permeability reduction at 100 °C ii) After preventing contamination no reduction. Confining pressure 20 MPa Short-term

Table A.1 (*Continued*)

No.	Reference	Stratigraphic unit Mineralogy	ϕ	Fluid	k at room temperature (mD)	Maximum temperature (°C)/permeability k (mD)	k after cooling (mD)	Comments
15	Schembre and Kovscek (2005)	Berea Sandstone Fired temperature N.R.	0.20–0.23	0.05 M NaCl; pH 10.	N.R.	180 °C No permeability reduction	N.R.	Confining pressure not reported, between 1.7 MPa and 2.8 MPa Short-term
16	Schembre and Kovscek (2005)	Berea Sandstone N.R.	0.20–0.23	i) 0.01 M NaCl; pH 7 ii) 0.01 M NaCl; pH 10 iii) 0.05 M NaCl; pH 10. iv) 0.2 M NaCl; pH 10.	N.R.	i) 180 °C/99% reduction ii) 180 °C/72% reduction iii) 180 °C/50% reduction *70% iv) 180 °C/67% reduction *87%	N.R.	Confining pressure not reported, between 1.7 and 2.8 MPa Short-term
17	Somerton and Mathur (1976)	Berea Sandstone N.R.	N.R. 0.19[b]	Distilled water	397 (±*10%*)	164 °C/235 mD	N.R.	Confining pressure 13.9 MPa Switching to 0.42 M KCl at elevated temperature reduces permeability to 125 mD. Cooling to 70 °C with 0.42 M KCl increases permeability to 205 mD Short-term
18	Somerton (1992) (citing Wong, 1979)	Berea Sandstone N.R.	N.R. 0.19[a]	i) 0.08 M KCl ii) 0.08 M KCl	N.R.	i) 156 °C/24% reduction ii) 156 °C/45% reduction	i) 1% reduction ii) 73% reduction	i) Confining pressure 3.5 MPa ii) Confining pressure 6.9 MPa Short-term
19	Stottlemyre (1981)	Massillon Sandstone N.R.	0.23	i) Distilled water w. contamination ii) Distilled water	i) 375 ii) 260 (±*10%*)	i) 25 °C/300 mD 150 °C/90 mD iii) 150 °C/260 mD		Confining pressure 15 MPa Contamination caused permeability reduction at room temperature, and further reduction with heating After preventing contamination no significant permeability reduction occurred with heating Observe quartz, kaolinite and metal hydroxides and oxides in effluent Short-term
20	Sydansk (1980)	Berea Sandstone Fired 450 °C N.R.	N.R. 0.19[a]	(i) + (iii) Distilled water (ii) + (iv) 0.52 M NaCl	N.R.	i) 22 °C/26% reduction ii) 22 °C/4% reduction iii) 85 °C/81% reduction iv) 85 °C/8% reduction		Confining pressure not reported Permeability reduction given for flow at constant temperature Short-term
21	Sydansk (1980)	Berea Sandstone Fired 1000 °C N.R.	0.19[a]	(i) + (iii) Distilled water (ii) + (iv) 0.52 M NaCl	N.R.	i) 22 °C/21% reduction ii) 22 °C/6% reduction iii) 85 °C/40% reduction iv) 85 °C/2% reduction	N.R.	Confining pressure not reported Permeability reduction given for flow at constant temperature Short-term

Table A.1 (*Continued*)

No.	Reference	Stratigraphic unit Mineralogy	ϕ	Fluid	k at room temperature (mD)	Maximum temperature (°C)/permeability k (mD)	k after cooling (mD)	Comments
22	Wei et al. (1986); Morrow et al. (1983)	Old Man Mountain Sandstone Grains: 50% quartz; 36% feldspar; 7% chert and rock fragments Cement: carbonate; possibly quartz	0.14	i) 0.79 M KNO_3 ii) N_2 gas.	i) 2.9 ii) 4.8 (±5%)	i) 68 °C/2.9 mD ii) 96 °C/4.8 mD	N.R.	Confining pressure 6.9 MPa Short-term
23	Wei et al. (1986); Morrow et al. (1983)	CIGE Sandstone Grains: 43% quartz; 23% feldspar; 20% chert and rock fragments Cement: 8% carbonate.	0.12	i) 0.79 M KNO_3 ii) N_2 gas	i) 0.3 ii) 1.2 (±5%)	i) 68 °C/0.3 mD ii) 96 °C/1.2 mD	N.R.	Confining pressure 6.9 MPa Short-term
24	Weinbrandt and Ramey (1975)	Berea Sandstone Fired 450 °C N.R.	0.19	Distilled water	106 (±5%)	149 °C/63 mD	110 °C/70 mD	Confining pressure 13.9 MPa Short-term
25	Weinbrandt and Ramey (1975)	Boise Sandstone Fired 450 °C N.R.	0.28	Distilled water	1970 (±5%)	79 °C/972 mD	27 °C/2080 mD	Confining pressure 13.9 MPa Short-term
E1	This study	Berea Sandstone N.R.	0.18	i) Distilled water ii) 0.34 M NaCl.	i) 9.8 13.7[b] ii) 6.5 8.3[b] (±10%)	i) 80 °C/1.4 mD 2.6[b] mD i) 80 °C/2.6 mD 2.9[b] mD	i) 5.4 9.7[b] ii) 5.4 9.8[b]	Confining pressure 2.8 MPa is sample PC2 Short-term

N.R., data not reported.
[a] Porosity not reported for the sample but assumed from other sources.
[b] Duplicate tests.

Table A.2
Mineralogy of the Berea and the Boise sandstones (Somerton et al., 1974), the Fontainebleau sandstone (French and Worden, 2013), the Massillon sandstone (Gray, 1956), and the St. Peter sandstone (Mungan, 1965).

Stratigraphic unit	Grains (% solid mass)	Clay minerals (% solid mass)	Cement (% solid mass)
Berea (Somerton et al., 1974)	Quartz: 68% Feldspar: 2%	Kaolinite and matrix: 19%	Calcite: 1%
Boise (Somerton et al., 1974)	Quartz: 39% Feldspar: 20%	Kaolinite and matrix: 35% Muscovite 5%	–
Fontainebleau (French and Worden, 2013)	Quartz	Kaolinite: <1%	Silica
Massillon (Gray, 1956)	Quartz: 73–88%	11–26%: illite, kaolinite, muscovite (mainly illite)	Silica Iron oxides
St. Peter (Mungan, 1965)	Quartz: >99%	Illite: <1%	Calcite: <1%

References

American Petroleum Institute, 1998. Recommended Practices for Core Analysis. Recommended Practice 40, 2nd ed. API, Washington, DC, pp. 6.18–6.32, February.

Andreassen, K.A., Fabricius, I.L., 2010. Biot critical frequency applied to description of failure and yield of highly porous chalk with different pore fluids. Geophysics 75, E205–E213.

Aruna, M., 1976. The effects of temperature and pressure on absolute permeability of sandstones. Stanford University, Stanford, CA, USA, pp. 102 p (PhD thesis).

Brunauer, S., Emmett, P.H., Teller, E., 1938. Adsorption of gases in multimolecular layers. Journal of the American Chemical Society 60, 309–319.

Baudracco, J., Aoubouazza, M., 1995. Permeability variations in Berea and Vosges sandstone submitted to cyclic temperature percolation of saline fluids. Geothermics 24, 661–677.

Blair, S.C., Deutsch, W.J., Kannberg, L.D., 1984. Laboratory permeability measurements in support of an aquifer thermal energy storage site in Minnesota. In: Proceedings of the 25th US Symposium on Rock Mechanics, Evanston, IL, USA, pp. 296–303.

Cassé, F.J., Ramey Jr., H.J., 1979. The effect of temperature and confining pressure on single-phase flow in consolidated rocks (includes associated paper 9087). Journal of Petroleum Technology 31, 1051–1059.

Crewes Properties Calculator. http://www.crewes.org/ResearchLinks/ExplorerPrograms/FlProp/FluidProp.htm (accessed on 22.09.12).

Derjaguin, B.V., Landau, L.D., 1941. Theory of the stability of strongly charged lyophobic sols and the adhesion of strongly charged particles in solutions of electrolytes. Acta Physicochimica USSR 14, 733–762.

Derjaguin, B.V., Landau, L.D., 1993. Theory of the stability of strongly charged lyophobic sols and of the adhesion of strongly charged particles in solutions of electrolytes. Progress in Surface Science 43, 30–59.

Donaldson, E.C., Kendall, R.F., Baker, B.A., Manning, F.S., 1975. Surface-area measurement of geologic materials. Old SPE Journal 15, 111–116.

Elimelech, M., Gregory, J., Jia, X., Williams, R.A., 1995. Deposition and aggregation—measurement. In: Modelling and Simulation. Butterworth-Heinemann, Woburn, USA, pp. 448.

French, M.W., Worden, R.H., 2013. Orientation of microcrystalline quartz in the Fontainebleau Formation, Paris Basin and why it preserves porosity. Sedimentary Geology 284–285, 149–158.

Fabricius, I.L., Baechle, G., Eberli, G.P., Weger, R., 2007. Estimating permeability of carbonate rocks from porosity and v_p/v_s. Geophysics 72, 185–191.
Fjaer, E., Holt, R.M., Horsrud, P., Raaen, A.M., Risnes, R., 2008. Petroleum related rock mechanics. Developments in Petroleum Science, vol. 53., 2nd ed. Elsevier, Amsterdam, pp. 514.
Gobran, B.D., Brigham, W.E., Ramey Jr., H.J., 1987. Absolute permeability as a function of confining pressure, pore pressure, and temperature. SPE Formation Evaluation 2, 77–84.
Gray, H.H., 1956. Petrology of the Massillon sandstone at the type locality. Ohio Journal of Science 56, 138–146.
Grim, R.E., 1953. In: Shock, R.R. (Ed.), Clay Mineralogy in International Series in the Earth Sciences. McGraw-Hill Book Company Inc. New York, p. 384.
Israelachvili, J.N., 2011. Intermolecular and Surface Forces, 3rd ed. Elsevier/Academic Press, Amsterdam, pp. 674.
Jerret, R.M., Hampson, G.J., 2007. Sequence stratigraphy of the upper Millstone Grit (Yeadonian, Namurian), North Wales. Geological Journal 42, 513–530.
Jing, X.D., 1990. The effect of clay, pressure and temperature on the electrical and hydraulic properties of real and synthetic rocks. Imperial College of Science Technology and Medicine, London, UK, pp. 280 (PhD thesis).
Jing, X.D., Archer, J.S., Daltaban, T.S., 1992. Laboratory study of the electrical and hydraulic properties of rocks under simulated reservoir conditions. Marine and Petroleum Geology 9, 115–127.
Khilar, K.C., Fogler, H.S., 1984. The existence of a critical salt concentration for particle release. Journal of Colloid and Interface Science 101, 214–224.
Kozeny, J., 1927. Ueber kapillare Leitung des Wassers im Boden. Sitzungsberichte der Wiener Akademie der Wissenschaften 136, 271–306.
Lorne, B., Perrier, F., Avouac, J.P., 1999. Streaming potential measurements: 1. Properties of the electrical double layer from crushed rock samples. Journal of Geophysical Research 104, 17857–17877.
Lund, J.W., Freeston, D.H., Boyd, T.L., 2011. Direct utilization of geothermal energy. 2010 worldwide review. Geothermics 40, 159–180.
Lyklema, J.J., de Keizer, A., Bijsterbosch, B.H., Fleer, G.J., Cohen Stuart, M.A., 1995. Electric double layers. In: Lyklema, J.J., de Keizer, A., Bijsterbosch, B.H., Fleer, G.J., Cohen Stuart, M.A. (Eds.), Fundamentals of Interface and Colloid Science, Volume II: Solid–Liquid Interfaces. Academic Press, Amsterdam, p. 232.
McKay, W.I., Brigham, W.E., 1984. Effects of temperature on the absolute permeability of consolidated sandstone. Technical Report DOE/SF/11564-3. Stanford University California, Petroleum Research Inst, pp. 43.
Milsch, H., Seibt, A., Spangenberg, E., 2009. Long-term petrophysical investigations on geothermal reservoir rocks at simulated in situ conditions. Transport in Porous Media 77, 59–78.
Morrow, N.R., Brower, K.R., Kilmer, N.H., 1983. Relationships of pore structure to fluid behavior in low permeability gas sands. Final Report, DOE/BC/10216-13 (DE84012721). U.S. Dept. of Energy, Bartlesville, pp. 60–71.
Mortensen, J., Engstrøm, F., Lind, I.L., 1998. The relation among porosity, permeability and specific surface of chalk from the Gorm Field Danish North Sea. SPE Reservoir Evaluation and Engineering 1, 245–251.
Mungan, N., 1965. Permeability reduction through changes in pH and salinity. Journal of Petroleum Technology 17, 1449–1453.
Ochi, J., Vernoux, J-F., 1998. Permeability decrease in sandstone reservoirs by fluid injection. Hydrodynamic and chemical effects. Journal of Hydrology 208, 237–248.
Piwinskii, A.J., Netherton, R., 1977. Permeability of Kayenta Sandstone to hypersaline brine at 10.3 MPa confining pressure and temperatures to 90 °C. In: Conference Proceedings, Third Workshop Geothermal Reservoir Engineering, Stanford University, Stanford CA, USA, p. 5.
Potter, J., Dibble, W., Nur, A., 1981. Effects of temperature and solution composition on the permeability of St. Peters sandstone—role of iron (III). Journal of Petroleum Technology 33, 905–907.
Ramachandran, R., Somasundaran, P., 1986. Effect of temperature on the interfacial properties of silicates. Colloids and Surfaces 21, 355–369.
Rosenbrand, E., Fabricius, I.L., 2012. Effect of hot water injection on sandstone permeability: an analysis of experimental literature. In: SPE Europec/EAGE Annual Conference, Copenhagen, Denmark, p. 11.
Schembre, J.M., Kovscek, A.R., 2005. Mechanism of Formation damage at elevated temperature. Journal of Energy Resources Technology 127, 171–180.
Sharma, M.M., Yen, T.F., 1984. Interfacial electrochemistry of oxide surfaces in oil-bearing sands and sandstones. Journal of Colloid and Interface Science 98, 39–54.
Somerton, W.H., Selim, M.A., 1961. Additional thermal data for porous rocks—thermal expansion and heat of reaction. Old SPE Journal 1, 249–253.
Somerton, W.H., El-Shaarani, A., Mobarak, S., 1974. High temperature behavior of rocks associated with geothermal type reservoirs. In: Presented at SPE California Regional Meeting, p. 16, SPE 4897-MS.
Somerton, W.H., Mathur, A.K., 1976. Effects of temperature and stress on fluid flow and storage capacity of porous rocks. In: Presented at the 17th U. S. Symposium on Rock Mechanics (USRMS), August 1976, Snow Bird, UT, USA, p. 8, SPE 76-0097.
Somerton, W.H., Janah, A.H., Ashqar, P.I., 1981. Thermal expansion of fluid saturated rocks under stress. In: Presented at SPWLA Twenty-second Annual Logging Symposium, June, p. 8, SPE 1991-D.
Somerton, W.H., 1992. Thermal properties and temperature-related behavior of rock/fluid systems. In: Chilingarian, G.V. (Ed.), Developments in Petroleum Science, vol. 37. Elsevier, Amsterdam, p. 257.
Stottlemyre, J.A., 1981. An investigation of temperature sensitivity of Ottawa Sand and Massillon Sandstone intrinsic permeabilities. University of Washington, Seattle, WA, USA, pp. 176 (PhD thesis).
Sydansk, R.D., 1980. Discussion of the effect of temperature and confining pressure on single-phase flow in consolidated rocks. Journal of Petroleum Technology 31, 1051–1059, J. Pet Tech, SPE 9087. In: Cassé, F.J., Ramey, H.J. Jr, 1979. The effect of temperature and confining pressure on single-phase flow in consolidated rocks (includes associated paper 9087).
Tenthorey, E., Scholz, C.H., Aharonov, E., 1998. Precipitation sealing and diagnesis. 1. Experimental results. Journal of Geophysical Research 103, 23951–23967.
Verwey, E.J.W., Overbeek, J.T.G., 1948. Theory of the Stability of Lyophobic Colloids. Elsevier, Amsterdam, pp. 205–209.
Wei, K.K., Morrow, N.R., Brower, K.R., 1986. Effect of fluid, confining pressure, and temperature on absolute permeabilities of low-permeability sandstones. SPE Formation Evaluation 1, 413–423.
Weinbrandt, R.M., Ramey, H.J., 1975. The effect of temperature on relative and absolute permeability of sandstones. Old SPE Journal 15, 376–384.
Wong, L., 1979. Effect of temperature and pressure on absolute permeability and formation resistivity factor of porous rocks. University of California, Berkeley, USA, pp. 68 (MS Research Report).

Geothermics 53 (2015) 225–235

Contents lists available at ScienceDirect

Geothermics

journal homepage: www.elsevier.com/locate/geothermics

Different effects of temperature and salinity on permeability reduction by fines migration in Berea sandstone

Esther Rosenbrand[a,*], Claus Kjøller[b], Jacob Fabricius Riis[a,1], Frans Kets[c], Ida Lykke Fabricius[a]

[a] Department of Civil Engineering, Technical University of Denmark, Kongens Lyngby, Denmark
[b] GEUS Core Laboratory, Geological Survey of Denmark and Greenland, Copenhagen, Denmark
[c] School of Earth and Environment, University of Leeds, Leeds LS29JT, United Kingdom

ARTICLE INFO

Article history:
Received 24 October 2013
Accepted 17 June 2014

Keywords:
Kaolinite mobilisation
Permeability reduction
Berea sandstone
Temperature effect
Heat storage

ABSTRACT

Hot water injection into geothermal aquifers is considered in order to store energy seasonally. Berea sandstone is often used as a reference formation to study mechanisms that affect permeability in reservoir sandstones. Both heating of the pore fluid and reduction of the pore fluid salinity can reduce permeability in Berea sandstone. These effects could be caused by mobilisation of fines by increasing the repulsive electrical double layer forces among sandstone grains and the fines. We investigated the reversibility and the dependence on flow velocity and flow direction of the permeability change by means of flow through experiments and examined thin sections of samples prior to and after tests. A permeability reduction at 20 °C with decreasing salinity was not reversed by restoring the salinity, whereas a permeability reduction due to heating to 80 °C was reversible by restoring the temperature to 20 °C. A reversible permeability increase with increasing flow rate was observed at 80 °C but not at 20 °C. We observed no difference in the distribution of kaolinite clay minerals in thin sections of untested and tested samples. Dissolution of iron bearing carbonates and precipitation of iron hydroxides was observed but no effect on permeability was found. The experimental results suggest that different mechanisms are responsible for permeability reduction depending on temperature and salinity.

1. Introduction

Seasonal storage of excess heat in warm geothermal aquifers is considered in order to make optimal use of available renewable energy resources. During the summer, geothermal water is heated prior to reinjection, raising the aquifer temperature. During the winter, the additional heat can be used for district heating. One concern is that the permeability of the aquifer is reduced by injection of heated brine, because permeability reduction may render geothermal production uneconomical. A literature review of the effect of heating on different sandstone formations indicates that heating causes permeability reduction in sandstone formations containing kaolinite clay particles (Rosenbrand et al., 2014).

Several authors have suggested that mobilisation of colloidal particles, such as kaolinite causes permeability reduction, and that the DLVO (Derjaguin and Landau, 1941; Verwey and Overbeek, 1948) theory can be used to predict particle mobilisation resulting from an increase in the electrical double layer (EDL) repulsion force among particles and the pore walls (Khilar and Fogler, 1984, 1987; Kia et al., 1987; Ochi and Vernoux, 1998; Schembre and Kovscek, 2005). These authors studied Berea sandstone, which is often used as a reference sandstone sample for reservoir rocks because it is relatively homogeneous and readily available (Churcher, 1991).

The permeability of a porous medium is controlled by porosity, pore geometry and the specific surface of the solids that is in contact with the fluid (Kozeny, 1927). An increase in the effective internal surface area is thus linked to a reduction in permeability. Fines are assumed to be initially located on the surface of quartz grains (Khilar and Fogler, 1984, 1987; Kia et al., 1987; Mungan, 1965; Ochi and Vernoux, 1998; Schembre and Kovscek, 2005). Kaolinite particles are flat plates that are typically encountered in small stacks, or booklets, in sandstones (Wilson and Pittman, 1977). When kaolinite is present as booklets, only part of the total kaolinite surface area contributes to the surface area that is effective for permeability.

* Corresponding author. Tel.: +45 45255085; fax: +45 45883282.
E-mail addresses: esro@byg.dtu.dk, estherrosenbrand@gmail.com (E. Rosenbrand), clkj@geus.dk (C. Kjøller), jacobriis84@gmail.com (J.F. Riis), F.B.Kets@leeds.ac.uk (F. Kets), ilfa@byg.dtu.dk (I.L. Fabricius).
[1] Present address: Schlumberger, Drilling & Measurements, Aberdeen, United Kingdom.

http://dx.doi.org/10.1016/j.geothermics.2014.06.004
0375-6505/

Notation

d	grain, m
e	elementary charge, C
k	absolute permeability, mD
k_B	Boltzmann's constant, J/K
q	interstitial flow velocity (Q/A), m/s
t	thickness of Stern layer, m
z	valence, –
A	cross sectional area, m^2
C	concentration of electrolyte, mol/l
E_{EDL}	electrical double layer energy, J
E_{vdW}	van der Waals energy, J
H	Hamaker constant, J
I	ionic strength of electrolyte, mol/l
$Kao_{wt\%}$	mass fraction of kaolinite relative to total sample mass, %
L	sample length, m
N_A	Avogadro's constant, mol^{-1}
P	pressure, Pa
Q	volumetric flow rate, m^3/s
R	radius, m
S_p	specific surface area per unit pore volume (ratio of grain surface area to pore volume), m^2/cm^3
S_s	specific surface area per unit solids volume (ratio of grain surface area to solids volume), m^2/cm^3
T	absolute temperature, K
α	threshold pressure gradient, Pa/m
ε_o	permittivity of vacuum, F/m
ε_r	relative dielectric permittivity of solution, –
κ^{-1}	Debye length, m
μ	dynamic viscosity, Pa s
ϕ	porosity, –
ρ_f	fluid density, kg/m^3
ρ_s	grain density, kg/m^3
σ	charge density, C/m^2
τ	shear yield stress, Pa
ψ	surface potential, V

Therefore fines mobilisation could increase the specific surface area of solids in contact with the fluid and reduce permeability.

The surface charge on kaolinite and on quartz in contact with pore water depends on temperature as well as on pH (Brady et al., 1996; Kia et al., 1987; Rodríguez and Araujo, 2006; Schembre and Kovscek, 2005). Due to the mineral structure, kaolinite particles have different charges on each of the faces and on the edges (Brady et al., 1996; Gupta and Miller, 2010; Gupta et al., 2011; Schofield and Samson, 1954). Berea sandstone pore water obtains a high pH of 8.6–9.5 when saturated with distilled water or NaCl solutions due, to buffering by carbonate cements (Kia et al., 1987). This results in a negative surface potential on quartz and on all sides of kaolinite particles (Gupta and Miller, 2010; Gupta et al., 2011; Kia et al., 1987; Rodríguez and Araujo, 2006; Schembre and Kovscek, 2005). The surface potential attracts oppositely charged ions; some of these may be bound to the surface whereas the others form a diffuse layer, which shields the surface potential (Israelachvili, 2011). According to the DLVO theory, the magnitude of the EDL repulsion between two negatively charged surfaces depends on the separation between the surfaces, the surface potentials, and the diffuse double layer thickness, which can be characterised by the Debye length (Eq. (1)).

$$\kappa^{-1} = \sqrt{\frac{\varepsilon_0 \varepsilon_r k_b T}{2 N_A e^2 I}} \quad (1)$$

where ε_0 is the dielectric permittivity of a vacuum, ε_r is the relative dielectric permittivity of the solution, k_b is the Boltzmann constant, T is temperature, N_A is Avogadro's constant, e is the charge on an electron and I is the ionic strength of the solution, which is the summation of the product of the concentration c and the valence z of all the ions in the solution, i.e. $I = 0.5 \sum c_i z_i^2$.

Reducing salinity reduces I and increases the Debye length (cf. Eq. (1)), which can result in particle mobilisation (Khilar and Fogler, 1984, 1987; Ochi and Vernoux, 1998; Schembre and Kovscek, 2005). Heating on the other hand, reduces the dielectric permittivity of water (Maribo-Mogensen et al., 2013; Michelsen and Mollerup, 2004). This effect exceeds the effect of the increase in T from 293 K to 352 K, and thereby the overall effect of heating is a reduction of the Debye length (Rosenbrand et al., 2014). As a consequence, heating would only increase the EDL repulsion if the surface potential increases as well (Rosenbrand et al., 2014). Electrophoresis measurements of kaolinite and quartz do show that the zeta potentials of kaolinite and quartz becomes more negative with heating (Rodríguez and Araujo, 2006; Schembre and Kovscek, 2005). The zeta potential is the potential on the interface between the fixed and the mobile ions in the EDL, and is often used as an estimate of the surface potential for homogeneously charged particles (Elimelech, 2010). Schembre and Kovscek (2005) modelled an increase in the EDL repulsion between kaolinite and quartz in the Berea sandstone with increasing temperature, and therefore suggested that observed permeability reductions were due to kaolinite mobilisation.

At 20 °C, the permeability reduction due to reducing the salinity was found to be irreversible when the salinity was subsequently restored (Khilar and Fogler, 1984). Therefore, some authors suggest that mobilised fines are subsequently filtered in pore constrictions (Bedrikovetsky and Caruso, 2014; Bedrikovetsky et al., 2011, 2012; Khilar and Fogler, 1984). Contrarily, the permeability reduction due to heating was observed to be reversible when the temperature was restored to room temperature in a number of tests (Baudracco and Aoubouazza, 1995; Cassé and Ramey Jr, 1979; Rosenbrand et al., 2014). This suggests that the particles were not attached in pore constrictions.

Several authors modelled the effects of thermal expansion on porosity and permeability, and found this insufficient to account for observed changes (Baudracco and Aoubouazza, 1995; Rosenbrand et al., 2014). Other authors suggested that heating affects the thickness of the water layers bound to the mineral surface (Cassé and Ramey Jr, 1979). If this, rather than particle mobilisation, caused a permeability reduction with increasing temperature, then reducing the salinity in a heated sample would mobilise particles and cause additional permeability reduction.

Dissolution of siderite (iron carbonate) and precipitation of hematite (iron oxide) was observed when an acid scale inhibitor was injected into siderite bearing sandstones (Hill et al., 2000). This did not affect the permeability in one sandstone formation, and only caused a small permeability reduction in another sandstone formation. The Berea sandstone also contains siderite and ankerite (iron bearing calcium magnesium carbonate), which can dissolve and result in iron oxide or hydroxide precipitation. The alteration of siderite to iron oxide or hydroxide would not be reversed by restoring the temperature to 20 °C, and therefore the effect of siderite dissolution and iron hydroxide precipitation on permeability would not be reversible.

In this paper, we investigate the difference between the effects of pore water salinity and temperature on permeability by means of flow-through experiments. In order to compare results to published data, tests are performed on Berea sandstone samples. The flow rate and salinity were systematically varied at 20 °C and at 80 °C and the reversibility of each effect was tested. Thin sections of the samples were examined before and after the tests to identify

possible changes in the kaolinite distribution and in the mineral composition of the sandstones. DLVO theory was used to estimate the relative effects of changing temperature and salinity on the interaction energy, both between kaolinite and quartz and among kaolinite particles.

2. Materials and methods

Permeability tests were performed on two Berea sandstone plugs (J1 and J2). He-porosity and Klinkenberg permeability (American Petroleum Institute, 1998) were measured prior to tests. Polished thin sections for transmitted light microscopy and for backscatter electron microscopy (BSEM) were made of an untested Berea sandstone sample from the same block and of both plugs after the tests; plugs were sectioned parallel to the sample axis. The grain density of three untested samples from the same block was determined from bulk volume from a combination of Archimedes' test using mercury and He-porosimetry. The specific surface areas of three untested samples from the same block, and of the tested samples, were measured using nitrogen adsorption (BET, Brunauer et al. (1938)). BET measurements were made using a Mircomeritics Gemini 2735 surface area analyser on 2 g of coarsely ground samples. Samples were degassed in nitrogen at 70 °C for 4 h prior to measurement, and adsorption was measured at four relative pressures between 0.05 and 0.24.

Permeability, k, is calculated from the total volumetric flow, Q, using Darcy's law (Eq. (2)),

$$k = \mu \frac{Q}{A} \frac{L}{(P_{in} - P_{out})} \tag{2}$$

where A, is the cross sectional area, P_{in} and P_{out} are the pressures at the inlet and outlet respectively, and L is the sample length. We calculated the viscosity, μ, at the relevant temperature and NaCl concentration using the CREWES Fluid Properties Calculator (2007). This does not reflect possible changes in the fluid composition due to the suspension of fines. The interstitial flow velocity q that is representative for the average flow rate inside the sandstone pores is given by Eq. (3).

$$q = \frac{Q}{\phi A} \tag{3}$$

The plugs were tested using a standard liquid permeability set-up as described in Rosenbrand et al. (2014). Each sample was saturated with 2.0 M NaCl solution and mounted in a Viton sleeve in a Hassler type core holder, which was placed inside an oven to control temperature. Full saturation was verified by an Archimedes' test. A confining pressure of 2.8 MPa was applied. Fluid was injected at a constant flow rate using a high precision Pharmacia P500 piston pump. Pressure was measured at the inlet of the sample using a Druck PDCR 910 transducer connected to a Druck DPI 280 pressure indicator. The outlet pressure was atmospheric.

Fig. 1a shows the test conditions at which permeability was measured. Sample J1 was maintained at 20 °C and the permeability was measured at two or three flow rates for each salinity. Salinity was reduced in the following steps: 2.0; 0.2; 0.02 and 0.002 M NaCl solution, and subsequently increased in corresponding steps. After the final 2.0 M NaCl step, the flow direction was reversed. After the first permeability measurements at 20 °C with 2.0 M NaCl solution, sample J2 was heated to 80 °C with no flow for 48 h. Subsequently, the salinity was reduced and increased as in sample J1. However, as flow rate affected permeability in sample J2, we investigated the hysteresis of the effect of flow rate by repeated cycles in which flow rate was increased and reduced (q = 4–520 μm/s). Fig. 1b shows the maximum and minimum flow velocities in each cycle. The range of flow rates that could be used in sample J1 was limited by the low permeability of the sample after the salinity was reduced (q = 1–58 μm/s). Apart from during the heating and cooling in sample J2, flow was maintained continuously for the duration of both experiments (21 and 153 days). Permeability was measured after the pressure gradient had stabilised. In order to check for gradual permeability changes, a constant flow rate was maintained for 23 days at 0.002 M NaCl concentration in sample J2. Tables listing all permeability measurements and the time at which these were made can be found in the supplementary files.

Darcy's law can be assumed valid as long as the Reynolds number (Eq. (4)) based on mean grain size, d, does not exceed a value between 1 and 10 (Bear, 1972). Using an average quartz grain size of 100 μm for Berea sandstone (Churcher, 1991) the Reynolds number remained below 0.02 in all tests. This indicates that Darcy's law is valid.

$$Re = \frac{\rho_f v_{Darcy} d}{\mu} \tag{4}$$

where v_{darcy} is the Darcy flux ($v_{darcy} = Q/A = q\phi$), and ρ_f is the fluid density.

No fines were observed in the effluent of J1, while the effluent of J2 was cloudy and discoloured, orange/brown, after approximately 100 days. After the effluent had become discoloured, it was discoloured for the remainder of the experiment. As a result of the discolouring, samples of the effluent from tests with 0.02 M NaCl, 0.2 M NaCl, and 2.0 M NaCl were collected at room temperature and stored for 2–5 days, prior to filtering through a 0.2 μm cellulose acetate filter. The filter papers were examined using BSEM and energy dispersive X-ray spectroscopy, EDS. There was insufficient crystalline material hampering mineral identification by X-ray diffraction. Contamination in the experimental set-up is unlikely as initial corrosion tests with a glass bead sample at 80 °C had negative results (Rosenbrand et al., 2014).

3. Results and discussion

3.1. Effective specific surface area

The average value of the BET specific surface area, $S_{S,BET}$, for three untested Berea sandstone samples from the same block is 1.4 m^2/g (Table 1). This is related to the specific surface of the pore space, S_p, by Eq. (5),

$$S_P = S_{S,BET} * \rho_s \frac{1-\phi}{\phi} \tag{5}$$

where ρ_s is the density of the solids. Inserting measured values (Table 1) of an untested Berea sandstone sample in Eq. (5) results in an S_p of 17 m^2/cm^3. The effective specific surface area that affects fluid flow in a homogeneous porous medium can also be estimated using the Kozeny (1927) equation (Eq. (6)):

$$S_p = \sqrt{\frac{c\phi}{k}} \tag{6}$$

where c is a parameter that can be related to porosity and pore geometry and is calculated based on the sample porosity after Mortensen et al. (1998), Eq. (7). For both samples J1 and J2 c is 0.20.

$$c = \left(4\cos\left(\frac{1}{3}\arccos\left(\varphi\frac{8}{\pi^3} - 1\right) + \frac{4}{3}\pi\right) + 4\right)^{-1} \tag{7}$$

At 20 °C and when saturated with 2.0 M NaCl, the effective S_p of sample J1 as calculated from permeability (Table 1) cf. Eq. (6), was only 1.5 m^2/cm^3. The effective S_p was increased to 18 m^2/cm^3 by reducing salinity to 0.002 M NaCl. Considering that the BET of the untested sandstone gave an S_p of 17 m^2/cm^3 (cf. Eq. (5)) this would suggest that prior to fines mobilisation, the surface area of

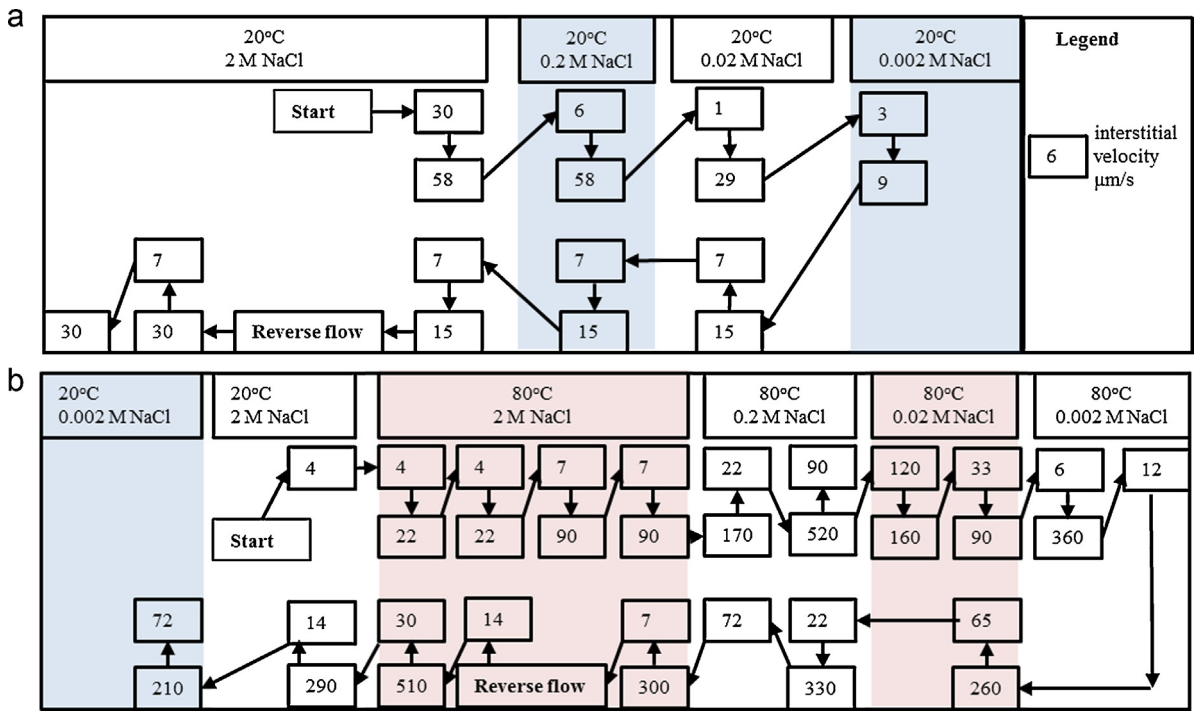

Fig. 1. Experimental procedure on sample J1 (a) and on sample J2 (b). The small boxes indicate interstitial flow velocities in µm/s and the large boxes indicate the temperature and salinity used. Arrows indicate the test sequence. Sample J1 was maintained at 20 °C and salinity was reduced in the following steps: 2.0; 0.2; 0.02 and 0.002 M NaCl solution, and subsequently increased. At 2.0 M NaCl the flow direction was reversed. After the first permeability measurement at 20 °C with 2.0 M NaCl solution, sample J2 was heated to 80 °C with no flow for 48 h. The flow rate was increased and reduced in repeated cycles and only the maximum and minimum flow velocities in each cycle are shown. In between measurements the flow velocity was maintained at the flow rate required for the next permeability measurement. The time interval between measurements for the full test procedure is provided in the supplementary material.

kaolinite was not effective to flow, whereas after fines mobilisation permeability was controlled by the kaolinite surface area. The Kozeny equation (1927) (Eq. (6)) is derived for flow in a homogeneous porous medium with a uniform pore size, where the effective S_p reflects the specific surface area of the grains normalised by the porosity and characterises the effective pore dimension. Therefore, artificial sands made from glass beads could be modelled by using their BET specific surface, but the method was found not to work for different natural sandstone formations including the Berea sandstone (Donaldson et al., 1975).

The Berea sandstone contains kaolinite clay particles that have a high specific surface area compared to the specific surface area of the quartz grains of the sandstone. The total surface area of kaolinite may be estimated from the kaolinite content, $Kao_{wt\%}$, of the Berea sandstone reported in literature, approximately 6–8 wt.% (Churcher, 1991), and the specific surface area of the kaolinite solids, $S_{s,kao}$, which is reported as 5–30 m^2/g (Santamarina et al., 2002). The Berea samples in this study have a porosity of 0.17, and by assuming a kaolinite solids area of 15 m^2/g (Aylmore, 1974), the total kaolinite surface per pore volume, $S_{p,kao}$, is 14–19 m^2/cm^3 (cf. Eq. (8)).

$$S_{p,kao} = \frac{Kao_{wt\%}}{100} S_{s,kao} * \rho_s \frac{(1-\phi)}{\phi} \quad (8)$$

Therefore, the kaolinite area could account for the majority of the surface area measured by BET. Kaolinite clay particles in the untested Berea sandstone can be observed in stacks that are concentrated locally in some pores and not in others (Fig. 2). Small pores have been observed among stacks of kaolinite particles in sandstones (Desbois et al., 2011; Wilson et al., 2014), but when the larger pores among quartz grains form a connected flow path, the larger pores would account for the majority of the flow through the sample. Therefore, at high salinity where kaolinite particles are not mobilised, permeability and the effective specific surface area calculated according to Eq. (6) reflects the specific surface area of the quartz grains, rather than the combined surface area of kaolinite and quartz. Kaolinite mobilisation could increase the surface area of kaolinite that affects flow when kaolinite particles obstruct

Table 1
Permeability and helium porosity of cleaned samples prior to testing. Grain density and BET specific surface area using nitrogen adsorption were determined on three untested samples from the same block. Liquid permeability was measured at 20 °C with 2.0 M NaCl at the start of the tests. BET specific area was measured on the samples tested after the test. Error in brackets is uncertainty on the last digit.

	Klinkenberg gas permeability (mD)	He-porosity[a] (%)	Grain density (g/cm^3)	BET area untested (m^2/g)	Liquid permeability[c] (mD)	BET area after test (m^2/g)
J1	20.6 (8)	17.3	2.670 (3)	1.4 (2)[b]	16	1.524 (3)
J2	15.6 (6)	16.6			8.3	1.418 (3)

[a] Estimated uncertainty 0.1 porosity %.
[b] Error is standard deviation among BET areas on 3 samples from the same block.
[c] Estimated uncertainty 10%: by error propagation of estimated uncertainty on pressure drop, flow rate, and viscosity and measured uncertainty length and area.

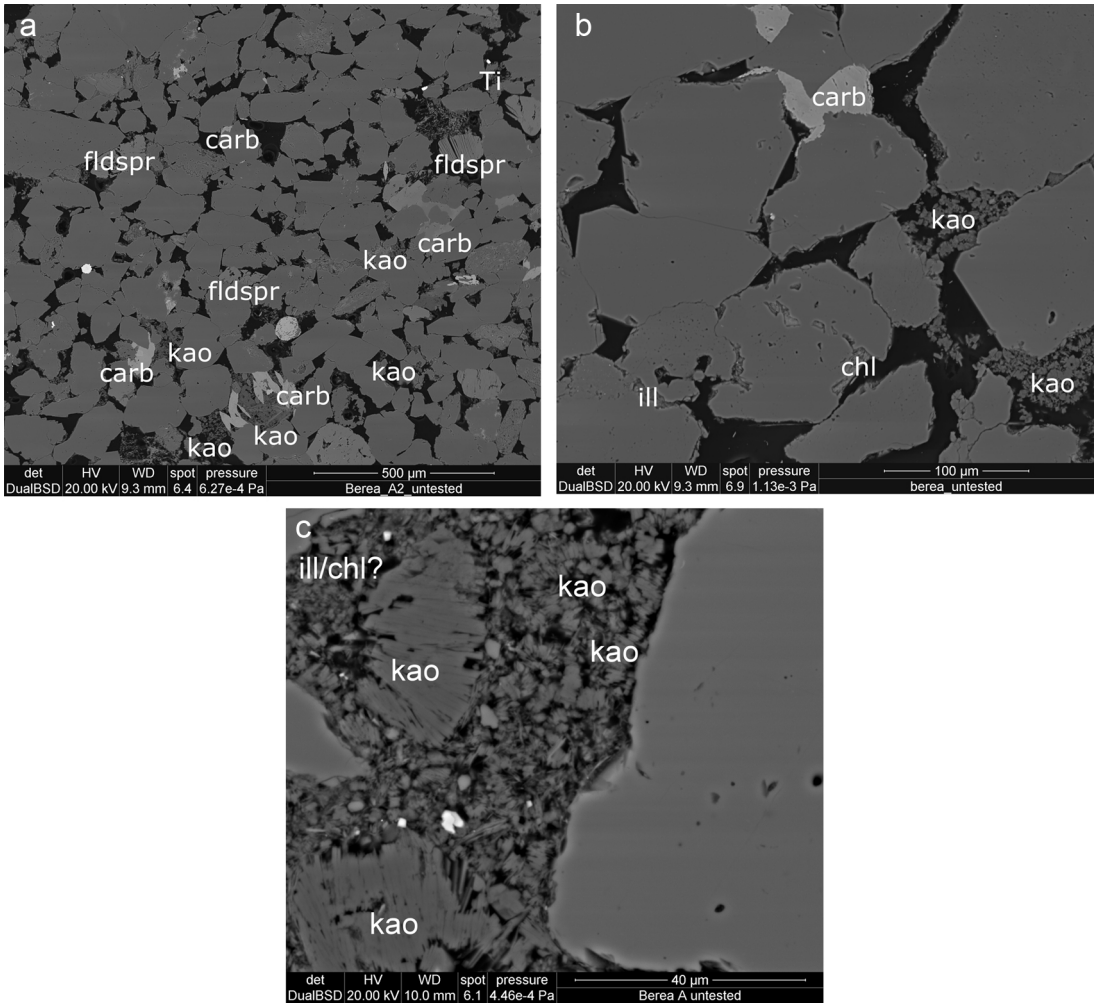

Fig. 2. Backscatter electron microscope (BSEM) images of untested Berea sandstone. Black areas constitute pore space, the grains are mainly quartz with some lighter coloured feldspar (fldspr) and there is lighter coloured carbonate cement (carb). Kaolinite (kao) is concentrated in some pores but not present in other pores (a and b). The flat kaolinite particles have diameters ranging from 1 μm to 30 μm, and these are predominantly observed in stacks (b and c). Some thin needle like particles of other clays illite (ill) or chlorite (chl), and white titanium oxide (Ti) particles are also observed (c).

the connected flow path among quartz grains. Thus, rather than bypassing the pores among kaolinite particles flow would be controlled by pores among kaolinite particles, so that the surface area of kaolinite controls the effective S_p.

3.2. *Effects of salinity, temperature, and flow velocity on permeability*

3.2.1. *Salinity*

Reducing the NaCl concentration in sample J1 at 20 °C reduced permeability and this change was largely irreversible when the NaCl concentration was restored (Fig. 3a). Subsequently, reversing the flow direction at 2.0 M NaCl did partially restore the permeability. Permeability decline due to a salinity reduction, a negligible increase of permeability after salinity restoration, and a partial restoration of permeability with reversing the flow direction are in accordance with results from Khilar and Fogler (1984) on Berea sandstone samples that were saturated with NaCl solution at room temperature.

Several authors attributed the effect of salinity to fines obstructing pore constrictions (Bedrikovetsky and Caruso, 2014; Bedrikovetsky et al., 2011, 2012; Khilar and Fogler, 1984, 1987; Kia et al., 1987; Ochi and Vernoux, 1998). Mechanisms from filtration theory include straining, by particles or particle aggregates that are larger than the pore constrictions, and bridging, by individual small particles that arrive at a pore throat simultaneously (Bedrikovetsky et al., 2011, 2012; McDowell-Boyer et al., 1986). Fig. 2 shows that the size of both pores and kaolinite particles varies. Therefore, both mechanisms could occur. However, due to their greater mass, larger particles may not be mobilised or transported (Bedrikovetsky et al., 2011). Filtered particles would not be remobilised when the EDL repulsion is reduced, which could account for the lack of effect of restoring salinity (Khilar and Fogler, 1984). On the other hand, reversing the flow direction would remove particle bridges from pore constrictions, and thereby restore the permeability if the grains reattach to the pore walls in the pore bodies (Khilar and Fogler, 1984). If the repulsion between kaolinite and quartz prevents reattachment, particles could be filtered at another pore constriction and permeability would not be restored.

Kaolinite has also been observed to form card-house aggregates by interaction among the differently charged faces and edges (Gupta et al., 2011; Schofield and Samson, 1954). In such an aggregate, the total surface area of each plate would contribute to the effective surface, rather than only the edges in a kaolinite stack, and thereby this would reduce the permeability compared to kaolinite booklets. A high effective specific surface area corresponds to a low permeability, and the maximum effective specific surface area was 18 m^2/cm^3 (cf. Eq. (6)) at 0.002 M NaCl at 20 °C, which is

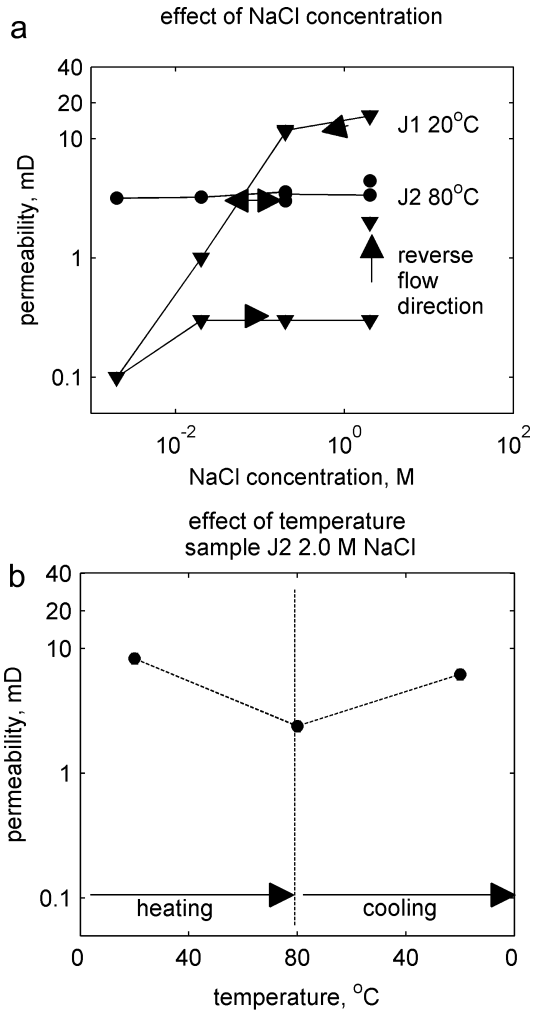

Fig. 3. (a) At 20 °C in sample J1 (black triangles) the permeability falls sharply when the NaCl concentration is reduced below 0.2 M and the effect is largely irreversible when NaCl concentration is subsequently restored. Reversing the flow direction partially restores permeability. At 80 °C in sample J2 (black circles), neither NaCl concentration nor flow direction affects the permeability. Interstitial flow velocity q = 70–95 μm/s for sample J2. (b) Heating caused a reversible permeability reduction in sample J2 with 2.0 M NaCl. Interstitial velocity q = 4–7 μm/s.

comparable to the estimated internal specific surface area of kaolinite (Section 3.1). However, acording to Gupta et al. (2011), above pH 8, both the particle faces and the edges would have a negative surface potential at room temperature. Card-house aggregates are normally observed at a lower pH when the kaolinite edges have a positive surface potential and are attracted to kaolinite faces that have a negative surface potential (Gupta et al., 2011; Schofield and Samson, 1954).

At pH 8–9 in a solution with a low salinity the EDL repulsion among kaolinite particles would prevent aggregation as card houses and particles would be expected to remain in suspension (Gupta et al., 2011; Schofield and Samson, 1954). Nonetheless, some authors observed that kaolinite particles in suspension at pH 8–9 form chains or porous networks in cryo-SEM images (Gupta et al., 2011; Zbik and Frost, 2009). Interaction among kaolinite particles is also reflected by a yield stress below which kaolinite suspensions do not shear (Johnson et al., 1998; Mpofu et al., 2003; Olphen, 1977). In bench top experiments where a kaolinite suspension was allowed to settle in a low salinity solution at pH 8, Zbik and Frost (2009) observed the formation of a gel, i.e. a 3D porous network of particles (Olphen, 1977), on the bottom of the vessel. If such a network were to form in the bottom of the pore bodies of kaolinite bearing pores this would reduce the effective pore volume and thereby reduce permeability. Increasing salinity would reduce the repulsion between kaolinite and quartz, allowing particles to reattach to the pore walls or re-aggregate as booklets and restore permeability. Therefore, it appears less likely that the irreversible salinity effect observed in sample J1 is due to a kaolinite suspension, whereas particle filtration would account for the results.

3.2.2. Temperature

Fig. 3b shows that the permeability was reduced by heating in sample J2 when saturated with 2.0 M NaCl solution. Reducing and restoring the salinity at 80 °C had no effect on permeability (Fig. 3a), but subsequent cooling to 20 °C restored the permeability to 80% of the original permeability at 20 °C. A reversible effect of temperature was also found in Berea sandstone samples that were heated to 80 °C or 90 °C with distilled water, solutions of 0.01–1.0 M NaCl and solutions of 0.004–0.4 M $CaCl_2$ (Baudracco and Aoubouazza, 1995; Rosenbrand et al., 2014). In those studies, 60–100% of the permeability prior to heating was recovered with cooling.

To investigate whether heating reduced permeability by mobilisation of particles or by a different mechanism, the salinity was reduced from 2.0 M to 0.002 M NaCl at 80 °C in sample J2. We observed no additional permeability reduction (Fig. 3a), which suggests that particles were already mobilised as a result of the high temperature. Other authors have reported that salinity reduction reduced the permeability in a sample that was heated to 60 °C (Khilar and Fogler, 1984). However, they did not report whether heating had already reduced permeability, which suggests this was not the case. In a study by Baudracco and Aoubouazza (1995) where permeability was measured at 10 °C increments, the permeability was observed to decrease above a threshold temperature, which varied between 50 °C and 70 °C in tests with distilled water, $CaCl_2$ solution and NaCl solution. Rosenbrand et al. (2014) also observed that the permeability reduction between 50 °C and 80 °C was greater than the reduction between 20 °C and 50 °C using 0.34 NaCl solution (Fig. 3b). This suggests that particles can be mobilised by heating when a threshold temperature is exceeded. If the temperature remained below the threshold temperature, a salinity reduction could mobilise particles and reduce permeability possibly irreversibly.

The reversibility of the heat-induced permeability reduction indicates that mobilised particles were not attached in pore constrictions. One possible cause for the permeability reduction is that particles formed a suspension of interacting particles in kaolinite bearing pores. Presumably the effect of temperature on the surface potential is reversible, whereby cooling would allow the particles to reattach to the pore walls or to re-aggregate in booklets restoring the permeability.

3.2.3. Flow velocity

Ochi and Vernoux (1998) observed that the permeability was reduced at room temperature when a critical flow velocity was exceeded, which they attributed to particle mobilisation by hydrodynamic forces. The critical flow velocity for NaCl solutions in their tests on Berea sandstone samples was one order of magnitude higher than the flow velocities used in the experiment on sample J1 at 20 °C, so accordingly flow velocity did not affect permeability in this experiment. Khilar and Fogler (1984) also found that a flow rate below the critical flow velocity did not affect permeability at room temperature. Ochi and Vernoux (1998) found that above the critical flow velocity, subsequent increases in the flow velocity caused further permeability reduction, which they attributed to mobilisation of additional fines, and the obstruction of additional pore constrictions.

By contrast, increasing the flow velocity increased the permeability in sample J2 at 80 °C, after the permeability had been reduced

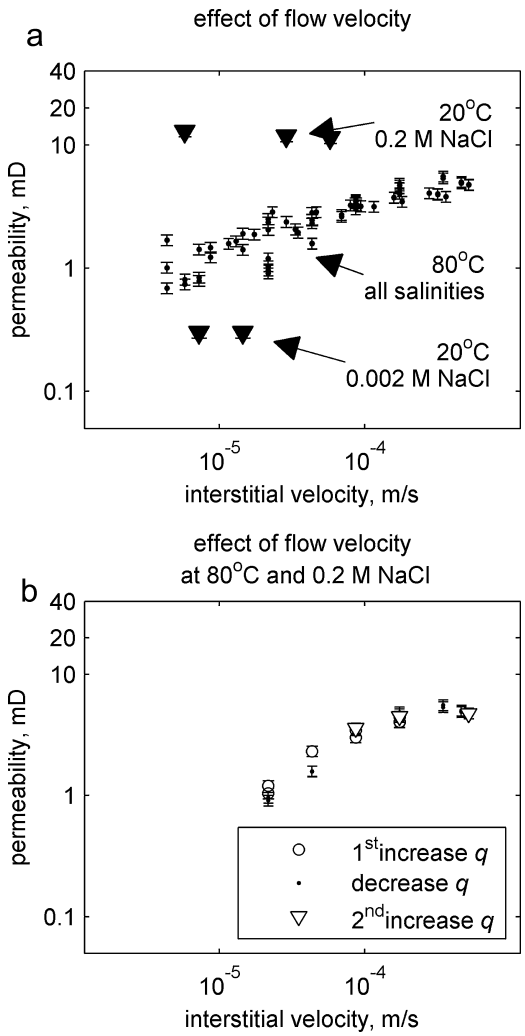

Fig. 4. (a) Increasing the interstitial velocity, q, had no significant effect on permeability at 20 °C in sample J1 neither before nor after the salinity reduction. At 80 °C, the permeability increased with increasing flow velocity independent of salinity in sample J2. (b) At 80 °C, the effect of flow velocity was reversible when the flow velocity is increased, reduced, and increased again.

by heating. No hysteresis was observed in cycles where the flow velocity was increased and reduced (Fig. 4). This indicates that increases in flow velocity did not result in additional obstruction of pore throats, but possibly that a greater pore volume was available for flow at high flow velocities.

Bedrikovetsky et al. (2011, 2012) suggest that increasing the flow velocity would indeed improve permeability as this would reduce particle filtration. They model reversible particle attachment by using a critical retention function, which is based on a mechanical equilibrium of hydrodynamic forces, DLVO forces, and gravitational forces on a particle (Bedrikovetsky et al., 2011, 2012). In this model, an increase in the flow velocity would reduce the maximum concentration of retained particles due to the higher mobilising hydrodynamic forces on particles that are on the grain surface. An increase in the EDL repulsion would reduce the maximum concentration of retained particles, by reducing the net DLVO attraction between particles and the grain surface. This model can predict the effect of flow velocity on permeability when a particle suspension is injected into a rock sample (Bedrikovetsky et al., 2011). At high flow rates, no particle capture takes place, whereas at lower flow rates particles are retained and permeability is reduced. Whereas this would account for the observed flow rate effect in our experiments, this would not account for the observed effect of temperature in sample J2. The higher EDL repulsion due to heating would reduce particle filtration, whereas cooling would increase filtration and thereby reduce permeability. We believe the reason for the different effect of temperature in our experiments is that Bedrikovetsky et al. (2011) model permeability as a function of the concentration of particles that is retained in the sample when external particles are injected, therefore the retained concentration can increase. By contrast, in our tests kaolinite particles were already present in the sandstone pores, the concentration of particles would not increase, and the change in permeability would be due to an alteration of the distribution of particles within the pores.

A kaolinite suspension of interacting particles with a yield stress might account for the effects of temperature, salinity and of flow rate observed at 80 °C. Due to the higher zeta potential at 80 °C than at 20 °C, the higher EDL repulsion among quartz and kaolinite might prevent particles from being filtered in pore constrictions. High flow rates could cause shear, and thereby increase the fraction of the pore volume that is free for fluid flow.

Rheological measurements of concentrated kaolinite suspensions indicate that these have a yield stress that depends on the concentration of kaolinite (Johnson et al., 1998). With 8% kaolinite in a typical Berea sample (Churcher, 1991; Khilar and Fogler, 1987) and a porosity of 0.17 the concentration of kaolinite in the pore volume would exceed 50 wt.% if all kaolinite were mobilised. The heterogeneous distribution of kaolinite in the pore space would result in a higher concentration of suspended particles locally. To estimate whether the flow velocities used in the test on sample J2 at 80 °C could shear a kaolinite suspension, we calculated the threshold pressure gradient α, required to overcome the yield stress, τ, of a Bingham fluid in a cylinder with radius R using Eq. (9) after Pascal (1981).

$$\alpha = \frac{2\tau}{R} \tag{9}$$

A yield stress of 200 Pa was used, as reported by Mpofu et al. (2003), for a 32 wt.% kaolinite suspension at room temperature and pH 10.5 in 0.001 M KNO_3 solution. Heating makes the surface potential more negative (Rodríguez and Araujo, 2006; Schembre and Kovscek, 2005), which would reduce the yield stress (Johnson et al., 1998). However, this effect would be to some degree offset by the lower pH of the pore fluid in the Berea sandstone, which makes the surface potential less negative. For R we used 8 μm, the average pore radius of a Berea sandstone sample from mercury injection by Baudracco and Aoubouazza (1995). This yields a threshold pressure gradient of 1 MPa/m (cf. Eq. (9)). During tests on J2 at 80 °C, the pressure differential over the sample varied between 0.01 MPa to 0.4 MPa, corresponding to an average pressure gradient of 0.2–7 MPa/m, indeed making shear possible. Due to the heterogeneous distribution of both particle concentration in the pores and of the pore size, the yield stress would vary locally. Therefore, successive increases in flow rate would cause shearing of the kaolinite suspension in successively more pores, resulting in the gradual increase in permeability with flow rate observed in Fig. 4.

The reversibility of the effect of flow rate would be observed when shear does not result in removal of kaolinite from the pore bodies. Accordingly no kaolinite was observed in the effluent, and we observed no significant alteration in the distribution of kaolinite in images of the tested sample. Shear might alter the orientation of kaolinite particles within the suspension and thereby reduce the suspension volume and increase the porosity that is effective to flow.

3.3. Sample alteration

BSEM images of the tested samples after experiments did not indicate a change in the distribution of kaolinite. Thus, after test

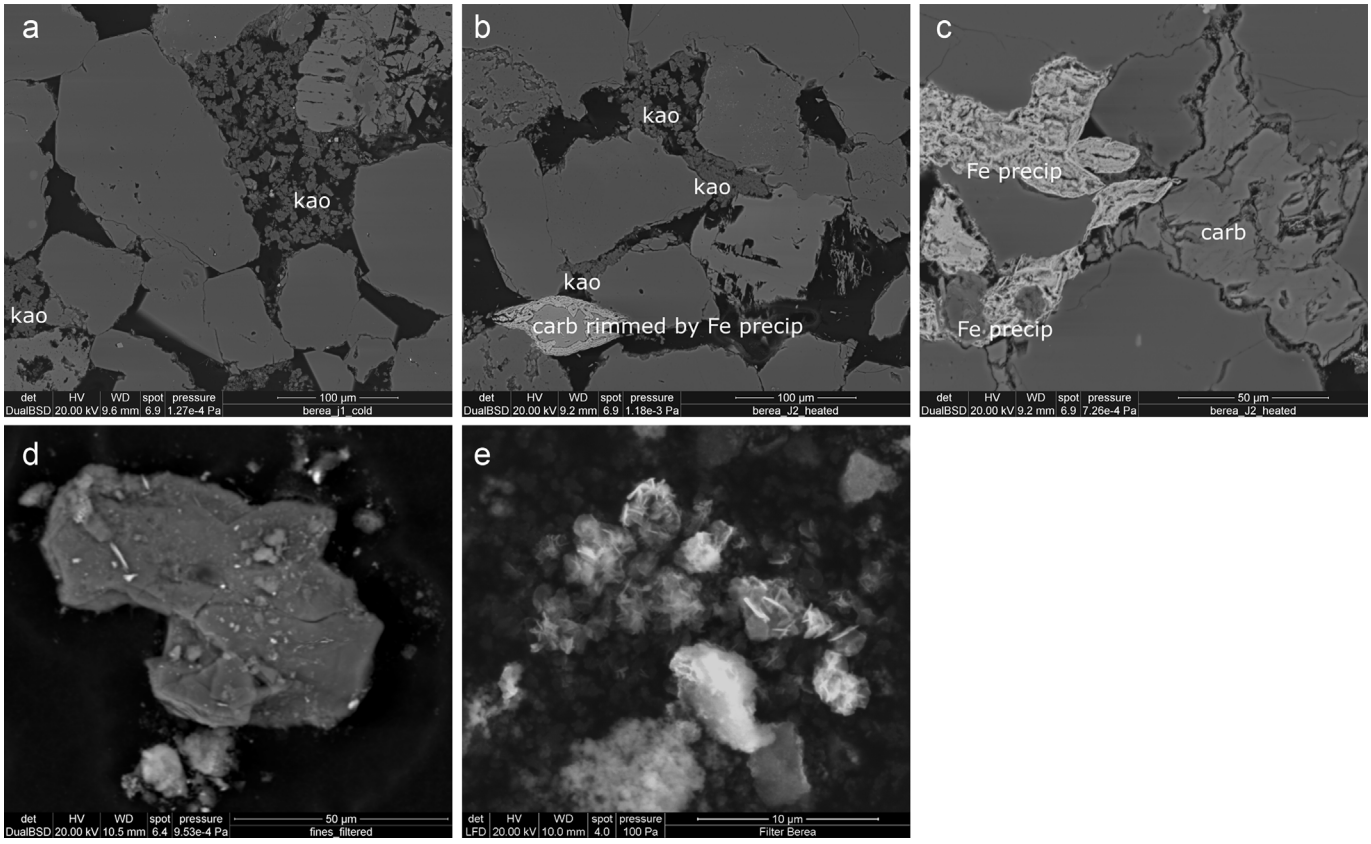

Fig. 5. BSEM images of samples after tests. Kaolinite (kao) is concentrated in some pores and not in others in the tested samples J1 (a) and J2 (b). In sample J2 iron hydroxide precipitates (Fe precip) are found rimming iron bearing carbonates (carb) (b) or in pores adjacent to carbonates (c). The particle remains after filtering the effluent mainly contained iron and silicon. We observed large particles, which also contained some aluminium (d) as well as smaller particles that contain iron and silicon (e).

in both samples J1 and J2 (Fig. 5a and b) kaolinite particles were still observed in some pores and not in others. However, in sample J2 we observed a clear reduction in the amount of iron bearing carbonate cement and the presence of iron hydroxide precipitates. The precipitates were observed rimming, or adjacent to remaining carbonate cement (Fig. 5b and c), suggesting that cement dissolution is the source of the iron. The iron hydroxide precipitation was mainly concentrated in lamina perpendicular to the sample axis, with a spacing of 1–4 mm, and precipitates were observed throughout the sample length. In sample J1 we only observed thin iron hydroxide rims on carbonate minerals in a few locations, most of the carbonate cement appeared unaltered.

We found a permanent 20% permeability reduction in sample J2 after heating and cooling, whereas heating reduced permeability by 50–90% depending on the flow rate. The reversible part of the permeability change would not be due to chemical alteration, this might be due to fines mobilisation into suspension. The irreversible 20% reduction could possibly be due to chemical alteration, but might also be due to a change in effective specific surface area due to redistribution of fines after mobilisation. Hill et al. (2000) reported that dissolution of siderite and precipitation of hematite rims caused no permanent permeability change in one sandstone formation and only a 10–24% permeability reduction in another sandstone formation. Whereas Hill et al. (2000) report precipitation of hematite, an iron oxide, the orange/brown colour of the precipitates observed using transmitted light microscopy in sample J2 suggests that these are goethite, an iron hydroxide. In solutions that are supersaturated with both goethite and hematite at 70 °C, both phases have been observed to precipitate (Hsu and Wang, 1980).

We observed particle aggregates in the remains after filtering the effluent from the tests on J2 (Fig. 5d and e). The elemental composition from EDX mainly reflects the carbon tape on which particles were observed. Particles contained mainly iron and silicon, besides the carbon and oxygen from the carbon tape. Some particles had a diameter larger than 50 μm (Fig. 5d), which suggests these may have aggregated or precipitated outside the sample when the effluent cooled, as the effluent was stored for several days at room temperature prior to filtration. The majority of the particles were smaller than 10 μm and these sometimes appeared in small aggregates (Fig. 5e). With a mean pore throat radius in the order of 8 μm as reported by Baudracco and Aoubouazza (1995) it appears unlikely that 50 μm particles were transported through the sample. We did not observe colloidal iron oxide or hydroxide particles that could have contributed to permeability reduction as mobile fines in the pores of the sandstone, in BSEM images of J2. Small titanium oxide particles were observed, however, these were also present in samples of untested Berea sandstone and in sample J1 (Figs. 1c and 4a).

In order to reduce the oxygen content in the injected brine, Milsch et al. (2009) flushed the brine with nitrogen gas in tests on Rotliegend sandstone. The brine in our tests was only degassed; the sample alteration indicates that degassing alone is insufficient to prevent oxidation of iron bearing carbonate minerals during experiments.

Cooling restored the permeability in sample J2, but subsequent salinity reduction at 20 °C from 2.0 M to 0.002 M NaCl reduced the permeability only from 6.5 mD to 3.0 mD. This effect was smaller than the salinity effect at 20 °C in sample J1 that had not been heated. The difference could be due to removal of kaolinite from the sample by particle transport or dissolution during the test at high temperature. Some authors have observed kaolinite fines in the effluent concurrent with the permeability reduction in tests on

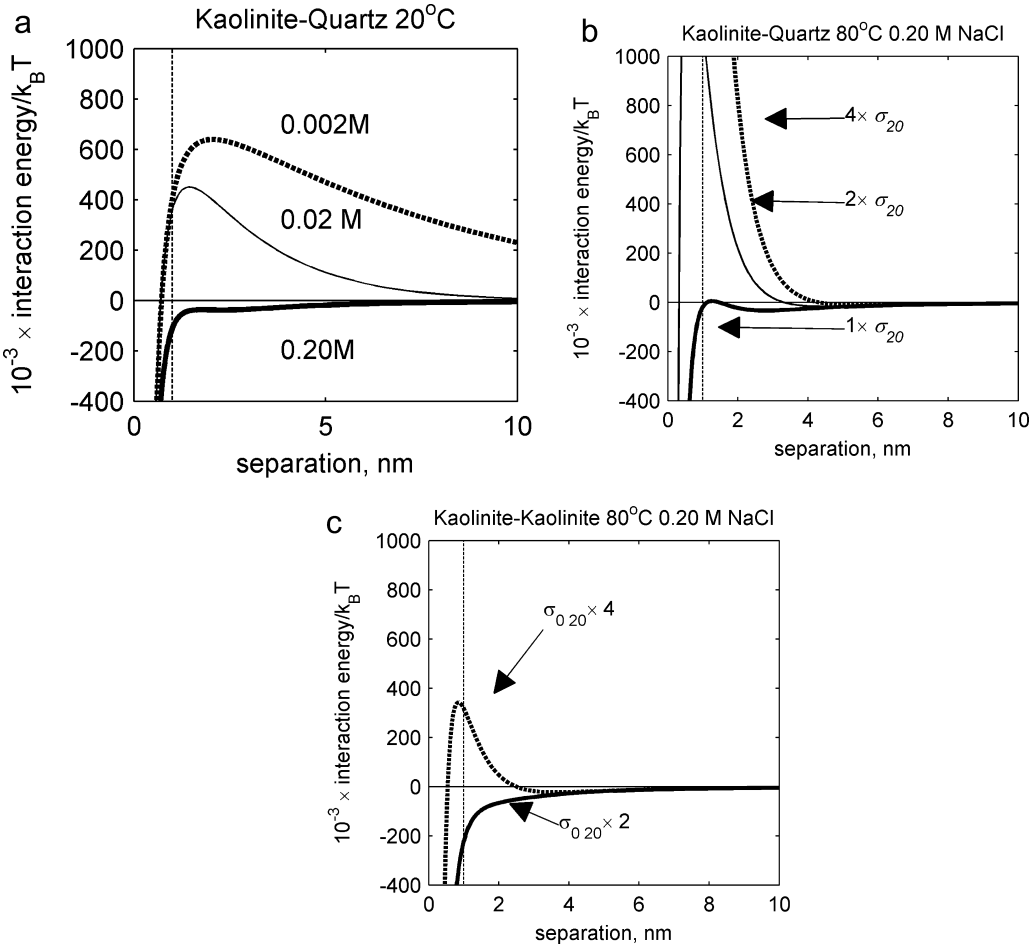

Fig. 6. Interaction energy between kaolinite and quartz as a function of separation: (a) at 20 °C at different NaCl concentrations; (b) at 80 °C and 0.20 M NaCl for cases where heating increases the surface charge of both minerals by a factor of 1, 2, or of 4. (c) Interaction energy among kaolinite particles at 80 °C and 0.2 M NaCl where heating increases the surface charge by a factor of 2 and by a factor of 4. Surface charges at 20 °C, $\sigma_{0,20}$: 12 mC/m^2 for kaolinite; 20 mC/m^2 for quartz. The interaction energies are scaled by the interacting surface area (4 μm^2). Dashed vertical line at 1 nm indicates the expected minimum separation between surfaces due to the adsorbed Stern layer.

some samples but not on other samples (Khilar and Fogler, 1984; Schembre and Kovscek, 2005). We did not observe kaolinite particles in the remains after filtering the effluent through 0.2 μm filters, and at 80 °C we observed no gradual change in permeability that would indicate removal of material. However, we only started to collect the effluent after a brown/orange discoloration of the effluent in sample J2 was observed. Therefore we cannot rule out the possibility that kaolinite was indeed removed from the sample. We observed no qualitative difference in the distribution of kaolinite in BSEM images of an untested and a tested sample, which also suggests that kaolinite was not transported out of the samples. The BET surface area was not reduced due to testing, and rather slightly increased (Table 1), however, this change is only slightly larger than the difference between duplicate measurements, and therefore the difference may not be significant.

The observed difference between the effect of a salinity reduction at 20 °C in sample J1 and in sample J2 after heating and cooling suggests that a permanent change in kaolinite or pore properties reduces the degree of kaolinite mobilisation. The reason for less effect of salinity at 20 °C after the long term experiment is unclear. Some authors suggest that dissolution of calcium bearing carbonate cements would release Ca^{2+} ions that can adsorb to the kaolinite surface and make the zeta potential less negative; thereby reducing the permeability reduction due to fines migration (Kia et al., 1987). However, it is unclear whether the quantity of dissolved carbonate cement would be sufficient to cause this effect.

3.4. Effect of heating and salinity on DLVO forces

In order to evaluate whether filtration or a particle suspension are probable at 20 °C and 80 °C, respectively, we compared the effects of temperature and salinity on the interaction energy profiles between quartz and kaolinite and among kaolinite particles using DLVO theory.

We used the Stern (1924) model for the double layer, accounting for the Stern layer of bound ions on the mineral surface, and the diffuse layer of ions in solution (Lyklema, 1991). The potential, ψ, on the Stern plane separating bound from mobile ions depends on the net charge density σ at the Stern plane, and on the temperature and salinity of the pore fluid according to Grahame's (1947, 1953) relation (Eq. (10)) (Israelachvili, 2011).

$$\sigma = \sqrt{8000 N_A \varepsilon_0 \varepsilon_r k_b T C} \sinh\left(\frac{e\psi}{2k_b T}\right) \quad (10)$$

where C is the concentration of NaCl in moles per litre divided by the standard state (i.e. 1 mol/kg H_2O), e is the charge on an electron, and T is the absolute temperature, and other parameters are as in Eq. (1). The relative dielectric permittivity of the solution was calculated as a function of temperature and salinity (Maribo-Mogensen et al., 2013; Michelsen and Mollerup, 2004). Zeta potentials at room temperature and pH 8 for kaolinite and quartz, by e.g. Johnson et al. (2000), Rodríguez and Araujo (2006) and Zbik and Frost (2009),

were used to estimate a representative σ for these minerals cf. Eq. (10), and by rearranging Eq. (10), ψ was calculated from σ for a given T and C. The EDL interaction energy between parallel plates was calculated using the linear superposition approximation (Gregory, 1975) (Eq. (11)).

$$E_{EDL} = \frac{64,000 N_A C}{\kappa} \tanh\left(\frac{e\psi_1}{4k_bT}\right) \tanh\left(\frac{e\psi_2}{4k_bT}\right) \exp(-\kappa(h-2t)) \quad (11)$$

where t is the distance between the Stern plane and the mineral surface, and h is the separation between the surfaces, and $1/k$ is known as the Debye length Eq. (1), which characterises the distance over which the potential is reduced by a factor $1/e$ (e is the natural logarithm) (Lyklema, 1991). Here Eq. (11) is used as this yields an intermediate solution between assuming a constant potential or a constant charge in the double layer. The potential would be constant if the surface potential immediately equilibrates during particle interactions, which is suggested to be unlikely on the time scale of collisions among suspended particles (Frens and Overbeek, 1972). By contrast constant charge would apply to a surface with a permanent surface charge, whereas the surface charge due to interaction with the pore fluid would be affected by an approaching double layer (Elimelech, 2010).

The van der Waals energy was calculated by Eq. (12) (Israelachvili, 2011):

$$E_{vdW} = \frac{H}{12\pi h} \quad (12)$$

where h is the separation between the plates and H is the Hamaker constant. We assumed $H = 2.26 \times 10^{-20}$ J, and independent of temperature and salinity as also done by Schembre and Kovscek (2005). The Born repulsion term can be included to account for repulsion at short separations (e.g. Schembre and Kovscek (2005)); however, this term was neglected as the adsorbed water in the Stern plane would be expected to limit the closest separation between two particles to approximately 1 nm (Khilar and Fogler, 1984).

The calculated interaction energy between quartz and kaolinite switches from attraction to repulsion between 0.2 M NaCl and 0.02 M NaCl, as indicated by the positive energy barrier at 0.02 M NaCl (Fig. 6a). Accordingly, we observed a sharp permeability reduction when the salinity was reduced from 0.2 to 0.02 M NaCl during tests on J1 (Fig. 3a). Without changing the surface charge density, at 0.2 M NaCl heating would not cause repulsive interaction energy; however, a two-fold increase in the surface charges results in an energy barrier and thereby could cause mobilisation (Fig. 6b). Brady et al. (1996) found an approximate doubling of the average surface charge of kaolinite between 25 °C and 80 °C at pH 8 by using potentiometric titration; for quartz an increase in the zeta potential, by a factor two between 25 °C and 45 °C was observed by Rodríguez and Araujo (2006) at the same pH.

Despite the net DLVO repulsion that caused particle mobilisation, some authors suggest that the mobilised particles could be filtered in pore constrictions (Khilar and Fogler, 1987). For particles to attach in pore constrictions, the hydrodynamic forces that transport particles to the pore constrictions would need to exceed the net DLVO repulsion. Fig. 6a and b show that doubling the surface potential increases the height of the energy barrier between kaolinite and quartz to a greater extent than increasing the EDL thickness by reducing salinity from 0.2 to 0.02 M NaCl. The higher repulsion between kaolinite and quartz would reduce the extent to which kaolinite can attach to quartz pore constrictions, and therefore make a kaolinite suspension more likely. Due to the lower average surface charge density of kaolinite as compared to quartz, the energy barrier between kaolinite surfaces (Fig. 6c) is lower than the energy barrier between kaolinite and quartz surfaces (Fig. 6b). Interactions among suspended kaolinite particles might affect the flow properties of the suspension and reduce the porosity that is effective to flow in kaolinite bearing pores.

4. Conclusion

We performed a sequence of flow through experiments on Berea sandstone samples to investigate the differences between the effect of heating and the effect of salinity change at 20 °C on kaolinite mobilisation and permeability reduction. We observed that (a) a permeability reduction due to heating from 20 °C to 80 °C was largely reversible with cooling; (b) reducing the NaCl concentration from 2.0 M to 0.002 M at 20 °C caused a permeability reduction that was not reversible when the salinity was restored; (c) the NaCl concentration did not affect the permeability at 80 °C; (d) for interstitial velocities between 1 μm/s and 58 μm/s, increasing the flow velocity increased permeability reversibly in a heated sample, but had no effect at 20 °C. Heating to 80 °C for 150 days resulted in dissolution of iron bearing carbonates and precipitation of iron hydroxides; however, this did not significantly affect the permeability.

The reversibility of the temperature effect and the different effects of NaCl concentration and flow rate at 20 °C and at 80 °C suggest that mobilised fines affect permeability by different mechanisms at 20 °C and at 80 °C. Filtration of particles, as suggested by several authors (e.g. Bedrikovetsky and Caruso, 2014; Khilar and Fogler, 1984, 1987), would account for the observations at 20 °C but not at 80 °C. We tentatively suggest that a higher repulsion between kaolinite and quartz at 80 °C could limit filtration; kaolinite particles might remain in suspension in the pore bodies and reduce the pore volume that is effective for flow. The difference is relevant to seasonal geothermal heat storage, because it indicates that the permeability reduction due to injection of hot water during the summer could be offset by increasing the injection flow rate. Furthermore, the permeability of the aquifer may recover when the temperature is reduced during the winter, and the permeability reduction that is observed when salinity is reduced at room temperature might not at 80 °C.

Acknowledgements

This research was funded by the Danish Council, (10-093934) for Strategic Research as part of the HeHo project grant. Thanks are due to Bjørn Maribo-Mogensen, DTU, Chemical Engineering for his computer codes to calculate the dielectric permittivity as a function of temperature and NaCl concentration and to Morten Kanne Sørensen, DTU, Civil Engineering, for BET and grain density data. Hector Ampuero Diaz (DTU Environment) prepared polished thin sections.

Appendix A. Supplementary data

Supplementary material related to this article can be found, in the online version, at doi:10.1016/j.geothermics.2014.06.004.

References

Aylmore, L.A.G., 1974. Gas sorption in clay mineral systems. Clays Clay Miner. 22, 175–183.
Baudracco, J., Aoubouazza, M., 1995. Permeability variations in Berea and Vosges sandstone submitted to cyclic temperature percolation of saline fluids. Geothermics 24, 661–677, http://dx.doi.org/10.1016/0375-6505(95)00027-5.
Bear, J., 1972. Dynamics of Fluids in Porous Media. American Elsevier, New York.
Bedrikovetsky, P., Caruso, N., 2014. Analytical model for fines migration during water injection. Transp. Porous Media 101, 161–189, http://dx.doi.org/10.1007/s11242-013-0238-7.
Bedrikovetsky, P., Siqueira, F.D., Furtado, C.A., Souza, A.L.S., 2011. Modified particle detachment model for colloidal transport in porous media. Transp. Porous Media 86, 353–383, http://dx.doi.org/10.1007/s1142-010-9626-4.
Bedrikovetsky, P., Zeinijahromi, A., Siqueira, F.D., Furtado, C.a., Souza, A.L.S., 2012. Particle detachment under velocity alternation during

suspension transport in porous media. Transp. Porous Media 91, 173–197, http://dx.doi.org/10.1007/s11242-011-9839-1.
Brady, P.V., Cygan, R.T., Nagy, K.L., 1996. Molecular controls on kaolinite surface charge. J. Colloid Interface Sci. 183, 356–364, http://dx.doi.org/10.1006/jcis.1996.0557.
Brunauer, S., Emmett, P.H., Teller, E., 1938. Adsorption of gases in multimolecular layers. J. Am. Chem. Soc. 60, 309–319, http://dx.doi.org/10.1021/ja01269 a023.
Cassé, F.J., Ramey Jr., H.J., 1979. The effect of temperature and confining pressure on single-phase flow in consolidated rocks (includes associated paper 9087). J. Pet. Technol. 31, 1051–1059, http://dx.doi.org/10.2118/5877-PA.
Churcher, P.L., 1991. Rock properties of Berea sandstone, Baker dolomite, and Indiana limestone. In: SPE International Symposium on Oilfield Chemistry, Anaheim, CA, pp. 431–466, http://dx.doi.org/10.2118/21044-MS.
2007. Crewes Properties Calculator [WWW Document], http://www.crewes.org/ResearchLinks/ExplorerPrograms/FlProp/FluidProp.htm (accessed 22.09.12).
Derjaguin, B.V., Landau, L.D., 1941. Theory of the stability of strongly charged lyophobic sols and the adhesion of strongly charged particles in solutions of electrolytes. Acta Physicochim. USSR 14, 633–662, http://dx.doi.org/10.1016/0079-6816(93)90013-L.
Desbois, G., Urai, J.L., Kukla, P.A., Konstanty, J., Baerle, C., 2011. High-resolution 3D fabric and porosity model in a tight gas sandstone reservoir:A new approach to investigate microstructures from mm- to nm-scale combining argon beam cross-sectioning and SEM imaging. J. Pet. Sci. Eng. 78, 243–257, http://dx.doi.org/10.1016/j.petrol.2011.06.004.
Donaldson, C.E., Kendall, F.R., Baker, B.A., Manning, F.S., 1975. Surface-area measurement of geologic materials. Soc. Pet. Eng. J. 15, 111–116, http://dx.doi.org/10.2118/4987-PA.
Elimelech, M., 2010. Particle Deposition and Aggregation: Measurement, Modelling and Simulation. Butterworth-Heinemann, Woburn, MA.
Frens, G., Overbeek, J.T., 1972. Repeptization and theory of electrocratic colloids. J. Colloid Interface Sci. 38, 376, http://dx.doi.org/10.1016/0021-9797(72)90253-6.
Grahame, D.C., 1947. The electrical double layer and the theory of electrocapillarity. Chem. Rev. 41, 441–501, http://dx.doi.org/10.1021/cr60130a002.
Grahame, D.C., 1953. Diffuse double layer theory for electrolytes of unsymmetrical valence types. J. Chem. Phys. 21, 1054–1060, http://dx.doi.org/10.1063/1.1699109.
Gregory, J., 1975. Interaction of unequal double layers at constant charge. J. Colloid Interface Sci. 51, 44–51, http://dx.doi.org/10.1016/0021-9797(75)90081-8.
Gupta, V., Hampton, M.A., Stokes, J.R., Nguyen, A.V., Miller, J.D., 2011. Particle interactions in kaolinite suspensions and corresponding aggregate structures. J. Colloid Interface Sci. 359, 95–103, http://dx.doi.org/10.1016/j.jcis.2011.03. 043.
Gupta, V., Miller, J.D., 2010. Surface force measurements at the basal planes of ordered kaolinite particles. J. Colloid Interface Sci. 344, 362–371, http://dx.doi.org/10.1016/j.jcis.2010.01.012.
Hill, P.I., Graham, G.M., J Dyer, S., Coleman, J.,2000. Iron release following mineral dissolution following scale inhibitor application In a North Alaskan Reservoir. In: SPE International Symposium on Formation Damage Control. Copyright 2000. Society of Petroleum Engineers Inc., Lafayette, LA, p. 7, http://dx.doi.org/10.2118/58727-MS.
Hsu, P.H., Wang, M.K., 1980. Crystallization of goethite and hematite at 70 °C. Soil Sci. Soc. Am. J. 44, 143–149, http://dx.doi.org/10.2136/sssaj1980.03615995004400010030x.
Israelachvili, J.N., 2011. Intermolecular and Surface Forces. Elsevier/Academic Press, Amsterdam, the Netherlands.
Johnson, S.B., Franks, G.V., Scales, P.J., Boger, D.V., Healy, T.W., 2000. Surface chemistry–rheology relationships in concentrated mineral suspensions. Int. J. Miner. Process 58, 267–304, http://dx.doi.org/10.1016/S0301-7516(99)00041-1.
Johnson, S.B., Russell, A.S., Scales, P.J., 1998. Volume fraction effects in shear rheology and electroacoustic studies of concentrated alumina and kaolin suspensions. Colloids Surf. A: Physicochem. Eng. Asp. 141, 119–130, http://dx.doi.org/10.1016/S0927-7757(98)00208-8.
Khilar, K.C., Fogler, H.S., 1984. The existence of a critical salt concentration for particle release. J. Colloid Interface Sci. 101, 214–224, http://dx.doi.org/10.1016/0021-9797(84)90021-3.
Khilar, K.C., Fogler, H.S., 1987. Colloidally induced fines migration in porous media. Rev. Chem. Eng. 4, 41–108.
Kia, S.F., Fogler, H.S., Reed, M.G., 1987. Effect of pH on colloidally induced fines migration. J. Colloid Interface Sci. 118, 158–168, http://dx.doi.org/10.1016/0021-9797(87)90444-9.
Kozeny, J., 1927. Über kapillare Leitung des Wassers im Boden. Sitzungsberichte der Akad. der Wissenschaften Wien. Math. Klasse 136, 271–306.
Lyklema, J., 1991. Fundamentals of Interface and Colloid Science. Academic Press, San Diego, CA.
Maribo-Mogensen, B., Kontogeorgis, G.M., Thomsen, K., 2013. Modeling of dielectric properties of aqueous salt solutions with an equation of state. J. Phys. Chem. B 117, 10523–10533, http://dx.doi.org/10.1021/jp 403375t.
McDowell-Boyer, L.M., Hunt, J.R., Sitar, N., 1986. Particle transport through porous media. Water Resour. Res. 22, 1901–1921.
Michelsen, M.L., Mollerup, J.M., 2004. Thermodynamic Models: Fundamentals & Computational Aspects. Tie-Line Publications, Holte, Danmark.
Milsch, H., Seibt, A., Spangenberg, E., 2009. Long-term petrophysical investigations on geothermal reservoir rocks at simulated in situ conditions. Transp. Porous Media 77, 59–78, http://dx.doi.org/10.1007/s11242-008-9261-5.
Mortensen, J., Engstrøm, F., Lind, I., 1998. The relation among porosity, permeability, and specific surface of chalk from the Gorm Field, Danish North Sea. SPE Reserv. Eval. Eng. 1, 245–251, http://dx.doi.org/10.2118/31062-PA.
Mpofu, P., Addai-Mensah, J., Ralston, J., 2003. Influence of hydrolyzable metal ions on the interfacial chemistry, particle interactions, and dewatering behavior of kaolinite dispersions. J. Colloid Interface Sci. 261, 349–359, http://dx.doi.org/10.1016/S0021-9797(03)00113-9.
Mungan, M., 1965. Permeability reduction through changes in pH and salinity. SPE J. Pet. Technol. 17, 1449–1453, http://dx.doi.org/10.2118/1283-PA.
Ochi, J., Vernoux, J.F., 1998. Permeability decrease in sandstone reservoirs by fluid injection: hydrodynamic and chemical effects. J. Hydrol. 208, 237–248, http://dx.doi.org/10.1016/S0022-1694(98)00169-3.
Olphen, H., 1977. An Introduction to Clay Colloid Chemistry. For Clay Technologists, Geologists, and Soil Scientists, 2nd ed. Wiley, New York, NY.
Pascal, H., 1981. Nonsteady flow through porous media in the presence of a threshold gradient. Acta Mech. 39, 207–224, http://dx.doi.org/10.1007/BF01170343.
Rodríguez, K., Araujo, M., 2006. Temperature and pressure effects on zeta potential values of reservoir minerals. J. Colloid Interface Sci. 300, 788–794, http://dx.doi.org/10.1016/j.jcis.2006.04.030.
Rosenbrand, E., Haugwitz, C., Jacobsen, P.S.M., Kjøller, C., Fabricius, I.L., 2014. The effect of hot water injection on sandstone permeability. Geothermics 50, 155–166.
Santamarina, J.C., Klein, K.A., Wang, Y.H., Prencke, E., 2002. Specific surface: determination and relevance. Can. Geotech. J. 39, 233–241, http://dx.doi.org/10.1139/t01-077.
Schembre, J.M., Kovscek, A.R., 2005. Mechanism of formation damage at elevated temperature. J. Energy Resour. Technol. 127, 171–180, http://dx.doi.org/10.1115/1.1924398.
Schofield, R.K., Samson, H.R., 1954. Flocculation of kaolinite due to the attraction of oppositely charged crystal faces. Discuss. Faraday Soc. 18, 135–145, http://dx.doi.org/10.1039/DF9541800135.
Stern, H.O., 1924. Zur Theorie der Elektrolytischen Doppelschicht. S. f. Electrochem. 30, 508.
Verwey, E.J.W., Overbeek, J.T.G., 1948. Theory of the Stability of Lyophobic Colloids. Elsevier, New York.
Wilson, L., Wilson, M.J., Green, J., Patey, I., 2014. The influence of clay mineralogy on formation damage in North Sea reservoir sandstones: a review with illustrative examples. Earth-Sci. Rev., http://dx.doi.org/10.1016/j.earscirev.2014.03.005.
Wilson, M.D., Pittman, E.D., 1977. Authigenic clays in sandstones; recognition and influence on reservoir properties and paleoenvironmental analysis. J. Sediment. Res. 47, 3–31.
Zbik, M.S., Frost, R.L., 2009. Micro-structure differences in kaolinite suspensions. J. Colloid Interface Sci. 339, 110–116, http://dx.doi.org/10.1016/j.jcis.2009.07.038.

Title ER2903-SS0704

Quantitative image analysis of sandstone mineralogy with application to hot water storage in geothermal aquifers

Authors

Esther Rosenbrand[a], Sven Sindern[b], Ida Lykke Fabricius[a],

Author Affiliations

a Technical University of Denmark, Department of Civil Engineering. Brovej 118, 2800 Kongens Lyngby, Denmark.

b RWTH Aachen University, Institute of Mineralogy and Economic Geology. Wüllnerstr. 2, 52062 Aachen, Germany.

Corresponding author

Esther Rosenbrand:

Mail: esro@byg.dtu.dk

Telephone: +45 4525 1416

Other authors

Ida Lykke Fabricius: ilfa@byg.dtu.dk

Sven Sindern: sindern@rwth-aachen.de

Abstract

Chemical reactions in geothermal aquifers can alter porosity and permeability depending on the mineralogy of the formation. We analysed polished thin sections of sandstones in the electron microscope by using energy dispersive X-ray spectrometry mapped by the QemScan system. By subsectioning images we quantified lamination and we studied spatial correlations among minerals using principal component analysis. In one sample hot NaCl solution had been injected for 150 days. Testing caused oxidation of siderite to iron hydroxides, and lamination on a mm scale became more pronounced in the tested sandstone sample. However, we found no significant effect on porosity and permeability.

Keywords: image analysis, lamination, sandstone, permeability, spatial correlation

Notation

c = parameter relating porosity to permeability and specific surface area, -

k = absolute permeability, L^2, m^2

l_{pix} = pixel length, L, μm

I = interface length per unit area sample, L^{-1}, m/mm^2

I_ϕ = interface length per unit pore area, L^{-1}, m/mm^2

K = parameter relating 2D interface length to 3D surface area, -

S = specific surface area per unit volume of bulk sample, L^{-1} , m^2/cm^3

S_ϕ = specific surface area per unit of pore volume, L^{-1} , m^2/cm^2

ϕ = total porosity, -

ϕ_I = porosity in image, -

41 1. Introduction

42 Energy storage by injecting hot, 150°C, water into warm, 75°C, geothermal aquifers is an option to manage
43 the seasonal imbalance between supply and demand for heat energy in Denmark. Two Triassic-Jurassic
44 formations in the Norwegian-Danish Basin that are currently used for geothermal energy production are
45 considered for hot water injection: the Gassum Formation sandstone and the Bunter Formation sandstone.
46 Injection and storage of hot water into sandstone aquifers could alter the petrophysical properties, porosity
47 and permeability, by mineral dissolution or precipitation (Milsch et al., 2008; Schepers and Milsch, 2013;
48 Sydansk, 1982; Tenthorey et al., 1998). Additionally, studies of sandstones that contain kaolinite show that
49 increasing the temperature reduces permeability, probably due to fines migration (Khilar and Fogler, 1987;
50 Rosenbrand et al., 2014; Schembre and Kovscek, 2005).

51 Image analysis can be used to investigate the effect of hot water injection on sandstone mineralogy and
52 permeability, and several authors use backscatter electron microscopy (BSEM) images to model
53 permeability, (Berryman and Blair, 1987; Blair et al., 1996; Borre et al., 1995; Solymar and Fabricius, 1999).
54 Some authors combine BSEM with energy dispersive X-ray spectroscopy (EDS), in order to determine the
55 mineralogy of the samples as well as the reactive surface areas of different minerals (Landrot et al., 2012;
56 Peters, 2009). In order to quantify alterations in mineralogy and permeability and to relate these to the
57 quantities measured during laboratory experiments on core samples the interrogation area used during image
58 analysis must be sufficiently large.

59 A minimum representative area (MRA) can be estimated by increasing the investigated area until a particular
60 property, stabilises as a function of the investigation area (Bear, 1972; Landrot et al., 2012; Solymar and
61 Fabricius, 1999). Some authors determine an MRA for quartz, the dominant mineral in sandstone, and use
62 this area to quantify accessible surface areas of other minerals (Landrot et al., 2012) . However,
63 heterogeneously distributed minerals, such as carbonate minerals and anhydrite would have a larger MRA
64 than more homogeneously distributed minerals. Heterogeneity in the form of lamination on a scale of
65 millimetres was observed in some sandstone formations including the Berea Formation (Knackstedt et al.,
66 2001). In order to model core scale permeability, image analysis would require an interrogation area that
67 exceeds the size of individual lamina.

68 The QemScan automatic scanning electron microscopy system was developed in order to analyse a large
69 interrogation area within a limited time. Samples are scanned over a raster and pixels are identified as
70 different minerals based on their BSEM intensity and EDS spectra (Ayling et al., 2012; Pirrie et al., 2004).
71 This allows quantification of MRA for all minerals in a sample, and generates data for statistical image
72 analysis.

In this study, we used image analysis of QemScan data to compare mineralogy and permeability of three untested sandstone samples, and one tested sandstone sample. The untested samples include: 1) a sample from the Berea Formation sandstone; 2) a sample from the Gassum Formation sandstone; 3) a sample from the Bunter Formation sandstone. The fourth sample is a sample of Berea sandstone after hot water had been injected for 150 days (Rosenbrand et al., under review). We quantified: mineralogy, total pore-mineral interface length and reactive surface area for different minerals. We estimated MRA for different minerals and confidence intervals on mineralogy in order to compare mineralogy among images. Lamination was investigated by means of subsectioning images parallel to the lamination. Statistical image analysis including principal component analysis, PCA, was used to quantify correlations among minerals within lamina of each sample as well as to distinguish the mineralogy among different formations, and to distinguish between the tested and untested samples. The effect of lamination on permeability was estimated using Kozeny's (1927) equation.

2.1 Sandstone samples

Four sandstone samples were included in this study, two samples (Gassum 7V and Bunter 2T) from the Norwegian-Danish Basin, and two samples of Berea sandstone from the Cleveland Quarries (Amherst, Ohio, USA). The sample from the Gassum Formation sandstone is dominated by quartz and has only a small amount of clay minerals. The samples from the Berea sandstone are dominated by quartz and contain kaolinite clay minerals as well as iron bearing carbonate minerals (Khilar and Fogler, 1987). The sample from the Bunter Formation sandstone has a relatively higher feldspar content as well as iron oxides or hydroxides, chlorite and illite clay minerals, carbonate minerals, and anhydrite. Plug samples of Gassum sandstone and Bunter sandstone were cut from reservoir cores with burial depths of 1560 m and 1655 m and cleaned by Soxhlet extraction with methanol and toluene prior to preparation. The Berea sandstone plugs were clean. Sample Berea A1 is one half of a plug that had been sectioned perpendicular to the sample axis. Sample Berea J2 is a full length plug, which had been tested by placing it in an oven at 80°C and injecting 80°C NaCl solution for 150 days (Rosenbrand et al., under review).

He-porosity and nitrogen gas permeability were measured on plug samples according to the Klinkenberg procedure (API, 1998; Klinkenberg, 1941). Subsequently, plug samples Berea A1 and Berea J2 were sectioned vertically, parallel to the plug axis, to prepare polished thin sections. Vertical side trims of plug samples from the Gassum and Bunter sandstone were used to prepare polished thin sections Gassum 7V and Bunter 2T. Specific surface area from nitrogen adsorption (BET, Brunauer et al. (1938)) was measured on 2 g of the crushed samples, which were degassed for four hours at 70°C.

2.2 Image acquisition

Images were acquired using a Quanta650F (FEI) scanning electron microscope using a beam intensity of 15kV and a working distance of 13mm. EDS spectra were detected with a Bruker Dual X-Flash5030 Detector. On each sample a 100 mm^2 area was scanned using BSEM and EDS in a raster with a pixel length, l_{pix}, 1.8 µm acquiring 2000 EDS counts per pixel. Subsequently the same area was scanned with l_{pix} 0.8 µm using only BSEM. Due to the larger interaction volume of the electron beam for the generation of fluorescence light a pixel length l_{pix} of 1.8 µm was chosen for EDS work, while the lower pixel length was appropriate for BSEM. Prior to scanning, calibration of the BSE detector was done using quartz, copper, and gold standards.

2.3 Mineral classification

The automatic identification of pore space and mineral phases is based on parameters, such as BSE intensity, X-ray count rate as well as X-ray energy and intensity derived from EDS spectra, which are defined in the species identification protocol (SIP) of the QemScan iDiscover (v.5.3) software (Ayling et al., 2012; Pirrie et al., 2004). The BSE intensity is an indication of the density of the specimen interacting with beam electrons; the density of the epoxy filling in the pore space is lower than the mineral density, therefore the pore space is black in BSEM images whereas minerals with a high density have a high grey level intensity. The software classifies pixels that fall below a user-defined threshold grey level intensity as pore pixels; subsequently mineral pixels are classified based on the elemental compositions from EDS spectra. For this study the SIP was prepared based on the *oil and gas v3.7* SIP (by FEI) in which additional categories were defined in order to account for interfering element information along grain boundaries and fine-grained minerals in the range of the spatial resolution, e.g., some iron oxide/hydroxide precipitates that had formed during heating in Berea J2 apparently contained silicium, which could be due to interaction of the electron beam with the underlying quartz grains. Several minerals were grouped for further analysis: illite and muscovite (IM); chlorite group minerals, mixed layer chlorite-smectite and biotite (CMB); dolomite and ankerite (DA); gypsum and anhydrite (GA); iron oxide/hydroxide; and titanium oxides. Feldspar minerals were also considered as one group.

Pixels may contain a combination of minerals when the pixel is on the boundary between two mineral grains. Therefore the SIP contains boundary categories, e.g. 25% quartz 75% kaolinite that were used for identification and subsequently these pixels were assigned to the mineral or group with the highest percentage contribution. However, not all possible interfaces were defined therefore some individual pixels remained unidentified. A pre-processing operation was performed whereby single unidentified pixels were assigned to the same mineral group as the neighbouring pixels. This was only applied to single unidentified pixels, pixels that were identified as a mineral or as porosity were unaffected.

3. Image analysis

Image analysis was performed on .tiff images exported from the QemScan software in which the pores and different minerals have distinct colours as classified by the SIP. Image analysis is done using Matlab 2012b (The MathWorks, USA).

3.1 Mineral content

Mineral content was determined by summing the number of pixels of a given colour. The fraction of an area occupied by a specific phase corresponds to the fraction of a volume occupied by this component, the Delesse principle. In order to estimate an error margin for variation within the sample, we used twice the standard deviation that was calculated from the mineral content in the four 25 mm^2 quarters of the image. The MRA were found by plotting mineral content as a function of increasing interrogation area, based on the representative elementary volume concept in Bear (1972).

3.2 Interface length

The interface length between the pores and minerals in a unit area, I_ϕ, was quantified based on the number of edges between porosity pixels and mineral pixels. Interface pixels were identified by subtracting the image that was shifted by one pixel from the original image; nonzero values indicate pixels that are on the interface between two phases. Multiplication by a mask of the porosity resulted in an image with only the interface between porosity pixels and minerals. This was done for four directions to identify four possible edges for each pixel. As in Borre et al. (1995) pixels on a diagonal interface, which have two connected edges that are part of the interface, were assigned a length $l_{pix}\sqrt{2}$ rather than $2l_{pix}$; similarly pixels with three interface edges would correspond to two diagonal boundaries, (i.e., in the cleavage planes of mica grains) and these were assigned a length $2l_{pix}\sqrt{2}$. Pixels with one and with four interface edges were assigned l_{pix} and $4l_{pix}$, and pixels with two interface edges on opposite sides of the pixel were assigned $2l_{pix}$. In some previous studies isolated pixels are neglected (Borre et al., 1995; Peters, 2009), however, with l_{pix} 1.8μm, single porosity pixels could contribute to flow and to reactive surface. Single pixels of minerals such as iron oxide/hydroxide pixels in the cleavage planes of micas would correspond to petrographic observations of the Bunter sandstone formation (Weibel et al., 2010). The interface length for different minerals was calculated in the same manner replacing the porosity mask with the mask of the desired mineral.

3.3 Heterogeneity: lamination and patches

Heterogeneity on the pore scale can be due to patchy distribution of minerals such as carbonates and anhydrite (Weibel et al., 2010), or to lamination (Knackstedt et al., 2001). Heterogeneity was quantified by calculating mineral content and I for subsections of the image. For lamination, the sample was divided into

thirty eight, 270 μm wide subsections that span the length (10300 μm) of the scanned area. This was done in the vertical and in the horizontal direction. The width of 270 μm is slightly larger than the size of the largest pores that were observed in studies using micro computed tomography in Berea sandstone (Bera et al., 2011; Peng et al., 2012). For heterogeneity due to patchy mineral formation, square subsections of the same area as the vertical and horizontal subsections were used, giving thirty six squares with a length of 1700 μm.

3.4 Multivariate analysis

The mineral composition of the subsections was expressed by 12 variables, i.e. porosity and 11 mineral groups. For each sample we calculated the correlation coefficient matrix based on the mineralogy of the thirty eight horizontal and the thirty six square subsections. In order to analyse correlations among groups of minerals, and differences among different sandstone formations and differences between tested and untested sandstone samples we used PCA by singular value decomposition of the centred normalised data. Centring reduces the mean square error (Miranda et al., 2008) , and without normalisation the results would be dominated by the volumetrically abundant phases quartz, feldspar and porosity only. The original variables were scaled by the loadings from PCA to obtain the principal component scores. The first principal component contains most variance; the subsequent PC's are orthogonal and account for successively less variance.

4. Permeability from images

Permeability can be estimated from porosity,ϕ, and specific surface area between solids and pores normalised by the pore volume, S_ϕ, according to the Kozeny (1927) equation:

$$k = \frac{c\phi}{S_\phi^2}$$

Eq. (1)

where c can be expressed as a function of porosity in Eq. (2) (Mortensen et al., 1998) .

$$c = \left(4cos\left(\frac{1}{3}arccos\left(\phi\frac{8}{\pi^3} - 1\right) + \frac{4}{3}\pi\right) + 4\right)^{-1}$$

Eq. (2)

In order to relate the 2D interface of a phase I to the 3D surface of this phase Eq. (3) is often used, where $K = 4/\pi$ (Peters, 2009; Solymar and Fabricius, 1999; Weibel, 1989).

$$S = KI$$

Eq. (3)

Equation 3 is strictly valid only for perfect spheres (Solymar and Fabricius, 1999). Based on 2D pore sizes from BSEM images and 3D sizes from computed micro-tomography (CMT), Crandell et al.(2012) found a value of $K = 2.11$ for a sediment packed column. Those authors corrected for the higher resolution of BSEM images by removing pores below the CMT resolution and adapting the porosity thresholds so that both methods gave the same porosity. We estimated permeability from images using Eq.(1-3) for different values of K.

In order to investigate the effect of heterogeneity on permeability, permeability was calculated for vertical, horizontal and square subsections of the image, and the harmonic and arithmetic averages were used to determine minimum and maximum permeabilities for the sample. Permeability was calculated for images with l_{pix} 1.8 μm and for images with l_{pix} 0.8 μm.

5. Results

5.1 Mineral abundance

Quartz is the dominant mineral in all four samples comprising over 60% of the area in the Berea samples and in Gassum 7V and over 34% in Bunter 2T. Pore area is the second most abundant in all samples followed by feldspars. These three phases contribute to over 90% of the sample area in the Berea samples and Gassum 7V, whereas Bunter 2T contains a larger amount of carbonate and clay minerals. In the three untested samples, the estimated error relative to the total image area is highest for quartz, however, relative to the quartz content, the error on the quartz content is low (Table 1). By contrast the error for less abundant phases with a patchy occurrence, such as gypsum/anhydrite in Bunter 2T or Gassum 7V is larger than the amount of gypsum/anhydrite in the image.

Table 1: Sample composition, error estimate is twice the standard deviation of four 25 mm^2 square subsections of the samples.

Mineral/mineral group	Gassum 7V % of total area (error)	Bunter 2T % of total area (error)	Berea A1 % of total area (error)	Berea J2 % of total area (error)	Difference Berea J2-Berea A1
Pores	26.0 (2)	25.2 (5)	14.3 (3)	14.3 (1.4)	0.0
Quartz	62.2 (6)	34.0 (11)	70.78 (10)	71.4 (6)	0.7
Feldspar	7.1 (4)	24.38 (97)	6.0 (6)	5.3 (6)	-0.7
Calcite	0.015 (9)	4.9 (3)	0.008 (3)	0.0035 (8)	-0.005
Siderite	0.016 (7)	0.23 (3)	0.85 (13)	0.16 (2)	-0.69
Dolomite/Ankerite	0.00024 (14)	0.31 (8)	0.4 (2)	0.31 (14)	-0.08
Kaolin	1.2 (2)	0.0026 (10)	2.9 (4)	2.4 (4)	-0.5
Illite/Muscovite	2.1 (3)	3.7 (6)	2.7 (3)	2.4 (3)	-0.3
Chlorite/Mixed illite-chlorite/Biotite	0.92 (11)	6.1 (4)	1.57 (4)	1.9 (2)	0.3
Iron oxide/hydroxide (Fe_2O_3/FeOOH)	0.09 (4)	0.68 (9)	0.12 (4)	1.13 (11)	1.01
Titanium oxides	0.257 (9)	0.13 (2)	0.27 (10)	0.5 (2)	0.2
Gypsum/Anhydrite	0.0012 (14)	0.3 (5)	0.00011 (32)	0	-0.00011

5.2 Minimum representative area

The MRA for porosity for the untested sandstone samples is shown in Figure 1. The MRA is approximately 20-30 mm^2 for Bunter 2T and for Berea A1, and 10-15 mm^2 for Gassum 7V. The smaller MRA of Gassum 7V could be due to the smaller grain size in the Gassum sandstone. Figure 2a shows the MRA for porosity for the tested Berea J2, porosity appears to stabilise between 8 mm^2 and 20 mm^2 but subsequently increases as the interrogation size is increased. A lamination of the porosity in the sample can be observed in a binary image of the porosity (Figure 2b).

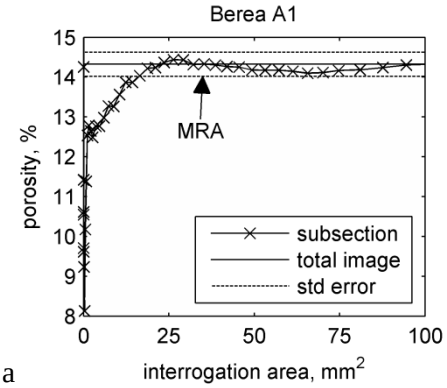

a

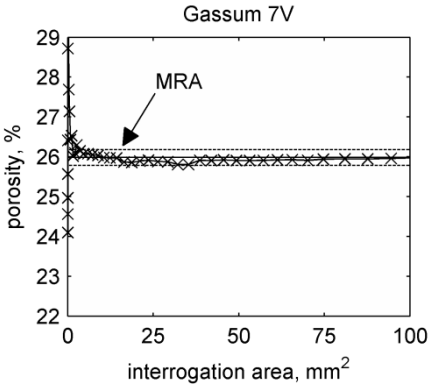

b

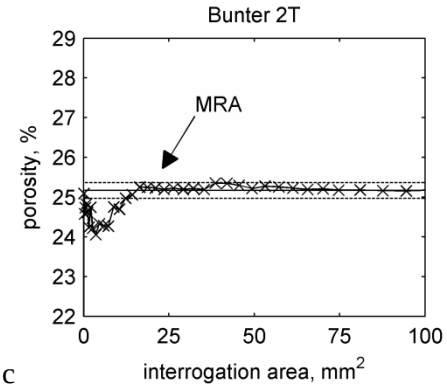

c

Figure 1: Porosity as a function of interrogation area in a subsection of the untested sandstone samples. The minimum representative area (MRA) is less than half the total area of investigation (100 mm^2).

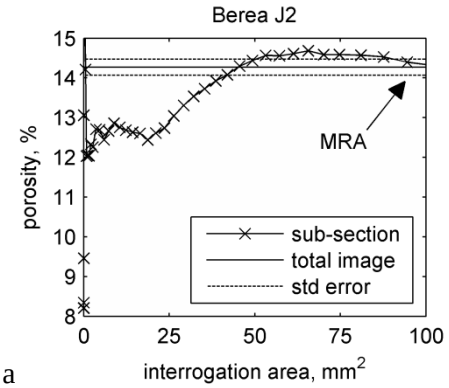

a

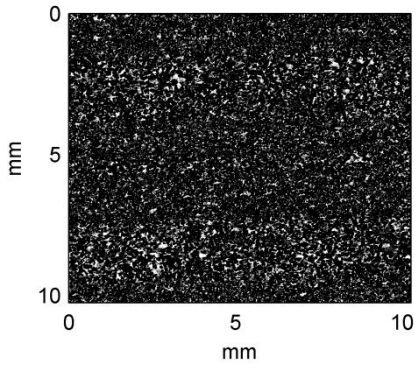

b

Figure 2: a) Porosity as a function of interrogation area in subsection of the tested Berea sample J2. A plateau is reached at 8 mm^2 but porosity then rises when the area is increased above 25 mm^2 resulting in a minimum representative area, MRA, that is approximately the size of the total image (100 mm^2). b) Binary image showing horizontal lamination at a scale of 2 mm in sample Berea J2, white is pores, black is minerals.

The MRA for the rock-forming minerals quartz and feldspar approximately are only 10 mm^2 for quartz and 20 mm^2 for feldspar in Gassum 7V, as compared to approximately 20 mm^2 for quartz and 75 mm^2 for feldspar in Berea A1, and approximately 60 mm^2 for both quartz and feldspar Bunter 2T. Despite differences, these MRA are clearly less than 100 mm^2. In contrast, elevated MRA values are observed for less abundant phases with a patchy occurrence (Figure 3a). The MRA for gypsum/anhydrite in Bunter 2T is larger than 100 mm^2 (Figure 3b). Minerals with a large MRA relative to the mineral content include calcite and dolomite/ankerite in Gassum 7V and in Berea A1, the MRA of calcite in Berea A1 is in the order of 75mm^2 (Figure 3c). In Berea J2 the MRA for feldspar is similar to the value of feldspar in Berea A1, 75 mm^2, whereas the MRA for quartz is higher in Berea J2 than in Berea A1, approximately 60 mm^2.

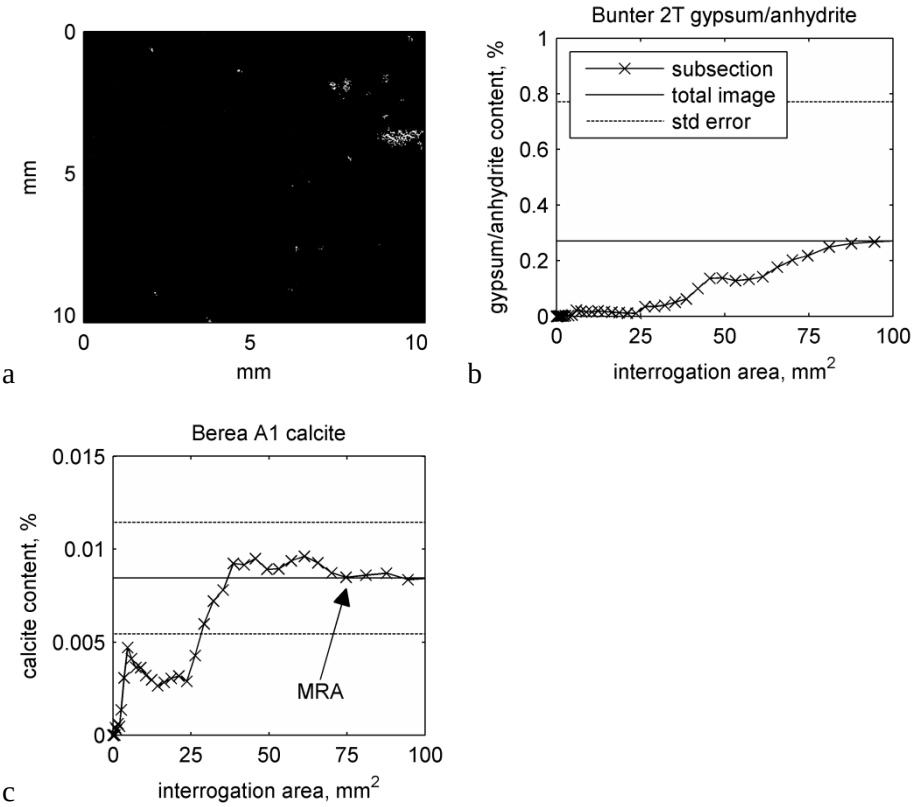

Figure 3: a) Binary image showing gypsum/anhydrite distributed in patches in sample Bunter 2T, white is gypsum/anhydrite black is other minerals and pores b) The minimum representative area (MRA) of gypsum/anhydrite in sample Bunter 2T exceeds the image size (100 mm^2), the error estimated from 25 mm^2 subsections yields error margins between 0 and 0.8% for anhydrite content c) The MRA of calcite in untested sample Berea A1is approximately 75 mm^2.

5.3 Lamination

Figure 4 shows variations in the mineralogy for horizontal sections in the untested Berea A1 and the tested Berea J2. In Berea J2, porosity shows two peaks at 2 μm and 8 μm that coincide with peaks in the feldspar content and the kaolinite content and troughs in the iron oxide/hydroxide and the quartz content. Troughs in the porosity correspond with peaks in the quartz and the iron oxide/hydroxide content. The range of porosities in the sections of Berea A1 is smaller (e.g. 12%-17% for 270 μm wide and 10300 μm long sections) than for Berea J2 (10%-19%). The more pronounced variation of mineral abundance and porosity is considered to show a lamination that is optically visible in the distribution of pores (Fig. 2b). The interface length of the quartz phase scaled by the quartz area, which is an estimate of the quartz grain size, also shows a more pronounced lamination in Berea J2 than in Berea A1. Lamination of the mineral abundance is also reflected in a higher variance of the mineral content in the subsections of Berea J2 (Table S1). The variance of the iron oxide/hydroxide content is 140 times larger and the variance of porosity is six times larger in Berea J2 than in Berea A1. The variance of porosity in Gassum 7V and in Bunter 2T is smaller than in Berea J2, these samples show no indication of lamination. Variance for all minerals is included in Table S1 of the supplementary material.

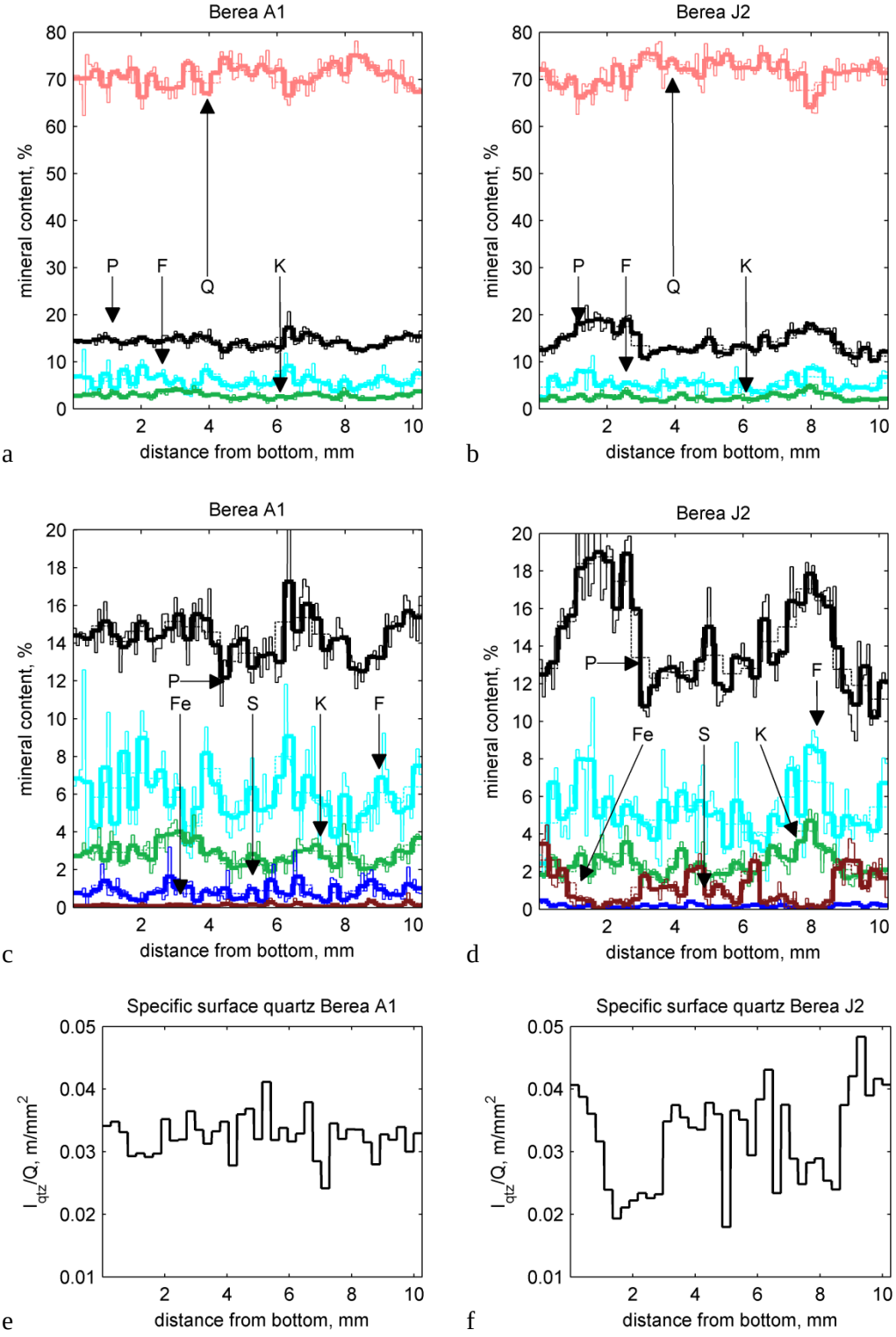

Figure 4: The fluctuations in the mineral content as a function of distance from the bottom of the image for horizontal subsections (width 270 μm, length 10300 μm) of the untested sample Berea A1(a and c); and tested sample Berea J2 (b and d) show a greater variability in tested sample Berea J2. In particular porosity and iron oxide/hydroxide is laminated. The variation in the interface length of the quartz phase scaled by the quartz area (I_{qtz}/Q), which is an estimate of the quartz grain size is higher in sample J2 (f) than in sample Berea A1 (e). (P=porosity; Q=quartz; F=feldspar; K=kaolin; S=siderite; Fe= Fe_2O_3/FeOOH.)

5.4 Multivariate analysis

Table 2 shows correlations with a correlation coefficient larger than 0.65 between minerals in the 270 μm wide horizontal subsections for the four sandstones. For the untested Gassum 7V and Bunter 2T, correlation coefficients for square and for horizontal subsections are comparable, which indicates that there was no distinct lamination. In the tested Berea J2 there are higher correlation coefficients between minerals in horizontal subsections than in square subsections, indicating that there is horizontal lamination in this sample. All four samples have a negative correlation coefficient for feldspar and quartz. As there is a limited area, these variables are not independent, and a negative correlation between rock forming minerals would be expected. In the untested Berea A1, the negative correlation between porosity and quartz (0.76) exceeds that in the tested Berea J2 (0.66), in the latter there is a stronger negative correlation between porosity and CMB and between porosity and iron oxide/hydroxide. Furthermore, for horizontal subsections in Berea J2, strong positive correlations are observed between iron oxide/hydroxide and: CMB, titanium oxides and siderite, and between CMB and IM, siderite and titanium oxides. Full correlation matrices for square and horizontal subsections are included in Tables S2-S9 supplementary material.

Table 2: Correlation coefficients exceeding 0.65 between minerals for horizontal subsections within each sandstone sample. Investigation areas are divided into thirty eight 270 μm wide subsections, 95% confidence interval in brackets. The full correlation coefficient matrices are in supplementary material. (IM=illite/muscovite; CMB=chlorite/mixed layer illite-muscovite/biotite; DA=dolomite/ankerite)

	Positive correlation coefficient>0.65 (95% limits)		**Negative correlation coefficient>0.65 (95% limits)**	
Berea A1	DA - Calcite	0.85 (0.7 - 0.9)	Porosity – Quartz	-0.76 (-0.6 - -0.9)
	Siderite - FeO/FeOOH	0.74 (0.6 - 0.9)	Quartz – Feldspar	-0.75 (-0.6 - -0.9)
Berea J2	CMB - IM	0.69 (0.5 - 0.8)	Porosity – Quartz	-0.66 (-0.4 - -0.8)
	CMB – Siderite	0.66 (0.4 - 0.8)	Porosity – CMB	-0.72 (-0.5 - -0.8)
	CMB – Titanium minerals	0.72 (0.5 – 0.8)	Porosity – Fe_2O_3/FeOOH	-0.69 (-0.5 - -0.8)
	Fe_2O_3/FeOOH - CMB	0.77 (0.6 - 0.9)	Quartz – Feldspar	-0.77 (-0.6 - -0.9)
	Fe_2O_3/FeOOH – Siderite	0.88 (0.8 – 0.9)		
	Fe_2O_3/FeOOH - Titanium oxides	0.84 (0.7 – 0.9)		
	Titanium oxides – Siderite	0.66 (0.4 - 0.8)		
Gassum 7V	CMB – Siderite	0.68 (0.5 – 0.8)	Quartz – Feldspar	-0.82 (-0.7 - -0.9)
	Fe_2O_3/FeOOH – Siderite	0.81 (0.7 – 0.9)		
Bunter 2T			Quartz - Feldspar	-0.83 (-0.7 - -0.9)

Principal component analysis (PCA) was performed to investigate correlations among minerals within samples and between samples for horizontal subsections and for square subsections. The mineral loadings for the first six PC are shown for PCA on: square and horizontal subsections of the four individual samples; square and horizontal subsections from the three untested samples combined; square and horizontal subsections from tested and untested Berea samples combined, are in supplementary material Tables S10-S13

Figures 5a and 5b show the mineral loadings and the subsection scores for the first four PC resulting from PCA on horizontal subsections of the horizontally laminated sample Berea J2. PC1 accounts for 46% of the variance, whereas PC 2, PC3, and PC4 account for only 13%, 12%, and 8% (Table S11 b). Iron oxide/hydroxide, Ti oxides, CMB and siderite, have large negative loading on PC1, as opposed to porosity and kaolinite that have high positive loading on PC1. On PC2 quartz has a high positive loading and feldspar a high negative loading. PC3 has a high positive loading on calcite and dolomite/ankerite, whereas PC4 has a high negative loading on illite/mica. The first PC from PCA on the untested samples contain a variance of 30% or lower, which reflects the low levels of correlation among minerals that were also shown in Table 2.

PCA for the subsections from all three untested sandstones sample combined (Figure 5b) shows that subsections from different samples do form distinct clusters on the plot of the first two PC, which account for 58 % and 20% of the variation. The PC1 has a negative loading on feldspar, iron oxide/hydroxide and CMB, which are most prevalent in Bunter 2T (Table 1), and positive loading for quartz and kaolinite which gives high scores for Gassum 7V and Berea A1. PC2 has a high loading on porosity, which gives high scores for Gassum 7V.

The distinction between tested Berea J2 and untested Berea A1 is less pronounced than the distinction among different formations (Figure 5c). The negative loading on iron oxide/hydroxide, titanium minerals, and CMB in PC1 results in lower scores for subsections of Berea J2 than Berea A1. The negative loading on carbonate cements in PC2 results in lower scores for subsections of Berea A1 on PC2.

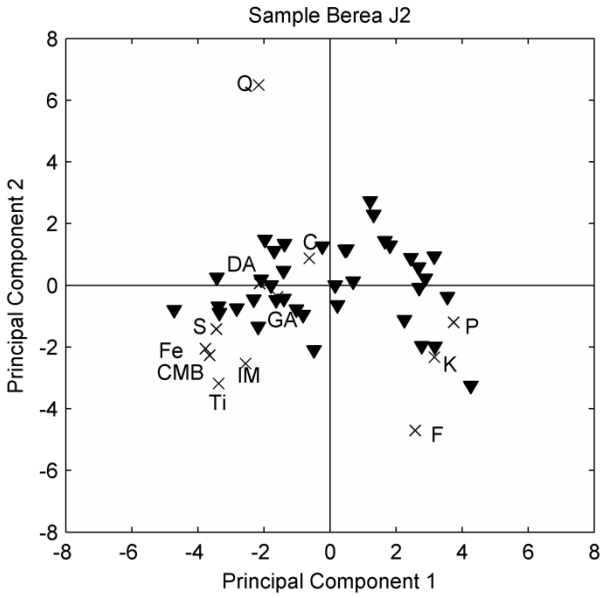
Sample Berea J2
Principal Component 2
Principal Component 1
Q
C
DA
GA
S
P
Fe
CMB
IM
K
Ti
F

328 a

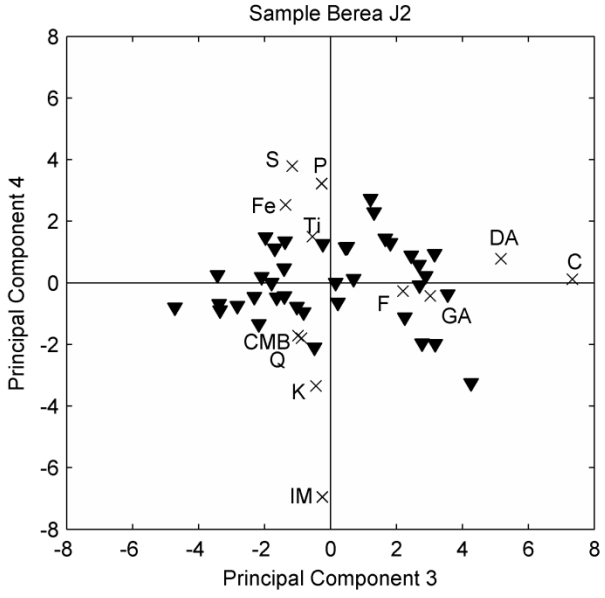
Sample Berea J2
Principal Component 4
Principal Component 3
S
P
Fe
Ti
DA
C
F
GA
CMB
Q
K
IM

329 b

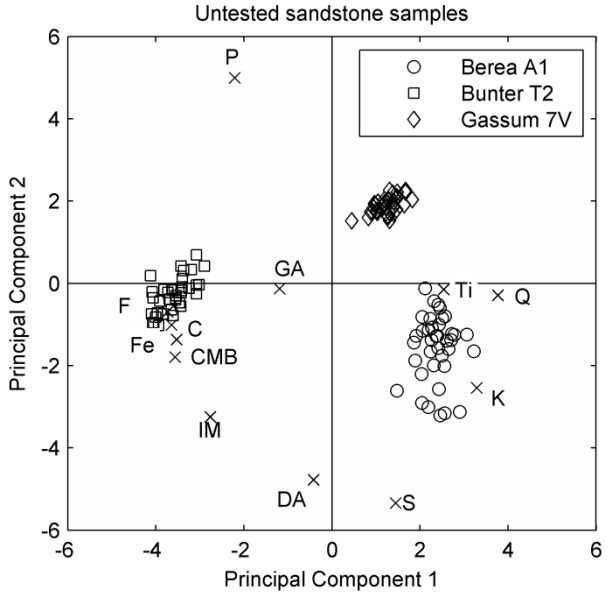

c

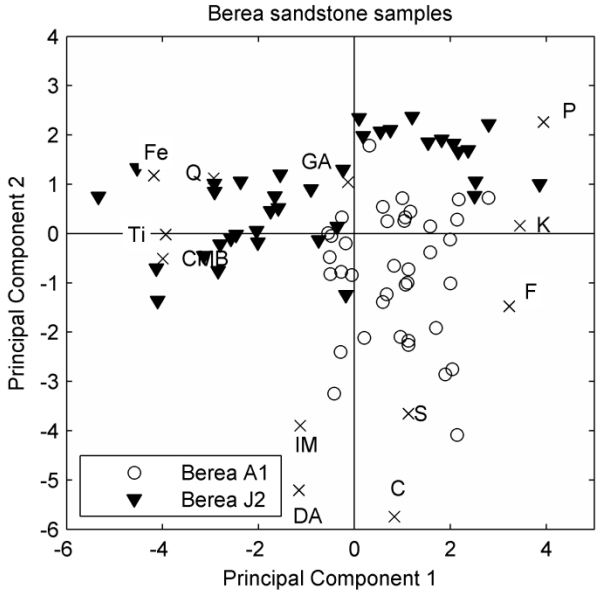

d

Figure 5: Plots of the first two principal components showing the mineral loading scaled by 10 (crosses) and principal component scores of horizontal subsections (270 μm wide, 10300 μm long). (P=porosity; Q=quartz; F=feldspar; K=kaolin; IM=illite/muscovite; CMB=chlorite/mixed layer illite-muscovite/biotite; C=calcite; S=siderite; DA=dolomite/ankerite; Fe= Fe_2O_3/FeOOH; Ti=Titanium oxides; GA=gypsum/anhydrite.)

340 5.5 Mineral pore interface length and surface area per pore volume

341 The porosity from helium injection and S_ϕ as calculated from BET surface area and helium porosity as well
342 as the image porosity and pore mineral interface length, I_ϕ, are shown in Table 3. The percentage of I_ϕ that
343 is made up by each mineral is shown together with composition on the solids in Figure 6. In all three
344 sandstone formations, quartz grains contribute less to the pore mineral interface than to the total solids area;
345 whereas the opposite holds for clay minerals, which predominantly formed as authigenic phases in the pore
346 space. Due to the low clay content in sample Gassum 7V, quartz makes up more than 70% of I_ϕ and clay
347 minerals less than 20%. By contrast in Berea A1 and J2 and in Bunter 2T, clay minerals make up 32-39% of
348 I_ϕ. Lamination of I_ϕ is shown in Figure 7. There is least variation in Gassum 7V, 0.36 < I_ϕ < 0.41 m/mm^2,
349 and a large variation in the tested Berea J2, 0.28 < I_ϕ < 0.54 m/mm^2.

350

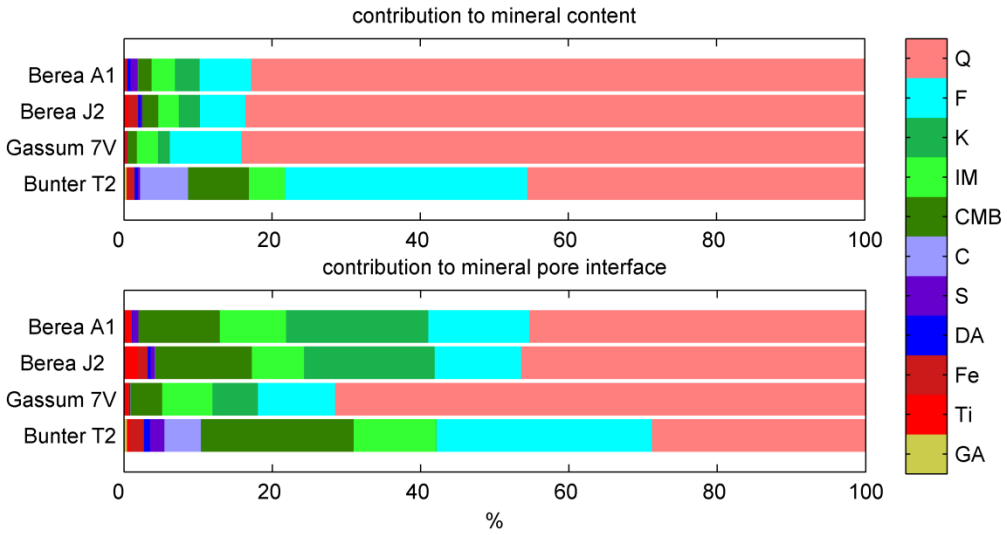

351

352 Figure 6: Top: contribution of minerals to the total solids area ; bottom contribution of minerals to the pore-
353 mineral interface (bottom). (Q=quartz; F=feldspar; K=kaolin; IM=illite/muscovite; CMB=chlorite/mixed
354 layer illite-muscovite/biotite; C=calcite; S=siderite; DA=dolomite/ankerite; Fe= Fe_2O_3/FeOOH; Ti=Ti-
355 oxides; GA=gypsum/anhydrite.)

356

Table 3: Porosity from core samples measured using helium; BET surface area normalised by He-porosity; pore perimeter length from images normalised by image porosity. Pixel length: 1.8μm. Both surface area per pore volume and pore interface length per pore area are given in units $\mu m^{-1} = m^2/cm^3 = m/mm^2$. Error estimate on image porosity and image pore interface length per pore area is twice the standard deviation of four 25 mm^2 square subsections of the samples.

	He-porosity	**Image porosity**	**Surface area per pore volume from BET m^2/cm^3**	**Pore interface length per pore area from images m/mm^2**
Berea A1	0.174[a]	0.143 (3)	16 (0.3)	0.40 (2)
Berea J2	0.166[b]	0.143 (14)	19 (0.4) [b]	0.408 (13)
Gassum 7V	0.286 [c]	0.260 (2)	14.2 (0.5)[d]	0.386 (9)
Bunter 2T	0.306 [c]	0.252 (5)	21 (2) [d]	0.292 (14)

[a] Estimated uncertainty 0.1 porosity %.

[b] From Rosenbrand et al. (under review).

[c] Porosity was measured on plugs whereas image analysis was done on side trims. The uncertainty is estimated from difference among neighbouring plugs 0.2 porosity %

[d] Error margin estimated from BET measurements on side trims of neighbouring plugs

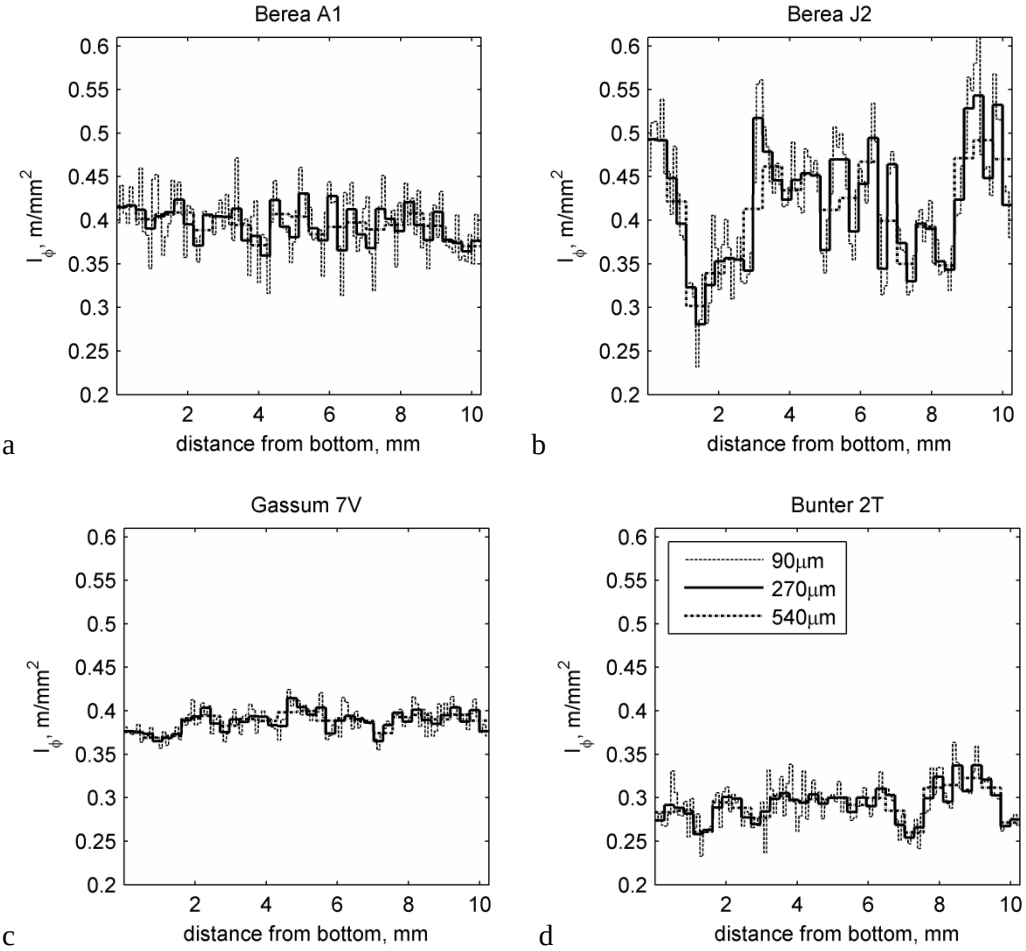

Figure 7: Pore-mineral interface length scaled by porosity (I_ϕ) for horizontal subsections (width 270μm, length 10300 μm).

6. Discussion

6.1 Mineralogy and minimum representative area

The size of the MRA and the estimated error margin for the mineral content is different for different minerals and for different sandstone samples (Table 1, Figures 1-3). This suggests that assuming the MRA of quartz would not be adequate to characterise the fraction of other minerals. Some authors suggest that 100 grains would suffice as an MRA for porosity (Blair et al., 1996) . With an average grain size in the order of 100 μm for Berea sandstone (Churcher, 1991), the proposed MRA would be 0.98 mm^2 for in a sample with 20% porosity. Figure 1c shows that the porosity content stabilises around 25 mm^2 in the untested Berea A1. This is a substantially larger area, however, this is consistent with findings of other authors who observed heterogeneity on a mm scale in the Berea sandstone (Knackstedt et al., 2001; Peng et al., 2012). In sample Berea J2 porosity showed an apparent stable value, which was representative only for a thin segment of the

image and the average porosity changed as the area was further increased. For this sample porosity appears to stabilize between 75 and 100 mm^2, however, possibly there is a greater variation on the sample scale (Figures 2a and 2b). This sample shows a more pronounced lamination in porosity and in mineral abundance than sample Berea A1 (Figure 4), which would result in higher MRA.

A higher error margin relative to the amount of a mineral present indicates a larger variation on the sample scale, which implies that large areas must be compared in order to distinguish between lithological characteristics that are due to deposition or diagenetic processes and test procedures. Petrographic analysis of Bunter sandstone samples from a different locality indicates that anhydrite is heterogeneously distributed on the scale of core samples (Weibel et al., 2010), suggesting that analysis of side trims is insufficient to quantify the gypsum/anhydrite content of specific plugs and changes in this during chemical reactions. This would require direct examination of the plugs before and after experiments by non-destructive methods, such as possibly micro CT scanning.

6.1.1 Alteration due to hot water injection

The difference between the areas of siderite and iron oxide/hydroxide in sample Berea J2 and sample Berea A1 is larger than the error margin for the variation of these minerals within Berea A1, suggesting the difference is due to chemical alteration. While iron oxide/hydroxide is also present in Berea A1, siderite is more abundant in that sample, as opposed to Berea J2 where iron oxide/hydroxide dominates. The reduction of siderite and increase in iron oxide/hydroxide indicates that siderite dissolution released the iron that formed the iron oxides/hydroxides. In siderite, iron is in the Fe^{2+} state, which would be oxidised to Fe^{3+} in the pore fluid containing oxygen. Due to the low solubility of Fe^{3+} it would precipitate in oxides/hydroxides. The presence of such minerals rimming siderite in Berea A1 shows that this reaction also took place to a minor extent during the diagenetic evolution of the Berea sandstone. During testing, at the pH 8-9 prevalent in the Berea samples saturated with a NaCl solution (Kia et al., 1987) the oxidation of Fe^{2+} and precipitation of Fe^{3+} may be enhanced. If iron oxide/hydroxide precipitated as goethite, dissolution would result in a comparable volumetric loss of siderite and gain of goethite in the sample. Accordingly the difference between siderite content in untested Berea A1 and tested Berea J2 is only 0.69% ± 0.15%, and the difference between the iron oxide/hydroxide content in the two samples is 1.01% ± 0.14%. The small difference could be due to sample heterogeneity and methodological bias. Indeed, BSEM images showed pores that are smaller than l_{pix} in the iron oxides/hydroxides so that the iron oxide/hydroxide content would tend to be overestimated.

Other minerals where the difference in content of Berea A1 and Berea J2 exceeds the error margin include titanium oxides, the group chlorite/mixed layer chlorite-smectite/biotite, feldspar, kaolinite, and illite/muscovite, whereby the first two are more and the remaining minerals are less abundant in the tested sample. Other authors have measured aluminium and silicium in the effluent during injection of NaOH

418 solution at 85°C in Berea sandstone (Sydansk, 1982), which could have resulted from dissolution of
419 feldspars and clay minerals such as illite and kaolinite. In that study, BSEM images also suggested that clay
420 minerals had precipitated on the grain surface during the experiments, which would be in accordance with
421 the increase in the group chlorite/mixed layer clays observed in sample Berea J2. However, we observed no
422 evidence of clay mineral precipitation on the pore walls of sample Berea J2, and the difference between the
423 content of these minerals in Berea A1 and Berea J2 is only slightly larger than the estimated error margin in
424 Berea J2. Therefore these differences could well be due to variation among samples.

425 6.1.2 Porosity

426 The image porosity is lower than the helium porosity for all samples and the discrepancy is largest in the
427 Bunter sandstone, which has the highest total clay mineral content (Tables 1 and 3). The image resolution is
428 not sufficient to resolve pores in the clay mineral fraction; therefore pixels may contain both pore space and
429 clay. These mixed pixels have a lower BSEM intensity than pixels containing only solids, and therefore
430 increasing the threshold intensity for porosity increases the pore area at the cost of the clay area (Peters,
431 2009). The porosity of the clay minerals in the sandstone pores can vary depending on the formation and the
432 type of clay mineral, however, a value in the order of 40-70% is typically found in sandstones bearing
433 kaolinite, illite or chlorite (Hurst and Nadeau, 1995; Vernik, 1994). This would account for the difference
434 between the helium porosity and the image porosity. Thus the sample porosity ϕ is the sum of the image
435 porosity ϕ_I and the unresolved porosity. Small pores have been suggested to make a negligible contribution
436 to fluid flow and permeability, due to the low flow velocity in these pores (Hossain et al., 2011), however,
437 these pores would contribute to the reactive surface area of both the micro porous clay minerals and of
438 minerals that are adjacent to clay minerals (Landrot et al., 2012). Thus the reactive interface of quartz might
439 be better estimated by the sum of the quartz pore interface and some fraction of the quartz clay interface.
440 This could increase the fraction of the reactive quartz interface length from 52% to 90% in Berea A1 if the
441 entire quartz clay mineral interface were considered reactive (Table A2 Appendix). Similarly accounting for
442 unresolved porosity in the clay minerals and in the iron oxide/hydroxide precipitates would increase the
443 reactive interface length of siderite from 23% to 88% in Berea J2 (Table A1 Appendix 1).

444 6.2 Lamination

445 We observed that lamination of porosity, mineral abundance, and of quartz specific interface length is more
446 distinct in Berea J2 after injection of hot NaCl solution compared to an untested Berea A1 (Figure 4). The
447 lamination of the mineral abundance is also shown by a larger variance for the composition of subsections,
448 and by a higher correlation among minerals in the multivariate analysis in Berea J2 than in Berea A1 as
449 discussed in Section 6.3. The variance and the correlation coefficients among minerals in subsections of
450 Bunter 2T and of Gassum 7V are also smaller than in Berea J2.

Lamination in the quartz specific interface length would be expected to be a sedimentary feature rather than due to experiments. The quartz specific interface length is only an estimate of the quartz grain size as the resolution is too low to distinguish interfaces between quartz grains or to distinguish between grains and quartz cement. However, areas with a higher quartz specific interface length and a higher porosity in Figure 4 do correspond to apparently coarser grained areas in Figure 8. In Berea A1 the lamination of the quartz grain size and of the porosity is less distinct than in Berea J2 (Figure 4) and Figure 8 does not show a distinct lamination in quartz grain size for Berea A1. This suggests that there is variation between A1 and J2 in the degree of lamination of grain sorting over a larger scale than the 100 mm^2 examined. By contrast the images do not show a significant difference in the mineral abundance, and the average specific interface of quartz is also similar, 0.33 m/mm^2 in Berea A1 and 0.32 m/mm^2 in Berea J2 (Table 1).

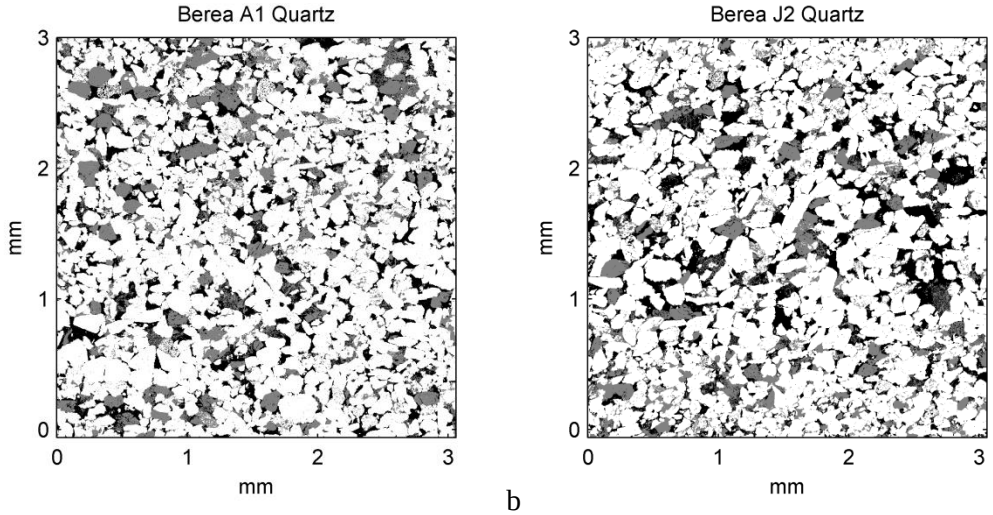

a b

Figure 8: Image of quartz (white), pores (black), and other minerals (gray) in Berea A1 (a) and in Berea J2 (b). Horizontal lamination in the grain size of quartz grains can be observed in sample J2. The origin corresponds to the bottom left hand corner of the total image therefore this corresponds to the lamination in the bottom 3 mm of the samples in Figures 4 and 7.

A lamination in siderite content of Berea A1 is observed, but peaks of siderite do not correspond to troughs in porosity and there is no correlation between siderite and porosity (Figure 4, Table 2). This suggests that siderite occurs both in finer grained and coarser grained areas. In Berea J2 peaks in iron oxide/hydroxide content do correspond to the finer grained lamina, which are observed in Figure 8. This would suggest that during testing with the hot NaCl solution iron oxides/hydroxide precipitates formed predominantly in the finer grained areas. It is uncertain to what extent this is due to initial lamination of the siderite.

6.3 Mineral correlations

A negative correlation between the quartz and feldspar is observed in all samples (Table 2), as would be expected because these minerals compose the loadbearing detrital grains of the sandstone. In untested samples, Gassum 7V and Berea A1, siderite is positively correlated to iron oxide/hydroxide, which suggests alteration of siderite to iron oxide/hydroxide during diagenesis. We found no correlation between siderite and iron oxide/hydroxide in sample Bunter 2T, where the distribution of iron oxide/hydroxide is related to the depositional environment and early diagenetic conditions according to Weibel et al. (2010).

In the untested Berea A1 a negative correlation between porosity and quartz could be due to quartz cementation, or to poor sorting. Quartz cementation (Churcher, 1991; Lene and Owen, 1969), and lamination of the porosity on the scale of 3 mm is observed in untested Berea sandstone samples (Knackstedt et al., 2001), which would correspond to laminations in porosity that are observed in Berea A1 in Figure 4a. In the tested Berea J2, a larger negative correlation between porosity and CMB and iron oxide/hydroxide than between porosity and quartz content suggests that these minerals could have a stronger effect on porosity than the quartz content. Thereby injection of hot NaCl solution appears to have enhanced existing lamination due to preferential precipitation of iron oxides/hydroxides in fine grained lamina.

The first PC for horizontal subsections of Gassum 7V, Bunter 2T and Berea A1 accounts for only a relatively low portion of the variance as compared to the first PC of Berea J2. This is due to the low level of correlation among minerals in the subsections of the untested samples. The higher correlation among minerals in Berea J2 is due to lamination of the mineral abundance within the sample. Accordingly the first PC, has high loadings on iron oxide/hydroxide and CMB, which appear to have precipitated during hot water injection. The second and third PC account for only a small amount of the variation and probably reflect a natural variation: PC2 reflects the anti-correlation between quartz and feldspar, and PC3 has a high loading on calcite. The large MRA of calcite in untested Berea A1 indicates that calcite is heterogeneously distributed, which would result in variation among sections with and without calcite (Figure 3a). The effect of lamination on the results of PCA can be seen by comparing the results for square and for horizontal subsections for Berea J2. The first PC still has high loading on iron oxide/hydroxide and CMB, however, this accounts for only 37% of the variance, as opposed to 46% in horizontal subsections. These minerals are in horizontal lamina, as shown in Figure 4d, therefore horizontal subsections capture this variation and have a higher correlation among minerals.

The principal component scores of the individual subsections in tested Berea J2 do not form distinct groups (Figures 5a and 5b), which indicates that the variations in mineralogy among lamina are gradual rather than distinct. By contrast, the different composition of the three untested sandstone samples allows a clear distinction between them using the first two PC (Figure 5c). The third PC has a high loading on

gypsum/anhydrite, which is present in some subsections of Bunter 2T but not in others. Therefore only the first two PC are used to differentiate among subsections from different sandstone samples.

The main variation among subsections of untested Berea A1 and tested Berea J2 is due to variation among lamina within J2, indicated by the similar loadings in PC1 for PCA on J2 alone and for PCA on Berea A1 and Berea J2 combined (Figures 5a and 5d). Therefore on PC1 subsections of Berea A1 and Berea J2 are not distinct. However, subsections can be reasonably grouped based on PC2, with a high negative loading on carbonate cement, which is more prevalent in Berea A1 than in Berea J2 (Table 1). PC3 has a high positive loading on quartz and a high negative loading on feldspars, which does not contribute to distinction between Berea A1 and Berea J2, but rather to distinctions within each sample, therefore only the first two PC, which account for 34% and 17% of the variance, can be used to distinguish between the tested and untested subsections.

This discussion shows that PCA is suitable to differentiate among the untested sandstones from different sampling areas as well as to distinguish between untested and tested samples.

6.4 Mineral-pore interface length and surface area per pore volume

The mineral pore interface length that was found from images is lower than the BET surface area (Table 3). Correction from 2D I to 3D S (Eq.3) would not account for this difference even with $K = 2.11$ as in Crandell (2012). Typically, the surface area or interface length increases with the resolution of the measurement (Berryman and Blair, 1987; Landrot et al., 2012; Peters, 2009; Solymar and Fabricius, 1999). With BET the resolution is the area occupied by one adsorbed nitrogen molecule, 0.162 nm^2 is often used (Sing, 2001), which is much less than the pixel size of 1.8 μm. The difference between the image surface area and the BET surface area is smallest in Gassum 7V, with the lowest clay content, and highest in Bunter 2T with the highest clay content. This is in accordance with the larger specific surface area of clay minerals as compared to quartz grains.

Whereas Bunter 2T has the highest S_ϕ based on the BET surface area, the I_ϕ from image analysis is the smallest of the four samples. This could be due to the type of clay minerals. The dominant clay group in the Bunter sandstone are the chlorite/mixed layer clays for which only 30% of the surface area forms an interface to porosity that is observable in images (Table A3 Appendix). By contrast, the Berea samples A1 and J2 contain predominantly kaolinite, which has 50% of the interface to porosity in images. Accordingly, kaolinite clay minerals are often observed as pore filling clay minerals in sandstones, whereas illite clay minerals are often considered pore lining, and chlorite clay minerals can take on a range of habits that can be pore lining or filling (Wilson and Pittman, 1977). The actual pore-clay interface of clay minerals would be larger due presence of pores below the image resolution (Landrot et al., 2012).

6.5 Permeability modelled from surface area

Permeability calculated applying Eq.(1) using BET specific surface area underestimates the Klinkenberg permeability by approximately two orders of magnitude (Table 4), which is in accordance with other studies on sandstones (Donaldson et al., 1975; Hossain et al., 2011). Better estimates are obtained by using I_ϕ, and Eq.(3) to estimate S_ϕ for $K = 4/\pi$ as in Peters (2009) and Solymar and Fabricius (1999), $K = 2.11$ as in Crandell et al. (2012) , and an intermediate value $K = 1.6$. The latter was found to match the Klinkenberg permeability for both Gassum 7V and for Bunter 2T (Table 4). The permeability calculated from image analysis for Bunter 2T is higher than for Gassum 7V, in accordance with the measured permeabilities, and in contrast to the permeabilities estimated from the BET specific surface area. As discussed in Section 6.3, the high BET surface area of Bunter 2T would be due to a high clay mineral content, which does not dominate permeability.

Heterogeneity of I_ϕ and ϕ does not have a strong effect on the permeability that was calculated by averaging the permeability of long horizontal and vertical and square subsections (Figure 9). The maximum difference is found for the horizontally laminated Berea J2, where the maximum permeability is 77 mD, estimated using the arithmetic mean for horizontal sections, and the minimum permeability is 61 mD, estimated using the harmonic mean of horizontal sections, using K=1.6 as in Table 4. This would suggest that an enhanced degree of lamination would not affect permeability significantly, And indeed the permeability measured at the end of hot water injection was only 20% less than at the start of hot water injection (Rosenbrand et al., under review).

The difference between measured and calculated permeability for the Berea samples A1 and J2 could be due to an insufficient resolution of the images. Some authors have found that the resolution required in order to calculate permeability from Eq.(1) is proportional to the effective S_p, and that using a lower resolution would overestimate permeability whereas a higher resolution would underestimate permeability (Blair et al., 1996). The effective specific surface of the Berea samples (1.2-1.5 m^2/cm^3) was approximately twice that of Gassum 7V (0.7 m^2/cm^3) and Bunter 2T (0.5 m^2/cm^3), which would suggest that doubling the resolution would result the same ratio of pixel length to effective surface ratio for which Eq.(1-3) in combination with $K = 1.6$ estimated permeability in the Gassum and Bunter samples. The estimated permeability for the Berea sandstone Berea A1 when scanned with l_{pix} = 0.83 μm is 35 mD, which is closer to the measured 19-23 mD.

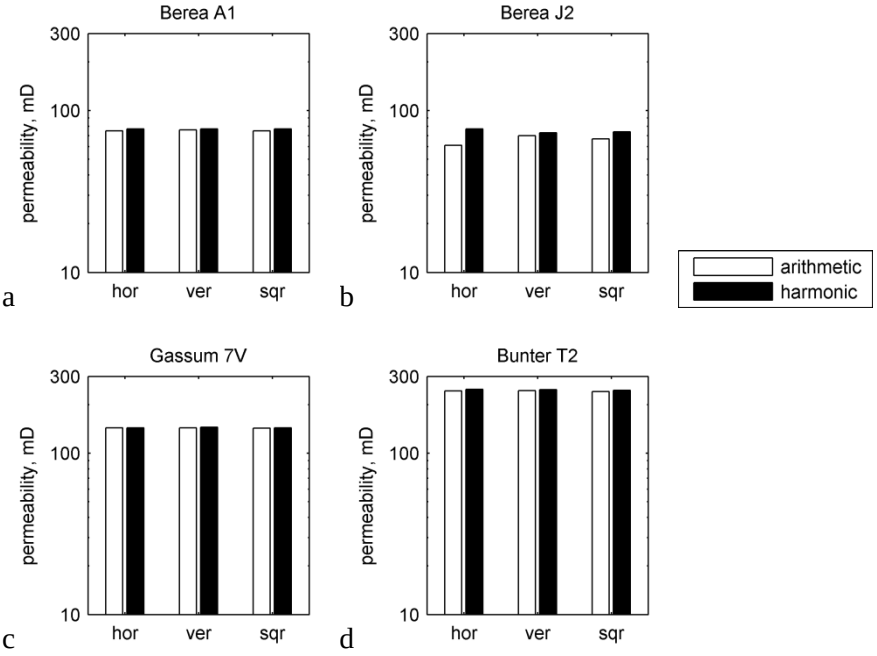

Figure 9: Average sample permeability estimated from horizontal (hor), vertical (ver) and square subsections of the image. Rectangular sections have width 270 μm and length 10300 μm (spanning the image) and square subsections have length 1700 μm (the same area), see text for further explanation.

Table 4: Measured Klinkenberg permeability, and permeability estimated from Kozeny's equation (Eq. 1) and experimental data (BET), and from images with two resolutions (l_{pix} 1.8 μm, l_{pix} 0.83 μm) for different factors K. (Error margins from error propagation on pore interface length per pore volume and image porosity in Tables 1 and 2).

			l_{pix} **1.8 μm**			l_{pix} **0.83 μm**
	Klinkenberg k mD	**k from BET mD**	**k from image $K = \frac{4}{\pi}$ mD**	**k from image $K = 2.11$ mD**	**k from image $K = 1.6$ mD**	**k from image $K = 1.6$ mD**
Berea A1	21 (2)[a]	0.11-0.18	280 (35)	33 (5)	68 (8)	35 (5)
Berea J2	15.6 (6)[b]	0.07-0.12	270 (35)	32 (5)	65 (8)	-
Gassum 7V	132 (5)[c]	0.28-0.35	600 (35)	71 (5)	144 (9)	136 (9)
Bunter 2T	270 (70)[c]	0.13-0.22	1040 (100)	122 (11)	250 (23)	250 (25)

[a] The sample was sectioned into two halves with permeabilities 19 mD and 23 mD.

[b] From Rosenbrand et al. (submitted)

[c] Thin sections were made from side trims and permeability was measured for neighbouring core plugs, error margin represents variation between adjacent plugs.

583 6.6 Fines migration

584 Several authors have suggested that kaolinite fines migration, caused by reducing the salinity of the injected
585 NaCl solution, can reduce permeability by around 90% in Berea sandstone samples (Khilar and Fogler, 1984;
586 Schembre and Kovscek, 2005). However, reducing salinity from 2.0 M NaCl to 0.002 M NaCl in sample
587 Berea J2, after this sample had been maintained at 80^{o}C during NaCl injection for 150 days, only reduced
588 permeability by 50%, whereas in another sample of Berea sandstone from the same block that had not been
589 heated, the same salinity reduction reduced permeability by over 90% (Rosenbrand et al., under review) .
590 This indicates that alteration of the sample during hot water injection reduced the extent to which kaolinite
591 fines migration affected permeability.

592 The kaolinite content of sample Berea J2 is slightly lower than that of Berea A1, however, the difference
593 between the two samples is approximately the same as the error margin of the kaolinite content (Table 1).
594 The diameter of kaolinite particles in the sandstone spans a range of 1-30 μm, and the largest particles would
595 not be expected to be mobilised by electrostatic forces due to their high mass (Rosenbrand et al., under
596 review). Thus the potentially mobile kaolinite content is lower than the total kaolinite content. Possibly,
597 dissolution of smaller particles that make up the mobile kaolinite content would reduce the sensitivity to
598 fines migration without significantly altering the total kaolinite content. Less than 1% of the kaolinite
599 interface was to iron oxide/hydroxide in sample Berea J2 (Table A4 appendix). This indicates that iron
600 oxide/hydroxide was not precipitated on the kaolinite particles, which might otherwise prevent mobilisation.
601 There were no significant differences in the interface length of kaolinite to pores or other minerals between
602 the untested Berea A1 and the tested Berea J2. Furthermore, we also found no correlations exceeding 65%
603 among kaolinite and other minerals in the horizontal subsections of the tested or the untested Berea A1 and
604 J2.

605 7. Conclusions

606 We applied image analysis in order to generate statistics on mineralogy, reactive surface area, and
607 heterogeneity on the sample scale. Lamination and relations among porosity and mineral groups were
608 quantified and used to compare samples by means of subsectioning images and multivariate data analysis
609 (PCA). We compared samples from Gassum sandstone, Bunter sandstone and Berea sandstone formations,
610 and studied the effect of hot water injection by comparing an untested sandstone sample to a sample in which
611 hot water had been injected for 150 days.

612 We found significant differences among the minimum representative areas of different minerals for different
613 formations. Heterogeneity, both in the form of patchy cementation and in the form of lamination of mineral
614 abundance, porosity, and specific interface length, were observed over a mm scale, suggesting that in order
615 to relate to core scale experiments in these sandstones, image analysis requires an interrogation area in the

order of several mm to cm. In more coarse grained rocks this would be different. PCA could be used to distinguish among samples from different localities, and to some extent between tested and untested samples of Berea sandstone. Lamination of mineral abundance, porosity, and specific interface length were more pronounced in the Berea sandstone sample after hot water injection than in the untested sample. A loss of siderite and a corresponding gain in iron oxide/hydroxide appear to have enhanced existing lamination. Image derived specific surface area was used to estimate permeability using Kozeny's equation. Using a constant ratio of pixel length to effective specific surface area, permeability was estimated within a 50% error margin for samples from the three formations.

Acknowledgements

QemScan was performed at the Professor Klockmann Laboratory of the Institute of Mineralogy and Economic Geology at RWTH Aachen by Roman Klinghardt of the Institute of Mineralogy and Economic Geology. Sample selection, cleaning, and conventional core analysis for the Gassum and Bunter samples was done at the Core Laboratory of the Geological Survey of Denmark and Greenland by Claus Kjøller, Hanne Holmslykke Dahl, and Hans Jørgen Lorenzen. Thin sections were prepared by Hector Ampuero Diaz at the Technical University of Denmark. This work is part of the Heat Storage in Hot Aquifers grant funded by the Danish Council for Strategic Research.

633 References

634 API, 1998. Recommended Practices for Core Analysis, API RP 40.

635 Ayling, B., Rose, P., Petty, S., Zemach, E., Drakos, P., 2012. QEMSCAN® Quantitative evaluation of
636 minerals by scanning electron microscopy: capability and application to fracture characterization in
637 geothermal systems., in: PROCEEDINGS, Thirty-Eighth Workshop on Geothermal Reservoir
638 Engineering Stanford University. p. 11.

639 Bear, J., 1972. Dynamics of fluids in porous media. American Elsevier.

640 Bera, B., Mitra, S.K., Vick, D., 2011. Understanding the micro structure of Berea Sandstone by the
641 simultaneous use of micro-computed tomography (micro-CT) and focused ion beam-scanning electron
642 microscopy (FIB-SEM). Micron 42, 412–418. doi:10.1016/j.micron.2010.12.002

643 Berryman, J.G., Blair, S.C., 1987. Kozeny–Carman relations and image processing methods for estimating
644 Darcy's constant. J. Appl. Phys. 62, 2221–2228. doi:http://dx.doi.org/10.1063/1.339497

645 Blair, S.C., Berge, P.A., Berryman, J.G., 1996. Using two-point correlation functions to characterize
646 microgeometry and estimate permeabilities of sandstones and porous glass. J. Geophys. Res. 101,
647 375,20320–20359.

648 Borre, M., Lind, I.L., Mortensen, J., 1995. Specific surface as a measure of burial diagenesis of chalk.
649 Zentralblatt für Geol. und Paläontologie 1071–1078.

650 Brunauer, S., Emmett, P.H., Teller, E., 1938. Adsorption of Gases in Multimolecular Layers. J. Am. Chem.
651 Soc. 60, 309–319. doi:10.1021/ja01269a023

652 Churcher, P.L., 1991. Rock Properties of Berea Sandstone, Baker Dolomite, and Indiana Limestone, in: SPE
653 International Symposium on Oilfield Chemistry. Anaheim, California, pp. 431–466.
654 doi:10.2118/21044-MS

655 Crandell, L.E., Peters, C.A., Um, W., Jones, K.W., Lindquist, W.B., 2012. Changes in the pore network
656 structure of Hanford sediment after reaction with caustic tank wastes. J. Contam. Hydrol. 131, 89–99.

657 Donaldson, C.E., Kendall, F.R., Baker B., A., Manning F., S., 1975. Surface-Area Measurement of Geologic
658 Materials. Soc. Pet. Eng. J. 15, 111–116. doi:10.2118/4987-PA

659 Hossain, Z., Grattoni, C.A., Solymar, M., Fabricius, I.L., 2011. Petrophysical properties of greensand as
660 predicted from NMR measurements. Pet. Geosci. 17, 111–125. doi:10.1144/1354-079309-038

661 Hurst, A., Nadeau, P.H., 1995. Clay microporosity in reservoir sandstones: an application of quantitative
662 electron microscopy in petrophysical evaluation. AAPG Bull. Assoc. Pet. Geol. 79, 563–573.

663 Khilar, K.C., Fogler, H.S., 1984. The existence of a critical salt concentration for particle release. J. Colloid
664 Interface Sci. 101, 214–224. doi:10.1016/0021-9797(84)90021-3

665 Khilar, K.C., Fogler, H.S., 1987. Colloidally induced fines migration in porous media. Rev. Chem. Eng. 4,
666 41–108.

667 Kia, S.F., Fogler, H.S., Reed, M.G., 1987. Effect of pH on colloidally induced fines migration. J. Colloid
668 Interface Sci. 118, 158–168. doi:10.1016/0021-9797(87)90444-9

669 Klinkenberg, L.J., 1941. The Permeability Of Porous Media To Liquids And Gases, in: Dril. Prod. Prac. API,
670 Tulsa, Oklahoma, pp. 200–213.

671 Knackstedt, M.A., Sheppard, A.P., Sahimi, M., 2001. Pore network modelling of two-phase flow in porous
672 rock: the effect of correlated heterogeneity. Adv. Water Resour. 24, 257–277. doi:10.1016/S0309-
673 1708(00)00057-9

674 Kozeny, J., 1927. Über kapillare Leitung des Wassers im Boden. Sitzungsberichte der Akad. der
675 Wissenschaften Wien, Math. Klasse 136, 271–306.

676 Landrot, G., Ajo-Franklin, J.B., Yang, L., Cabrini, S., Steefel, C.I., 2012. Measurement of accessible reactive
677 surface area in a sandstone, with application to CO2 mineralization. Chem. Geol. 318-319, 113–125.
678 doi:10.1016/j.chemgeo.2012.05.010

679 Lene, G., Owen, D.E., 1969. Grain orientation in a Berea sandstone channel at South Amherst Ohio. J.
680 Sediment. Petrol. 39, 737–743.

681 Milsch, H.H., Spangenberg, E., Kulenkampff, J., Meyhoefer, S., 2008. A new apparatus for long-term
682 petrophysical investigations on geothermal reservoir rocks at simulated in-situ conditions. Transp.
683 Porous Media 74, 73–85. doi:10.1007/s11242-007-9186-4

684 Miranda, A., Borgne, Y.-A., Bontempi, G., 2008. New Routes from Minimal Approximation Error to
685 Principal Components. Neural Process. Lett. 27, 197–207. doi:10.1007/s11063-007-9069-2

686 Mortensen, J., Engstrøm, F., Lind, I.., 1998. The Relation Among Porosity, Permeability, and Specific
687 Surface of Chalk From the Gorm Field, Danish North Sea. SPE Reserv. Eval. Eng. 1, 245–251.
688 doi:10.2118/31062-PA

689 Peng, S., Hu, Q., Dultz, S., Zhang, M., 2012. Using X-ray computed tomography in pore structure
690 characterization for a Berea sandstone: Resolution effect. J. Hydrol. 472–473, 254–261.
691 doi:http://dx.doi.org.globalproxy.cvt.dk/10.1016/j.jhydrol.2012.09.034

692 Peters, C.A., 2009. Accessibilities of reactive minerals in consolidated sedimentary rock: An imaging study
693 of three sandstones. Chem. Geol. 265, 198–208. doi:10.1016/j.chemgeo.2008.11.014

694 Pirrie, D., Butcher, A.R., Power, M.R., Gottlieb, P., Miller, G.L., 2004. Rapid quantitative mineral and phase
695 analysis using automated scanning electron microscopy (QemSCAN); potential applications in forensic
696 geoscience. Spec. Publ. Geol. Soc. LONDON 232, 123–136.

697 Rosenbrand, E., Haugwitz, C., Jacobsen, P.S.M., Kjøller, C., Fabricius, I.L., 2014. The effect of hot water
698 injection on sandstone permeability. Geothermics 50, 155–166.

699 Rosenbrand, E., Kjøller, C., Riis, J.F., Kets, F., Fabricius, I.L., under review. Different effects of temperature
700 and salinity on permeability reduction by fines migration in Berea sandstone. Geothermics.

701 Schembre, J.M., Kovscek, A.R., 2005. Mechanism of Formation Damage at Elevated Temperature. J. Energy
702 Resour. Technol. 127, 171–180. doi:10.1115/1.1924398

703 Schepers, A., Milsch, H., 2013. Dissolution-precipitation reactions in hydrothermal experiments with quartz-
704 feldspar aggregates. Contrib. to Mineral. Petrol. 165, 83–101. doi:10.1007/s00410-012-0793-x

705 Sing, K., 2001. The use of nitrogen adsorption for the characterisation of porous materials. Colloids Surfaces
706 A Physicochem. Eng. Asp. 187, 3–9.

707 Solymar, M., Fabricius, I.L., 1999. Image analysis and estimation of porosity and permeability of Arnager
708 Greensand, Upper Cretaceous, Denmark. Phys. Chem. Earth, Part A Solid Earth Geod. 24, 587–591.
709 doi:10.1016/S1464-1895(99)00084-8

710 Sydansk, R.D., 1982. Elevated-Temperature Caustic/Sandstone Interaction: Implications for Improving Oil
711 Recovery (includes associated papers 11348 and 11548). Soc. Pet. Eng. J. 22, 453–462.
712 doi:10.2118/9810-PA

713 Tenthorey, E., Scholz, C.H., Aharonov, E., Leger, A., 1998. Precipitation sealing and diagnesis1:
714 Experimental results. J. Geophys. Res. 103, 23967.

715 Vernik, L., 1994. Predicting lithology and transport properties from acoustic velocities based on
716 petrophysical classification of siliciclastics. Geophysics 59, 420–427.

717 Weibel, E.R., 1989. Measuring through the microscope: development and evolution of stereological
718 methods. J. Microsc. 155, 393–403.

719 Weibel, R.H., Olivarius, M., Nielsen, L.H., Abramovitz, T., Kjøller, C., 2010. Petrography and diagenesis of
720 the Triassic and Jurassic sandstones, eastern part of the Norwegian-Danish Basin., Danmark og
721 Grønlands Geologiske Undersøgelse Rapport.

722 Wilson, M.D., Pittman, E.D., 1977. Authigenic clays in sandstones; recognition and influence on reservoir
723 properties and paleoenvironmental analysis. J. Sediment. Res. 47, 3–31.

724

725

726 Appendix 1

727 Table A1: Siderite interface to other minerals and pores, pixel length: 1.8μm.

	Berea A1 % of total length	Berea J2 % of total length	Gassum7V % of total length	Bunter 2T % of total length
Pores	19	23	37	36
Quartz	21	8	7	14
Feldspar	0.6	0.7	0.7	3
Calcite	0	0	0	0
Siderite	0	0	0	0
Dolomite/Ankerite	2	0	0	0
Kaolin	0	0	0.9	0
Illite/Muscovite	1.5	2	4	1.4
Chlorite/Mixed layer Chlorite-Smectite/Biotite	10	11	28	31
Iron oxide/ hydroxide (Fe_2O_3/FeOOH)	44	54	22	14
Titanium oxides	0	0	0	0
Gypsum/Anhydrite	0	0	0	0

728

729 Table A2: Quartz interface to other minerals and pores, pixel length: 1.8μm.

	Berea A1 % of total length	Berea J2 % of total length	Gassum 7V % of total length	Bunter 2T % of total length
Pores	52	53	84	42
Quartz	0	0	0	0
Feldspar	5	4	3	16
Calcite	0	0	0	3
Siderite	1.0	0	0	1.0
Dolomite/Ankerite	0	0	0	0
Kaolin	7	5	3	0
Illite/Muscovite	21	18	6	14
Chlorite/Mixed layer Chlorite-Smectite/Biotite	11	12	3	21
Iron oxide/hydroxide (Fe_2O_3/FeOOH)	0	2	0	1.5
Titanium oxides	2	3	0.6	0
Gypsum/Anhydrite	0	0	0	0

730

731

732 Table A3: Chlorite, mixed layer, biotite interface to other minerals and pores, pixel length: 1.8μm.

	Berea A1 % of total length	**Berea J2 % of total length**	**Gassum 7V % of total length**	**Bunter 2T % of total length**
Pores	29	31	37	29
Quartz	25	26	19	20
Feldspar	4	4	5	20
Calcite	0	0	0	2
Siderite	1.1	0.7	0.7	2
Dolomite/Ankerite	0	0	0	0.8
Kaolin	15	13	15	0
Illite/Muscovite	21	19	20	20
Chlorite/Mixed layer Chlorite-Smectite/Biotite	0	0	0	0
Iron oxide/hydroxide (Fe_2O_3/FeOOH)	0.5	2	2	4
Titanium oxides	2	3	1.2	0.5
Gypsum/Anhydrite	0	0	0	0

733

734 Table A4: Kaolin interface to other minerals and pores, pixel length: 1.8μm.

	Berea A1 % of total length	**Berea J2 % of total length**	**Gassum 7V % of total length**	**Bunter 2T % of total length**
Pores	56	57	50	12
Quartz	17	16	25	26
Feldspar	1.4	1.0	1.0	24
Calcite	0	0	0	0
Siderite	0	0	0	0
Dolomite/Ankerite	0	0	0	0
Kaolin	0	0	0	0
Illite/Muscovite	9	7	9	21
Chlorite/Mixed layer Chlorite-Smectite/Biotite	16	17	14	13
Iron oxide/hydroxide (Fe_2O_3/FeOOH)	0	0	0	0
Titanium oxides	0.6	0.9	0	0
Gypsum/Anhydrite	0	0	0	0

735

736

737 Table A5: Iron oxide/hydroxide interface to other minerals and pores, pixel length: 1.8μm.

	Berea A1 % of total length	**Berea J2 % of total length**	**Gassum 7V % of total length**	**Bunter 2T % of total length**
Pores	6	23	42	25
Quartz	16	30	11	21
Feldspar	1	1	1	4
Calcite	0	0	0	1
Siderite	62	24	11	11
Dolomite/Ankerite	2	3	0	1
Kaolin	0	0	1	0
Illite/Muscovite	1	2	5	2
Chlorite/Mixed layer Chlorite-Smectite/Biotite	7	11	29	40
Iron oxide/hydroxide (Fe_2O_3/FeOOH)	0	0	0	0
Titanium oxides	4	4	0	2
Gypsum/Anhydrite	0	0	0	0

738

739

Permeability in Rotliegend Gas Sandstones to gas and brine as predicted from NMR, mercury injection and image analysis

Esther Rosenbrand[1], Ida Lykke Fabricius[1], Quentin Fisher[2], Carlos Grattoni[2]

1 – Department of Civil Engineering, Technical University of Denmark, Brovej 118, 2800 Kgs, Lyngby, Denmark

2 – School of Earth and Environment, University of Leeds, Leeds, LS2 9JT, UK

Addresses:

Postal: Esther Rosenbrand, Technical University of Denmark, Brovej building 118, 2800 Kongens Lyngby, Denmark.

Email: esro@byg.dtu.dk

Phone: +45 45 25 14 16

Postal: Ida Lykke Fabricius, Technical University of Denmark, Building 119 Brovej 118, 2800 Kongens Lyngby, Denmark.

Email: ilfa@byg.dtu.dk

Phone:+45 45252162

Postal: Quentin Fisher, room 7.134, School of Earth and Environment, Maths/Earth and Environment Building, The University of Leeds, Leeds LS 9JT, United Kingdom.

Email: q.j.fisher@leeds.ac.uk

Phone: +44(0) 113 34 31920

Postal: Carlos Grattoni, room 7.126, School of Earth and Environment, Maths/Earth and Environment Building, The University of Leeds, Leeds LS 9JT, United Kingdom.

22 Email: C.A.Grattoni@leeds.ac.uk

23 Phone: +44(0) 113 34 35214 / 30474

24

Permeability characterization of low permeability, clay-rich gas sandstones is part of production forecasting and reservoir management. The physically based Kozeny (1927) Equation linking permeability with porosity and pore size is derived for a porous medium with a homogeneous pore size, whereas the pore sizes between grains (sand and clay) in tight sandstones can range from nm to μm. We analysed the permeability of 63 Rotliegend sandstone samples to gas and to brine. Samples are grouped based on principal component analysis. Gas permeability was calculated for each pore size increment based on pore size distributions from nuclear magnetic resonance (NMR) transverse relaxation data in combination with mercury injection data. The sandstone texture as defined from image analysis rather than total clay content indicates whether permeability is controlled by smaller pores or by larger pores. So we demonstrate how the use of image analysis can improve NMR based permeability modelling. Permeability to brine is modelled by assuming a bound water layer on the mineral pore interface. The measured brine permeabilities are lower than predicted based on bound water alone for these illite rich samples. Based on the fibrous textures of illite as visible in electron microscopy we speculate that these may contribute to a lower brine permeability.

Keywords: permeability; tight sandstone; bound water; image analysis; NMR

Nomenclature

b = slip factor, t^2L/m, 1/Pa

c = parameter relating porosity to permeability and specific surface area, -

d_s= density of solids, m/L^3, kg/m^3

d_A= density of mineral A, m/L^3, kg/m^3

$f_{NMR,i}$ = fraction of pore volume corresponding to i^{th} T_2 time $T_{2,i}$, -

$f_{Hg,i}$ = fraction of pore volume corresponding to i^{th} capillary pressure increment for mercury injection, -

$f_{\phi_{eff}}$ = fraction of pore volume that controls permeability, -

$fw_{nmr,i}$ = fraction of mobile pore water corresponding to i^{th} $T_{2,i}$ time, -

k = absolute permeability, L^2, m^2, mD

k_a = apparent permeability to gas flow, L^2, m^2, mD

k_w = brine permeability, L^2, m^2, mD

M = molar mass, m/n, g/mol

P_c = capillary pressure, m/t^2L, Pa

r = pore radius, L, m

r_{eff} = effective pore radius for pores that control permeability $r_{eff} = 2/S_{p,eff}$, L, m

$r_{max,gas}$ = maximum pore radius that controls permeability to gas, L, m

$r_{max,brine}$ = maximum pore radius that controls permeability to brine, L, m

R_g = gas constant, $L^2m/(s^2Tn)$, J/mol K

S = specific surface area per bulk volume, L^{-1}, m^2/cm^3

S_p = specific surface area per pore volume, L^{-1}, m^2/cm^3

$S_{p,i}$ = specific surface area per pore volume for pores with T_{2i}, L^{-1}, m^2/cm^3

$S_{p,eff}$ = specific surface area per pore volume for pores that control permeability, L^{-1}, m^2/cm^3

$Sw_{P,i}$ = specific surface area per pore volume for mobile water, L^{-1}, m^2/cm^3

T = temperature, T, K

$T_{2,i}$ = i^{th} T_2 time, t, s

$T_{2,i_{max}}$ = maximum T_2 time that controls permeability, t, s

$T_{2,Gmean}$ = geometric mean T_2 time, t, s

V = bulk volume of sample, L^3, m^3

V_{Hg}= volume of mercury injected, L^3, m^3

γ = surface tension, m/t^2, N/m

θ= contact angle, °

λ = mean free path length gas, L, m

μ = viscosity, m/tL, Pa.s

ρ = surface relaxivity, L/t, m/s

τ = thickness of immobile water, L, m

ϕ = porosity, -

ϕ_{eff} = porosity that controls permeability, $\phi f_{\phi_{eff}}$, -

78 1. Introduction

79 The Permian Rotliegend sandstones remain a significant source of gas within Europe. Historically,
80 production has been primarily from reservoirs with moderate to high permeability, 10 mD-1D, in fields such
81 as the Groningen gas field in the north of the Netherlands, which has a high productivity. For future supply,
82 exploration targets tight gas sandstone reservoirs that have less favourable properties (Gaupp and Okkerman,
83 2011).

84 Permeability is a critical parameter as it controls the production rate. Therefore a significant amount of effort
85 has been invested in permeability modelling. For a homogeneous porous medium, Kozeny (1927) derived
86 Eq. (1)

87 $$k = \frac{c\phi}{S_p^2} \quad (1)$$

88 where k is permeability, ϕ is porosity, S_p is the specific surface area, per unit pore volume $S_p = S/\phi$ and c
89 is a parameter that accounts for pore geometry. Using the mean grain size to estimate S_p, and a constant
90 value for c, Walderhaug et al. (2012) found that the Kozeny Equation predicts permeability in sandstone
91 samples with less than 3% clay content and porosity higher than 6-14% within a factor four for most
92 samples. An estimate of S_p based on the mean grain size would be too low in sandstones with a high clay
93 mineral content, as the specific surface area of clay minerals is significantly higher than that of grains. For
94 clay free samples with a porosity less than 6-14%, pores may not form a connected so that the permeability is
95 lower than predicted by Eq. (1) (Mavko and Nur, 1997; Walderhaug et al., 2012). Mavko and Nur (1997)
96 suggested accounted for this by reducing the porosity in the Kozeny Equation by a factor that is related to the
97 percolation threshold porosity.

98 Tight gas sandstones can have a high clay mineral content and a low porosity (Desbois et al., 2011). The clay
99 minerals are present in the space between the grains that compose the sandstone framework, and a significant
100 amount of the total porosity may indeed be pores between the clay particles (Desbois et al., 2011). The

101 porosity and size of the pores among clay particles depends on the type, the abundance, and on the
102 morphology of the clay minerals, so that pore sizes within sandstones range can from nanometres to
103 micrometres (Desbois et al., 2011; Landrot et al., 2012).

104 Hossain et al. (2011) used low field nuclear magnetic resonance (NMR) to find an S_p distribution, in order to
105 model permeability using Eq. (1) for sandstones that contain different pore sizes. They calculated
106 permeability for the fraction of the porosity that corresponds to each S_p interval and the total permeability is
107 the sum of the permeability present in the entire pore volume. In NMR, hydrogen nuclei in water saturated
108 samples are aligned in a permanent magnetic field and flipped in a temporary magnetic field, and the
109 consequent rate of decay of magnetisation is measured and converted to a transverse relaxation time, T_2,
110 distribution (Coates et al., 1999). The decay rate of magnetisation is higher near the water-mineral interface
111 than in the bulk water. So in the fast diffusion regime, in which the majority of hydrogen nuclei are relaxed
112 at the water mineral interface by surface relaxation, the T_2 time reflects S_p Eq. (2)

113 $$T_2 = \frac{1}{\rho S_p} \quad (2)$$

114 where ρ is the surface relaxivity. This is a measure of the rate at which relaxation occurs at the surface. The
115 surface relaxivity depends on the mineral-fluid interaction, and in particular on the presence of iron, in
116 silicates, in iron oxides, iron hydroxides, and in iron carbonates where ρ is high (Keating and Knight, 2007,
117 2010; Matteson and Tomanic, 2000). Several authors combined NMR with pore-throat distributions obtained
118 from mercury injection to estimate an effective ρ (Coates et al., 1999; Dastidar et al., 2006; Mbia et al.,
119 2014).

120 In sandstones where the larger pores do form a connected flow path, these pores would make the dominant
121 contribution to flow. By contrast, when clay minerals are abundant larger pores may only be connected
122 through smaller pores (Landrot et al., 2012). This would suggest that, analogous to an electrical system with
123 resistors in series, the higher S_p of the smaller pores would control the total permeability. In this case only

124 the smaller fraction of the pores is effective for permeability modelling; so that the larger pores contribute to
125 the volume of gas that can be produced but not to the permeability.

126 The permeability as measured using brine is in many cases lower than permeability measured using gas
127 (Heid et al., 1950; Jones and Owens, 1980). One reason could be that the presence of a layer of bound water
128 on the mineral pore interface reduces the mobile fluid volume for brine flow as compared to gas flow
129 (Andreassen and Fabricius, 2010; Byerlee, 1990; Heid et al., 1950; Luffel et al., 1993; Solymar et al., 2003).
130 This would have a greater effect in samples that are controlled by pores with a high S_p, as a higher fraction
131 of the porosity is immobile. In samples containing delicate clay minerals, drying of samples can furthermore
132 increase gas permeability as compared to brine permeability by alteration of the clay morphology (de Waal
133 et al., 1988; Luffel et al., 1993). Thin illite clay fibres that grow perpendicular to the grain surface may
134 collapse onto the grain surface due to capillary tension forces during drying, and the effect is found to be
135 partially reversible when samples are saturated again (Luffel et al., 1993).

136 The effect of clay minerals on permeability depends on the clay mineral type, the clay morphology, the clay
137 content and distribution of clay minerals in the sandstone. Clay content and type can be quantified using X-
138 ray diffraction XRD (Hillier, 1999, 2000; Wilson and Pittman, 1977). The morphology and distribution of
139 clay minerals in the pores can be analysed using backscatter electron microscopy, BSEM, and scanning
140 electron microscopy, SEM, in combination with image analysis on BSEM images (Peters, 2009; Solymar et
141 al., 2003; Solymar and Fabricius, 1999).

142 In this study we analysed 63 Rotliegend sandstone samples to model permeability to gas and to brine. The
143 samples were classified into five groups based on mineralogy by using principal component analysis, PCA.
144 The mineralogy was determined using quantitative XRD. BSEM images were analysed to characterise clay
145 morphology and clay distribution in the pores for the five groups. Pore size distributions were measured
146 using mercury injection porosimetry and low field NMR. Surface relaxivity was estimated by combining
147 specific surface area as found from mercury injection and from NMR data. Permeability was modelled by
148 using the pore size distribution from NMR as in Hossain et al. (2011). The fraction of the pores that controls

149 permeability was estimated by comparison to the measured gas permeability. The fraction of clay-free
150 porosity as determined from image analysis indicated in which samples larger pores contribute to
151 permeability. Brine permeability was modelled by reducing the porosity to brine by an immobilised layer on
152 the mineral-fluid interface, but in several cases an unrealistically thick immobile water layer was predicted.
153 This indicates that bound water is not the only cause of the lower brine permeability, which might also be
154 due to the presence of fibrous illite.

155

156 ## 2. Geological setting

157 The Rotliegend sandstones were deposited in the South Permian Basin (SPB), which is bounded by the Mid-
158 North Sea High and the Ringkøbing-Fyn High in the north and by the London-Brabant Massif and the
159 Rhenish High in the South. In an East-West direction, the SPB ranges from the eastern UK to central Europe
160 (Gaupp and Okkerman, 2011).

161 Diagenetic processes in the Rotliegend sandstones were studied by several authors and Gaupp and Okkerman
162 (2011) review how these processes affect reservoir quality. Authigenic minerals that are abundant throughout
163 the SPB include quartz, carbonates, iron oxides, illite, chlorite and kaolin (Gaupp and Okkerman, 2011). The
164 red colour of many samples is due to the presence of hematite (Torrent and Schwertmann, 1987). The
165 sandstones are sometimes grey due to bleaching during diagenesis (Gaupp and Okkerman, 2011), however
166 hematite may still be present in the form of small grains between clay particles (Desbois et al., 2011).
167 Regional diagenetic processes were affected by the chemistry of ground waters, uplift, temperature history,
168 and later fluid flow, resulting in variations in the clay mineral distribution (Gaupp and Okkerman, 2011).

169 ## 3. Experimental methods

170 We studied 63 samples from six wells from sectors in the North Sea and from sectors in Poland. Samples
171 have a current burial depth in the range of 2440-3961 m. Cylindrical plugs with ~3.8 cm diameter and 4-6

172 cm length were cut from reservoir cores. Plugs were cleaned using a Soxhlet extractor using a mixture of
173 methanol and dichloromethane.

174 Polished thin sections for BSEM were produced from side trims. Polished thin sections and stubs of fractured
175 samples were examined using a CAMSCAN CS44 high performance scanning electron microscope equipped
176 with a secondary electron detector and a high resolution solid state four quadrant back scattered electron
177 (BSE) detector. Representative images using BSE were taken for each sample and saved with 256 grey
178 levels.

179 Mineralogy was quantified using XRD, using a spray technique as described in Hillier (1999, 2000) in order
180 to produce samples without significant preferred orientations. The samples were dried in an oven at 60°C for
181 48 hours prior to measurements.

182 Porosity was measured using a helium gas expansion porosimeter. Gas permeability was measured by flow
183 of helium gas parallel to the plug axis. Samples were subjected to in situ confining stress in order to close
184 fractures that resulted from unloading, and at 6.7 MPa pore pressure in order to minimise the effect of gas
185 slip. For samples with permeability below 0.1 mD, permeability was measured using a pulse-decay technique
186 (Jones, 1997) using a modified Corelabs PDP 200 pulse decay permeameter that has been adapted so that
187 measurements can be made at up to 70 MPa confining pressure. Permeability was calculated using the
188 software for the PDP 200 supplied by Corelabs as in Jones (1997). Samples with a higher permeability were
189 measured using steady state permeametry (API, 1998). Brine permeability was measured using 200,000 ppm
190 NaCl solution and full saturation was verified by using NMR.

191 Mercury was injected into the evacuated core plugs by increasing the pressure stepwise up to 413.7 MPa (60
192 000 psi). Capillary pressure can be related to pore radius, r, by the Washburn (1921) Equation (3):

193 $$r = -\frac{2\gamma\cos(\theta)}{P_c} \quad (3)$$

where P_c is the capillary pressure, γ is the surface tension and θ is the contact angle. For mercury injection γ=0.48 N/m and θ=140°. Mercury measurements were performance corrected.

NMR T_2 relaxation time measurements were performed on brine saturated samples using a MARAN ULTRA from Oxford Instruments, which has a 51 mm probe and a 2 MHz operating frequency. The Carr-Purcel-Meiboom-Gill (CPMG) pulse sequence was used to generate the magnetization decay with an echo spacing of 0.1 ms, and repeat delay of 10 s between successive scans. The decaying magnetization was mapped to a T_2 distribution using the WinDXP programme software provided by Oxford Instruments. The signal amplitude was calibrated using standards with a known volume of doped water.

4. Image Analysis

Image analysis was performed on images with a pixel length of 3 μm using Matlab 2012b (The MathWorks). Pores between clay particles can be smaller than the pixel size. Pixels that contain both clay minerals and porosity have a lower brightness than pixels that contain only minerals (Peters, 2009). Therefore a first threshold was used to segment the image in to the darker porosity and clay mineral fraction and the lighter other minerals. A second lower threshold was used to segment clay-free porosity and the clay fraction, whereby the clay fraction consists of pixels containing both clay minerals and pores between clay particles. Thresholds were selected based on the histogram of pixel intensity (Figure 1). We did not equalise histograms for different samples as these have different shapes; e.g., some samples have a distinct peak of clay-free porosity and others do not. BSEM images with a pixel length of 0.6 μm, and SEM images were used in order to characterise clay morphology.

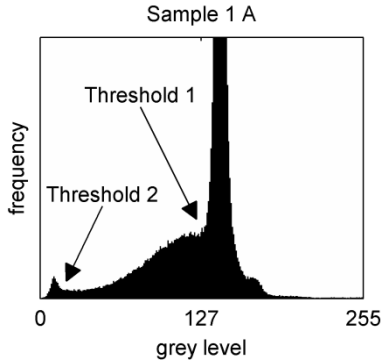

Figure 1: Histogram of pixel intensity for a backscatter electron microscopy image of sample 1A. Threshold 1 separates solid grains, with a higher intensity, from clay minerals and pore volume. Threshold 2 separates pixels that contain clay minerals and pore area, with a higher intensity, from pore area without clay minerals.

5. Principal component analysis of mineralogy

The samples were grouped based on PCA of the mineralogy from XRD. In order to include porosity in the characterisation, the mass fraction of each mineral was converted to the volume fraction relative to the solids volume by Eq. (4), and the volume fraction relative to the bulk volume, including porosity as given by Eq. (5)

$$solids\,volume\ fraction(\mathrm{A}) = solids\,mass\ fraction(\mathrm{A})\frac{d_s}{d_A} \tag{4}$$

where d_A is the density of mineral A, and d_s is the sample density.

$$bulk\,volume\ fraction(\mathrm{A}) = solids\,volume\ fraction(\mathrm{A})\left(1-\phi\right) \tag{5}$$

PCA was performed by singular value decomposition of the centred normalised data. Centring data reduces the mean square error (Miranda et al., 2008); normalisation of the variance was required in order to include the contribution of volumetrically less abundant phases, such as the clay minerals. The loadings on the orthonormal principal components, PC, were used to analyse correlations among mineral groups. In order to group samples, these were mapped onto axes spanned by the first four PC. This yielded three distinct groups, containing 9, 11, and 43 samples; including additional PC did not aid in subgrouping the 43 samples. A second PCA was therefore applied on only the set of 43 samples in order to subgroup these into three groups.

6. Results

6.1 Sample grouping based on mineralogy

The average mineralogy from XRD for the five groups of samples is shown in Table 1. Samples are subarkoses or arkoses according to the classification of McBride (1963). Illite/mica is present in all samples, additionally some samples contain kaolin and other samples contain chlorite. Although distinction between chlorite and kaolin clay minerals based on XRD may be difficult for iron rich chlorite minerals (Grim, 1953), petrographical analysis did not indicate errors in the XRD analysis of these minerals. The sum of the clay mineral contents ranges from 6% to 16% of the solid mass.

The standard deviation of the clay mineral content is small relative to the average clay content within a group, but the standard deviation of contents of feldspars, calcite, siderite, pyrite, and sulphate minerals is higher than the average content of these minerals. This indicates that samples within a group have similar clay mineralogy, whereas those minerals with a higher standard deviation are present in some samples and not in others.

Table 1: Average mineral content for the five groups from XRD given as mass %. Standard deviation within groups is given in brackets.

	Gr. 1		**Gr. 2**		**Gr. 3**		**Gr. 4**		**Gr. 5**	
Quartz	72	(4)	78	(5)	75	(3)	79	(3)	76	(5)
Albite	0.6	(0.9)	4.3	(0.7)	1.6	(0.4)	2.7	(1.4)	4.4	(1.2)
Microcline	5.4	(0.3)	0.2	(0.4)	1.9	(1.4)	4.9	(0.7)	5.4	(1.3)
Calcite	0	(0)	0	(0)	0.06	(0.13)	0.04	(0.07)	0.07	(0.13)
Dolomite	6	(4)	4	(2)	6	(4)	5.5	(1.3)	3.6	(1.3)
Siderite	0.5	(0.5)	0.01	(0.03)	2	(2)	0	(0)	0.8	(0.7)
Illite/Mica	5	(1.0)	10	(2)	9	(3)	6.7	(1.1)	8	(2)
Kaolinite	10.8	(1.0)	0	(0)	3.4	(1.3)	0	(0)	0	(0)
Chlorite	0	(0)	6	(2)	0	(0)	0	(0)	2.2	(0.7)
Pyrite	0.4	(0.4)	0.1	(0.2)	0.3	(0.4)	0.01	(0.04)	0	(0)
Anhydrite	0.01	(0.02)	0.02	(0.03)	0.4	(0.8)	0.3	(0.9)	0	(0)
Barite	0	(0)	0	(0)	0.08	(0.2)	0	(0)	0	(0)
no samples	***9***		***11***		***14***		***22***		***7***	

Figure 2 shows the mineral loadings and the sample scores mapped onto the first three PC, for the PCA on the entire dataset. The loadings on the minerals are dominated by the difference between samples in Group 1, which have a distinctly higher kaolin content and a lower illite/mica, albite, and quartz content, and Group 2,

which have a higher chlorite and illite/mica content compared to the remaining 43 samples (Table 1). Accordingly there is a high loading on these minerals on PC1. PC2 and PC3 have a high loading on minerals that are only present in very few samples in the dataset, such as barite and pyrite, which would not warrant an additional grouping. Therefore a second PCA analysis was applied in order to group the remaining 43 samples. Again PC1 distinguishes kaolin rich samples in Group 3 from chlorite rich samples in Group 5, samples in Group 4 contain neither kaolin nor chlorite minerals (Figure 3). The first two PC are sufficient to subgroup the data into three groups. PC3 and PC4 have high loadings on pyrite, calcite and illite/mica, for which there are similar variations among samples within groups and among the groups themselves (Table 1 and Table A2). The loadings for the first six PC for the PCA on all data and for the PCA on 43 samples are given in Table A1 and Table A2 in Appendix A.

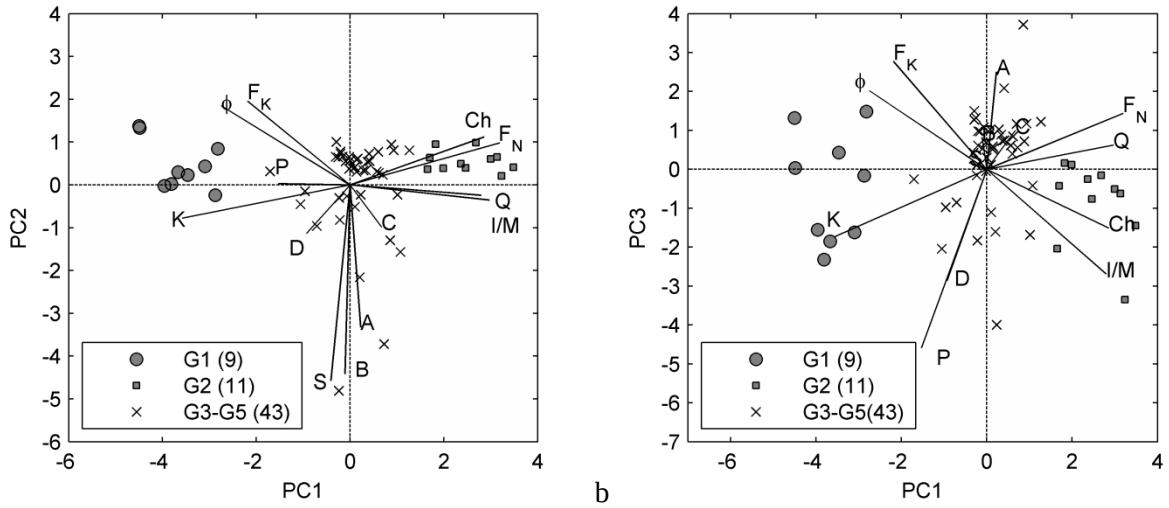

a b

Figure 2: Principal component, PC, loadings on minerals (lines) and principal component scores (symbols) for all 63 samples grouped into Group 1 (9 samples), Group 2 (11 samples) and the remaining 43 samples, Groups 3-5. (ϕ = porosity; A = anhydrite; B = barite; C=calcite; Ch = chlorite; D = dolomite/ankerite; F_K = microcline; F_N = albite; I/M = illite/mica; K= kaolin; P = pyrite; Q = quartz; S = siderite)

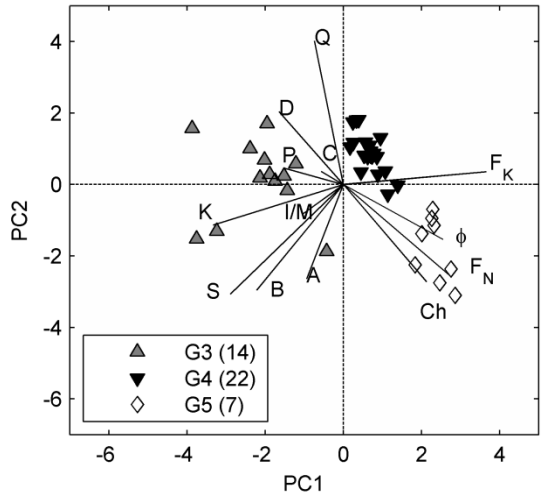

Fig 3 Principal component, PC, loadings on minerals (lines) and principal component scores (symbols) for 43 samples that are grouped into Group 3 (14 samples), Group 4 (22 samples) and Group 5 (7 samples).

(ϕ = porosity; A = anhydrite; B = barite; C=calcite; Ch = chlorite; D = dolomite/ankerite; F_K = microcline; F_N = albite; I/M = illite/mica; K= kaolin; P = pyrite; Q = quartz; S = siderite)

6.2 Pore geometry

6.2.1 Image analysis

Figure 4 shows the BSEM images and the segmented BSEM images for two characteristic samples from each group. The A samples represent samples with a relatively low mean T_2, and samples B represent a higher mean T_2, Table 2 shows how many samples have a T_2 distribution that is similar to sample A and sample B for each group. The area fractions of clay minerals and all pores, and of only clay-free pores, are shown in Table 2. The area of the clay fraction including all pores equals the sum of the He-porosity and the clay solid volume from XRD for all ten samples. This indicates that the interrogation area in image analysis was representative. Images at 0.6 μm/pixel resolution were acquired in order to characterise clay morphology, therefore no quantitative analysis was applied to these.

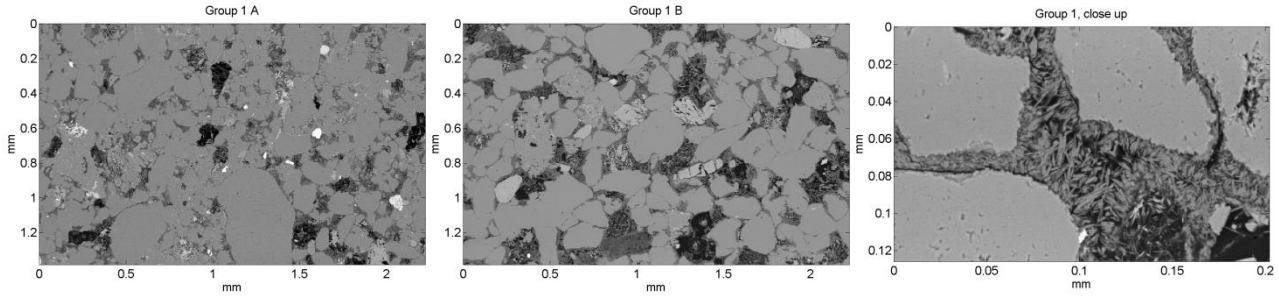

285

286 a b c

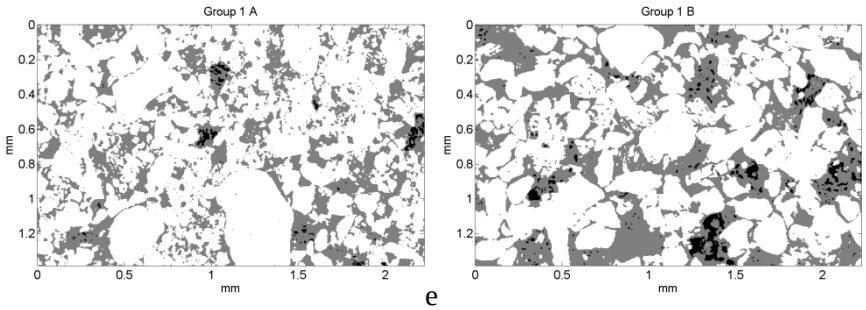

287 d e

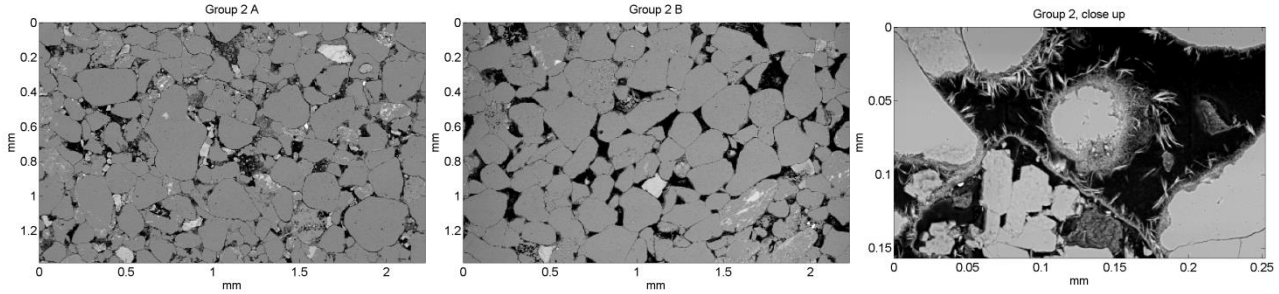

288

289 f g h

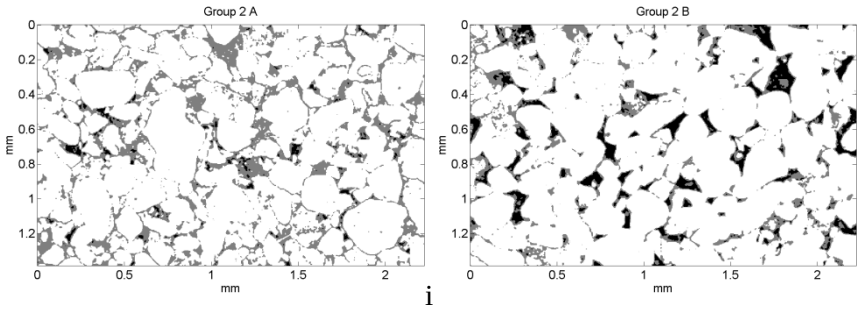

290 h i

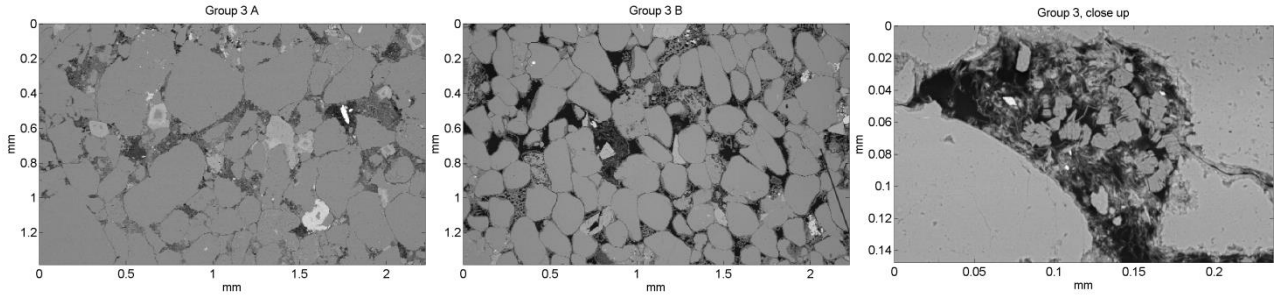
Group 3 A
Group 3 B
Group 3, close up
mm

j k l

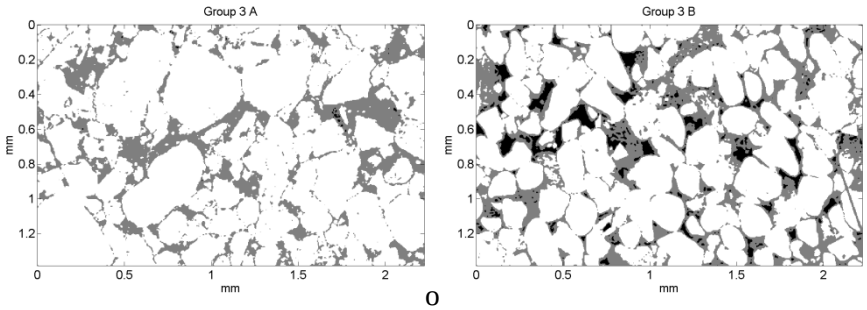
Group 3 A
Group 3 B
mm

n o

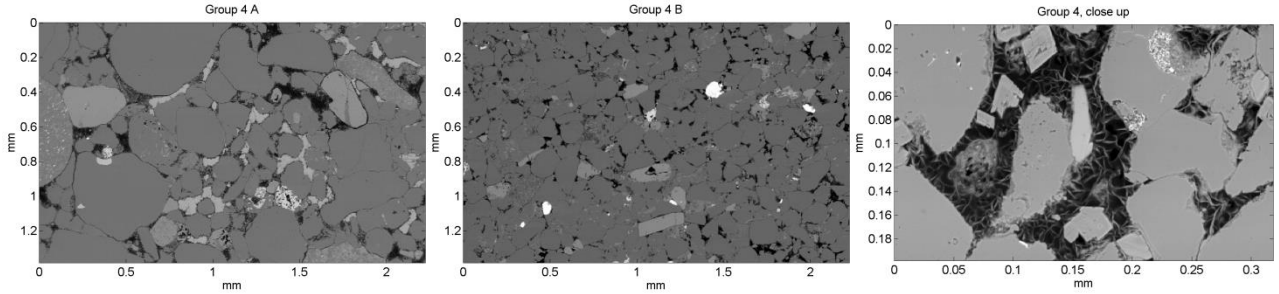
Group 4 A
Group 4 B
Group 4, close up
mm

p q r

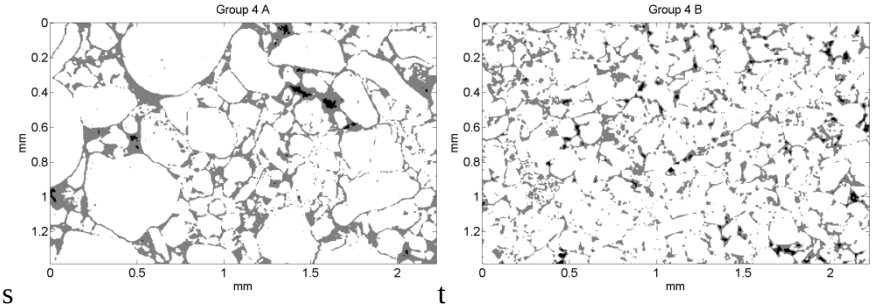
Group 4 A
Group 4 B
mm

s t

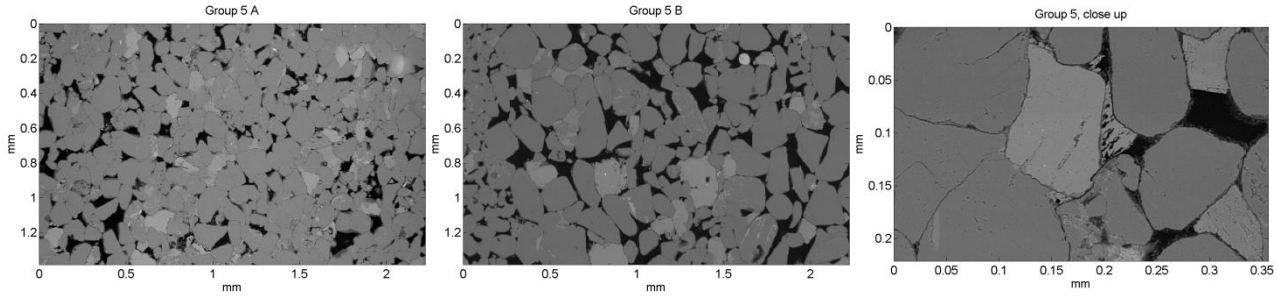

u v w

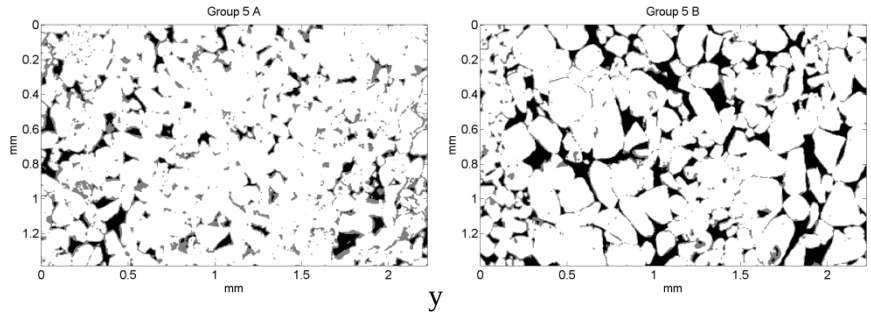

x y

Figure 4: Representative backscatter electron microscopy (BSEM) images for a sample with a lower mean NMR T_2 (samples A) and a sample with a higher mean T_2 (samples B) from each of the five groups. Below BSEM images are processed images where white pixels are grains, grey pixels contain clay and porosity and black pixels are clay-free porosity. Pixel length of images used for image analysis is 3 μm/pixel, for close up images 0.6μm/pixel. Orientation unknown.

Table 2: Image analysis with a resolution of 3 μm/pixel was used to quantify the area fractions. Error margins in brackets on image analysis data are based on the maximum difference among two or three images of the same sample. Clay volume per sample from XRD is calculated using Eq. (4) and Eq. (5). Error margins for the clay volume are based on clay mineral densities as in (Durand et al., 2000; Grim, 1953)

			Experimental		Images	
		Nr of samples with similar NMR T_2 distribution	He-porosity (m^3/m^3) %[a]	Clay (XRD) (m^3/m^3) %	Clay+ all pores (m^2/m^2) %	Clay-free pores (m^2/m^2) %
Gr 1	**A**	7	12.2	16 (3)	32 (3)	1.0 (0.2)
	B	2	19.5	12 (2)	37 (2)	2.5 (0.4)
Gr 2	**A**	5	10.3	13 (3)	19 (1.1)	1.4 (0.3)
	B	6	11.1	11 (3)	17 (1.0)	4.2 (1.1)
Gr 3	**A**	8	9.2	11 (2)	20 (0.8)	0.3 (0.5)
	B	6	17.5	12 (3)	31 (2)	4.1 (0.7)
Gr 4	**A**	4	9.2	4.5 (1)	17 (3)	0.49 (0.04)
	B	16	10.6	5.1 (1)	19 (3)	1.17 (0.11)
Gr 5	**A**	3	16.4	7.0 (2)	19 (0.9)	4.6 (0.3)
	B	4	17.9	6.6 (2)	23 (0.9)	13.2 (0.9)

5.3.2 NMR data and mercury injection porosimetry

NMR yields a T_2 time distribution where the amplitude, $f_{NMR,i}$ is the fraction of the total porosity that corresponds to a given T_2 time, $T_{2,i}$, thus $\phi\, f_{NMR,i}$ is the pore volume that corresponds to $T_{2,i}$. Similarly $f_{Hg,i}$ is the fraction of the total porosity that is injected for a capillary pressure increment, $P_{c,i}$, and $\phi\, f_{Hg,i}$ is the corresponding pore volume. Figure 5 shows the NMR curves and the differential mercury saturation curves. To compare the logarithmically spaced NMR data to mercury data, the pore diameters on mercury injection are equally spaced on the logarithmic axis (Lenormand, 2003).

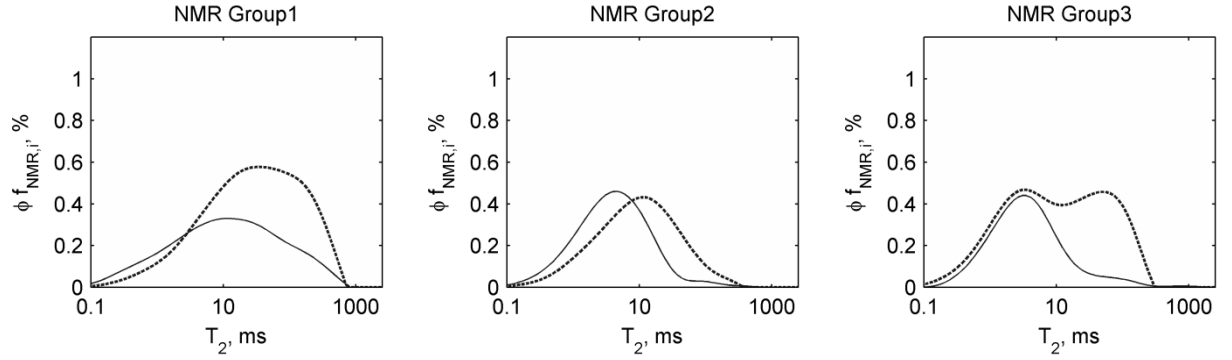

a b c

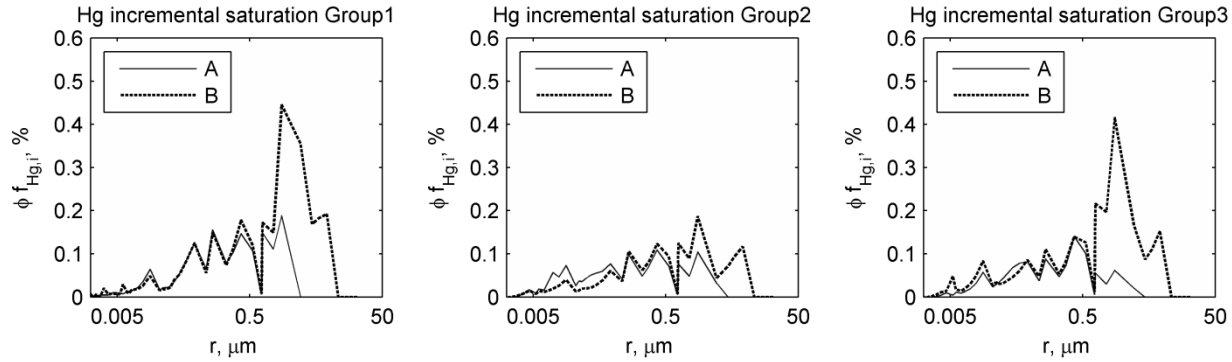

d e f

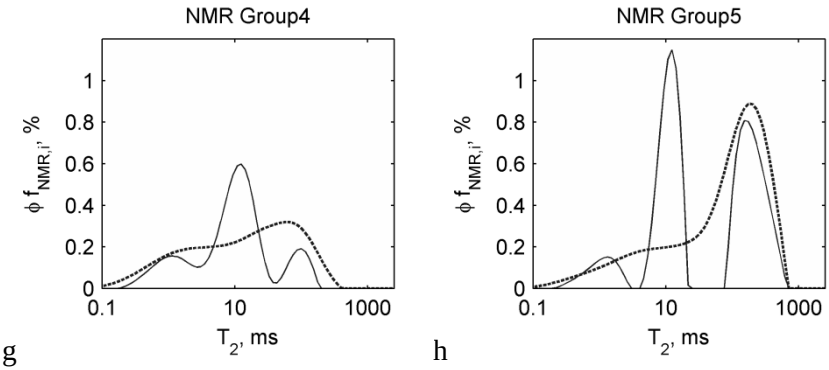

g h

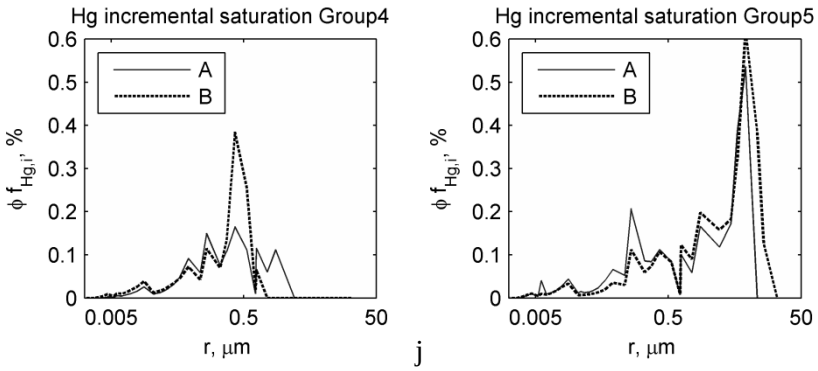

i j

Figure 5: Differential NMR plots and radii obtained from incremental mercury injection (Hg) using the Washburn equation for representative samples with a lower mean T_2 (samples A) and a higher mean T_2

(samples B). The fraction of the porosity, f_i that corresponds to a given T_{2i} or r_i is multiplied by the sample porosity in % ϕ in order to show differences among the total porosity of the samples as well as their pore size distribution.

6.3 Permeability

Figure 6a shows scatter in the permeability-porosity trend, which is largest in groups 3 and 5 and least in groups 1 and 4. Samples from Group 5 tend to have a high permeability relative to their porosity. The relation between porosity and the ratio of gas permeability to brine permeability likewise shows scatter, (Figure 6b).

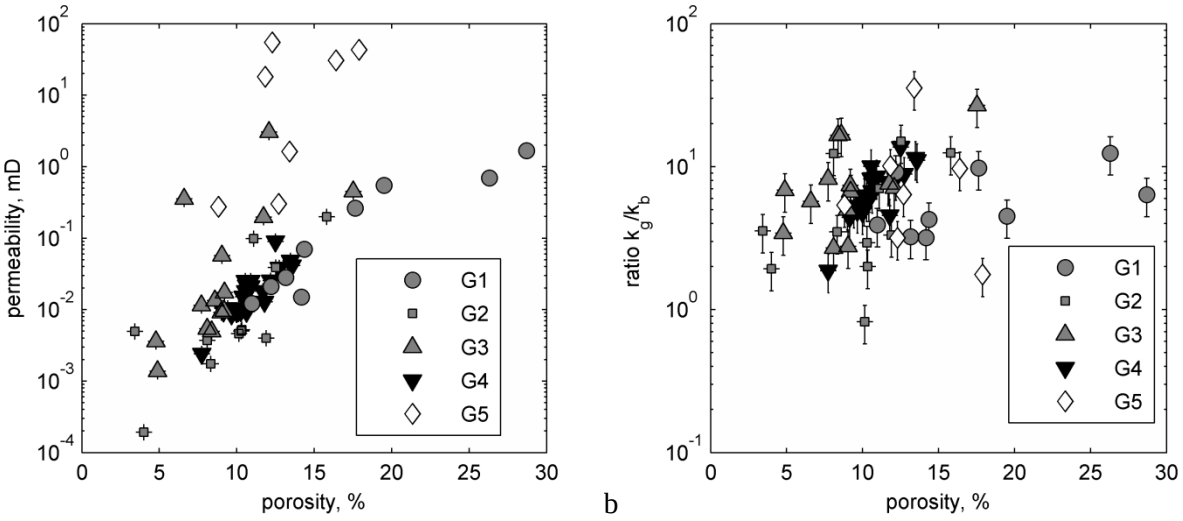

a b

Figure 6: a) Porosity and gas permeability, k_g, at in situ confining stress for 63 samples divided into five subgroups based on mineralogy. b) The ratio of gas permeability to brine permeability, k_b, ranges between 1 and 30 and shows no correlation with porosity.

342 # 7. Discussion

343 ## 7.1 Sample grouping based on mineralogy

344 Samples from the same well had similar scores in PCA and were therefore categorised in the same group.
345 This indicates that differences in mineralogy are dominated by regional variations in sediment supply and
346 diagenesis. The high loadings on kaolin and on chlorite minerals in PC1, indicate that these minerals account
347 for a large portion of the variability among samples (Figures 2 and 3). Accordingly, some authors have
348 described regional variation in the clay mineralogy of Rotliegend sandstones in the Netherlands in terms of
349 clay provinces (Gaupp and Okkerman, 2011).

350 Variation of the kaolin and chlorite clay content among samples within groups is less than variation among
351 different groups; as a consequence of this the five groups are characterised mainly by the clay mineral
352 content (Table 1). By contrast, variation of albite and microcline, siderite, pyrite, anhydrite, and barite
353 content within groups is high. The high loadings on these minerals in the second and third PC are due to only
354 a few outlier samples that were therefore not assigned individual groups (Figure 2). The effect of clay
355 content and clay morphology on permeability is addressed using the results from image analysis, NMR, Hg-
356 injection, and permeability measurements in the following sections.

357 The dataset is too small to use PCA to derive general relations among minerals based on the loadings on
358 minerals in PCs. The PCA on 63 samples results in a PC1 with opposite high loadings on chlorite minerals
359 and on porosity, whereas PC1 from PCA on 43 samples has positive and same sign loadings for these
360 variables. The nine samples in Group 1 dominate the PCA on 63 samples, these have a relatively high
361 porosity and contain no chlorite. The PCA on 43 samples does not include Group 1, and as a consequence
362 PC1 reflects seven samples in Group 5 that have a high porosity as well as chlorite clay minerals. Therefore
363 we used PCA only to group samples, and not to provide general correlations among minerals and porosity.
364 The relatively low variance contained in the first PC's furthermore reflects a low level of correlation among
365 minerals and mineral groups (Appendix A).

366 ## 7.2 Pore geometry

Group 1

Kaolin clay particles are distributed throughout the pore bodies in samples from Group 1 (Figure 4a-e). Pore filling, as opposed to grain lining, kaolin is often observed in sandstones, whereby flat kaolin plates can be observed as stacks 'booklets' or as loose plates (Wilson and Pittman, 1977). As kaolin is dispersed through the pore bodies, and is present in nearly all pores, there is little clay-free porosity in the segmented images (Figure 4d and e; Table 2).

All samples in Group 1 have a single broad T_2 peak, which indicates a continuous range of pore sizes (Figure 5a). Whereas the maximum T_2 time is the same in samples 1A and 1B; the maximum pore throat size from mercury injection is higher in sample 1B than in sample 1A (Figure 5d). This could be due to a higher connectivity among larger pores in sample 1B, whereas in sample 1A larger pore bodies are only accessed through smaller pore throats. Sample 1B has a higher clay-free porosity in images, and a larger pore volume with a high T_2, which suggests a higher connectivity among larger pores (Table 2, Figure 4a).

Group 2

Whereas the kaolin clay particles are dispersed throughout the pore bodies in Group 1, the illite/mica and chlorite platelets in Group 2 samples are observed closer to the grain surface (Figure 4f-h). Therefore a larger fraction of the porosity is clay-free than in Group 1 samples (Figure 4i and j; Table 2). We observe both clay platelets in random orientation to the grains and a thin layer of clay minerals parallel to the grain surface (Figure 4h). Other authors have also observed layers, or sheets of illite clay minerals parallel to the grain surface, from which thin illite laths or fibres protrude into the pore space (Desbois et al., 2011; Wilson and Pittman, 1977). This morphology of illite, forming sheets that extend into laths was also observed in SEM and BSEM images of groups 3 and 4 (Figures 4m and 4r and Figure 7).

The NMR curves show a single peak with a larger maximum T_2 for sample 2B than for sample 2A (Figure 5b). Accordingly mercury injection curves for samples 2A and 2B show a broad pore size distribution with larger pores in sample 2B (Figure 5e).

Group 3

The illite/mica and kaolin clay minerals in Group 3 show a variety of morphologies including kaolin booklets, kaolin or illite/mica platelets, and illite fibres both parallel to the grain surface and protruding into the pore volume (Figure 4 k-m and Figure 7).

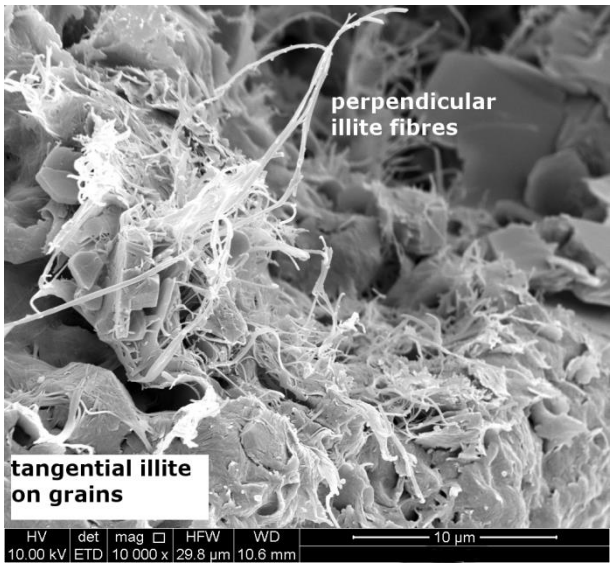

Figure 7: Scanning electron microscopy (SEM) image of illite in sample 3B. Dense tangential mats of illite can be seen on the grain surface as well as illite fibres that protrude into the pore space perpendicular to grains.

Sample 3A represents eight samples with a high clay mineral content whose NMR curves are accordingly skewed towards smaller pores (Figure 5c). Sample 3B represents three samples that also have a significant NMR peak at larger T_2. Accordingly sample 3B has a higher clay-free pore area (Figure 4n and o; Table 2). The mercury injection curve for sample 3B shows only one peak at large pore sizes, as opposed to the two approximately equal peaks in the T_2 distribution (Figure 5c and f). The lack of a peak for smaller pore sizes in the mercury injection data could be due to incomplete mercury saturation, however with a maximum capillary pressure of 413.7 MPa, the minimum accessible pore size would be 2 nm cf. Eq. (3). Alternatively, the collapse of illite fibres on the grain surface during drying as observed by Luffel et al. (1993), or

deformation of illite during the Hg-injection experiment, could have increased the porosity in large pores at the expense of smaller pores and thereby cause the difference between the shapes of the NMR and the mercury injection curves.

Group 4

The illite/mica minerals in Group 4 are mainly observed as thin fibres that bridge the pores (Figure 4r). This results in a low clay-free pore area, despite the relatively low clay mineral content (Figure 4s and t; Table 2). Accordingly Desbois et al. (2011) observe a higher porosity and larger pores in fibrous illite perpendicular to the grains, than in the illite that forms denser mats with smaller pores parallel to the grain surface. Considering that the same mass fraction of fibrous illite would have a larger effect on the pore geometry than tangential illite, the clay-free pore volume from image analysis characterises the effect of clay minerals on the pore geometry more effectively than the clay content from XRD combined with helium porosimetry.

The NMR curve (Figure 4g) of sample 4A shows distinct peaks, indicating a discontinuous pore size distribution, which could be related to poor sorting (Figure 4p). As the inter-granular space is nearly entirely composed of the clay fraction, the maximum pore size would be expected to reflect pores in between the clay particles (Figure 4s and 4t). The maximum pore sizes from mercury injection are 1.5 μm and 0.8 μm in samples 4A and 4B respectively (Figure 5i), which is in the same order of size as the pores in fibrous illite observed by other authors in Rotliegend gas sandstone (Desbois et al., 2011).

Group 5

In Group 5 only a very thin layer of chlorite or illite fibres that are perpendicular to the grain surface is observed, resulting in a high clay-free porosity (Figure 4w). Whereas samples in Group 4 have a similar clay content per pore volume as Group 5 samples, in Group 4 samples clay minerals bridge the pores whereas in Group 5 samples they only line the grains, which results in a lower clay-free porosity (Table 2). As discussed above, this indicates that image analysis provide a better quantification of the effect of clay minerals on the pore geometry than quantitative XRD.

The mercury injection curves of the two samples have a similar shape, with a high peak for large pores that indicates connectivity among large pores (Figure 5j). The prominent peak for smaller T_2 that is observed in NMR for sample 5A is absent in the mercury injection curve (Figure 5 h and j). As discussed for sample 3B, this might be due to incomplete saturation or alteration of the clay morphology during sample drying, or due to deformation of illite during the Hg-injection experiment.

7.3 Surface relaxivity

Surface relaxivity was estimated from surface area per bulk volume, S, from mercury injection and S from NMR. Capillary pressure from mercury injection can be integrated over the volume of mercury injected to obtain S in Eq. (6) (Giesche, 2006; Rootare and Prenzlow, 1967).

$$S = -\frac{1}{V\gamma\cos(\theta)}\int P_c dV_{Hg} \tag{6}$$

where V_{Hg} is the volume of mercury injected, and V is the sample bulk volume. For stepwise injection of mercury where $f_{Hg,i}$ is the fraction of the porosity that is filled by mercury for the pore pressure increment $P_{c,i}$, so that $\phi f_{Hg,i} = dV_{Hg,i}/V$, then S is given by Eq. (7).

$$S = -\frac{\phi}{\gamma\cos(\theta)}\sum P_{c,i} f_{Hg,i} \tag{7}$$

The specific surface area from NMR is given by summation of the surface area for each T_2 time over the pore volume Eq. (8).

$$S = \frac{\phi}{\rho}\sum \frac{f_{NMR,i}}{T_{2,i}} \tag{8}$$

Where $f_{NMR,i}$ is the fraction of the porosity that corresponds to $T_{2,i}$. Assuming 100% mercury saturation, ρ is given by Eq. (9).

$$\rho = \frac{-\gamma \cos(\theta) \sum \frac{f_{NMR,i}}{T_{2,i}}}{\sum P_{c,i} f_{Hg,i}} \quad (9)$$

Groups 1, 2 and 5 have a mean ρ of 8-9 μm/s; groups 3 and 4 have mean ρ of 12-13 μm/s. For the entire dataset ρ = 10 μm/s with standard deviation 4 μm/s. The surface relaxivity of quartz (99.5% SiO_2) and kaolin samples (purity 99.9%) measured using high salinity NaCl solution are only 3.6 μm/s and 3.9 μm/s respectively (Alam et al., 2014). However, iron bearing minerals, such as siderite, chlorite, or hematite, can increase the surface relaxivity (Keating and Knight, 2007, 2010; Matteson and Tomanic, 2000). Keating and Knight (2010) measured ρ exceeding 19 μm/s for mixtures of quartz and siderite with an iron content of 0.6%, and they found that ρ increases with iron content. Keating and Knight (2007) showed that quartz sand coated with hematite has ρ greater than 18 μm/s, whereas sand coated with goethite with the same iron content has ρ of only 1.6 μm/s, indicating that the structural relation in which iron is present affects ρ.

All 63 samples contain Fe-dolomite, samples in groups 2 and 5 contain chlorite, and samples in groups 3 and 5 contain siderite. However, Figure 8 shows no correlation between the content of iron bearing minerals from XRD and ρ. This would be expected as the effect of iron on surface relaxivity depends on the specific surface and type of iron bearing minerals. Samples in groups 3 and 4 are red, which indicates the presence of hematite and could possibly account for a higher mean ρ in these groups. However, hematite grains can also be present as grains among clay minerals in Rotliegend sandstone samples that are white or grey (Desbois et al., 2011).

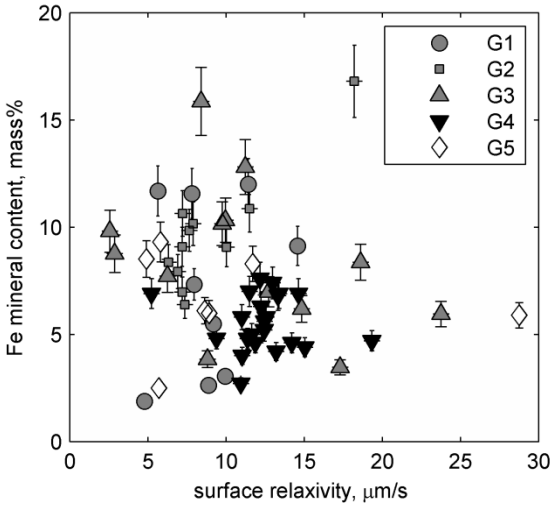

Figure 8: The iron bearing mineral content (dolomite, siderite, pyrite and chlorite) from X-ray diffraction (XRD) and surface relaxivity as calculated from mercury injection data.

Differences among ρ for different groups could also be due to the experimental methods. Mercury injection reflects the minimum size of the pores, pore throats, through which larger pores, pore bodies, are accessed, whereas NMR directly measured pore bodies (Coates et al., 1999; Dastidar et al., 2006). Incomplete mercury saturation would yield a higher ρ cf. Eq. (9). Some authors match the modes for the differential mercury injection curve and the differential NMR data in order to estimate ρ, (Coates et al., 1999; Dastidar et al., 2006). For samples in Group 5, this results in ρ ranging from 1 μm/s to 300 μm/s, as opposed to 5-12 μm/s from Eq. (9) . The large range, and in particular the outliers where ρ exceeds values reported by Keating and Knight (2007, 2010) suggest that ρ estimated from the modes of the curves are more sensitive to experimental artefacts than ρ estimated from S. This would be expected as connectivity among pore bodies, and the ratio of pore body to pore throat size would primarily affect larger pores, whereas S is controlled by the smaller pores. Other authors match the cumulative mercury data and cumulative NMR curves (Mbia et al., 2014). For samples with different shapes of NMR and Hg curves such as 1B, 4A, 3B, and 5A only a segment of the total curves overlaps for a given ρ. When ρ is chosen so that the curves overlap for the smallest pores, the results are comparable to ρ calculated from S.

487 7.4 Modelling permeability to gas

488 The permeability k_i in each $T_{2,i}$ interval was calculated using Eq. (10) (Hossain et al., 2011).

489 $$k_i = c_i \rho^2 \phi f_{NMR;i} {T_{2,i}}^2 \quad (10)$$

490 where c is a function of porosity Eq. (11) (Mortensen et al., 1998).

491 $$c_i = \left(4cos\left(\frac{1}{3} arccos\left(\phi f_{NMR,i} \frac{8}{\pi^3} - 1 \right) + \frac{4}{3}\pi \right) + 4 \right)^{-1} \quad (11)$$

492 To estimate the range of pores that control permeability, k_i was summed up to i_{max}, where the cumulative
493 permeability equals the measured permeability. The fraction of the porosity in these pores, $f_{\phi,eff}$, is given
494 by Eq. (12).

495 $$f_{\phi,eff} = \sum_{i=1}^{i_{max}} f_{NMR,i} \quad (12)$$

496 The maximum pore size that controls permeability, $r_{max,gas}$, is calculated from $T_{2,i_{max}}$ using Eq. (2) for
497 cylinders where $r = 2/S_p$. As it is not certain whether differences in ρ from Eq. (9) among samples reflect
498 artefacts during mercury injection experiments, we used ρ 10 μm/s ±4 μm/s. A lower ρ reduces k_i in Eq. (10)
499 and accordingly results in a higher i_{max} and a higher $f_{\phi,eff}$. However, ρ has a relatively small effect on the
500 maximum effective pore size, $r_{max,gas}$, as a lower ρ offsets a higher $T_{2,i_{max}}$ in Eq.(2). Figure 9 shows k_i and
501 the effect of ρ on $T_{2,i_{max}}$ for three characteristic samples.

502 Sample 1A characterises samples that have a broad single peak in the NMR curve, those samples represented
503 by 1A, 1B, 2A, 2B, 3A, 4B (Figure 5; Table 2). The $T_{2,i_{max}}$ approximately coincides with the mode of the T_2
504 distribution and with the geometrical mean T_2, $T_{2,Gmean}$. Sample 4A is representative for samples with
505 multiple peaks where smaller pores up to T_{2Gmean} control permeability (Table 2). Sample 5B characterises
506 samples where larger pores, with a $T_2 > T_{2,Gmean}$ also contribute to permeability. This includes samples with

distinct peaks as well as samples with a single peak in the NMR curve, samples are represented by 5 A, 5B, and 3B (Figure 5; Table 2)

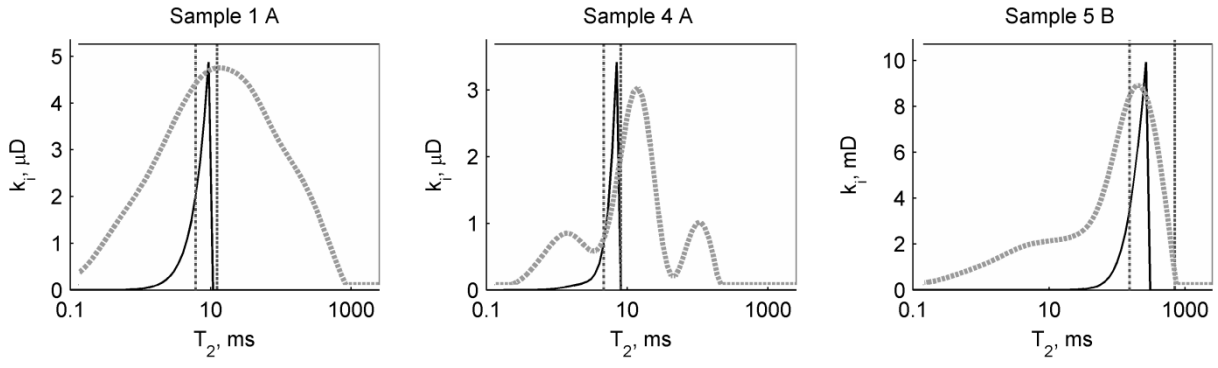

a b c

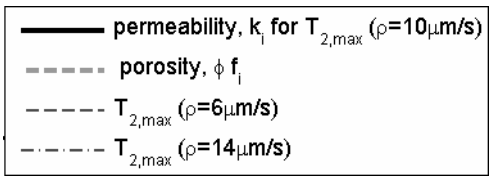

Figure 9: The permeability for each segment of the porosity distribution k_i is shown for the pores that dominate permeability by assuming surface relaxivity ρ =10μm/s. To achieve the measured permeability only a part of the porosity is required. This is 50%, 40% and 90% of the total porosity in samples 1A, 4A and 5B respectively. The full pore size distribution, $\phi\ f_i$ is shown by the dashed grey line; vertical dashed black lines indicate T_2 time of the largest pores that dominate permeability, $T_{2,max}$ when permeability is modelled using $\rho = 6$ μm/s and $\rho = 14$ μm/s.

The measured permeability corresponds to the summation of k_i up to T_{2Gmean}, for ρ 10 ± 4 μm/s for the majority of samples in Groups 1, and 4, as well as some of the samples groups 2 and 3 (Figure 10). The clay-free porosity from image analysis is less than 2% for samples where $T_{2,max} \approx T_{2Gmean}$ (1A, 2A, 3A, 4A, 4B, Table 2). Samples with a higher clay-free porosity require summation over a larger portion of the porosity, indicating a higher connectivity among larger pores. Accordingly, Hossain et al. (2011) require summation

over the full pore volume in order to model permeability for samples where micro-pores are concentrated in glauconite pellets and macro-porosity is in the order of 20%. As permeability rises proportional to $1/S_p^2$ the permeability per T_2 increment rises sharply with T_2; therefore the largest connected pores make a dominant contribution to the sample permeability (Figure. 9).

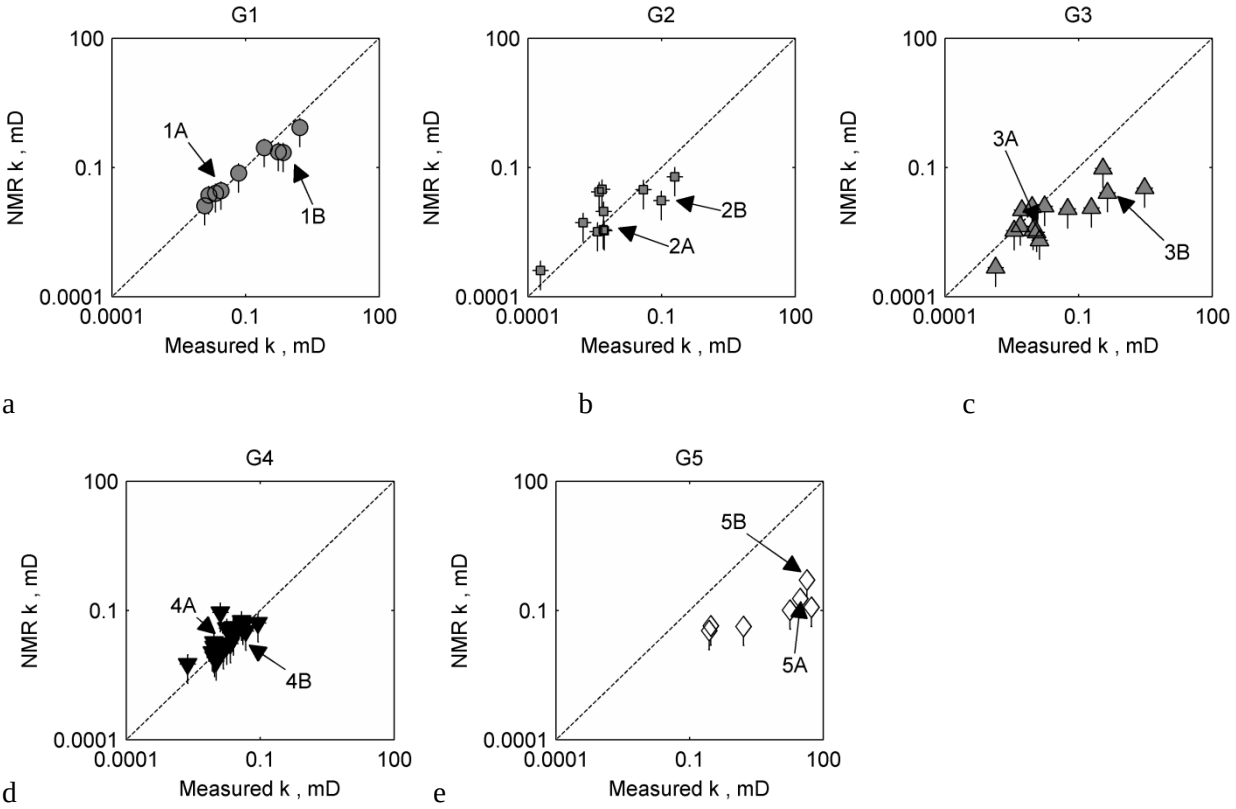

Figure 10: NMR permeability (*k*) from summation of permeability of pores up to the mean T_2 time, T_{2Gmean}, for $\rho = 10 \pm 4$μm/s. Permeability is dominated by pores smaller than T_{2Gmean} in groups G1, G2 and G4 whereas the majority of the samples in G3 and G5 have a higher permeability.

Connectivity cannot be directly measured from 2D image analysis, however, the fraction of clay-free porosity indicates in which samples clay-free pores are connected. Sample 1B is the sample with the lowest clay free porosity, 2.5%, in which $T_{2,max} > T_{2Gmean}$. This is in the same order as percolation threshold porosity values that are used for clay-free sandstones with a low porosity by e.g. Mavko and Nur (1997) and Walderhaug et al. (2012). In those samples, the percolation threshold would relate to the minimum porosity that is required in order for the porosity to form a connected path through the sample. In these samples, a clay-free porosity threshold would be required for the clay-free pores to form a connected path; in samples with a lower clay-free porosity, clay-free pores would be connected through pores in the clay mineral fraction and those pores would control permeability.

The fraction of the clay-free porosity does not predict $f_{\phi,eff}$, e.g., Samples 5A and 5B have the same $f_{\phi,eff}$, although sample 5B has a three times higher clay-free porosity (Tables 2 and 3). The extent to which larger pores contribute to flow would depend on the pore shape and 3D connectivity, which is not characterised by only clay-free porosity. Similarly the clay-free porosity threshold would be sample dependent, and the minimum of 2.5% found by us is based on analysis of a limited number of samples. The image resolution would also affect the fraction of clay free porosity, because at a higher resolution a higher clay-free porosity can be resolved. Nonetheless, for a comparison among a set of sandstones using the same images, image segmentation, rather than the shape of the NMR curve or the clay content from XRD, gave the best prediction of samples in which permeability would be controlled by smaller pores and where permeability can be modelled by summation of k_i up to T_{2Gmean}.

555 Table 3: Effective fraction of porosity is the fraction of porosity that accounts for the measured permeability.
556 The maximum effective pore radius corresponds to maximum T_2 of the effective fraction of porosity, and
557 effective specific surface $S_{p,eff}$ is calculated from the measured permeability and the total effective porosity.
558 Immobile layer thickness is the thickness of bound water that would result in the measured brine
559 permeability if the maximum effective pore radius to brine flow were the same as to gas flow. Refer to text
560 for details. Error margins in brackets indicate result range for ρ 6-14 μm/s.

Group		Measured Permeability mD	Effective fraction of porosity	Maximum effective radius to gas μm rho=10μm/s	$S_{p,eff}$ m^2/cm^3 rho=10μm/s	Immobile layer thickness nm
1	A	0.021	0.49 (0.07)	0.20 (0.02)	23 (2)	40 (10)
	B	0.55	0.55 (0.09)	0.70 (0.04)	6.1 (0.5)	120 (30)
2	A	0.0052	0.55 (0.11)	0.09 (0.02)	45 (5)	10 (2)
	B	0.099	0.68 (0.12)	0.35 (0.05)	12.0 (1.1)	100 (20)
3	A	0.0096	0.70 (0.12)	0.11 (0.03)	35 (3)	22 (4)
	B	0.45	0.76 (0.08)	0.81 (0.07)	7.6 (0.4)	210 (20)
4	A	0.0094	0.40 (0.10)	0.15 (0.03)	27 (4)	35 (5)
	B	0.022	0.46 (0.07)	0.231 (0.010)	20 (2)	45 (5)
5	A	31	0.87 (0.11)	5.0 (0.3)	0.96 (0.06)	1100 (100)
	B	43	0.87 (0.14)	5.7 (0.7)	0.85 (0.07)	550 (50)

561

562

563 When permeability is controlled by a fraction of the pore volume, the specific surface area that is effective
564 with regards to permeability in Eq. (1) would be the specific surface relative to the fraction of pores that
565 control permeability. The mean effective specific surface, $S_{p,eff}$, was calculated from the effective porosity
566 and permeability by using Eq. (13)

567 $$S_{p,eff} = \sqrt{\frac{c\phi f_{\phi_{eff}}}{k}} \quad (13)$$

568 Figure 11 shows a positive correlation between $S_{p,eff}$ and volumetric clay content per inter-granular volume
569 (porosity + clay mineral volume) whereby samples in different groups fall on different lines. Samples

dominated by illite fibres in Group 4 have the highest $S_{p,eff}$ for a given clay content, whereas samples containing a larger kaolin or mica/illite platelets (Group 1 and 3) show a lower $S_{p,eff}$. This also indicates that permeability is indeed controlled by the specific surface of pores in among clay particles, and accordingly the specific surface of illite is higher than the specific surface of kaolin (Matteson and Tomanic, 2000; Santamarina et al., 2002). Those samples from group 5, represented by 5A and 5B where large pores control flow accordingly show a low $S_{p,eff}$ (Figure 11; Table 3).

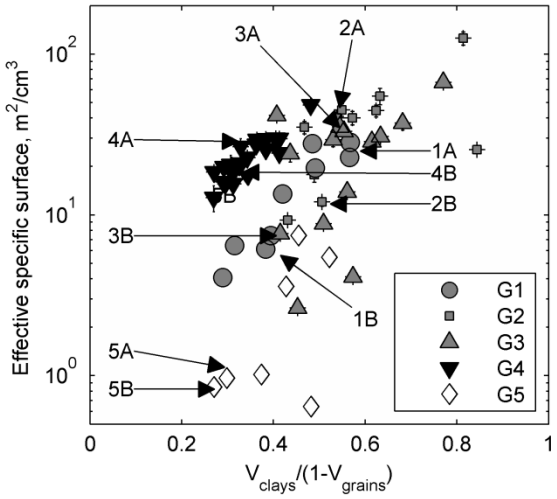

Figure 11: Effective specific surface area versus clay volume scaled by inter-granular volume $(V_{clay})/(1 - V_{grains})$. Samples from different groups have different clay types and different clay morphologies, this results in a different effective specific surface area for a given clay content.

582 7.4.1 Gas slip

583 Gas slip contributes to gas flow when the mean free path length of gas molecules, λ, is approximately one to
584 three orders of magnitude smaller than a characteristic length $0.001 < \frac{\lambda}{r} < 0.1$ (Cao et al., 2009). With a
585 pore pressure of 6.7 MPa, $\lambda \approx 3$ nm for helium c.f. Eq. (14) (Loeb. 1927) .

586
$$\lambda = \frac{\mu}{P}\sqrt{\frac{\pi R_g T}{2M}} \tag{14}$$

587 where μ is the gas viscosity, P is the mean pore pressure, R_g is the gas constant, T is temperature and M is
588 the molar mass of the gas. A higher apparent permeability due to gas slip is related to the true permeability
589 by Eq. (15) and Eq. (16) (Klinkenberg. 1941).

590
$$k_a = k\left(1 + \frac{b}{P}\right) \tag{15}$$

591
$$b = \frac{4c\lambda P}{r} \tag{16}$$

592 As a first approximation to characterize the effect of gas slip on our results we used the mean effective radius
593 r_{eff} in Eq. (16). The effect of gas slip cf. Eq. (15) and Eq. (16) would be largest for sample 2A, which has
594 the smallest r_{eff} (Table 3); in this sample k_a/k = 1.3. The summation of k_i up to the lower true
595 permeability k yields r_{max} = 0.076 ± 0.007 μm as compared to the r_{max} = 0.087 ± 0.008 μm/s for the
596 measured permeability and $f_{\phi,eff}$ = 0.51 ± 0.11 as compared to 0.55 ± 0.11. The difference due to slip is
597 smaller than the difference due to the error margin on ρ. For the other samples that have a larger r_{eff} the
598 effect of gas slip would be even smaller.

599 6.5 Modelling permeability to brine

600 The measured brine permeability is lower than the measured gas permeability for all samples (Figure 6b). On
601 average gas permeability is eight times higher than brine permeability; which is significantly larger than the

602 effect of gas slip estimated in Section 6.4. One reason for the difference in permeability to brine and water
603 could be a layer of bound water on the mineral surface that reduces the pore volume that is available to brine
604 flow (Andreassen and Fabricius, 2010; Heid et al., 1950; Luffel et al., 1993; Solymar et al., 2003). Another
605 reason could be the reversible collapse of fibrous illite during drying (De Waal et al., 1988; Luffel et al.,
606 1993).

607 The effect of bound water can be modelled as a reduction of the effective pore size. Solymar et al. (2003) did
608 this by modelling a layer of bound water on the grain surface in images. However, this requires images with
609 a higher resolution than the 3 μm in Figure 4. Therefore we model the effect of bound water on the pore size
610 distribution from NMR. The free pore volume that is available to water, $\phi fw_{nmr,i}$, is given by the fraction
611 that is available to air, $\phi f_{NMR,i}$, minus the thickness of bound water, τ, on the grain surface Eq. (17):

612 $$\phi fw_{NMR,i} = \phi f_{NMR,i} - \tau S_i \tag{17}$$

613 Substitution of Eq. (2) where $S_p = S/\phi$ gives Eq. (18).

614 $$\phi fw_{NMR,i} = \phi f_{NMR,i} - \frac{\tau\phi}{\rho T_{2,i}} \tag{18}$$

615 Whereas $\sum f_i = 1$, i.e. all porosity is available for gas flow, due to bound water $\sum f_{i,w} < 1$. As a first
616 approximation, S is constant so that the specific surface per pore volume of free water, $Sw_{p,i}$ is Eq. (19)

617 $$Sw_{p,i} = \frac{S_i}{fw_{NMR,i}\phi} = \frac{S_i}{f_{NMR,i}\phi}\frac{f_{NMR,i}}{fw_{NMR,i}} = S_{p,i}\frac{f_{NMR,i}}{fw_{NMR,i}} \tag{19}$$

618 Substitution into Eq. (10) yields the brine permeability, $k_{w,i}$, of pores for a given T_{2i} in Eq. (20), where $c_{w,i}$
619 is cf. Eq. (11) using $fw_{NMR,i}$.

620 $$k_{w,i} = \rho^2 c_{w,i}\phi fw_{NMR,i}T_{2,i}^2\left(\frac{fw_{NMR,i}}{f_{NMR,i}}\right)^2 \tag{20}$$

We assumed that those pores that do not control gas flow because they are connected through smaller pores, also do not control brine flow. Therefore, from summation of $k_{w,i}$ up to the same maximum $T_{2,i}$ that was obtained from gas permeability and the measured brine permeability we estimated the value of τ that would be required to account for the measured permeability difference between gas and brine. Figure 12 shows the gas and the brine porosity and permeability distributions for representative samples.

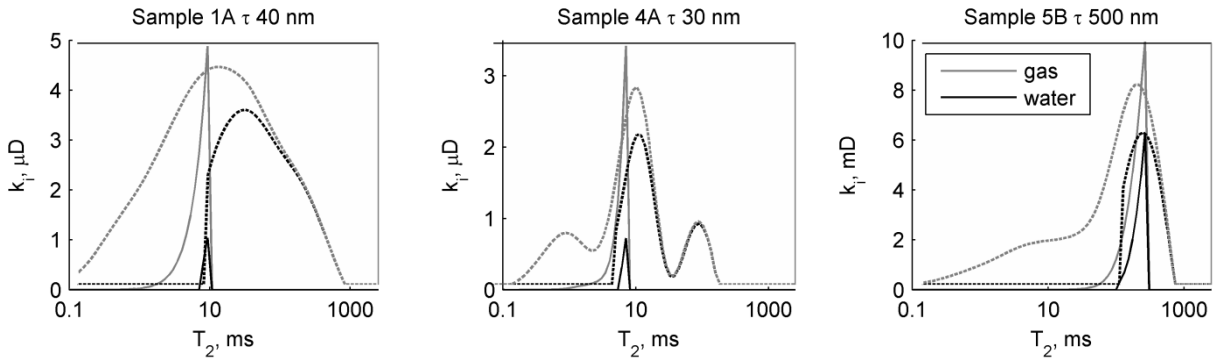

a b c

Figure 12: The permeability k_i is shown up to the maximum T_2, $T_{2,max}$, where the cumulative k_i equals the measured permeability for gas. Brine permeability is shown for the immobile layer thickness, τ, which accounts for the measured water permeability. The porosity to brine is lower than the porosity to gas due to the immobile water on the pore walls.

For samples in groups 1, 3 and 4, τ is in the order of 50 nm, whereas for samples in Group 5, τ ranges up to 1 µm (Fig. 13). Measurements of the bound water layer are affected by the experimental techniques used (Goertz et al., 2007), however, experiments with flow through thin quartz capillaries indicate a bound water layer thickness of 8 nm (Zheleznyi et al., 1972). The higher estimated τ suggests that other factors contribute to the lower brine permeability.

This could be the alteration of fibrous illite clay minerals as suggested by Luffel et al. (1993). Those authors found that the effect was larger in samples with a lower permeability and caused a permeability increase of a factor five to gas in a sample with 0.7 mD permeability. All groups contain 5% illite or more, and clay fibres perpendicular to the grain surface can be observed in BSEM and SEM images (Figures 4 and 7). These samples were also air dried; therefore the presence of illite perpendicular to the grains indicates that not all

illite was affected by drying, which was also observed in North Sea samples by Wilson et al. (2014). The additional reduction of the effective pore size to brine was estimated by calculating the maximum effective pore size for brine permeability, $r_{max,brine}$ for τ 10 nm. Figure 14 shows that the difference between $r_{max,brine}$ and $r_{max,gas}$ increases with $r_{max,gas}$.

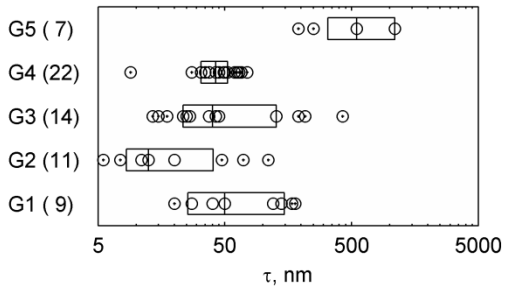

Figure 13: The thickness of bound water, τ that would need to be invoked in order to account for the measured difference between gas and brine permeability if the same pores controlled flow. The mobile porosity to brine may be lower than to gas due to a combination of bound water on the mineral surface and to illite fibres that are perpendicular to the grain surface in a saturated sample but collapse on the grain surface during drying.

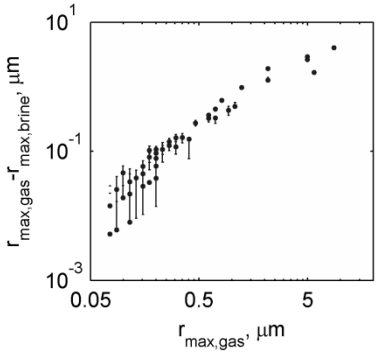

Figure 14: When a bound water layer thickness of 10 nm is assumed, the size of the largest pores that are effective for gas flow $r_{max,gas}$ exceeds the size of the largest pores that contribute and the largest pores that are effective for brine flow, $r_{max,brine}$. The difference $r_{max,gas} - r_{max,brine}$ is shown on the y-axis and $r_{max,gas}$ is shown in the x-axis. Error bars indicate $r_{max,gas} - r_{max,brine}$ for bound water layer thickness 5 and 20 nm.

8 Conclusions

We analysed permeability to brine and to gas for 63 Rotliegend sandstone samples by means of nuclear magnetic resonance transverse relaxivity data, mercury injection, X-ray diffraction, and image analysis.

- Principal component analysis, PCA, of the sample mineralogy showed that clay mineralogy dominates variations among samples, and that samples from the same geographical location are grouped together.
- Permeability to gas was modelled using the pore size distribution from NMR to estimate which pores control flow. The range of pores that control flow depends on the distribution of clays in the pore volume, rather than on the total clay content; therefore image analysis rather than quantitative XRD indicates in which samples permeability is controlled by small pores.
- The measured gas permeability could be accounted for by the fraction of porosity that with a pore size smaller the mean pore size in 38 out of 63 samples.
- Surface relaxivity was estimated from the specific surface area as calculated from mercury injection data and the specific surface area from NMR data.
- Permeability to brine was modelled by including a bound water layer, a water layer of 10 nm was insufficient to account for the measured permeability. This indicates that other factors such as the presence of fibrous illite contribute to the lower brine permeability.

9. Acknowledgements

We acknowledge Aurelian, BG, BP, EBN, Shell and Wintershall. Rosenbrand acknowledges funding from the Otto Mønsted fund and the Danish Council for Strategic Research.

680 References

681 Alam, M. M., Katika, K., Fabricius, I. L., 2014. Effect of salinity and specific ions on amount of bound
682 water on quartz, calcite and kaolinite, as observed by NMR transverse relaxation time (T2). In 76th
683 EAGE Conference and Exhibition. Amsterdam RAI, The Netherlands: Amsterdam RAI, The
684 Netherlands

685 Andreassen, K., Fabricius, I. L., 2010. Biot critical frequency applied to description of failure and yield of
686 highly porous chalk with different pore fluids. GEOPHYSICS. 75, E205–E213

687 API, 1998. Recommended Practices for Core Analysis, API RP 40. Washington: American Petroleum
688 Institute: Washington

689 Byerlee, J., 1990. Friction, overpressure and fault normal compression. Geophys. Res. Lett. 17, 2109–2112

690 Cao, B., Sun, J., Chen, M., Guo, Z., 2009. Molecular Momentum Transport at Fluid-Solid Interfaces in
691 MEMS/NEMS: A Review. Int. J. Mol. Sci. 10, 4638–4706

692 Coates, G. R., Xiao, L., Prammer, M. G., 1999. NMR Logging Principles and Applications. Houston:
693 Halliburton Energy Services: Houston

694 Dastidar, R., Sondergeld, C. H., Rai, C. S., 2006. NMR Desaturation and Surface Relaxivity Measurements
695 on Clastics Rocks. In SPE EUROPEC/EAGE Annual Conference and Exhibition. Vienna, Austria

696 De Waal, J. A., Bil, K. J., Kantorowicz, J. D., Dicker, A. I. M., 1988. Petrophysical Core Analysis Of
697 Sandstones Containing Delicate Illite. Log Anal. Sept-Oct, 317–331

698 Desbois, G., Urai, J. L., Kukla, P. A., Konstanty, J., Baerle, C., 2011. High-resolution 3D fabric and porosity
699 model in a tight gas sandstone reservoir: A new approach to investigate microstructures from mm- to
700 nm-scale combining argon beam cross-sectioning and SEM imaging. J. Pet. Sci. Eng. 78, 243–257

Durand, C., Cerepi, A., Brosse, E., 2000. Effect of pore-lining chlorite on petrophysical properties of low-resistivity sandstone reservoir. In Proceedings - SPE Annual Technical Conference and Exhibition.

Gaupp, R., Okkerman, J. A., 2011. Diagenesis and reservoir quality of Rotliegend sandstones in the Northern Netherlands - A review. Soc. Sediment. Geol. SEPM Spec. Publ. 98, 193–226

Giesche, H., 2006. Mercury porosimetry: a general (practical) overview. Part. Part. Syst. Charact. 23, 9–19

Goertz, M. P., Houston, J. E., Zhu, X.-Y., 2007. Hydrophilicity and the viscosity of interfacial water. Langmuir. 23, 5491–5497

Grim, R. E., 1953. Clay Mineralogy. (Vol. 1). New York: McGraw-Hill Book Company inc.: New York

Heid, J. G., McMahon, J. J., Nielsen, R. F., Yuster, S. T., 1950. Study of the Permeability of Rocks to Homogeneous Fluids. American Petroleum Institute

Hillier, S., 1999. Use of an air brush to spray dry samples for X-ray powder diffraction. Clay Miner. 34, 127–135

Hillier, S., 2000. Accurate quantitative analysis of clay and other minerals in sandstones by XRD: comparison of a Rietveld and a reference intensity ratio (RIR) method and the importance of sample preparation. Clay Miner. 35, 291–302

Hossain, Z., Grattoni, C. A., Solymar, M., Fabricius, I. L., 2011. Petrophysical properties of greensand as predicted from NMR measurements. Pet. Geosci. 17, 111–125

Jones, F. O., Owens, W. W., 1980. A Laboratory Study of Low-Permeability Gas Sands. SPE J. Pet. Technol. 32, 193–199

Jones, S. C., 1997. A Technique for Faster Pulse-Decay Permeability Measurements in Tight Rocks. SPE Form. Eval. 12, 19–26

722 Keating, K., Knight, R., 2007. A laboratory study to determine the effect of iron oxides on proton NMR
723 measurements. Geophysics. 72, E27–E32

724 Keating, K., Knight, R., 2010. A laboratory study of the effect of Fe (II)-bearing minerals on nuclear
725 magnetic resonance (NMR) relaxation measurements. Geophysics. 75, F71–F82

726 Kozeny, J., 1927. Über kapillare Leitung des Wassers im Boden. Sitzungsberichte Der Akad. Der
727 Wissenschaften Wien, Math. Klasse. 136, 271–306

728 Landrot, G., Ajo-Franklin, J. B., Yang, L., Cabrini, S., Steefel, C. I., 2012. Measurement of accessible
729 reactive surface area in a sandstone, with application to CO2 mineralization. Chem. Geol. 318-319,
730 113–125

731 Lenormand, R., 2003. Interpretation of mercury injection curves to derive pore size distribution. In
732 International Symposium of the Society of Core Analysts. Pau France

733 Luffel, D., Herrington, K., Walls, J., 1993. Effect of Drying on Travis Peak Cores Containing Fibrous Illite.
734 SPE Adv. Technol. Ser. 1, 188–194

735 Matteson, A., Tomanic, J., 2000. NMR relaxation of clay/brine mixtures. SPE Reserv. Eval. Eng. 3, 408–413

736 Mavko, G., Nur, A., 1997. The effect of a percolation threshold in the Kozeny-Carman relation. Geophysics.
737 5, 1480–1482

738 Mbia, E. N., Fabricius, I. L., Krogsbøll, A., Frykman, P., Dalhoff, F., 2014. Permeability, compressibility
739 and porosity of Jurassic shale from the Norwegian-Danish Basin. J. Pet. Geosci. (In press)

740 McBride, E. F., 1963. A classification of common sandstones. J. Sediment. Res. 33, 664–669

741 Miranda, A., Borgne, Y.-A., Bontempi, G., 2008. New Routes from Minimal Approximation Error to
742 Principal Components. Neural Process. Lett. 27, 197–207

743 Mortensen, J., Engstrøm, F., Lind, I. ., 1998. The Relation Among Porosity, Permeability, and Specific
744 Surface of Chalk From the Gorm Field, Danish North Sea. SPE Reserv. Eval. Eng. 1, 245–251

745 Peters, C. A., 2009. Accessibilities of reactive minerals in consolidated sedimentary rock: An imaging study
746 of three sandstones. Chem. Geol. 265, 198–208

747 Rootare, H. M., Prenzlow, C. F., 1967. Surface areas from mercury porosimeter measurements. J. Phys.
748 Chem. 71, 2733–2736

749 Santamarina, J. C., Klein, K. A., Wang, Y. H., Prencke, E., 2002. Specific surface: determination and
750 relevance. Can. Geotech. J. 39, 233–241

751 Solymar, M., Fabricius, I. L., 1999. Image analysis and estimation of porosity and permeability of Arnager
752 Greensand, Upper Cretaceous, Denmark. Phys. Chem. Earth, Part A Solid Earth Geod. 24, 587–591

753 Solymar, M., Fabricius, I. L., Middleton, M., 2003. Flow characterization of glauconitic sandstones by
754 integrated Dynamic Neutron Radiography and image analysis of backscattered electron micrographs.
755 Pet. Geosci. 9, 175–183

756 Torrent, J., Schwertmann, U., 1987. Influence of hematite on the color of red beds. J. Sediment. Petrol. 57,
757 682–686

758 Walderhaug, O., Eliassen, a., Aase, N. E., 2012. Prediction of Permeability In Quartz-Rich Sandstones:
759 Examples from the Norwegian Continental Shelf and the Fontainebleau Sandstone. J. Sediment. Res.
760 82, 899–912

761 Washburn, E. W., 1921. The Dynamics of Capillary Flow. Phys. Rev. 17, 273

762 Wilson, M. D., Pittman, E. D., 1977. Authigenic clays in sandstones; recognition and influence on reservoir
763 properties and paleoenvironmental analysis. J. Sediment. Res. 47, 3–31

764 Wilson, L., Wilson, M. J., Green, J., Patey, I., 2014. The Influence of Clay Mineralogy on Formation
765 Damage in North Sea Reservoir Sandstones: A Review with Illustrative Examples. Earth-Science Rev.
766 (accepted manuscript)

767 Zheleznyi, B. V, Zorin, Z. M., Sobolev, W. D., Churaev, N. V, 1972. Experimental study of properties of
768 water in thin films and fine capillaries. Bull. Int. Assoc. Eng. Geol. 5, 57–61

769

Appendix A: Principal Component Analysis

Table A1: Orthonormal principal components loadings for minerals for principal component analysis on 63 samples. Mineral content is centred and normalised. Values greater than 0.35 are bold.

	PC1	**PC2**	**PC3**	**PC4**	**PC5**	**PC6**
variance explained %	26	18	13	13	8	7
Quartz	**0.37**	-0.04	0.08	**0.40**	0.00	**0.38**
Albite	**0.40**	0.12	0.18	-0.21	-0.20	**-0.38**
Microcline	-0.27	0.25	**0.35**	0.22	-0.28	**-0.38**
Calcite	0.08	-0.12	0.12	0.36	**0.65**	**-0.46**
Dolomite	-0.12	-0.14	**-0.36**	**0.44**	-0.30	0.08
Illite/mica	**0.35**	-0.03	-0.34	-0.13	0.11	-0.34
Kaolin	**-0.45**	-0.10	-0.22	-0.15	0.14	-0.05
Chlorite	**0.36**	0.14	-0.19	**-0.42**	0.03	0.11
Pyrite	-0.19	0.00	**-0.57**	-0.06	-0.17	-0.33
Siderite	-0.05	**-0.57**	0.02	-0.11	0.25	-0.02
Barite	-0.01	**-0.55**	0.10	-0.21	-0.11	0.13
Anhydrite	0.03	**-0.42**	0.31	-0.10	**-0.42**	-0.28
Pores	-0.34	0.23	0.25	**-0.36**	0.24	0.13

Table A2: Orthonormal principal components loadings for minerals for principal component analysis on 43 samples. Mineral content is centred and normalised. Values greater than 0.35 are bold.

	PC1	**PC2**	**PC3**	**PC4**	**PC5**	**PC6**
variance explained %	30	18	14	10	8	8
Quartz	-0.11	**0.49**	-0.33	-0.11	-0.02	-0.33
Albite	0.33	-0.33	0.04	-0.09	**-0.35**	0.30
Microcline	**0.44**	0.06	-0.01	0.12	-0.31	-0.05
Calcite	-0.07	0.02	-0.07	**-0.83**	-0.14	0.16
Dolomite	-0.22	0.21	0.00	0.17	0.09	0.77
Illite/mica	-0.13	-0.08	**0.58**	-0.15	-0.25	-0.33
Kaolin	**-0.43**	-0.12	0.12	-0.06	0.08	0.07
Chlorite	0.27	-0.33	0.23	-0.19	0.33	0.10
Pyrite	-0.19	0.09	**0.54**	0.29	-0.14	0.01
Siderite	**-0.34**	**-0.40**	-0.08	-0.12	0.20	-0.07
Barite	-0.26	**-0.40**	-0.24	0.19	0.07	-0.18
Anhydrite	-0.11	**-0.37**	-0.35	0.20	**-0.49**	0.01
Pores	**0.36**	-0.13	-0.03	0.10	**0.52**	-0.11

778

Appendix C: Conference Papers

- Conference paper I: Effect Of Hot Water Injection On Sandstone Permeability: An Analysis Of Experimental Literature.
  Co-authors: Fabricius, IL
  Proceedings of the EAGE Annual Conference and Exhibition incorporating SPE Europec, Copenhagen,4-7 June 2012, 11pp.

- Conference paper II: Thermally induced permeability reduction due to particle migration in sandstones: the effect of temperature on kaolinite mobilisation and aggregation
  Co-authors: Fabricius, IL; Yuan, H
  Proceedings of the Thirty-Seventh Workshop on Geothermal Reservoir Engineering Stanford University Stanford California, 30 January- 1 February 2012, 9pp.

- Conference paper III: Kaolinite Mobilisation in Sandstone: Pore Plugging vs. Suspended Particles
  Co-authors: Fabricius, IL; Kets,F
  Proceedings of the Thirty-Eighth Workshop on Geothermal Reservoir Engineering Stanford University Stanford California, 11-13 February 2013, 12 pp.

SPE 154489

Effect Of Hot Water Injection On Sandstone Permeability: An Analysis Of Experimental Literature

Esther Rosenbrand, SPE, Center for Energy Resources Engineering Technical University of Denmark and Ida Lykke Fabricius, SPE, Center for Energy Resources Engineering, Technical University of Denmark

This paper was prepared for presentation at the EAGE Annual Conference & Exhibition incorporating SPE Europec held in Copenhagen, Denmark, 4–7 June 2012.

Abstract

The seasonal imbalance between supply and demand of renewable energy requires temporary storage, which can be achieved by hot water injection in warm aquifers. This requires that the permeability and porosity of the aquifer are not reduced significantly by heating.

We present an overview of published results regarding the effect of temperature on sandstone permeability. These tests are performed with mineral oil, nitrogen gas, distilled water and solutions of NaCl, KCl, $CaCl_2$ as well as brines that contain a mixture of salts. Thirteen sandstone formations, ranging from quartz arenites to formations with a significant fraction of fine particles including clay minerals are investigated. The porosities range from 0.10 to 0.30 and permeabilities span the range from 1 to 1000 md. To compare different rock types, specific surface is determined from permeability and porosity using Kozeny's equation.

Heating causes thermal expansion, which results in porosity reduction if the sandstone is confined. The maximum effect of porosity reduction as a result of thermal expansion on permeability is modelled and compared the change in specific surface that is computed from the reported data. This does not account for all the permeability reductions observed.

Permeablity reduction occurs both when distilled water is the saturating fluid as well as in tests with NaCl, KCl or $CaCl_2$ solutions, however, this is not the case in tests with mineral oil or nitrogen gas. The formation of a filter cake or influx of colloidal particles due to corrosion of the apparatus at elevated temperature causes permeability reduction in a number of investigations. Mobilisation of internal particles, particularly kaolinite particles, is considered a probable mechanism of permeability reduction for the other experiments reviewed here.

The parameters that strongly affect the success of heat storage therefore include the quality of the equipment and particularly the prevention of corrosion, as well as the sandstone lithology and its interaction with the reservoir fluid.

Introduction

An imbalance in supply and demand of renewable energy requires seasonal storage, which can be achieved by hot water injection in warm aquifers. This requires that the permeability and porosity of the aquifer are not reduced significantly by heating. The mechanisms responsible for possible porosity and permeability reduction must be identified, in order to select geological formations that are suitable for heat storage.

The effect of heating on sandstone permeability is addressed in multiple laboratory studies, but results vary widely among investigations ranging from no change to a 99% permeability decline. A systematic interpretation of the body of published data involves comparison between different lithological units and different experimental procedures to assess under which conditions permeability reduction occurs. The quality of the experimental data varies; in a number of cases experimental error is discovered and verified to be the only cause of the permeability reduction. However, there exist both mechanical and physico-chemical mechanisms that can lead to permeability reduction of sandstone at elevated temperature.

Chemical interaction of the fluid and the experimental apparatus causes a permeability reduction in a number of investigations (Potter et al. 1981; Stottlemyre 1981; Milsch et al. 2009). Corrosion products result in formation of a filter cake at the sample inlet or clogging of the sandstone pores. Mechanical problems (Sageev et al. 1980) and insufficient time for equilibration of the sample can result in unreliable data. Furthermore, the viscosity value used to compute permeability from experimental data may differ from the actual viscosity due to chemical dissolution or precipitation.

Thermal expansion of the solid frame occurs in all types of sandstone, resulting in porosity reduction when the rock is prevented from expanding. The effect of thermal expansion on permeability is predicted by e.g., Stottlemyre (1981), Somerton (1992) and Baudracco and Aoubouazza (1995). Somerton (1992, pp 192-193) predicts the largest permeability reduction, of approximately 20% for heating from 20 to 90˚C; whereas Stottlemyre (1981) and Baudracco and Aoubouazza (1995) predict a reduction of less than 5% for the same temperature range. The variation is due to differing assumptions regarding the expansion of the solids and the bulk volume, as well as to the different models used to relate porosity to permeability.

Porosity reduction can furthermore be due to increased compressibility of the sandstone at elevated temperature. Measurements of sandstone compressibility in 8 samples indicate pore volume compressibility is on average 20% higher at 200˚C than at room temperature (Von Gonten and Choudhary 1969).

Fluid mineral interaction can result in a different permeability of the same sandstone sample to different saturating fluids (Wei et al. 1986; Baudracco and Aoubouazza 1995). One mechanism that can explain this is the formation of an electrical double layer (EDL) on the surface of the grains (Andreassen and Fabricius 2010). The EDL in sandstone is a consequence of interaction of the quartz surface with water molecules resulting in a surface charge that attracts oppositely charged ions [e.g., Revil et al. (1996) and Lorne et al. (1999)]. The EDL is comprised of the layer of ions adsorbed to the surface and a diffuse layer of attracted ions. Water in part of the EDL can be presumed to be less mobile than in the bulk solution (Tchistiakov 2000). The thickness of the EDL depends on how effectively the surface charge is shielded, which is affected by the solution composition as well as by temperature.

Swelling of certain clay minerals in contact with aqueous solutions can cause permeability reduction. The degree of swelling is affected by both the clay mineral structure and the solution composition (Sposito et al. 1999), and its effect on permeability depends on the distribution of clays in the sandstone pores (Tchistiakov 2000).

Particle mobilisation and their subsequent filtration can lead to significant permeability reductions (Mungan, 1965). Mobilisation of kaolinite particles due to heating can be attributed to an increase in the electric double layer repulsive force acting between the quartz and kaolinite surfaces (Schembre and Kovscek 2004). The surface forces acting on a colloid can be computed using Derjaguin-Landau-Verwey-Overbeek (DVLO) theory. This is used to predict the kaolinite particle mobilisation observed as a consequence of a reduction of the ionic strength. The reduction of the ionic strength causes an increase in the EDL force on the kaolinite particles [e.g., Khilar and Folger (1984), Tchistiakov (2000), Schembre and Kovscek (2004)]. The effect of heating on particle mobilisation, however, is not observed in all investigations. Khilar and Folger (1984) report that heating does not affect the ionic strength at which kaolinite particles are mobilized; Schembre and Kovscek (2004) on the other hand do find particle mobilisation as a consequence of heating.

Typically fines are clay minerals residing in the space between quartz grains but other sources exist. Blair et al. (1984) suggest that dissolution of silica or calcite cement can also release fines. Grain cracking due to differential thermal expansion of the mineral constituents is furthermore suggested as a possible source of fines by Stottlemyre (1981). Zuo et al. (2010) observe this process in the Pingdingshan sandstone and find it occurs predominantly when temperatures exceed 150°C.

In this paper, the use of the surface area per unit pore volume, S_p, is introduced, as a measure to compare porosity and permeability change of different geological formations. An extensive compilation of published data regarding permeability change as a consequence of heating is used to investigate the extent to which different mechanisms affect S_p.

Theory

Specific Surface

The specific surface, S, is defined as the surface area/rock volume ratio. This appears in the Kozeny (1927) equation to relate permeability, k, to porosity, φ, of a homogenous sedimentary rock:

$$k = \frac{c\varphi^3}{S^2} \quad \text{.....(1)}$$

The factor c accounts for the geometry of the porous medium, and can be expressed as a direct function of porosity (Mortensen et al. 1998).

$$c = \left(4cos\left(\frac{1}{3}arccos\left(\varphi\frac{8}{\pi^3} - 1\right) + \frac{4}{3}\pi\right) + 4\right)^{-1} \quad \text{.....(2)}$$

The ratio S_p (Eq. 3), expresses the surface area per unit of pore volume. This is inversely related to the pore radius i.e., $r \propto 1/S_p$, and thereby allows comparison of porosity and permeability changes between lithologies with different porosity.

$$S_p = \frac{S}{\varphi} = \sqrt{\frac{c\varphi}{k}} \quad \text{.....(3)}$$

To predict the effect of a porosity change on S_p, S_p is expressed as a function of S_s (Eq. 4) where S_s is the surface area per unit volume of solids (Eq. 5).

$$S_p = \frac{(1-\varphi)S_S}{\varphi} \quad \text{.....(4)}$$

$$S_s = \frac{S}{1-\varphi} \quad \text{.....(5)}$$

Grain shape and surface roughness affect the S_s of sandstone grains, but the effect of heating on these is presumed to be minor. An increase in volume can therefore be expected to reduce S_s, however, the extent of this is unknown. To predict an upper limit of the change in S_p as a consequence of thermal expansion we assume S_s to be constant in Eq. 4.

Porosity Change

Porosity change due to thermal expansion is determined by the expansion of both the solids and the bulk volume. In-situ, the bulk volume is prevented from expanding and expansion of the solids induces porosity reduction. On the other hand, in laboratory tests the bulk expansion depends on the confining pressure. The linear thermal expansion coefficients, α, measured for three sandstone lithologies by Somerton et al. (1981) are similar to that of quartz perpendicular to the c-axis. In this case the porosity remains constant with temperature change. The porosity, $\varphi_{\Delta T}$, after a temperature change, ΔT, is computed using Eq. 6 where α_{solid} and α_{bulk} are the linear thermal expansion coefficients of the solid and the bulk respectively.

$$\varphi_{\Delta T} = 1 - \frac{(1-\varphi_0)(1+3\alpha_{solid}\Delta T)}{1+3\alpha_{bulk}\Delta T} \quad \ldots\ldots(6)$$

Electrical Double Layer

The formation of an EDL on the quartz surface is expected to lead to a reduction in the mobility of the fluid closest to the surface, and consequently a reduction in the effective pore space. For a detailed description of the electrical charge on the mineral surface and the charge distribution in the EDL in sandstone the reader is referred to Revil et al. (1996) and Lorne et al. (1999). Silanol groups (SiOH) form by interaction of the quartz surface with water; the gain or loss of H^+ results in a surface charge that depends on the H^+ concentration (pH) of the solution. The surface charge attracts oppositely charged ions, resulting in the formation of a diffuse layer whose charge counters the surface charge. The concentration of ions in the EDL is dependent on their concentration in the solution (Lorne et al. 1999). The thickness of the EDL is characterized by the inverse Debye parameter κ^{-1} (Eq. 7), which predicts the distance over which the surface potential is reduced by a factor 1/e, for a flat surface with a limited surface charge in a solution of a low ionic strength (Lyklema 1995).

$$\kappa^{-1} = \sqrt{\frac{\varepsilon_0 \varepsilon_r k_B T}{2e^2 N_A I}} \quad \ldots\ldots(7)$$

k_B is the Boltzmann constant, ε_0 is the vacuum permittivity, ε_r the relative permittivity of the solution, N_A the Avogadro number, e is the electron charge and I is the ionic strength of the solution and T is the absolute temperature. This does not account for the size of the adsorbed ions or the surface geometry (Lyklema 1995).

Eq. 7 suggests that heating results in an increase of κ^{-1} (Andreassen and Fabricius 2010), this applies only when ε_r is assumed constant. A temperature rise causes a more than proportional reduction in the relative permittivity of water. Accounting for this change implies that κ^{-1} is reduced as a consequence of heating. It can be presumed that the thickness of the water layer immobilized in the EDL is similarly reduced. This effect is only present in polar solutions with a low ionic strength. At a high ionic strength (i.e. greater than 0.7 M for NaCl solution) the EDL can be considered to be reduced to a single layer (Revil et al. 1996) and heating can be expected to have no effect on its thickness.

Kaolinite mobilisation

Particle mobilization is predicted to result from an increase in EDL repulsive forces between kaolinite and quartz that can be due to a reduction of ionic strength or to an increase in temperature (Tchistiakov 2000; Schembre and Kovscek 2004).

Kaolinite is a mineral consisting of a silica and alumina sheet and has a different charge on faces and edges (Grimm). The different charges affect the aggregation of suspensions of kaolinite, with different pH the particles collect face face or edge face (Gupta etc.). This affects the rheology of kaolinite suspensions

Heating makes the overall charge more negative (Rodri and Rama).

Data

Data from 17 publications addressing the effect of temperature on permeability of sandstones is presented in **Table 1**. The data represents 13 sandstone formations, ranging from clean sandstones with a high quartz content (Fontainebleau, Massilon and St. Peters Sandstone) to sandstones with a significant clay content (Berea, Boise). When one paper addresses more sandstones, each lithological unit is given a different Arabic number. Experiments consisting of multiple steps, i.e. where different fluids are tested in the same lithology, the steps are indicated by Roman numerals, i.e., No. 1i, 1ii. Firing, heating the sample to temperatures in the range of 400-1000˚C prior to testing, alters the structure of clay minerals (Shaw 1991). For this reason, fired cores are considered as a different lithology from unfired cores.

The clay content and mineralogy are not reported for several tests performed on the Berea and the Boise sandstones. The former consists predominantly of quartz, and contains a fine fraction of up to 20%, where kaolinite is the dominating clay mineral (Somerton et al. 1974). The latter consist of quartz, feldspar and plagioclase grains and contains 35% of fines including kaolinite (Somerton et al. 1974).

Porosity is not reported in all cases. For tests on Berea or Boise sandstone where the measured permeability is reported, the porosity values based on data from related investigations are assumed. For less commonly studied lithologies as well as experiments where the permeability is not reported, the qualitative results are included in the discussion, however our emphasis is placed on results from the more thoroughly documented tests.

In tests 12, 14 and 19, an important conclusion is that the cause of permeability reduction is contamination of the sandstone sample by iron oxides or hydroxides related to corrosion of the equipment. Subsequent tests where this is prevented are performed in those studies; however, in the remaining investigations the absence of corrosion products is not explicitly addressed.

Method

To compare the effect of heating in different lithologies, S_p is computed from the porosity and permeability measurements. As opposed to the permeability, porosity is measured only at room temperature in the majority of the experiments. To account for thermal expansion, the error margin on the porosity measurement is increased as a function of temperature. The minimum porosity is computed using the lower error margin of the porosity measurement in combination with Eq. 6 where α_{bulk} is set to zero. This predicts the porosity assuming that no bulk expansion occurs; the linear thermal expansion coefficient of quartz perpendicular to the c-axis is used for $\alpha_{mineral}$ (Fjaer et al. 2008, pp 441). The maximum porosity at elevated temperature is assumed to be the upper error margin of the reported porosity; it is assumed that $\alpha_{bulk} = \alpha_{mineral}$, i.e., no porosity reduction due to thermal expansion. For permeability the error margins as given in Table 1 are used.

To investigate the effect of heating in situations where there is no electrical double layer formation, data is divided into tests performed with an aqueous solution and those performed with oil or nitrogen gas. Tests with aqueous solutions are furthermore grouped according to the effect of heating on S_p.

Experiments

Tests were performed on Berea sandstone cores, each core was first flooded with distilled water and the temperature was increased from 23˚C to 80˚C and subsequently reduced. At 23˚C the injection fluid was changed to 0.34 M NaCl and the test was repeated. The test parameters are shown in Table 2. Permeability measurements are made at each step using different flow rates (10, 20 and 40 ml/hr).

Results

The predicted maximum porosity reduction resulting from thermal expansion is shown in **Fig. 1a.** Porosity measurements at a confining stress of 14 MPa by Jing et al. (1992) agree with the predicted values. The measured porosity change is caused by both thermal expansion and the increase in compressibility due to heating, whereas the prediction accounts only for thermal expansion. This suggests the increased compressibility has a negligible effect under these test conditions.

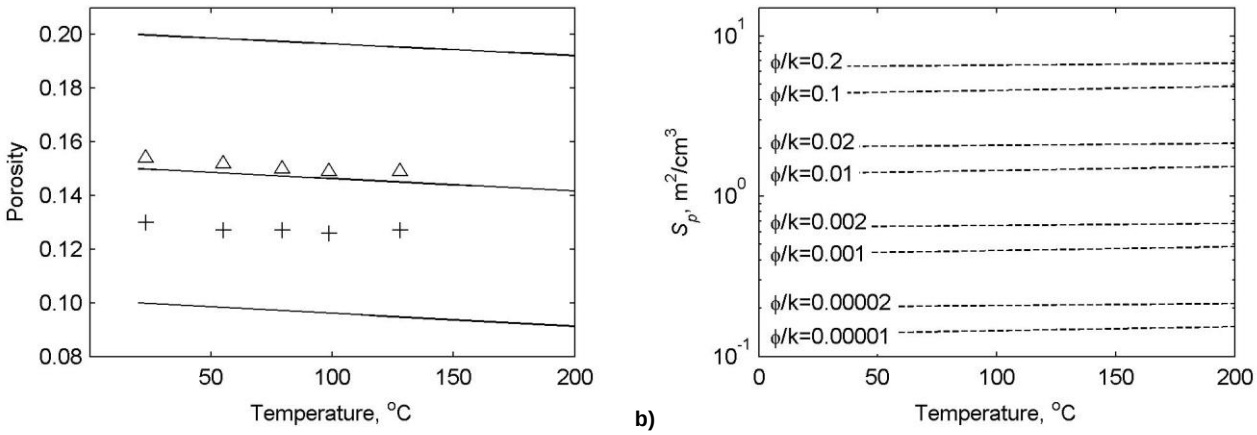

Fig. 1 a) Porosity declines as a function of temperature due to thermal expansion. Lines represent the modeled reduction for a 100% quartz sample. Measured porosity from sandstone samples No. 9 (crosses) and No. 10 (triangles) indicate a similar porosity change. Numbers refer to Table 1.
b) Modeled S_p increases as a consequence of porosity reduction, curves are shown for samples with initial porosity of 0.10 and 0.20 and permeability 1-, 10-, 100-, 1000 md.

The modeled porosity reduction has a minor effect on S_p. **Fig. 1b** shows the computed S_p as a function of temperature. The predicted permeability change resulting from the changes in S_p and φ is larger in rocks with a lower porosity. These have a larger fraction of solids expanding into a smaller volume of pore space. For a rock with a porosity of 0.10, thermal expansion is predicted to cause at most a reduction from 100 to 88 md for a temperature rise of 100°C.

The increase in S_p due to heating does not exceed the predicted maximum effect of thermal expansion in tests performed with an inert saturating fluid, mineral oil or nitrogen gas (**Fig. 2).** In a number of experiments, the permeability at elevated temperature is the same as the permeability at room temperature suggesting that the pore volume is not affected by heating. The lithological units in this figure include both clean sandstones with a high quartz content and a negligible clay fraction (No. 1) as well as samples containing a significant amount of feldspars, matrix and clay minerals (No. 6). The numbers in the figures refer to the sample numbers in Table 1.

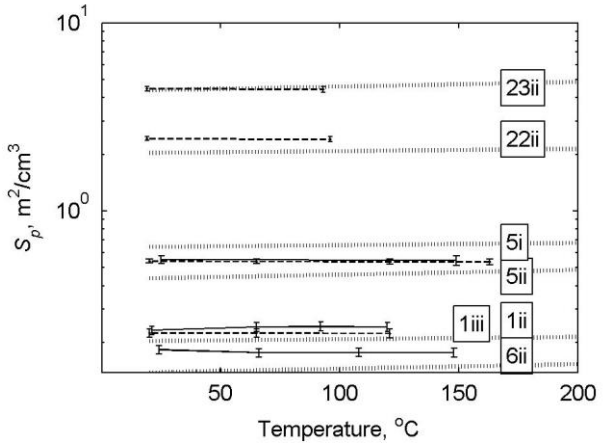

Fig 2: S_p as a function of temperature for samples tested using mineral oil (solid lines) and nitrogen gas (dashed lines), as well as S_p as a function of temperature modeled as a consequence of thermal expansion. Numbers correspond to tests in Table 1.

In tests where an aqueous solution saturates the sample, the permeability reduction ranges from no change **(Fig. 3a)** to a significant reduction **(Figs. 3b, 3c, 3d)**. There is no case where permeability increases as a function of temperature. Tests where the temperature subsequently is reduced indicate that this leads to complete (Fig. 3b) or very significant permeability recovery (Fig. 3c).

Fig. 3a shows tests where no permeability reduction occurs. This is the case for the relatively clay free sandstone sample where contamination is prevented (No. 19iii) as well as samples where the clay mineralogy has been altered by firing, one at a temperature exceeding 700˚C (No. 7) and one where the firing temperature is not reported (No. 15). In tests No. 8 and No. 11 kaolinite mobilisation causes permeability reduction at room temperature, but subsequent heating causes no further reduction. Samples No. 22 and No. 23 contain kaolinite, however, their permeability is not reduced. These samples are only heated up to 68˚C, and are saturated with a KCl solution with an ionic strength of 0.79 M.

The effect of temperature is reversible in the majority of the tests performed with distilled water (Fig 4. b). Exceptions are test No. 19ii (Fig. 3c) due to colloid contamination, and test No. 3i. This sample contains smectite and illite in the clay fraction; whereas the other samples tested with distilled water contain predominantly kaolinite (Fig. 3b).

The S_p at room temperature of samples No. 2 and No. 3 is different when distilled water, NaCl or $CaCl_2$ solution (both with ionic strength of 1M) are the saturating fluids. In sample No. 2 the permeability is higher to distilled water (No. 2i) and $CaCl_2$ solution (No. 2iii) than to NaCl solution (No. 2ii). The S_p increase as a consequence of heating is reversible in the first two cases but during the test with NaCl solution the permeability of the sample is reduced permanently. For sample No. 3 on the other hand the permeability is lowest to $CaCl_2$ solution (No. 3iii), and increases when distilled water is used (No. 3i), it is highest when NaCl solution is the saturating fluid (No. 3ii). In tests where the saturating fluid is KCl, no permeability reduction occurs when the ionic strength is 0.79 M (No. 22i and No. 23i, Fig. 4a). For tests with NaCl with an ionic strength of 0.86 M (No. 9 and No. 10, Fig. 3d) the change in S_p is only slightly greater than predicted due to thermal expansion.

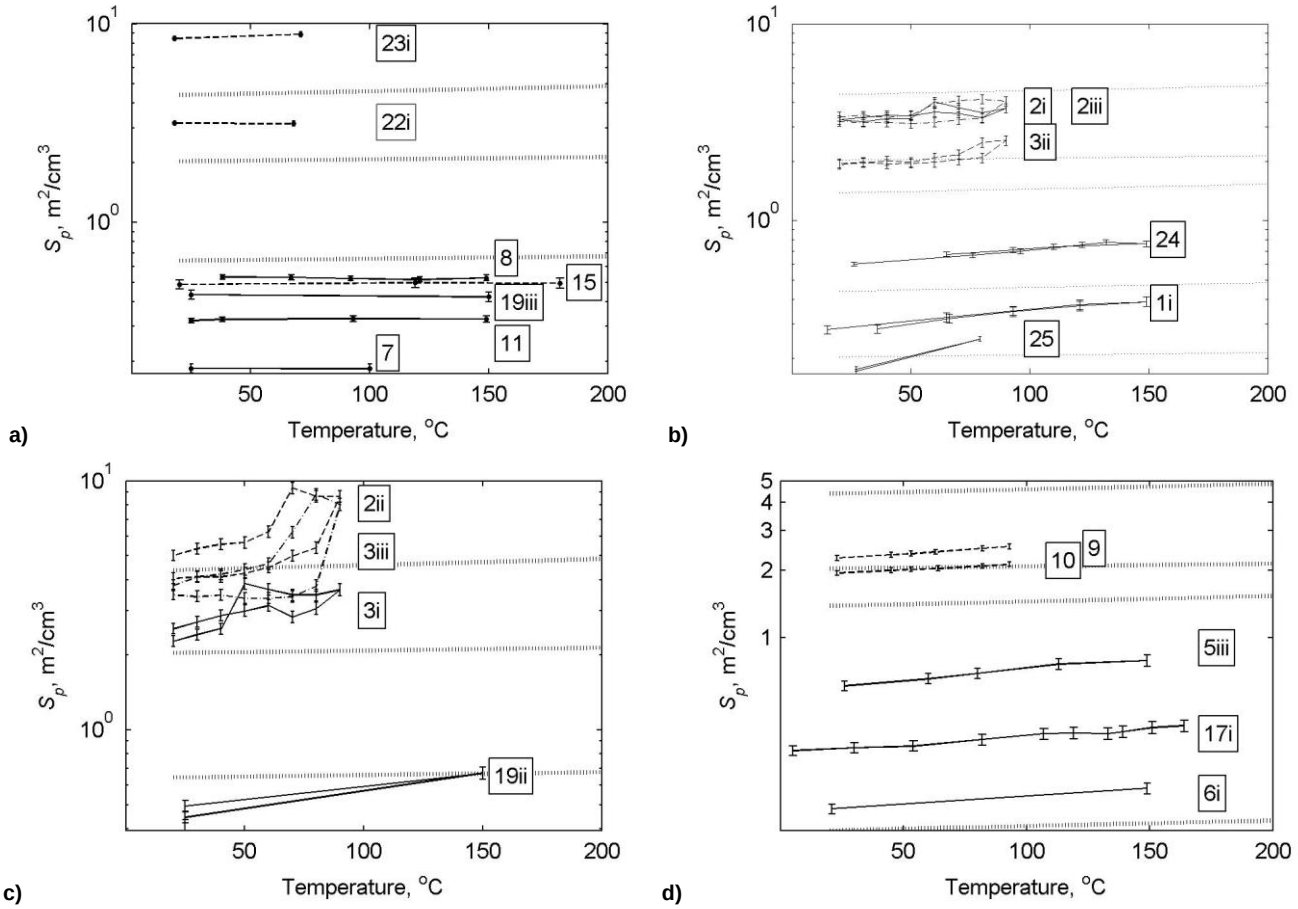

Fig 3: S_p versus temperature; solid and dashed lines indicate flow with distilled water and brine respectively. Dotted lines are the predicted effect of thermal expansion. The results are grouped according to those where there is (a) no permeability change (b) an entirely reversible change (c) a partially reversible change (d) the reversibility is not investigated. The effect in No. 19ii is found to be due to colloid contamination. Numbers correspond to tests in Table 1.

The change in S_p with heating was similar in the two experiments performed. Our results for one sample are plotted in **Figure 4** along with data from other tests performed on Berea samples using water or NaCl solutions. At 23 ˚C the permeability is not dependent on the flow rate. The difference between the permeability measured with a flow rate of 10ml/hr and that measured at 20 ml/hr increases with increasing temperature. This effect occurred in both samples, both during the test phase with distilled water and that with brine.

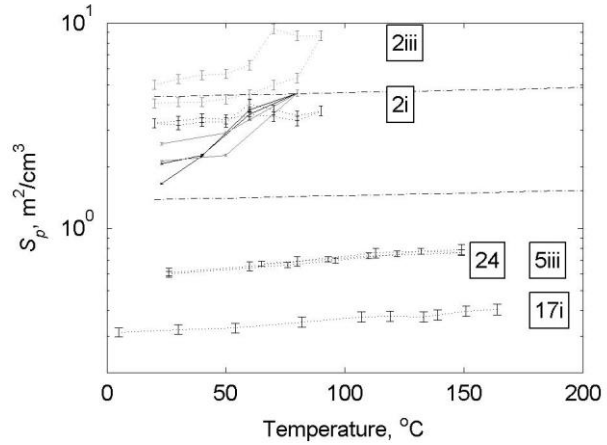

Fig 3: S_p versus temperature; solid lines are experimental data from this study, dotted lines indicate literature data. Black lines are tests performed with distilled watter, gray lines are tests with NaCl.

Discussion

Colloidal contamination is noted in multiple studies. At elevated temperature iron oxide and hydroxide colloids can be transported into the sample and result in the formation of a filter cake (Piwinksii and Netherton 1977; Milsch et al. 2009), or the clogging of pores (Potter et al. 1981; Stottlemyre 1981). The permeability reduction in the latter case is partially reversible with cooling (Fig. 3c, No. 19ii). In experiments where measures are taken to prevent colloidal contamination, heating causes no change in S_p (Fig. 3, No.19iii). Colloid contamination is not ruled out for any of the tests where a reversible or partially reversible change is observed. However, it is less probable that colloid contamination is the cause of the changes observed in No. 5iii and No. 6i (Fig. 3b) as these tests are part of the same investigation as No. 7 (Fig. 3a) where no permeability reduction occurs. A similar argument holds for the tests No. 14 and No. 16.

Increased compressibility can be considered not to cause a significant permeability reduction in these experiments. Strain measurements by Stottlemyre (1981) show that the average sample length does not change at a constant confining stress of 15 MPa. Measurement of pore volume reduction during heating at a confining stress of 14 MPa by Jing et al. (1992) (Fig. 1) furthermore indicate no porosity reduction greater than expected as a consequence of thermal expansion. At higher temperature or under higher confining stress, porosity reduction due to increased compressibility may be more significant, but it is negligible as a mechanism of permeability reduction for the test conditions of the tests discussed in this paper.

Thermal expansion is found to have a minor effect on permeability in the tests considered in this review. The predicted permeability reduction is highest for sandstones with a lower porosity where an increase in temperature of 100˚C causes a 12% permeability reduction. However, the majority of the permeability measurements in samples where the fluid is inert show no change in permeability (Fig. 2), suggesting that the pore volume is not reduced due expansion of the solids.

There are no cases where the permeability increases with temperature, indicating that thermal contraction of the EDL does not significantly affect porosity. This effect is expected to be more significant in samples with a high S_p. The samples in this review with the highest S_p (No. 22 and No. 23) are tested with gas, in which case no EDL forms, or with a 0.79M KCL solution wherefore the EDL is expected to be reduced to a minimum thickness.

Clay minerals are present in the tests where a permeability reduction is observed in Figs. 3b, 3c and 3d (with the exception of 19ii where the effect is found to be due to colloid contamination). Kaolinite is the dominant clay mineral in the majority of the samples where a permeability reduction is observed. In samples 7 and 21 that have been fired at temperatures exceeding 600˚C, heating has no effect on the Sp during flow with distilled water. It is suggested (check) that the kaolinite mineral loses its hydrationwater irreversibly at temperatures exceeding 600˚C changing its surface properties thereby preventing mobilization by EDL repulsion. In those investigations, samples fired at lower temperatures where the kaolinite is present do show an increase in Sp with heating during flow with distilled water (tests 5 and 20). This suggests kaolinite mobilisation is a probable contribution to the permeability reduction. In tests No. 16 and No. 20, kaolinite is found in the effluent fluid at elevated temperature supporting the hypothesis of kaolinite particle mobilisation.

Mobilisation of kaolinite may also be due to hydrodynamic drag forces. Permeability reduction at constant temperature due to fines migration is reported by McKay and Brigham (1984) and by Gobran et al. (1987) for samples containing kaolinite. Subsequent temperature increase has no effect on the permeability (Fig. 3a, No. 8 and 11). However, Sydansk (1980) observes both permeability reduction at room temperature and further reduction at 85˚C (No. 20). The difference can be expected to be due to the relative magnitude of the Stokes drag force of the fluid on the particles and the magnitude of the EDL repulsive force. The magnitude of the EDL force is dependent on both the negative surface charge of the particles, that becomes more negative with increasing temperature, and the range over which the charge acts, which increases as the ionic strength decreases. The effect of heating on mobilisation is expected to be greater in solutions with a low ionic strength.

The literature data analysed do not show a robust correlation between the permeability reduction and the ionic strength of the solution. Tests 2 and 3 show a similar or greater effect of heating on permeability for solutions with an ionic strength of 1 M than with distilled water in the same sample. Our test results also show a similar effect of heating in the tests with distilled water and the test with 0.34 M NaCl. Switching from distilled water to 0.34 M NaCl solution in our test resulted in a relatively small increase in permeability which is in general accordance with the reduction of the EDL repulsion causing less particles to be mobilized. Reduction of the ionic strength at room temperature in a kaolinite bearing sandstone, is reported to cause a sharp reduction in permeability, in the order of 90% or more, that is not or only marginally reversible when the strength is subsequently increased [e.g., Mungan (1965), Khilar and Folger (1984), Tchistiakov (2000)].

Both in tests performed here and in the literature data, the permeability reduction caused by heating is for the greater part reversible, (Figs 3b and c, and 4). The difference magnitude of the permeability reduction due to heating, max 50%, and that due to the reduction of ionic strength, up to 99%, and the difference in the reversibilities of the two effects may indicate that a different mechanism causes the permeability change. Reducing the ionic strength may mobilise particles from the pore walls and cause them to aggregate in the pore throats forming firm clogs. Heating similarly causes mobilisation, but due to the change in the surface charge the particles are prevented from forming stable aggregates in the pore throats, instead forming a suspension with a higher viscosity than water. This results in an apparent reduction of the permeability that is less than when the pores are clogged. The heterogeneous surface charge on kaolinite particles smaller reduction of permeability. The increase of the temperature increases the viscosity of the solution and thereby the Stokes drag force on the mobilized particles. This may remove them

Alternatively the reversibility when the sample is cooled may be d

The reversibility of the effect of heating on permeability is not explained by the EDL repulsive forces alone, as these are reduced with cooling which can be expected to result in particles being more firmly plugged in the pores. A possible cause of remobilization of plugged particles is the increase in fluid viscosity as the temperature is reduced. A reduction of the temperature or an increase of the flow rate increase the Stokes shear force on the particles, and remobilisation may account for a recovery of the permeability. In the experiments performed for this study at elevated temperatures increasing the flow rate results in a permeability increase. This is not addressed in the tests reviewed, however in tests by McKay and Brigham (1984), where the permeability is reduced steadily at room temperature, increasing the flow rate results in a sudden increase in permeability.

Particles may also be released when silica cement dissolves (Somerton et al. 1981, Blair et al. 1984). Significant permeability reduction after prolonged flow at elevated temperature is reported by Blair et al. (1984) for a sample that does not contain clay minerals (No. 4) where concentrations of silicium and calcium in the effluent are found to increase at elevated temperature. The effect of dissolved of silica on the viscosity of distilled water is measured by Stottlemyre (1981) and reported to be negligible for concentrations in the order of that measured in the effluent.

Conclusion

Heating causes mineral expansion and porosity reduction under confined conditions; within the temperature and stress ranges studied in this paper the effect of this on permeability is negligible. Permeability reductions are only found in tests where a non inert fluid is used. Colloidal contamination as a consequence of corrosion can cause significant permeability reductions at elevated temperature. In this review of published experimental data, particle migration is a probable mechanism contributing to permeability reduction for tests where permeability reduction results from heating. The lithologies where significant permeability reductions are observed contain kaolinite, with one exception where particle release can be related to silica cement dissolution. Heating has less effect in cores where the clay mineralogy has been altered by firing at temperatures over 600˚C, or in samples where no kaolinite minerals are present.

Permeability reduction due to heating is observed when distilled water is the saturating fluid as well as when solutions of KCl, NaCl, $CaCl_2$, or artificial brines resembling in situ fluid composition are used; however, not all tests with these fluids result in permeability reduction. The permeability change is found to be reversible to a large extent when the temperature is reduced.

Based on this study, it is recommended that formations with a low kaolinite clay content are selected for heat storage. The composition of the injected fluid can affect both permeability and the effect of heating; the specific interaction between the fluid and the sample mineralogy requires laboratory testing. Finally the prevention of colloid contamination and corrosion at elevated temperature is an important requirement for successful heat storage.

Nomenclature

e = Elementary charge, q, C
I = Ionic strength of electrolyte, n/L^3, mol/L
k = Absolute permeability, L^2, m^2
k_B = Boltzmann's constant, mL^2/t^2T, J/K
N_A = Avogadro number, n^{-1}, mol^{-1}
S = Specific surface area (grain surface area to total rock volume), L^2/L^3, $m^2/\mu m^3$
S_s = Specific surface area per unit solids volume (grain surface area to solids volume), L^2/L^3, $m^2/\mu m^3$
S_p = Specific surface area per unit pore volume (grain surface area to pore volume), L^2/L^3, $m^2/\mu m^3$
α = Linear thermal expansion coefficient, T^{-1}, $^oC^{-1}$
ε_o = Permittivity of vacuum, q2t2/mL3 , F/m
ε_r = Relative dielectric permittivity
κ^{-1} = Inverse Debye parameter, L, m
φ = Porosity

SI-metric conversion factors

^oF	× (^oF-32)/18		= ^oC
ft	× 3.048*	E-01	= m
psi	× 6.894 757	E+00	= kPa

References

Andreassen, K.A. and Fabricius, I.L. 2010. Biot critical frequency applied to description of failure and yield of highly porous chalk with different pore fluids *Geophysics* **75** (6): E205-E213. http://dx.doi.org/10.1190/1.3504188.

Aruna, M. 1976. The Effects of Temperature And Pressure on Absolute Permeability of Sandstones. PhD dissertation, Stanford University, Stanford, California (April 1976).

Baudracco, J. and Aoubouazza, M. 1995. Permeability variations in Berea and Vosges sandstone submitted to cyclic temperature percolation of saline fluids. *Geothermics* **24** (5-6): 661-677. http://dx.doi.org/10.1016/0375-6505(95)00027-5.

Blair, S.C., Deutsch, W.J. and Kannberg, L.D. Laboratory Permeability Measurements In Support Of An Aquifer Thermal Energy Storage Site In Minnesota. In *Proc of the 25. US symposium on rock mechanics, Evanston, IL, USA*, 296-303

Casse, F.J. and Ramey Jr, H.J. 1979. The Effect of Temperature and Confining Pressure on Single-Phase Flow in Consolidated Rocks (includes associated paper 9087). *J. Pet Tech* **31** (8): 1051-1059. SPE-5877-PA. http://dx.doi.org/10.2118/5877-PA.

Fjaer, E., Holt, R.M., Horsrud, P. et al. 2008. *Petroleum related rock mechanics*, volume 53 of *Developments in Petroleum Science*, second edition. Amsterdam: Elsevier.

Gobran, B.D., Brigham, W.E. and Ramey Jr., H.J. 1987. Absolute Permeability as a Function of Confining Pressure, Pore Pressure, and Temperature. *SPE Form Eval* **2**(1): 77-84. SPE-10156-PA. http://dx.doi.org/10.2118/10156-PA.

Jing, X.D., Archer, J.S. and Daltaban, T.S. 1992. Laboratory study of the electrical and hydraulic properties of rocks under simulated reservoir conditions. Marine and Petroleum Geology 9 (2): 115-127. http://dx.doi.org/10.1016/0264-8172(92)90084-R.

Khilar, K.C. and Folger, H.S. 1984. The existence of a critical salt concentration for particle release. *J. Colloid Interface Sci.* **101** (1): 214-224. DOI: 10.1016/0021-9797(84)90021-3.

Kozeny, J. 1927. Ueber kapillare Leitung des Wassers im Boden. *Sitzungsberichte der Wiener Akademie der Wissenschaften* **136** 271-306.

Lorne, B., Perrier, F. and Avouac, J.P. 1999. Streaming potential measurements: 1. Properties of the electrical double layer from crushed rock samples. *J. Geophys. Res* **104** (17): 17857-17877. http://dx.doi.org/:10.1029/1999JB900156.

Lyklema, J.J., de Keizer, A., Bijsterbosch, B.H. et al. 1995. *Electric Double Layers*. In *Volume II: Solid-Liquid interfaces. Fundamentals of Interface and Colloid Science*, ed. J.J. Lyklema, A. de Keizer, B.H. Bijsterbosch et al. Chap 3, 1-232. Academic Press.

McKay, W.I. and Brigham, W.E. 1984. Effects of temperature on the absolute permeability of consolidated sandstone. Technical Report DOE/SF/11564-3, Stanford University California. Petroleum Research Inst. (01 April 1984). http://dx.doi.org/: 10.2172/5154742.

Milsch, H., Seibt, A. and Spangenberg, E. 2009. Long-term Petrophysical Investigations on Geothermal Reservoir Rocks at Simulated In Situ Conditions. *Transport in Porous Media* **77** (1): 59-78. http://dx.doi.org/10.10007/s11242-008-9261-5.

Morrow, N.R., Brower, K.R. and Kilmer, N.H. 1983. Relationships Of Pore Structure To Fluid Behavior In Low Permeability Gas Sands Final Report, DOE/BC/10216-13 (DE84012721), U.S. Dept. of Energy, Bartlesville (Sept., 1984), 60-71.

Piwinskii, A.J. and Netherton, R. 2003. Permeability of Kayenta Sandstone to Hypersaline Brine at 10.3 MPa Confining Pressure and Temperatures to 90{degrees}C. In *Conference: Proceedings, Third Workshop Geothermal Reservoir Engineering, Stanford University, Stanford, CA, Dec. 14-15, 1977*.

Potter, J., Dibble, W. and Nur, A. 1981. Effects of temperature and solution composition on the permeability of St. Peters sandstone-Role of iron (III). *J. Pet Tech* **33** (5): 905-907. SPE-9011-PA. http://dx.doi.org/10.2118/9011-PA.

Revil, A., Darot, M. and Pezard, P. 1996. From surface electrical properties to spontaneous potentials in porous media. *Surveys in Geophysics* **17** (3): 331-46. http://dx.doi.org/10.1007/BF01904047.

Sageev, A., Gobran, B., Brigham, W. and Ramey Jr, H. 1980. The effect of temperature on the absolute permeability to distilled water of unconsolidated sand cores. In *Proceedings, Sixth Workshop Geothermal Reservoir Engineering, Stanford University, Stanford, California, December 16-18, 1980*.

Shaw, C.J., Churcher, L.P. and Hawkins, F.B. The Effect of Firing on Berea Sandstone. *SPE Form Eval* **6** (1): 72-78. http://dx.doi.org/ 10.2118/18463-PA.

Schembre, J.M. and Kovscek, A.R. 2004. Thermally Induced Fines Mobilization: Its Relationship to Wettability and Formation Damage. Paper SPE 86937-MS presented at the SPE International Thermal Operations and Heavy Oil Symposium and Western Regional Meeting, 01/01/2004. http://dx.doi.org/10.2118/86937-MS

Somerton, W.H., El-Shaarani, A. and Mobarak, S. 1974. High Temperature Behavior Of Rocks Associated With Geothermal Type Reservoirs. Paper SPE 4897-MS presented at the SPE California Regional Meeting San Francisco, California, 4-5 April 1974. http://dx.doi.org/10.2118/4897-MS.

Somerton, W.H. and Mathur, A.K 1976. Effects of Temperature and Stress on Fluid Flow and Storage Capacity of Porous Rocks. Paper SPE 76-0097 presented at The 17th U.S. Symposium on Rock Mechanics (USRMS), August 25 - 27, 1976 , Snow Bird, UT.

Somerton, W.H., Janah, A.H. and Ashqar, P.I. 1981. Thermal expansion of fluid saturated rocks under stress. Paper SPE 1991-D presented at the SPWLA Twenty-second Annual Logging Symposium, June 23-26, 1981.

Somerton, W.H. 1992. *Thermal properties and temperature-related behavior of rock/fluid systems*. Volume 37 of *Developments in Petroleum Science* ed. G.V. Chilingarian. Amsterdam: Elsevier.

Sposito, G., Skipper, N., Sutton, R., et al. 1999. Surface geochemistry of the clay minerals. *Proceedings of the National Academy of Sciences of the United States of America* **96** (7): 3358-3364. http://dx.doi.org/10.1073/pnas.96.7.3358

Sydansk, R.D. 1980. Discussion of the Effect of Temperature and Confining Pressure on Single-Phase Flow in Consolidated Rocks. *J. Pet Tech* SPE 9087. http://dx.doi.org/10.2118/5877-PA.

Stottlemyre, J.A. 1981. An Investigation Of Temperature Sensitivity Of Ottawa Sand And Massilon Sandstone Intrinsic Permeabilities. PhD dissertation, University of Washington, Seattle, Washington, United States (March 1981).

Tchistiakov, A.A. 2000. Colloid Chemistry of In-Situ Clay-Induced Formation Damage. Paper SPE 58747-MS presented at the SPE International Symposium on Formation Damage Control, 23-24 February 2000, Lafayette, Louisiana. http://dx.doi.org/ 10.2118/58747-MS

Von Gonten, W.D. and Choudhary, B.K. 1969. The Effect of Pressure and Temperature on Pore Volume Compressibility. Preprint SPE2526 to be presented at the 44th Annual Fall Meeting of the Society of Petroleum Engineers of AIME, Denver, Colorado, September 28-October 1.

Wei, K.K., Morrow, N.R. and Brower, K.R. 1986. Effect of fluid, confining pressure, and temperature on absolute permeabilities of low-permeability sandstones. *SPE Form Eval* **1** (4): 413-423. SPE-13093-PA. http://dx.doi.org/10.2118/13093-PA.

Weinbrandt, R.M. and Ramey, H.J. 1975. The Effect of Temperature on Relative and Absolute Permeability of Sandstones. SPE J. 15 (5): 376-384. SPE4142-PA. http://dx.doi.org/10.2118/4142-PA.

Zuo, J., Xie, H., Zhou, H. Peng, S. 2010. SEM in situ investigation on thermal cracking behaviour of Pingdingshan sandstone at elevated temperatures. Geophysical Journal International 181 (2): 593-603. DOI: 10.1111/j.1365-246X.2010.04532.x.

Table 1: Overview of the literature data reviewed. Error margins for permeability measurements are those reported, or they are estimated from scatter in the reported data. Where neither is available, an error margin of 10%, indicated in italic, is assumed. Results in bold indicate that permeability reductions are reported to result from contamination by colloidal particles that do not originate in the core.
*** porosity not reported for the sample but assumed from other sources**

No.	Authors	Strati-graphic Unit	Φ	*k*, md (error margin)	Clay content Mineralogy	Fluid	Temperature, °C	Confining Stress/ Pore pressure, MPa	Permeablity ratio $k_{T\ high}/k_{T\ low}$
1	Aruna (1976)	Massilon Sandstone Fired (300°C)	0.22	i) 585 ii) 866 iii) 923 *(±10%)*	Low clay content Kaolinite	i) distilled water ii) mineral oil iii) N_2 gas	i) 24-149 ii) 20-121 iii) 20-121	13.9/ 1.4	i) 0.52 ii) 0.92 iii)1.00
2	Baudracco and Aoubouazza (1995)	Berea Sandstone	0.20	3.9 *(±10%)*	8% Mainly kaolinite	i) distilled water ii) 1M NaCl iii) 0.4 M $CaCl_2$	20-90	0.2/ 0.1	i) 0.75 ii) 0.70 iii) 0.55
3	Baudracco and Aoubouazza (1995)	Vosges Sandstone	0.20	10.2 *(±10%)*	4% Mainly kaolinite and illite, 0.5% smectite	i) distilled water ii) 1M NaCl iii) 0.4M $CaCl_2$	20-90	0.2/ 0.1	i) 0.55 ii) 0.38 iii) 0.22
4	Blair (1984)	Ironton-Galesville Sandstone	-	-	Low clay content	i) synthetic ground-water	20-150	6.2/ 2.4	0.20
5	Casse and Ramey (1979)	Berea Sandstone Fired (450°C)	0.19*	i) 130 ii) 132 iii) 106 (±5%)	-	i) mineral oil ii) N_2 gas iii) distilled water	i)25-149 ii) 20-160 iii) 26-146	13.8/ 1.4	i) 1.00 ii) 1.00 iii) 0.56
6	Casse and Ramey (1979)	Boise Sandstone Fired (450°C)	0.28*	i) 2063 ii) 1930 (±5%)	-	i) distilled water ii) mineral oil	21- 153	13.8/ 1.4	i) 0.65 ii) 1.00
7	Casse and Ramey (1979)	Boise Sandstone fired (760°C)	28*	1852 (±5%)	-	distilled water	20-100	13.8/ 1.4	95
8	Gobran et al. (1987)	Berea Sandstone	0.19*	138 (±5%)	-	distilled water	38-149	13.8/ 1.4	1.00
9	Jing et al. (1992)	Millstone Grit Series Sandstone	0.13	6.5 (±5%)	5% Mica	0.86 M NaCl	23-93	13.8/ 1.4	0.76
10	Jing et al. (1992)	Upper Coal Measures Sandstone	0.17	4.7 (±5%)	5% Clay minerals	0.86 M NaCl	23-93	13.8/ 1.4	0.80
11	McKay and Brigham (1984)	Fontaine-bleau Sandstone	0.11	260 (±5%)	Low clay content Kaolinite	distilled water	25-149	13.8/ 1.4	0.97
12	Milsch et al. (2009)	Rotliegend Sandstone	0.11	200 (±0.36)	<10% clay Illite, chlorite	synthetic formation brine	150	50.0/ 5.0	1.00 (*k* at room temp. not reported)
13	Piwinskii	Kayenta	-	50	-	i) synthetic	100		**0.02**

	and Netherton (1977)	Sandstone				brine unfiltered			(*k* reported as function of flow volume)
14	Potter et al. (1981)	St. Peters Sandstone	-	i) 554 ii) 1071 (±5%)	<1% clay	i)+ii) distilled water w. colloids iii) distilled water	i) 25 ii) 100 iii) 100	20.0/ 2.5	**i) 1.00** **ii) 0.65** iii) 1.00 (*k* reported as function of flow volume)
15	Schembre and Kovscek (2004)	Berea Sandstone Fired (temp ?)	0.19*	100-250	-	0.05 M NaCl	20-180	1.7-2.8/ -	0.95
16	Schembre and Kovscek (2004)	Berea Sandstone	0.19*	100-250	-	0.01 M NaCl (pH 7)	20-120	1.7-2.8/ -	0.01
17	Somerton and Mathur (1976)	Berea Sandstone	0.19*	397 (±10%)	-	i) distilled water ii) switch distilled water to 0.04 M KCl	i) 5-165 ii) 190	13.9/ 1.4	i) 0.59 ii) k_{salt}/k_{water} 0.53
18	Somerton (1992)	Berea Sandstone	0.19*	-	-	i) 0.08 M KCl ii) 0.08 M KCl iii) 0.08 M KCl	i) 27-156 ii) 27-156 iii) 20-160	i) 6.9/ 1.4 ii) 3.5/1.4 iii) 13.4/1.4	i) 0.54 ii) 0.76 iii) 0.77
19	Stottlemyre (1981)	Massilon Sandstone	0.23	i) 375 ii) 300 ii) 260 *(±10%)*	~ 10% clay Kaolinite	i)+ii) distilled water w. colloids iii) distilled water	i) 25 ii) 25-150 iii) 25-150	15.0/ 6.0	**i) 0.92** **ii) 0.30** iii) 1.03
20	Sydansk (1980)	Berea Sandstone Fired (450°C)	0.19*	-	-	i)+iii) distilled water ii)+iv) 0.32M NaCl	i) +ii) 22 iii)+iv) 85	-	i) 0.74 ii) 0.96 iii) 0.19 iv) 0.92
21	Sydansk (1980)	Berea Sandstone Fired (1000°C)	0.19*	-	-	i)+iii) distilled water ii)+iv) 0.32M NaCl	i) +ii) 22 iii)+iv) 85.	-	i) 0.79 ii) 0.94 iii) 0.60 iv) 0.98
22	Wei et al. (1986) ; Morrow et al. (1983)	Old Man Mountain Sandstone	0.14	3.21 (±5%)	5-10% clay Kaolinite	i) 0.79 M KNO_3 ii) N_2 gas	i) 18-68 ii) 19-96	6.9/ -	i) 1.00 ii) 1.00
23	Wei et al. (1986) ; Morrow et al. (1983)	CIGE Sandstone	0.12	0.41 (±5%)	5-10% clay Kaolinite	i) 0.79 M KNO_3 ii) N_2 gas	i) 18-71 ii) 19-93	6.9/ -	i) 1.00 ii) 1.00
24	Weinbrandt and Ramey (1975)	Berea Sandstone Fired (450°C)	0.19	106 (±5%)	-	distilled water	26-149	13.8/ 1.4	0.61
25	Weinbrandt and Ramey (1975)	Boise Sandstone Fired (450°C)	0.28	1970 (±5%)	-	distilled water	27-79	13.8/ 1.4	0.49

PROCEEDINGS, Thirty-Seventh Workshop on Geothermal Reservoir Engineering
Stanford University, Stanford, California, January 30 - February 1, 2012
SGP-TR-194

THERMALLY INDUCED PERMEABILITY REDUCTION DUE TO PARTICLE MIGRATION IN SANDSTONES: THE EFFECT OF TEMPERATURE ON KAOLINITE MOBILISATION AND AGGREGATION.

Esther Rosenbrand*, Ida Lykke Fabricius*, Hao Yuan[+]

*Department of Civil Engineering
[+]Department of Chemical Engineering
Center for Energy Resources Engineering
Technical University of Denmark
Brovej, Building 119
Kgs. Lyngby, 2800, Denmark
e-mail: esro@byg.dtu.dk

ABSTRACT

The seasonal imbalance in supply and demand of renewable energy requires seasonal storage, which potentially may be achieved by hot water injection in geothermal aquifers to minimize heat loss by advection. A reduction of porosity and permeability is a risk of heating the rock above the in-situ temperature. Published data indicate that the permeability reduction can be a consequence of the mobilisation of kaolinite particles. Particle mobilisation as a result of changes in physico-chemical conditions is often addressed using the DLVO theory (Derjaguin and Landau, 1941; Verwey and Overbeek, 1948). Mobilisation occurs due to similar surface charges on kaolinite and quartz grains which causes a detachment force on the kaolinite particles. Permeability reduction as a result of mobilisation requires the released particles to be captured in the pore throats. Data indicate that the permeability reduction can be reversible, implying captured particles are remobilised when the temperature is reduced.

This paper considers the effects of mineralogy and hydrodynamic forces on particle mobilisation and aggregation. The mineral surface charge originates from the interaction between the particles and the saturating fluid and is affected by both the fluid composition and the temperature. Kaolinite particles have a heterogeneous surface charge distribution that can play an important role in the particle aggregation in the pore throats, leading to permeability damage. The reduction of temperature causes an increase in the hydrodynamic force on the aggregated particles at pore throats. It can remobilise particles and lead to permeability recovery.

We discuss the mineral structure of quartz and kaolinite and estimate the effects of heating on the surface charges using published data. The DLVO theory is used to model the interaction energy between quartz and kaolinite particles for different saturating fluids. The results are compared to the published data addressing the effect of temperature on permeability. This provides a qualitative explanation for the observed changes in permeability with temperature for the tests with distilled water.

INTRODUCTION

Renewable energy production results in excess heat production during the summer in Denmark. This can be used in the municipal district heating system in winter, provided seasonal storage is available. Injection of heated water into sandstone aquifers that are currently exploited for geothermal energy is a promising and potential storage method. The in-situ temperatures of 60-100˚C reduce heat loss from the water that is injected at temperatures in the range of 150-200˚C.

Permeability reduction during hot water injection in sandstones is reported in some cases. Possible causes include: mineral precipitation; pore volume reduction due to thermal expansion of the solid fraction or compaction due to an increase in the pore volume compressibility; clogging by colloidal contamination and mobilisation of clay particles. Experimental data often show a recovery of the permeability when the temperature is reduced, (Weinbrandt and Ramey, 1975; Aruna, 1976; Casse and Ramey, 1979; Baudracco and Aoubouazza, 1995). An overview of published data by Rosenbrand and Fabricius (2012) indicates that the presence of kaolinite is the common factor in the experiments where permeability reduction is observed; when no kaolinite is present no permeability reduction is observed. However, there are tests where no permeability reduction occurs and kaolinite is present. This includes tests performed with distilled water and those with solutions with dissolved KCl or NaCl.

The mobilisation of kaolinite particles may not affect the porosity but the transport of kaolinite particles from the surface of the grains to the pore throats, as

illustrated in Figure 1, can cause a significant permeability reduction.

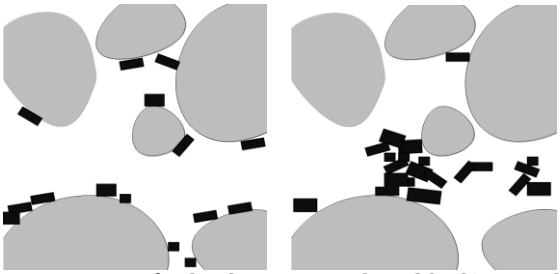

Figure 1: Left: kaolinite particles (black) initially present on the surface of quartz grains (gray). Right: mobilized particles aggregate and bridge pore throats.

Kaolinite mobilisation due to the change in temperature, ionic strength, or pH can be predicted using the DLVO theory (Khilar and Folger, 1984; Schembre and Kovscek, 2005). The DLVO theory accounts for the interaction of van der Waals attraction and the electrical double layer (EDL) force between the charged quartz and kaolinite surfaces. The sign and the order of magnitude of the surface charge depend on interaction with water molecules that adsorb on the mineral surface. At pH 6 both quartz and kaolinite have negative charges which attract oppositely charged ions that form a diffuse layer on the surface. Together the adsorbed and diffuse layers compose what is known as the electrical double layer (EDL). The EDL force results from the interaction of the double layers of two particles and is repulsive for similarly charged particles. It can result in repulsion between the particles when the EDL force exceeds the van der Waals force.

The kaolinite mineral consists of two different sheets that are bonded together (Grim, 1953). As a result, the surface charge is not uniformly distributed. In the solutions with a low pH, different sides of the mineral may have an opposite sign, resulting in flocculation of kaolinite suspensions (Wang and Siu, 2006).

When kaolinite particles are attached to the grain surface (Figure 1), heating can cause an increase of the EDL force between kaolinite and quartz resulting in the mobilisation of particles. Interaction between the suspended particles may cause the formation of a large aggregate that bridges the pore throat (Figure 1). The stability of the bridges is reduced at higher flow velocities due to larger hydrodynamic forces (Sen and Khilar, 2006). At constant flow velocity, the hydrodynamic forces may also be increased as a function of the fluid viscosity which increases when temperature is reduced. Together with the reduced repulsion from the quartz surface, the above mechanism can be a reason that cooling can recover the permeability.

To understand the effects of the temperature on the mobilisation and the aggregation of particles, we consider the nature of the surface charge on kaolinite and quartz, and use the DLVO theory to estimate the effects of temperature on the EDL interaction between particles. Some of the published experimental results using different solutions and flow rates are compared to examine whether the observed permeability changes can be explained in the context of particle mobilisation and bridging. Due to the large number of parameters that affect these forces and the uncertainties of quantifications, the available data are insufficient to verify this mechanism.

SURFACE CHARGE ON QUARTZ AND KAOLINITE

Quartz (SiO_2) is built up of silica tetrahedra that consist of one silicium atom bonded to 4 oxygen atoms. Each oxygen atom is shared by two tetrahedra. On the mineral surface bonds are broken, which results in reactive sites. These interact with water molecules to form silanol groups that gain or lose H^+ dependent on the solution pH as shown in Eq. 1 (Lorne et al., 1999).

$$\begin{aligned} Si-OH &\rightleftharpoons Si-O^- + H^+ \\ Si-OH + H^+ &\rightleftharpoons Si-OH_2^+ \end{aligned} \qquad \text{Eq. 1}$$

When the solution contains additional cations, M^+ or anions, A^-, these may react with the surface sites as shown in Eq. 2 (Lorne et al. 1999).

$$\begin{aligned} Si-OH + M^+ &\rightleftharpoons Si-OM + H^+ \\ Si-OH + A^- &\rightleftharpoons Si-A + H_2O \end{aligned} \qquad \text{Eq. 2}$$

The overall surface charge is determined by the number of positive and negative adsorbed ions. The pH at which the surface charge is zero is referred to as the point of zero charge, PZC, (Rudzinski et al., 1999).

The kaolinite mineral ($Al_2Si_2O_5(OH_4)$) consists of a silica sheet bonded to an alumina sheet as illustrated in Figure 2. In the silica sheet, silica tetrahedra are arranged in a hexagonal pattern so that 3 oxygens are shared between tetrahedra, and the remaining oxygens point in the same direction (Figure 2, top). These oxygens are bonded to two aluminum atoms from the alumina sheet (Figure 2, bottom). It consists of alumina octahedra where an aluminum atom is bonded to 4 hydroxyl groups and to two oxygens from the tetrahedral sheet. The hydroxyl groups in the alumina sheet are shared between two octahedra.

It has often been assumed only the broken bonds on the edges result in surface sites that interact with water molecules and have a pH dependent surface charge. The faces on the other hand are assumed to

be charged due to ion substitution in the silica and alumina sheets. However, the partially ionic nature of the covalent bonds in the silica tetrahedra and alumina octahedra leaves the surface groups on the faces polarized, which can allow ion adsorption. Data from Huertas et al. (1998), Gan and Franks (2006), and Gupta and Miller (2010), show that the face charges are affected by the pH which indicates ion adsorption to surface sites. Sites associated with Al atoms have a different reaction constant than those associated to Si atoms, and those associated to broken bonds will differ from those on the faces. Therefore a distinct surface charge is expected on the two faces and on the edges of the kaolinite.

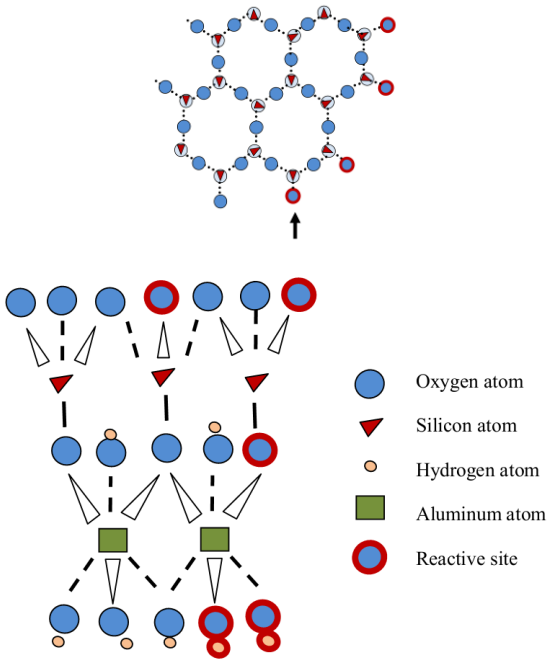

Figure 2: Representation of the kaolinite structure, Top: 001 face of the tetrahedral silica sheet; silica tetrahedra form a hexagonal pattern with oxygens on the tips of the tetrahedra all pointing below the plane (represented by light blue circles). Bottom: side view of kaolinite mineral indicated by arrow. Oxygen atoms below the silicium atoms are shared with aluminum atoms in the octahedral sheet. These are bonded to hydroxyl groups.

Different methods exist to approximate the surface charge, Ψ. Potentiometric titrations are used to determine the number of protons adsorbed to the mineral surface. Electro-kinetic methods are used to determine the charge on the interface between immobilized ions and mobile ions in the EDL, the zeta potential, ζ. The location in the EDL of this interface is a matter of debate (Elimelech et al., 1995), and due to shielding by adsorbed ions the magnitude of ζ will be smaller than the surface potential. Experimentally, the absolute magnitude of ζ is found to decline with increasing ionic strength (Adekola et al. 2010). However, ζ is often used to approximate Ψ due to a lack of alternative data.

For kaolinite particles, these methods yield a charge that is averaged over the entire particle. Atomic force microscopy (AFM) allows the determination of the surface charge on the individual faces of the kaolinite mineral. The interaction force between a surface and a probe with a known surface charge is measured, and DLVO theory is used to derive the surface charge of the mineral. Gupta and Miller (2010) measure the charge on the alumina and silica face of well crystallized kaolinite. To determine the edge charge, Gupta et al. (2011) compare the face surface charges from AFM data to data from potentiometric titration. At pH 6, this results in a surface charge density of the edges that is one order of magnitude greater than that on the faces. The relative contribution of the faces and edges to the average surface charge of the particle depends on the ratio of the edge to face surface areas.

PZC data at ambient temperature for quartz and kaolinite from different studies is shown in Table 1.

Table 1: PZC values of quartz surface and average on kaolinite particle from Kosmulski (2006). Data for alumina and silica faces and edges of kaolinite from Gupta et al. (2011).

quartz	kaolinite average	alumina face	silica face	kaolinite edges
<3	<2.4 - 6	6-8	<4	4-6

The PZC for the average charge on kaolinite particles shows significant variation. In addition to the size and shape of the particles, ion substitution and the degree of crystallinity affect the relative numbers of face and edge surface sites. Du et al. (2010) observe stepped faces on kaolinite with a poor crystallinity, increasing the relative number of broken bonds and reactive sites.

Effects of temperature on surface charge

The temperature affects the equilibrium constants for the reactions on the surface sites (Brady et al. 1996), and thereby the surface charge. The effect of temperature on the surface potential, Ψ, resulting from protonation of an oxide surface has been estimated using Eq. 3 by Rudzinksi (1999) and by Schembre and Kovscek (2005). e is the elementary charge, k_B is the Boltzmann constant and T the temperature (K).

$$\Psi = 2.303\frac{k_B T}{e}\left(PZC - pH\right) \qquad \text{Eq. 3}$$

Eq. 3 is based on the Nernst law for the surface charge in the presence of potential determining ions.

The presence of other ions that interact with the surface sites can affect both the surface charge and the effect of temperature on this. The change of the Ψ as a function of T is greater when the difference between the PZC and the solution pH is greater, hence injection of fluid with a pH of 6 or higher can be expected to cause a stronger reduction of the Ψ for quartz than for kaolinite.

Based on a review of published experimental data Kosmulski (2003) suggests that the PZC is reduced when the temperature is raised. Considering that the PZC for the alumina face of kaolinite reported by Gupta and Miller (2010) is between pH 6 and 8, heating in a solution of pH 6 may result in the Ψ switching from positive to negative. The magnitude of the Ψ of the alumina face will change little due to the small value of *(PZC-pH)*.

There are relatively few experimental studies addressing the effect of temperature on the surface charge of quartz and kaolinite. Figure 3 shows streaming potential data for the ζ of quartz and kaolinite in solutions with a pH 4 or higher. Both minerals have an average negative ζ in this pH range, and heating causes a reduction of the ζ. The differences between the measured values can be attributed to the differences between the ionic strengths and ionic species in the solutions used. A difference between the crystallinity of the samples tested, and hence the surface site density, can also contribute to the difference in the data. Both datasets show the ζ of quartz is reduced to a greater extent by heating at pH 8 than at pH 6, as predicted by Eq. 3.

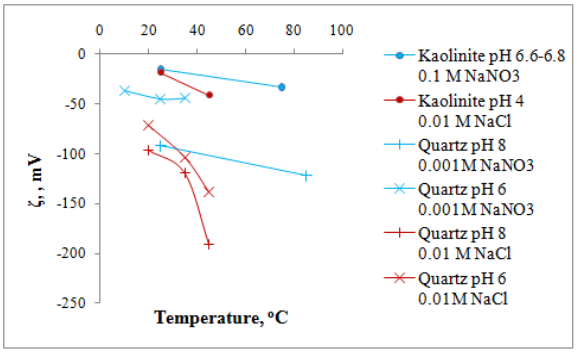

Figure 3: Data of ζ as function of temperature for kaolinite and quartz. Red data Rodríguez and Araujo (2006); blue data Ramachandran and Somasundaran (1986).

The effect of heating on the surface potential in a solution with pH 6 is estimated in Figure 4. This shows ζ data for quartz and kaolinite and Ψ data for the two sides of kaolinite and gibbsite (a mineral with the same structure as the alumina sheet), as well as the temperature dependency of these estimated from Figure 3 and Eq. 3. Due to the small difference between the PZC of alumina and the pH, the Ψ is expected to change little as a consequence of heating. The Ψ of the kaolinite silica face is in the same range as the ζ of the quartz mineral surface. The ζ data may under-estimate the Ψ due shielding by adsorbed ions, however, the lack of alternative data justifies the use of the ζ for quartz.

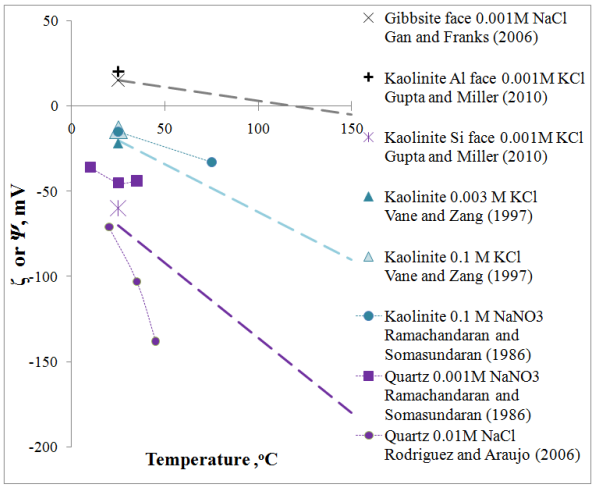

Figure 4: Data of Ψ (crosses) and ζ (closed symbols) and estimated Ψ as a function of temperature for: Alumina face of kaolinite (gray); average for kaolinite particle (blue) and the quartz mineral surface (purple).

DLVO INTERACTION ENERGY

The DLVO theory is used to predict the interaction energy between the quartz grains and the kaolinite particles. The interaction energy results from the summation of the EDL interaction and the van der Waals interaction energies (Eq. 4).

$$\Phi_T = \Phi_{vdW} + \Phi_{EDL} \qquad \text{Eq. 4}$$

The van der Waals interaction energy, Φ_{vdW}, results from spontaneous magnetic and electrical polarization due to the proximity of particles and acts over a short separation distance. For the interaction between a flat plate and a sphere of radius a_1 separated at a distance h this is calculated by Eq. 5 (Bedrikovetsky et al. 2010).

$$\Phi_{vdW} = \frac{A_{132}}{6h}\left(\frac{2*\left(1+\frac{a_1}{h}\right)}{\frac{a_1}{h}*\left(2+\frac{a_1}{h}\right)} + \ln\left(\frac{\frac{a_1}{h}}{2+\frac{a_1}{h}}\right)\right) \qquad \text{Eq. 5}$$

A_{123} is the Hamaker constant for the interaction between two different materials that have Hamaker constants A_{11} and A_{22} in a medium with Hamaker constant A_{33} as given in Eq. 6 (Visser, 1972).

$$A_{132} = \left(\sqrt{A_{11}} - \sqrt{A_{33}}\right)\left(\sqrt{A_{22}} - \sqrt{A_{33}}\right) \quad \text{Eq. 6}$$

Values of 8.86×10^{-20} J for silica, 6.5×10^{-20} J for quartz 1.52×10^{-19} J for alumina and 3.70×10^{-20} J for water from Bergstrøm (1997) are used. The Hamaker constant for a kaolinite particle is approximated as the geometric mean of the values for silica and alumina (1.16×10^{-19} J). These values are assumed to be constant with temperature as a first approximation.

The surface charge on the minerals attracts ions with an opposite charge forming a diffuse layer on the particle surface. The Poisson-Boltzmann relation gives the variation of electrical potential with distance from the surface in the EDL, subject to the assumption that the surface charge is uniformly distributed on the mineral surface, the ions are point charges and the properties of the fluid are constant with distance from the surface (Elimelech et al., 1995). The interaction energy, Φ_{EDL}, due to the potential in the EDL on a quartz grain and that on a kaolinite particle is approximated by Eq. 7 (Elimelech et al., 1995) for a spherical particle and a flat surface,

$$\Phi_{EDL} = \frac{\varepsilon_0 \varepsilon_{rs} a_i}{4}\left(\begin{array}{l} 2\Psi_1\Psi_2 \ln\left(\dfrac{1+\exp(-\kappa h)}{1-\exp(-\kappa h)}\right) \\ \\ +\left(\Psi_1^{\,2} + \Psi^2_{\,2}\right)\ln\left(1-\exp(-2\kappa h)\right) \end{array}\right)$$

Eq. 7

where ε_{rs} is the relative permittivity of the solution ε_0 is the vacuum permittivity, and Ψ_1 and Ψ_2 are the surface charges on the quartz surface and the kaolinite respectively. The inverse Debye parameter, κ^{-1}, characterizes the distance over which the surface charge is reduced to a value 1/e i.e. 1/2.72 (Lyklema, 1995). Eq. 8 expresses κ^{-1} where I is the ionic strength and N_A is Avogadro's number.

$$\kappa^{-1} = \left[\frac{\varepsilon_{rs}\varepsilon_0 k_B T}{N_A e^2 I}\right]^{\frac{1}{2}} \quad \text{Eq. 8}$$

It assumes that the surface potential on the kaolinite particles is uniformly distributed.

The total interaction energy, Φ_T, between a kaolinite particle and the quartz surface is computed using the surface potentials given in Table 2. The values for kaolinite represent the average charge on the kaolinite particles. Figure 5 shows the interaction energy between quartz and kaolinite scaled by k_BT, a measure of the thermal energy. Negative interaction energy represents attraction.

Table 2: Ψ values estimated from data in Figures 3 and 4. Values at 150˚C have low accuracy due to extrapolation beyond the data range.

	Ψ, mV (25˚C)	**Ψ,** mV (150˚C)
Quartz grain	-70	-180
Kaolinite average	-10	-80

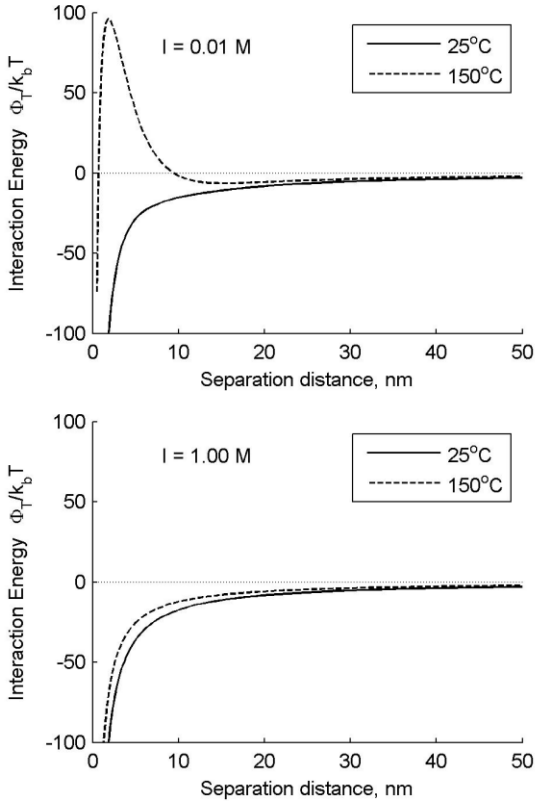

Figure 5: Interaction energy, Φ_T, between quartz surface and a spherical kaolinite particle (a_i=0.5μm).

At 25˚C the attractive forces between the quartz surface and the particles with the average kaolinite surface potential are dominant. Heating up to 150˚C changes the interaction energy into repulsion in the solutions with an ionic strength of 0.01 M. For separations smaller than 1 nm the van der Waals forces dominate. However, the fluid layer adsorbed to the mineral surface can be expected to prevent the particle from approaching the surface this closely (Khilar and Folger, 1984). The interaction energy at 150˚C shows a secondary energy minimum around 12 nm separation. It is suggested that particles may be captured via the minimum provided that the interaction energy is sufficiently attractive (Redman et al., 2004). Hydrodynamic forces can be expected

to be more significant than DLVO forces at the distance.
When the ionic strength of the solution is 1 M, the interaction energy between the quartz and the kaolinite particles is negative at both 25˚C and 150˚C. The high ionic strength reduces the range of the EDL force so that van der Waals attraction dominates.

HYDRODYNAMIC FORCES

The hydrodynamic force that the fluid exerts on a particle depends on both the fluid velocity and the fluid viscosity. The flow velocity field in pores is non-uniform. Assuming laminar flow and a non slip condition on the solid surface, the flow velocity can be expected to increase with the distance from the quartz grains towards the center of the pores. Additionally, the pore geometry can be expected to result in flow channels as well as in pockets with low flow velocities (Bear, 1972). A schematic representation of expected flow velocity variations is shown in Figure 6.

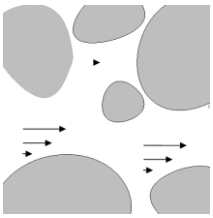

Figure 6: Schematic representation of flow from left to right through a sandstone sample. The arrow length represents fluid velocity. The highest velocities are expected in the center of channels parallel to the flow direction.

The velocity field in Figure 6 implies the hydrodynamic force on particle aggregates bridging the pore throats is greater than that on particles on the grain surface or in pockets with little flow.
Figure 7, computed using the program provided by Mao (Mao and Duan, 2009), shows the reduction in viscosity of distilled water with temperature. Heating from 25˚C to 150˚C causes a more than 4 fold reduction in the viscosity.

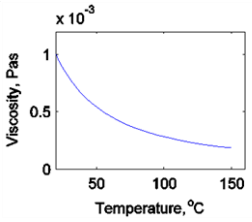

Figure 7: The viscosity of distilled water decreases non- linearly as a function of temperature.

DISCUSSION

The kaolinite mobilisation with increasing temperature can be attributed to an increase in the absolute magnitude of the surface potential of both kaolinite and quartz. Different sides of the kaolinite mineral have a different surface charge. Gupta et al. (2011) show that despite the larger surface area of the faces, the surface potential of the edges is dominant in determining the average surface potential of the kaolinite particle due to the higher charge density on the edges. The average surface potential for kaolinite is used to approximate the EDL interaction energy between quartz grains and the kaolinite particles at 25˚C and 150˚C. This results in repulsion of the particles from the grain surface in solutions with low ionic strength, while it is insensitive to the temperature at high ionic strength due to increased shielding of the surface potential.
The smaller absolute magnitude of the surface potential on the faces compared to the edges of kaolinite can be expected to influence the interactions between suspended particles. The change in the surface potential of the alumina face due to heating is expected to be smaller than that of the edges or that of the quartz grains. It may cause an attractive total interaction energy between kaolinite particles that have been mobilized due to heating.
The flowing fluid carries and concentrates particles in the pore throats, where they can aggregate and form bridges, resulting in a permeability reduction. A reduction of the temperature reduces the absolute magnitude of the surface charges and the repulsive interaction energy. It tends to make bridged particles more stable. The effect can be offset by the increase in the hydrodynamic force with cooling which has a greater effect in the flow channels than on the grain surfaces. The dislodged particles may be recaptured via attachment on the surface of the sand grains downstream.
The mechanism correlating the temperature change and the permeability change requires the domination of both the electrostatic forces and the hydrodynamic drag on the particles. When the flow rate is low, cooling may not cause a remobilisation of aggregated grains. When it is high, heating may not cause additional mobilisation.
Quantification of the DLVO interaction energies and the hydrodynamic forces is complicated by the number of influential parameters. To the best of our knowledge, the effect of the heterogeneous surface charge distribution of kaolinite on the structure of the EDL is uncertain. The values assumed for the surface charges and the Hamaker constants, particularly at elevated temperature are based on the limited data. The characteristics of the porous medium, including i.e., the pore geometry, the mineral content, the crystallisation and the surface roughness, affect both the interaction energy and the hydrodynamic forces.

The computed forces thus serve only for an indicative comparison of the interaction energies.

The above described mechanism is in agreement with the observations of the permeability reductions in kaolinite bearing sandstones reported by Weinbrandt and Ramey (1975), Somerton and Mathur (1976), Casse and Ramey (1979), Sydansk (1980), Jing et al. (1992), Baudracco and Aoubouazza (1995), and Schembre and Kovscek (2005). The temperature is not subsequently reduced in all studies, but where it is the case the permeability reduction is found to be largely reversible. When the temperature is raised in successive increments the permeability also reduces in steps. Each temperature step increases the EDL repulsive force, provoking fines mobilisation from the grain surface, and reduces the fluid viscosity, reducing the destabilizing hydrodynamic force on the aggregated particles.

In a number of experiments kaolinite mobilisation causes permeability reduction during injection at room temperature (Sydansk, 1980; McKay and Brigham, 1984; Gobran et al., 1987). Heating has a negligible effect in some cases (McKay and Brigham, 1984; Gobran et al., 1987). In the tests by Sydansk (1980), permeability reduction is observed during injection at room temperature and heating causes an additional permeability reduction. The interstitial flow velocity in the first two tests is higher than in a number of tests where reversible permeability reduction occurs as a consequence of heating; however, the number of publications with reported flow velocity is limited. To examine whether the interaction of hydrodynamic and EDL forces is as proposed, experiments where permeability is measured as a function of temperature for different flow velocities are needed.

A high ionic strength may result in the reduction of the thickness of EDL and the repulsive EDL force (Figure 5). DLVO theory is used to explain particle mobilisation caused by a reduction of the ionic strength of the saturating solution in a number of studies, e.g., Khilar and Folger (1984). Experiments by Sydansk (1980) as well as by Schembre and Kovscek (2005) with NaCl show the effect of temperature on permeability is greater in solutions with a lower ionic strength. No permeability reduction is observed in tests with 0.79 M KCl in two different kaolinite bearing sandstones (Wei et al., 1986); on the other hand, tests with a 0.86 M solution of NaCl (Jing et al., 1992), as well as those with 1.0 M NaCl and $CaCl_2$ (Baudracco and Aoubouazza, 1995) do show permeability reduction with temperature, which is reversible with cooling in the latter two cases.

Besides the flow velocity differences, there may be other reasons why the temperature increase causes the permeability reduction in some tests with a high ionic strength but not in others. The size and charge of dissolved ions affects the strength of their interaction with the mineral surface (Khilar and Folger, 1984) and thereby the surface charge and EDL force. The surface charge of other rock forming minerals, such as feldspars, can be expected to differ from that of quartz. The clay content and the distribution of clay in the sandstone pores affect the amount of particle mobilisation and bridging. Based on scanning electron microscopy images, Tchistiakov (2000) suggests that kaolinite particles dispersed throughout the sandstone are mobilized to a greater extent than the kaolinite present in relatively isolated pockets that can result from the weathering of a feldspar grain. Furthermore, the possibility that the permeability change is due to a different mechanism is not ruled out in the tests compared here. Cement dissolution can release particles causing clogging (Blair et al. 1984). Experimental error, in particular contamination by colloidal particles released from the experimental equipment at elevated temperature, is detected in a number of experiments (Potter et al., 1980; Stottlemyre, 1980) and not ruled out in other tests.

CONCLUSION

Kaolinite mobilisation is one of the mechanisms that can contribute to the permeability reduction in sandstones as a consequence of heating. The available data indicate that quartz and kaolinite have an average negative surface charge that becomes more negative due to heating. As a result, the repulsive interaction energy between the quartz grains and kaolinite particles is increased. Kaolinite is a sheet mineral consisting of two different sheets. It has a different surface charge on the two different faces as well as on the edges of the mineral. The interactions between different sides of the suspended kaolinite particles may promote particle aggregation and bridging in the pore throats which subsequently reduces the permeability of sandstones. The increase in the permeability at reduced temperatures can be attributed to the enhanced hydrodynamic force on the bridged particles and attachment of particles to the quartz grain surface.

Due to the number of parameters affecting particle mobilisation and permeability reduction, comparison of published data is insufficient to verify the proposed mechanism. Further investigation under controlled conditions is required to verify the proposed mechanism of particle induced permeability reduction.

REFERENCES

Adekola, F., Fedoroff, M., Geckeis, H., Kupcik, T., Lefevre, G., Luetzenkirchen, J., Plaschke, M., Preocanin, T., Rabung, T., Schild, D. (2010), "Characterization of acid-base properties of two gibbsite samples in the context of literature results," *Journal of Colloid and Interface Science*, **354,** (1), 306-317.

Aruna, M. (1976), "The Effects of Temperature and Pressure on Absolute Permeability of Sandstones," *PhD dissertation*, Stanford University, Stanford, California (April 1976).

Baudracco, J. and Aoubouazza, M. (1995), "Permeability variations in Berea and Vosges sandstone submitted to cyclic temperature percolation of saline fluids," *Geothermics*, **24,** (5-6), 661-677.

Bear, J. (1972), "Dynamics of Fluids in Porous Media," *American Elsevier Publishing Company Inc.*, pp 32-45.

Bedrikovetsky, P., Siqueira, F.D., Furtado, C.A., Souza, A.L.S. (2010), "Modified Particle Detachment Model for Colloidal Transport in Porous Media,' *Transport in Porous Media*, **86,** (2), 353-383.

Bergstrøm, L. (1997), "Hamaker constants of inorganic materials," *Advances in Colloid and Interface Science*, **70,** 125-169.

Blair, S.C., Deutsch, W.J. and Kannberg, L.D. (1984), "Laboratory Permeability Measurements In Support Of An Aquifer Thermal Energy Storage Site In Minnesota," In *Proc of the 25. US symposium on rock mechanics, Evanston, IL, USA*, 296-303.

Brady, P.V., Cygan, R.T. and Nagy, K.L. (1996), "Molecular Controls on Kaolinite Surface Charge," *Journal of Colloid and Interface Science*, **183,** (2), 356-364.

Casse, F.J. and Ramey Jr, H.J. (1979), "The Effect of Temperature and Confining Pressure on Single-Phase Flow in Consolidated Rocks" (includes associated paper 9087). *Journal of Petroleum Technology*, **31,** (8), 1051-1059.

Derjaguin, B. V. and Landau, L. D. (1941), "Theory of the stability of strongly charged lyophobic sols and the adhesion of strongly charged particles in solutions of electrolytes," *Acta Physicochimica USSR*, **14**, 733-762.

Elimelech, M., Gregory, J., Jia, X. and Williams, R.A., (1995), "Particle Deposition and Aggregation - Measurement, Modelling and Simulation," Elsevier.

Du, J., Morris, G., Pushkarova, R.A. and Smart, R.S.C. (2010), "Effect of Surface Structure of Kaolinite on Aggregation, Settling Rate, and Bed Density," *Langmuir*, **26**, (16), 13227-13235.

Gan, Y. and Franks, G.V. (2006), "Charging Behavior of the Gibbsite Basal (001) Surface in NaCl Solution Investigated by AFM Colloidal Probe Technique," *Langmuir*, **22**, (14), 6087-6092.

Gobran, B.D., Brigham, W.E. and Ramey Jr., H.J. (1987), "Absolute Permeability as a Function of Confining Pressure, Pore Pressure, and Temperature," *SPE Formation Evaluation*, **2,** (1), 77-84.

Grim, R.E. (1953), "Clay Mineralogy," in *International Series in the Earth Sciences*, ed. R.R. Shrock, McGraw-Hill Book Company inc.

Gupta, V. and Miller, J.D. (2010), "Surface force measurements at the basal planes of ordered kaolinite particles," *Journal of Colloid and Interface Science*, **344,** (2), 362-371.

Gupta, V., Hampton, M.A., Stokes, J.R., Nguyen, A.V. and Miller, J.D. (2011), "Particle interactions in kaolinite suspensions and corresponding aggregate structures," *Journal of Colloid and Interface Science*, **359,** (1), 95-103.

Huertas, F.J., Chou, L. and Wollast, R. (1998), "Mechanism of Kaolinite Dissolution at Room Temperature and Pressure: Part 1. Surface Speciation," *Geochimica et Cosmochimica Acta*, **62,** (3), 417-431.

Jing, X.D., Archer, J.S. and Daltaban, T.S. (1992), "Laboratory study of the electrical and hydraulic properties of rocks under simulated reservoir conditions," *Marine and Petroleum Geology*, **9,** (2), 115-127.

Khilar, K.C. and Folger, H.S. (1984), "The existence of a critical salt concentration for particle release," *Journal of Colloid and Interface Science*, **101** (1), 214-224.

Kosmulski, M. (2003), "A literature survey of the differences between the reported isoelectric points and their discussion," *Colloids and Surfaces A: Physicochemical and Engineering Aspects*, **222,** (1-3), 113-118.

Kosmulski, M. (2006), "pH-dependent surface charging and points of zero charge: III. Update," *Journal of Colloid and Interface Science*, **298,** (2), 730-741.

Lorne, B., Perrier, F. and Avouac, J-P. (1999), "Streaming potential measurements. 1. Properties of the electrical double layer from crushed rock samples," *Journal of Geophysical Research*, **104**, (B8), 17857-17877.

Lyklema, J.J., de Keizer, A., Bijsterbosch, B.H., Fleer, G.J. and Cohen Stuart, M.A.C. (1995), Electric Double Layers. *Chap 3* In *Volume II: Solid-Liquid interfaces. Fundamentals of Interface and Colloid Science*, ed. J.J. Lyklema, A. de Keizer, B.H. Bijsterbosch, Fleer, G.J. and Cohen Stuart, M.A.C., 1-232. Academic Press.

Mao, S. and Duan, Z. (2009), "The viscosity of aqueous alkali-chloride solutions up to 623 K,

1,000 bar, and high ionic strength," *International Journal of Thermophysics*, **30,** (5), 1510-1523.

McKay, W.I. and Brigham, W.E. (1984), "Effects of temperature on the absolute permeability of consolidated sandstone," Technical Report DOE/SF/11564-3, Stanford University California. Petroleum Research Institute.

Potter, J., Dibble, W. and Nur, A. (1981), "Effects of temperature and solution composition on the permeability of St. Peters sandstone-Role of iron (III)," *Journal of Petroleum Technology*, **33,** (5), 905-907.

Ramachandran R. and Somasundaran P. (1986), "Effect of temperature on the interfacial properties of silicates," *Colloids and Surfaces*, **21,** 355-369.

Redman, J.A., Walker, S.L. and Elimelech, M. (2004), "Bacterial Adhesion and Transport in Porous Media: Role of the Secondary Energy Minimum," *Environmental Science and Technology*, **38,** (6), 1777-1785.

Revil, A., Darot, M. and Pezard, P. (1996), "From surface electrical properties to spontaneous potentials in porous media," *Surveys in Geophysics*, **17,** (3), 331-46.

Rodríguez, K. and Araujo, M. (2006), " Temperature and pressure effects on zeta potential values of reservoir minerals," *Journal of Colloid and Interface Science*, **300,** (2), 788-794.

Rosenbrand, E. and Fabricius, I.L. (2012) "Effect Of Hot Water Injection On Sandstone Permeability: An Analysis Of Experimental Literature," *SPE154489 for presentation at the EAGE Annual Conference and Exhibition incorporating Europec to be held in Copenhagen 4-7 June 2012.*

Rudzinski, W., Charmas, R. and Piasecki, W. (1999), "Searching for Thermodynamic Relations in Ion Adsorption at Oxide/Electrolyte Interfaces Studied by Using the 2-pK Protonation Model," *Langmuir*, **15,** (25), 8553-8557.

Schembre, J.M. and Kovscek, A.R. (2005), "Mechanism of Formation Damage at Elevated Temperature," *Journal of Energy Resources Technology* **127,** (3), 171-180.

Sen, T.K. and Khilar, K.C. (2006), "Review on subsurface colloids and colloid-associated contaminant transport in saturated porous media," *Advances in Colloid and Interface Science*, 119, **(2-3)**, 71-96.

Somerton, W.H. and Mathur, A.K. (1976), "Effects of Temperature and Stress on Fluid Flow and Storage Capacity of Porous Rocks," *SPE Paper 76-0097 presented at The 17th U.S. Symposium on Rock Mechanics (USRMS), August 25 - 27, 1976 , Snow Bird, UT.*

Stottlemyre (1981), "An Investigation Of Temperature Sensitivity Of Ottawa Sand And Massilon Sandstone Intrinsic Permeabilities," PhD dissertation, University of Washington, Seattle, Washington, United States (March 1981).

Sydansk, R.D. (1980), "Discussion of the Effect of Temperature and Confining Pressure on Single-Phase Flow in Consolidated Rocks," *Journal of Petroleum Technology*, **32**, (8), 1329-1330.

Tchistiakov, A.A. (2000), "Colloid Chemistry of In-Situ Clay-Induced Formation Damage," *presented at the SPE International Symposium on Formation Damage Control, 23-24 February 2000, Lafayette, Louisiana.*

Vane, L.M. and Zang, G.M. (1997), "Effect of aqueous phase properties on clay particle zeta potential and electro-osmotic permeability: Implications for electro-kinetic soil remediation processes," *Journal of Hazardous Materials*, **55,** (1-3), 1-22.

Verwey, E. J. W. and Overbeek, J. T. G. (1948), "Theory of the stability of lyophobic colloids," *Elsevier* Amsterdam.

Visser, J. (1972), "On Hamaker constants: A comparison between Hamaker constants and Lifshitz-van der Waals constants," *Advances in Colloid and Interface Science*, **3**, (4), 331-363.

Wang, Y.-H. and Siu, W.-K. (2006), "Structure characteristics and mechanical properties of kaolinite soils. I. Surface charges and structural characterizations," *Canadian Geotechnical Journal*, **43,** 587-600.

Wei, K.K., Morrow, N.R. and Brower, K.R. (1986), "Effect of fluid, confining pressure, and temperature on absolute permeabilities of low-permeability sandstones," *SPE Formation Evaluation*, **1,** (4), 413-423.

Weinbrandt, R.M. and Ramey, H.J. (1975), "The Effect of Temperature on Relative and Absolute Permeability of Sandstones," *SPE Journal*, **15,** (5), 376-384.

Yuan, H. and Shapiro, A. (in press), "Colloid Transport and Retention: Recent Advances in Colloids Filtration Theory" in *Colloids: Classification, Properties and Applications.* Ed. P.C. Ray et al., Nova Science Publisher.

PROCEEDINGS, Thirty-Eighth Workshop on Geothermal Reservoir Engineering
Stanford University, Stanford, California, February 11-13, 2013
SGP-TR-198

KAOLINITE MOBILISATION IN SANDSTONE: PORE PLUGGING VS SUSPENDED PARTICLES

Esther Rosenbrand[1], Ida Lykke Fabricius[1], Frans Kets[2]

[1]Technical University of Denmark,
Dept. of Civil Engineering, Brovej 118
Kongens Lyngby, 2800, Denmark
esro@byg.dtu.dk

[2] University of Leeds
School of Earth and Environment
Leeds LS2 9JT, United Kingdom

ABSTRACT

The effect of temperature and salinity on sandstone permeability is critical to the feasibility of heat storage in geothermal aquifers. Permeability reduction has been observed in Berea sandstone when the salinity of the pore water is reduced as well as when the sample is heated. Several authors suggest that this effect is due to kaolinite clay mobilisation from the quartz grain surface; the mobilised particles subsequently plug the pore throats and reduce the permeability irreversibly. The expected hysteresis is observed when the salinity is reduced and increased; however, in contradiction with the throat plugging theory, the effect of heating is found to be reversible with cooling. In laboratory experiments we heated Berea sandstone from 20°C to 80°C and observed a reversible permeability reduction. The permeability of the heated samples increased at higher flow rates. We propose that in this case the mobilised kaolinite particles either remain suspended and thereby increase the fluid viscosity, or form porous aggregates that can be destabilized by hydrodynamic forces.

To address how the pore scale distribution of kaolinite relates to the permeability of the entire sample, we relate permeability to the effective specific surface, S_p. The effective specific surface represents the average surface area that resists the flow through the sample of a volume of fluid. We propose that flow paths with a small S_p contribute more than proportionately to the total volume flux. Kaolinite mobilisation in pores with a small S_p diverts fluid flow through pores with a higher S_p, and thereby reduces permeability of the entire sample.

In this paper, we use the DLVO theory to compare how temperature and salinity affect the surface interaction forces between quartz and kaolinite, as well as the interaction forces among kaolinite particles to evaluate whether heating can be expected to a) mobilise particles and b) result in kaolinite forming a suspension rather than plugging the pore throats.

INTRODUCTION

The permeability of a sandstone aquifer is critical to the successful extraction of water for geothermal energy production. Mineral-fluid interaction alters permeability when this causes dissolution or precipitation (Milsch et al. 2009), clay swelling, or clay mobilisation (Mungan, 1965; Gray and Rex, 1966; Khilar and Fogler, 1983, 1984; Kia et al. 1987; Schembre and Kovscek, 2005). We address the mechanism by which kaolinite mobilisation affects the permeability of the Berea sandstone. Kaolinite is the dominant clay mineral in the Berea sandstone, and accounts for approximately 6% (Baudracco and Aoubouazza, 1995) to 9% of the solid mass (Shaw et al., 1991).

Kaolinite particles are mobilised by an increase in the electrical double layer (EDL) repulsive force between quartz and kaolinite (Kia et al., 1987; Schembre and Kovscek, 2005). The EDL force acts between electrically charged surfaces. Kaolinite and quartz surfaces have broken bonds that interact with water molecules. The resulting surface groups have a charge that depends on their protonation. The equilibrium constants for the protonation reactions depend on both the pH and on the temperature (Brady et al., 1996). The surface charge attracts oppositely charged ions. These ions form the EDL on the surface that counters the surface charge. Inside the EDL the potential falls with distance from the surface. The distance over which the surface potential is reduced by a factor 1/e is given by the Debye length, which characterizes the thickness of the EDL (Lyklema et al., 1995). The concentration of counter-ions at a given point inside the EDL depends on the surface potential and the ionic strength of the solution. As two surfaces with the same charge

approach, the overlap of their double layers causes a repulsive force between the EDLs (Israelachvili, 2011). Reducing the ionic strength increases the EDL thickness and the magnitude of the EDL repulsion. Heating reduces the EDL thickness. However, data on the surface charge of kaolinite (Brady et al., 1996), as well as data on the surface potential of both kaolinite and quartz show a significant increase in the magnitude of these with heating (Rodríguez and Araujo, 2006). This increase can offset the reduction of the EDL thickness, and can result in a net increase of the EDL repulsion (Khilar and Fogler, 1984; Schembre and Kovscek, 2005).

According to the DLVO (Derjaguin and Landau, 1941, 1993; Verwey and Overbeek, 1948) theory, the EDL repulsion is counteracted by van der Waals attraction. Changes in the ionic strength or temperature, in the 20^{o}C to 80^{o}C range, are assumed to have a negligible effect on the magnitude of the van der Waals attraction between mineral surfaces interacting across water or brine (Khilar and Fogler, 1984; Schembre and Kovscek, 2005; Israelachvili, 2011). When the EDL repulsion exceeds the van der Waals attraction, kaolinite particles are mobilised. Due to the different rates by which the magnitude of the EDL and the van der Waals force fall with separation between the surfaces, the net interaction energy typically shows an attractive primary energy minimum at short separations where van der Waals forces dominate (negative interaction energy represents attraction). At greater separation the EDL force causes a peak in the interaction energy (Israelachvili, 2011). The net interaction energy is considered to be repulsive when the peak is positive, even if there is attraction at smaller and larger separations (Khilar and Fogler, 1983, 1984; Kia et al. 1987; Schembre and Kovscek, 2005).

Currently it is assumed that the mobilised particles form plugs in the pore throats, resulting in a sharp drop in permeability (Mungan, 1965; Gray and Rex, 1966, Khilar and Fogler, 1984; Schembre and Kovscek, 2005). Rosenbrand et al (submitted) found that reducing the ionic strength at 20^{o}C causes a permeability reduction that is not reversed by increasing the ionic strength. This hysteresis is expected for plugged pores, and is also observed in the Berea sandstone by e.g., Mungan (1965) and by Khilar and Fogler (1984). The permeability only increases significantly when the flow direction was reversed both in our experiment and in tests by Khilar and Fogler (1983). Rosenbrand et al. (under review) found that heating the sandstone from 20^{o}C to 80^{o}C causes a smaller permeability reduction than reducing the ionic strength does, and that the effect of temperature is reversible with cooling. A reversible effect of temperature is also found by Aruna (1976), Baudracco and Aoubouazza (1995) and Cassé and Ramey (1979). This reversibility is not predicted by the particle plugging hypothesis. Furthermore, reversing the flow direction did not significantly affect permeability, but increasing the flow velocity improved permeability significantly.

At elevated temperature, the permeability remained approximately constant as the ionic strength was reduced from 2.0M to 0.002 M NaCl and increased again (Rosenbrand et al., submitted). If heating only mobilised a fraction of the kaolinite, the reduction of the ionic strength would be expected to affect permeability in the heated samples by mobilising the remaining kaolinite. This suggests that the kaolinite is present as unstable aggregates or in suspension rather than as stable plugs in the pore throats.

A more negative surface charge on the kaolinite at 80^{o}C, and thereby a higher EDL repulsion, could account for these observations. A higher EDL repulsive force among kaolinite particles may prevent mobilised kaolinite from forming stable aggregates. Individual particles may be small enough to pass through the pore constrictions, however, when the concentration of suspended particles is high, the particles can obstruct each others' passage through the pore and form particle bridges (McDowell-Boyer et al., 1986). Particle bridges can be destabilized by increasing the hydrodynamic drag forces (Sen and Khilar, 2006).

Rather than being transported to the pore constrictions, the suspended kaolinite may alter the rheology of the pore fluid. Kaolinite suspensions behave as non-Newtonian fluids that only shear when a yield stress is exceeded (Johnson et al., 1998). Both unstable particle bridges as well as a non-Newtonian suspension can account for the increase in permeability with flow velocity observed in our experiments.

The interaction forces between kaolinite particles are affected by the crystal shape of the kaolinite. Kaolinite particles are typically hexagonal platelets, made up of layers with one silica sheet bonded to an alumina sheet. A particle consists of a number of such layers that are connected by hydrogen bonds between adjacent alumina and silica sheets. The particle thereby has one silica face and one alumina face, and the edges have broken bonds where the mineral structure is interrupted. This results in different surface charges on the two faces and on the edges of the particle (Brady et al., 1996) and hence in different EDL interaction forces. Kaolinite forms compact stacked aggregates when there is attraction among the faces, and larger 'card house' structures when there is attraction between the edges and the faces (Schofield and Samson 1954, Wang and Siu, 2006; Gupta et al., 2011). In the untested Berea sandstone, compact stacks of kaolinite particles are observed by Shaw et al. (1991). If these reorient to card houses, this reduces porosity and increases the effective surface area in contact with the fluid.

In this paper we show how the distribution of kaolinite on the pore scale affects the effective specific surface that resists fluid flow. We use the Kozeny (1927) equation to relate the effective

specific surface per unit pore volume, S_p, to the sample permeability. We then use the DLVO theory to compare the effects of ionic strength and of temperature on the interaction energy between charged surfaces in order to evaluate the likelihood of the different scenarios for the kaolinite distribution.

METHOD

Effective specific surface

Kozeny's (1927) equation (Eq. 1) relates the effective specific surface per unit of rock volume, S, to the porosity, φ, and permeability, k, for a homogeneous porous medium. Following Mortensen et al. (1998) the parameter c is taken to depend on the porosity. The porosity can be assumed constant during experiments where the sample is allowed to expand whilst it is heated. The permeability change is due to change in the effective specific surface area.

$$k = \frac{c\varphi^3}{S^2} \qquad \textit{(Eq. 1)}$$

The ratio $S_p=S/\varphi$, is the effective specific surface area per unit of pore volume. S_p is inversely proportional to the average pore diameter. The permeability is determined using Darcy's law (Eq.2) from the volumetric flow rate, Q, through the sample. Here, A is the cross sectional area, ΔP is the pressure difference over the sample length, L, and μ is the fluid viscosity.

$$k = \mu \frac{Q}{A} \frac{L}{\Delta P} \qquad \textit{Eq. (2)}$$

The fluid on the solid surface is stationary according to Poiseuille's law. Therefore we expect a higher flow rate in pores with a lower S_p. Thereby, the pores with a smaller specific surface can be expected to contribute more to the total flow rate, *and* the average permeability is expected to be dominated by the flow through pores with a smaller specific surface.

Kaolinite mobilisation can directly increase the effective surface area in a pore, when compact aggregates are dispersed. It can also plug a pore with a low S_p, and divert flow through pores with a larger S_p. In both cases the effective specific surface of the sample is increased, and the permeability in Eq. 1 is reduced.

Kaolinite distribution

Kaolinite in the Berea sandstone is often observed in locally high concentrations (Schembre and Kovscek, 2005). The kaolinite particles are present in compact stacks (Shaw et al., 1991) and present a relatively small effective surface area. This is the initial condition in the permeability experiments at 20°C and high ionic strength. The net interaction force among kaolinite particles, as well as between quartz and kaolinite can be expected to be attractive in these conditions.

Both reducing the ionic strength at 20°C, and heating to 80°C reduce the permeability, indicating kaolinite is mobilised. This is generally attributed to repulsion between the quartz and kaolinite surfaces. (Khilar and Fogler, 1983, 1984; Schembre and Kovscek, 2005; Rosenbrand et al., under review).

At 20°C, mobilised kaolinite is perceived to form aggregates that plug the pore throats (e.g., Khilar and Fogler, 1984). The mobilised kaolinite particles may flocculate and form aggregates that are too large to pass through the pore throats as shown in Scenario 1 (Figure 1a). Flocculation can occur even if there is repulsive interaction energy at a given separation between surfaces subject to the conditions that the repulsive energy is small relative to the thermal energy and that there is attraction for smaller separations (Hogg et al. 1966). In our case, due to flow, collisions between particles may have sufficient energy to overcome the repulsive energy barrier and attach in the energy minimum at close separation. Alternatively, if the suspended particles repel each other strongly enough to prevent aggregation, they may form particle bridges in the pore constrictions as shown in Scenario 2 (Figure 1b). The key difference between these two scenarios is the stability of the particle aggregates. The relatively high repulsion among particles in Scenario 2 implies that the particle bridges can be destabilised and removed from the pore constriction by an increase in hydrodynamic forces (Sen and Khilar, 2006), whereas stable aggregates that are strained in the pore constriction are not expected to be remobilised (Bedrikovetsky et al., 2012). In Scenarios 1 and 2, the S_p increases primarily due to a diversion of fluid flow through pores with a higher S_p.

Scenario 3 (Figure 1c) shows kaolinite forming the voluminous card-house aggregates described by Schofield and Samson (1954) and Wang and Siu (2006). These form when there is attraction between kaolinite edges and faces, but repulsion among the kaolinite faces. The hydrodynamic forces are insufficient to overcome the gravitational forces on these larger aggregates, and/or the attractive forces tying the aggregate to the quartz, and they are not transported to the pore throats. In Scenario 3, the S_p is increased because the surface area of the kaolinite in contact with the fluid is increased and the effective porosity is reduced by the more voluminous kaolinite aggregate.

Scenario 4 (Figure 1d) shows a kaolinite suspension where the kaolinite particles repel each other, as in Scenario 2. In Scenario 4, however, the strong repulsive interaction energy prevents the formation of particle bridges in the pore throats. The surface area

of the kaolinite in contact with the fluid is increased, increasing S_p. Even when the EDL repulsion among kaolinite particles is high, interactions among the suspended particles result in a yield stress of the suspension (Johnson et al., 1998). Zbik and Frost (2009) observed that kaolinite particles form a structured network even in stable suspensions. Interactions between the electrical double layers of the particles can be expected to affect the orientation of the suspended particles.

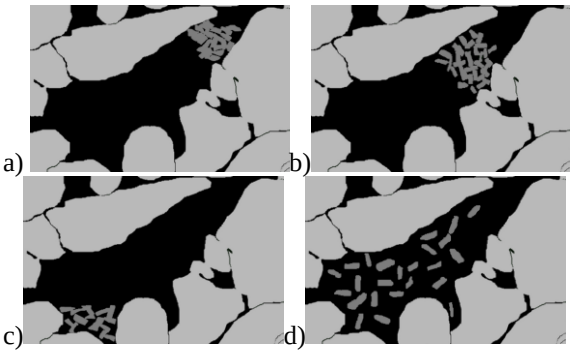

Figure 1: a) stable kaolinite aggregates that are too large to pass the pore constriction. b) kaolinite particles forming a particle bridge c) voluminous kaolinite aggregates in the pore body. d) kaolinite suspension in the pore body. Modified from Rosenbrand et al. (submitted)

Interaction energy

The DLVO theory is used to compare the effect of temperature and ionic strength on the net interaction energy between two surfaces. As a first approximation we consider the interaction forces between parallel plates. Kaolinite particles are platelets rather than spherical particles, and the radius of quartz grains relative to the kaolinite size is large, so that the surface can be approximated as a plane.

Van der Waals interaction

As a first approximation, we assume the van der Waals interaction is not affected by heating or by ionic strength. Atomic force microscopy (AFM) measurements on mica plates indicate that the van der Waals forces are not significantly affected by ionic strength (Israelachvili and Adams, 1978). The van der Waals interaction energy, E_{vdW}, between plates per square meter is given by Eq. 3 (Israelachvili, 2011):

$$E_{vdW} = -\frac{A_H}{12\pi h^2} \qquad \textit{(Eq. 3)}$$

The separation between the mineral surfaces is given by h. A_H is the Hamaker constant that is determined by the intrinsic properties the two surfaces and the intervening medium. We use $A_H = 2.2\times10^{-20}$ J; this is comparable to values that are used for interactions between kaolinite and quartz in aqueous NaCl solution by Kia et al. (1987) and by Schembre and Kovscek (2005).

EDL interaction

We consider the electrical double layer as composed of two layers based on the Stern model (Stern (1924) in Lyklema (1995)). The Stern layer, the distance between the surface and the Stern plane, accounts for small-scale surface roughness, directly adsorbed water molecules and the size of the hydrated counter-ions. Beyond the Stern plane, the ions in the diffuse part of the double layer are treated as point charges after the Gouy-Chapman theory (Gouy (1909), Chapman (1913) in Lyklema, 1995). In the diffuse part of the EDL, the potential drop with distance is characterized by the Debye length, κ^{-1} (Eq. 4).

$$\kappa^{-1} = \sqrt{\frac{\varepsilon_0 \varepsilon k_B T}{2N_A e^2 I}} \qquad \textit{(Eq. 4)}$$

Here ε is the relative permittivity of the solution, ε_0 is the vacuum permittivity, k_B, is Boltzmann's constant, T, is the absolute temperature, N_A, is Avogadro's number, e, is the electron charge and I is the ionic strength of the solution $I = \frac{1}{2}\sum C_i z_i^2$ where C is the concentration and z the valence of the ions. Temperature and ionic strength directly affect κ^{-1}, and they also influence ε. We calculate the permittivity as a function of T and I after Michelsen and Mollerup (2007).

The interaction energy due to the overlapping double layers can be calculated exactly by solving the Poisson-Boltzmann equation. This requires numerical methods, but analytical solutions based on simplifications can give results closely approximating the exact solution (Gregory, 1975). The boundary conditions that are required for both the numerical and the analytical solutions have a significant effect on the interaction at small separations. The assumption that the charge in the double layers is constant as the surfaces approach results in an estimate of the upper bound for the EDL repulsion. The lower bound is obtained by the assumption that the potential at the Stern plane is constant. This assumption, however, leads to the prediction that the EDL force between surfaces with different magnitude charge of the same sign, flips from repulsion to attraction at short separations. Gregory (1975) suggests the use of an intermediate condition, represented by the linear superposition approximation

(LSA) Eq. 5. This solution does not lead to a change of sign of the EDL interaction force with separation distance. Rather than assuming constant potential or charge on the surfaces, the potential midway between the Stern planes is assumed to be given by the summation of the potentials of the individual double layers at this position. The assumption that the double layers do not affect each other is probably not valid for separations less than κ^{-1} (Elimelech et al., 1995).

$$E_{EDL} = \frac{64000 N_A C}{\kappa} \gamma_1 \gamma_2 \exp(-\kappa D) \quad (Eq.\ 5)$$

Here, C is the concentration of the monovalent electrolyte in moles per litre, D is the separation between the Stern planes, and γ_i is the reduced surface potential which for monovalent electrolyte solutions is given by:

$$\gamma_i = \tanh\left(\frac{e\psi_{0,i}}{4k_B T}\right) \quad (Eq.\ 6)$$

The potential at the Stern plane should be used for the surface potential, $\psi_{0,}$ according to Frens and Overbeek (1972). The zeta potential ζ, is generally used to estimate the ψ_0, (Elimelech et al., 1995). This can be measured using particle electrophoresis experiments. The ζ values reported in the literature for kaolinite at pH 8 vary significantly. This is partially because the ψ_0 depends on the ionic strength as well as on ψ_0 (Frens and Overbeek, 1972). To compare data from experiments at different electrolyte concentrations we used the relation between the ψ_0 and the charge on the Stern plane, σ_0 after Grahame (1947).

$$\sigma_0 = \sqrt{8000 N_A \varepsilon_0 \varepsilon k_B T C^+} \sinh\left(\frac{e\psi_0}{2k_B T}\right) (Eq.\ 7)$$

By comparing the σ_0 rather than the ζ we reduced the variation that is due to the different ionic strengths used to measure the ζ. Still, at pH 8, the values of the σ_0 for kaolinite from different investigations (Johnson et al., 1998; Rodriguez and Araujo 2006; Zbik and Frost, 2009) vary in the range between 11 mC/m^2 and 22 mC/m^2. This can be expected to be caused by differences in the particle shape and size. The value of the ζ is an average for the entire particle, but the different sides of kaolinite particles have different charge densities. Gupta and Miller (2010) measure the σ_0 on both the alumina and the silica faces using AFM. Gupta et al. (2011) conclude that the σ_0 on the edges must be significantly higher than the σ_0 on the faces to account for the value of the ζ at pH 8. Particles with a larger ratio of edge to face surface area can therefore be expected to have a higher average σ_0, and therefore a higher ζ. Brady et al. (2006) observe that the faces of their kaolinite particles are not planar but show steps. This effectively adds broken bonds or edge surface to the particle faces and can be expected to increase both the face σ_0 and the average σ_0 for the particle. Brady et al. (2006) use potentiometric titration in combination with chemical modelling to estimate distribution of surface charge. Their data suggests that the σ_0 on the edges is in the order of 3 times as high as the average σ_0.

Heating is observed to increase the ζ by a factor 2 for both kaolinite and for quartz when these are heated from 20^{o}C to 45^{o}C (Rodríguez and Araujo, 2006). Brady et al. (2006) observe an approximate doubling of the σ_0 of kaolinite for a temperature increase from 25^{o}C to 70^{o}C.

We calculated the value of the ψ_0 from the $\sigma_{0,20}$ at 20^{o}C using Eq. 7. We assumed that the Stern plane is 0.5 nm removed from the surface. This corresponds approximately to one layer of adsorbed water plus the radius of the hydrated counter-ions. Thereby the distance, D, for the EDL force as defined in Eq. 5 is 1 nm less than the separation between mineral surfaces, h. The net interaction energy was calculated for kaolinite with $\sigma_{0,20}$ ranging from $\sigma_{0,20}$ =7 mC/m^2 to $\sigma_{0,20}$ =22 mC/m^2. The lower values can be expected only on the faces, whereas the higher values correspond to measured ζ values. To account for the significantly higher edge charge density values between $\sigma_{0,20}$=27mC/m^2 and $\sigma_{0,20}$=37 mC/m^2 were used. However, the interaction energy of the edges was scaled by 0.2 μm^2 whereas that for the faces is scaled by 4 μm^2 to account for the difference in surface area. For quartz we used $\sigma_{0,20}$=22 mC/m^2 to $\sigma_{0,20}$=32 mC/m^2 based on data from Rodríguez and Araujo (2006) and from House and Orr (1992).

We calculated the interaction energy at 80^{o}C for both the same $\sigma_{0,20}$ as at 20^{o}C as well as for a two- and for a four-fold increase in $\sigma_{0,20}$ that may result from heating.

RESULTS

Reducing the ionic strength causes a significant increase of the κ^{-1}, whereas heating has a negligible effect (Figure 2a; Eq. 4). For a constant σ_0, the magnitude of the ψ_0 increases significantly when ionic strength is reduced according to Eq. 7. Heating to 80°C also increases the magnitude of the ψ_0 but to a lesser extent (Figure 2b).

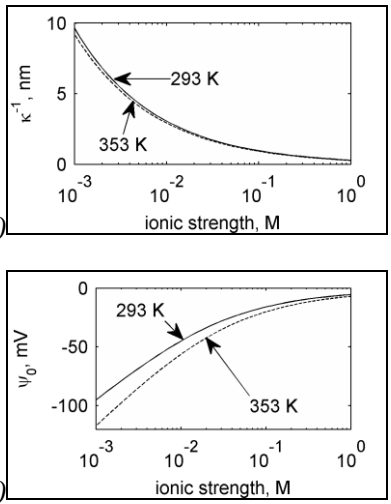

Figure 2: (a) the reduction of the ionic strength increases the Debye length, κ^{-1}.
(b) reducing the ionic strength also increases the magnitude of the surface potential, ψ_0 at a constant surface charge. The effect of heating on κ^{-1} and ψ_0 is less significant than the effect of ionic strength.

Figure 3 shows the effect of ionic strength on the net interaction energy between quartz and kaolinite at 20°C. At high ionic strength, both κ^{-1} and ψ_0 are low and the van der Waals forces dominate. The peak of the interaction energy profile switches from attraction (negative interaction energy) to repulsion (positive interaction energy) between ionic strengths 0.2 and 0.02 M. Due to the thickness of the Stern layer, the minimum separation between surfaces is 1 nm. For separations between Stern planes, *D*, that are less than approximately κ^{-1}, (indicated by the vertical dotted line in the figures) the calculated EDL interaction energy depends strongly on the assumption of constant potential or constant charge (Gregory, 1975). We limit the analysis to the interaction energies at greater separations. Therefore we do not compare the maximum height of the interaction barriers, but rather the interaction values at a larger separation.

The value of the $\sigma_{0,20}$ of kaolinite varies in literature, however, this variation does not change the sign of the interaction energy at 3 nm separation between the kaolinite and quartz surfaces, (*D=h-1 nm*) at 0.2 M (Figure 4a) and 0.02 M (Figure 4b). These figures show an attractive interaction at 0.2 M and repulsion at 0.02 M ionic strength for the range of $\sigma_{0,20}$ that we consider representative of faces or of the average charge. Only for the relatively high negative $\sigma_{0,20}$ that can be expected on the edges, there is repulsion at both ionic strengths. The interaction energy is calculated as energy per square meter, and the total energy is therefore scaled by the interacting areas. Due to the smaller surface area of the edges, 0.2 μm^2, compared to the faces, 4 μm^2, the energy for the interactions between the edges of kaolinite and quartz is lower than for the interaction between the faces of kaolinite and quartz. This does not imply that attachment between quartz and the edges is more probable than between quartz and the faces. The difference is comparable to the difference between pressure and force.

Mobilisation due to heating was observed even at high ionic strengths (Rosenbrand et al, under review). Figure 5a shows that the interaction energy between quartz and kaolinite remains negative when the temperature is increased from 20°C to 80°C at 0.34 M ionic strength. Heating only causes repulsion when the σ_0 increases due to heating. Figure 5b shows that the increase in the surface charge density σ_0, required for repulsive interaction energy at 2.0 M ionic strength is four times $\sigma_{0,20}$ rather than the twofold increase that caused repulsion at 0.34 M ionic strength. At larger separations (4-7 nm) this curve shows a negative minimum, a minimum at this distance may indicate a stable configuration at this distance (Hahn and O'Melia, 2004).

If heating increases the σ_0, this also increases the repulsive interaction among kaolinite particles. Figure 6a shows the calculated interaction energy between a kaolinite face with a $\sigma_{0,20}$ 11 mC/m^2; which corresponds to the lower range of the ζ in literature, and all sides of the kaolinite particle at 20°C and 0.02 M ionic strength, which is repulsive at all separation distances. Assuming that heating to 80°C increases the surface potential by a factor four, the interaction energy at close separations increases sharply even when partly compensated by the effect of a relatively high, 0.2 M, ionic strength (Figure 6b).

At 20°C the kaolinite particles are expected to form relatively stable aggregates even at a low ionic strength. The interaction energy at 20°C and 0.02 M is less repulsive than the interaction energy at 80°C and 0.2 M, which can be expected to result in a higher aggregate stability at 20°C. The difference between the interaction energy at 20°C and 0.02M ionic strength and the energy at 80°C and 0.2 M depends on the separation distance, (Figure 6c). At small separations, the interaction energy is higher in the heated sample due to the higher σ_0 . At greater separations the effect of the higher ionic strength at 80°C outweighs the effect of the higher σ_0 and there is a higher repulsion at 20°C.

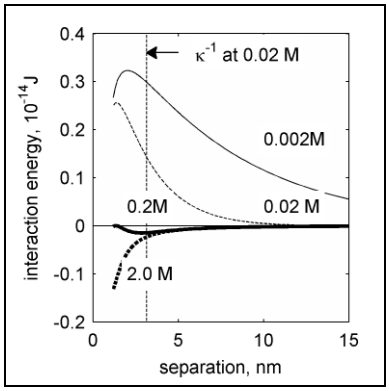

Figure 3 interaction energy as a function of separation between surfaces of kaolinite and quartz with $\sigma_{0,20}$ between 11mC/m^2 and 27 mC/ m^2. The Debye length increases as the ionic strength falls.

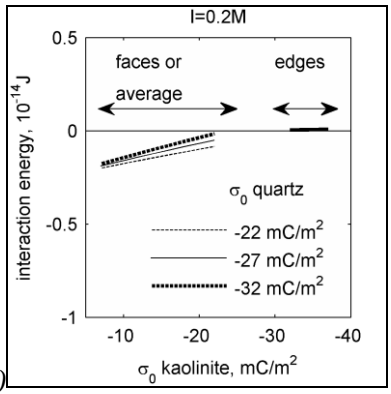

a)

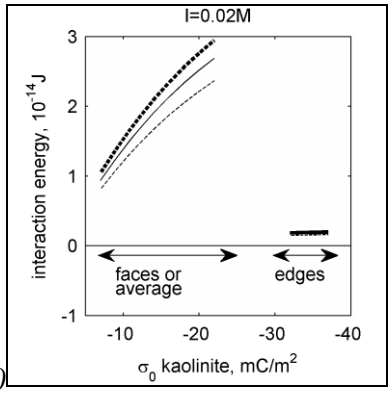

b)

Figure 4 the interaction energy between kaolinite faces and quartz at 2 nm between Stern planes (3 nm between surfaces) is attractive at 0.2M (a) and repulsive at 0.02 M (b) for the range of $\sigma_{0,20}$ based on face or average particle charge. For the edges with a higher surface charge density there is repulsion both at 0.2M and 0.02M.

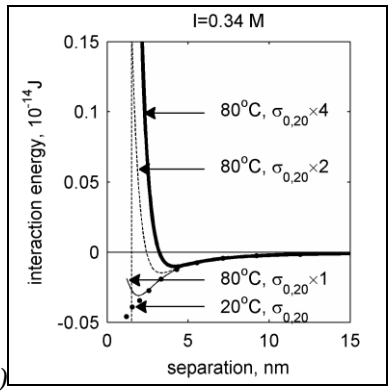

a)

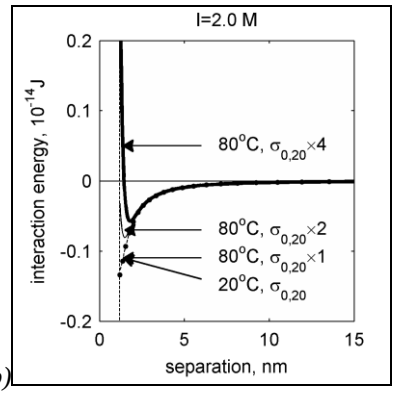

b)

Figure 5: Heating can increase the surface charge density and thereby result in a repulsive interaction energy between kaolinite and quartz at small separations. At 0.34 M ionic strength, a), the interaction energy becomes repulsive if heating increases σ_0 by a factor two compared to $\sigma_{0,20}$. At 2.0 M ionic strength there is only repulsion for a fourfold increase in $\sigma_{0,20}$.

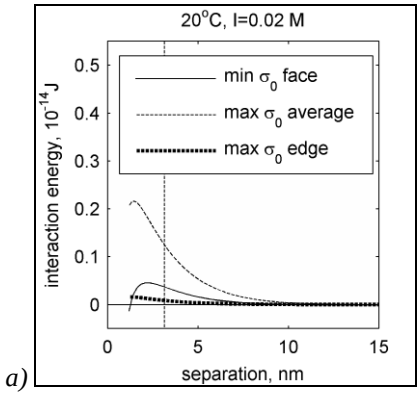

a)

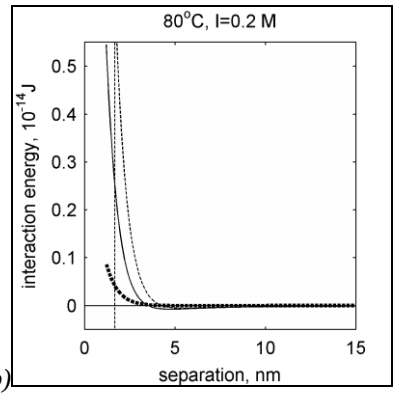

b)

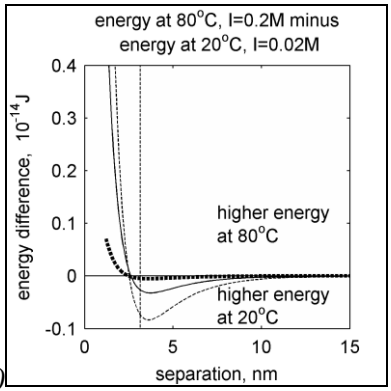

c)

Figure 6: Comparison of the interaction energy among kaolinite particles at 20°C and 0.02 M ionic strength (a) to the interaction energy at 80°C (b) and 0.2 M ionic strength. The repulsive interaction energy is highest in the heated sample for small separations (c) (when the surface charge density increases by a factor 4 compared to the surface charge density at 20 °C.

DISCUSSION

Heating from 20°C to 80°C has less effect on the Debye length, κ^{-1}, than ionic strength does, according to Eq. 4 (Figure 1a). However, Israelachvili and Adams (1978) suggest that Eq. 4 may under-predict the thickness of the double layer at higher ionic strengths. Their measurements of the forces between mica surfaces indicate that the potential in the double layer falls less steeply than predicted by Eq. 4. A greater double layer thickness would result in greater repulsive interaction energy between surfaces with the same sign charge than we calculated. This effect would be greatest for our calculation of the interaction energy at 2.0 M.

The permeability reduction due to reduction of ionic strength, at 20°C, that was observed in experiments has been interpreted as kaolinite mobilisation. The calculated net interaction energy switched from attractive to repulsive between these ionic strengths (Figure 3a). Furthermore, Figure 4a and Figure 4b show that the switch from an attractive to a repulsive interaction energy can be expected to occur between these ionic strengths for a wide range of surface charge densities representative for the quartz-kaolinite system. Repulsion dominated the quartz to kaolinite edge interaction even at 0.2 M ionic strength. This suggests that the average charge on the kaolinite particle or possibly only the charge on the faces is relevant to predict mobilisation. Currently the zeta potential, ζ, which represents the average surface charge, is often used to predict kaolinite mobilisation in Berea sandstone (e.g., Kia et al. 1987; Schembre and Kovscek, 2005).

Heating from 20°C to 80°C was observed to reduce permeability in experiments with distilled water, as well as in tests with solutions of 0.34 M and 2.0 M NaCl. With a constant σ_0, Eq. 7 predicts that the surface potential, ψ_0 is higher at 20°C that at 80°C (Figure 1b). Figure 4 shows that this increase was not sufficient to cause repulsion at either 0.34 M or 2 M ionic strength. A doubling of the $\sigma_{0,20}$ was sufficient to cause a repulsive interaction at 0.34 M, but the mobilisation we observed at 2.0 M ionic strength would require a fourfold increase in the $\sigma_{0,20}$ to obtain a repulsive interaction energy for the minimum separation between surfaces. We limit ourselves to the distance range beyond twice the 0.5 nm Stern layer. No quantification is made of attractive forces at smaller distances, but we note that at closer approach the van der Waals interaction suggests strong attraction (Eq. 3). Figures 5a and 5b do show another minimum for separations around 4-7 and 2-4 nm separation respectively. It has been suggested that particles can be loosely attached in this secondary minimum, from where they are more easily mobilised by hydrodynamic forces (Hahn and O'Melia, 2004). It appears unlikely that particles were attached in the secondary minimum at 80°C because the ionic strength had no effect on permeability whereas the secondary minimum is eliminated at low ionic strength. The secondary minimum is only present for a narrow range of separations; surface roughness can be expected to cause variation in the separation. The higher repulsive interaction at smaller distances may be expected to have a dominant effect.

The effect of heating on the surface potential can be significant. Electrophoresis data from Rodríguez and Araujo (2006) indicate that the ζ increases by a factor 2 when the sample is heated from 20°C to 45°C. This might possibly be extrapolated to match the increase required at 2.0 M. However, potentiometric titrations indicate only an approximate doubling of the surface charge when a sample is heated from 25°C to 70°C (Brady et al., 1996). The effect of a change in σ_0 on the interaction energy depends on the EDL thickness, which may be under-predicted by Eq. 4 at 2.0 M ionic strength. In that case a smaller change in σ_0 could cause mobilization. Furthermore, we have assumed that the effect of heating on the van der Waals interaction was negligible. We have also assumed that the Stern layer thickness was not affected by heating, and that the dielectric properties of fluid in the Stern layer were the same as the dielectric properties of the bulk fluid. All of these assumptions can be challenged; however, we lacked the evidence to support alternative assumptions. With these assumptions, Figure 5 indicates that the effect of heating on the EDL interaction is less than the effect of ionic strength on the EDL interaction if the σ_0 is constant. However, heating does increase the σ_0; whether the increase is sufficient to cause particle mobilisation is subject to discussion.

Scenario 1 can explain the stability of the aggregates at 20°C; here there is attraction among kaolinite particles even at low ionic strength. Figure 6a shows a small repulsive interaction energy between a kaolinite surface with a σ_0 representative of the faces and kaolinite surfaces with values representative of the average σ_0 and of the σ_0 on the edges at 20°C and 0.02 M ionic strength. The interaction between the surface and another surface with a kaolinite face σ_0 was attractive at short separations. However, the divergence between the different formulations for the EDL force is particularly significant at separations less than κ^{-1} (Gregory, 1975). We consider the interaction energy in this region to be more uncertain than those at larger separations. At greater separations there is repulsive interaction energy. However, suspended particles may aggregate despite a repulsive interaction energy barrier if their thermal energy is sufficient to overcome this (Hogg et al. 1966). Therefore, we do not rule out Scenario 1 based on these calculations. Even if particles do not aggregate due to the repulsive interaction, particles transported to the pore constrictions may still form particle bridges as in Scenario 2.

Scenario 3 appears unlikely. The repulsive interaction energy for the edges is lower than for the faces due to their smaller area. However, as also noted by Gupta et al. (2011), at pH 8 the edges have a high negative charge density, which makes it unlikely that they attach to the negatively charged faces. The observation that the permeability of the heated samples does not depend on the ionic strength also indicates that Scenario 3 is less likely. The stability of the aggregates can be presumed to depend on the interaction energy among kaolinite particles and thereby on the double layer length. Scenario 4 is more plausible with repulsion among kaolinite particles.

As the DLVO calculations did not rule out Scenarios 1, 2 or 4, we considered these in combination with the permeability test data. Particles had been mobilised at 20°C by the reduction of the ionic strength and at 80°C they had been mobilised by heating.

At 20 °C increasing the ionic strength to 0.2 M or 2.0 did not improve the permeability. Figure 3 shows there is attraction between kaolinite and quartz at 0.2 and 2.0 M ionic strength. In the case of Scenario 4, the particles would be expected to re-attach to the grain surface. This can be expected to reduce specific surface and improve permeability, however, we did not observe a permeability recovery. The combination of DLVO theory and experimental observations rather suggests Scenarios 1 or 2 dominate at 20°C. These predict an irreversible permeability reduction. These scenarios are comparable to the current models for particle plugging (e.g. Khilar and Fogler 1984). At 80 °C the permeability reduction is reversible, and furthermore permeability increases at higher flow rates. This allows us to rule out Scenario 1, of stable aggregates. Scenario 3 has been ruled out based on the repulsive interaction energy between the edges and faces, leaving Scenarios 2 and 4. The observed reversibility with cooling suggests the particles are in suspension rather than as particle bridges. A reduction in the repulsive EDL force due to cooling would make the bridges more stable, rather than improve the permeability. This suggestion is supported by the observation that changing the flow direction had no significant effect on permeability at 80°C. However, the improvement in permeability with cooling may be due to removal of particle bridges by the increase in fluid viscosity and hydrodynamic forces. The lack of effect of flow direction may be due to the fact that when this was done at 80°C the particles formed bridges at the other side of the pore, since they were still repelled by the quartz surface. At 20°C the flow direction was reversed at high ionic strength so that particles could re-attach to the quartz grains. Scenario 2 might therefore prevail at both 20°C and 80°C, whereby the difference in the effect of flow velocity on permeability was due to the difference in the magnitude of the EDL repulsion.

Four different scenarios were proposed to explain permeability data in terms of kaolinite distribution. The permeability data suggest that a repulsive interaction energy prevails between kaolinite particles at high ionic strength at 80°C. This is supported by data showing that the surface charge density of the minerals increases with heating and by DLVO calculations based on this. The DLVO theory

is successful in predicting the kaolinite mobilization caused by the reduction in ionic strength at room temperature (Khilar and Fogler, 1984, Kia et al. 1987). We applied the DLVO theory to predict kaolinite mobilization for a range of different surface charge densities at 20°C and found that the ionic strength interval where mobilisation occurs was robust to the variation that can be expected for the kaolinite surface charge density. We then used the same EDL model and parameters to investigate kaolinite mobilization due to heating, and to investigate kaolinite aggregation at 20°C and at 80°C. The high uncertainty in the effect of heating on the relevant parameters, ζ and A, limits even a qualitative comparison of the effects of ionic strength and temperature.

CONCLUSION

The ionic strength at which permeability reduction occurs in laboratory experiments is within the same order of magnitude as the ionic strength that causes a repulsive interaction energy between kaolinite and quartz at 20°C. This ionic strength is robust for the range of surface potentials reported for different kaolinites in literature.

Heating can be expected to increase the surface charge density. In the framework of the DLVO theory this can lead to particle mobilisation and prevent particles aggregation. This would imply that at elevated temperature, pore throat plugging by stable particle aggregates is an unlikely mechanism of permeability reduction. The effect of temperature on other relevant parameters is not established well enough to make reliable estimates of inter-particle forces at elevated temperature.

ACKNOWLEDGEMENT

Thanks are due to Bjørn Maribo-Mogensen, DTU, Chemical Engineering for his program that allows calculation of the dielectric permittivity as a function of temperature and ionic strength.

REFERENCES

Aruna, M. (1976), "The Effects of Temperature and Pressure on Absolute Permeability of Sandstones," *PhD dissertation*, Stanford University, Stanford, California (April 1976).

Baudracco, J. and Aoubouazza, M. (1995), "Permeability variations in Berea and Vosges sandstone submitted to cyclic temperature percolation of saline fluids," *Geothermics,* **24,** 661-677.

Bedrikovetsky, P., Zeinijahromi, A., Siqueira, F.D., Furtado, C.A. and de Souza, A.L.S. (2012), "Particle Detachment Under Velocity Alternation During Suspension Transport in Porous Media," *Transport in Porous Media,* **91**, 173-197.

Brady, P.V., Cygan, R.T. and Nagy, K.L. (1996), "Molecular Controls on Kaolinite Surface Charge," *Journal of Colloid and Interface Science,* **183,** 356-364.

Cassé, F.J. and Ramey Jr, H.J. (1979), "The Effect of Temperature and Confining Pressure on Single-Phase Flow in Consolidated Rocks" (includes associated paper 9087). *Journal of Petroleum Technology,* **31,** 1051-1059.

Chapman, D.L. (1913) "A contribution to the theory of electrocapillarity," *Philosophical Magazine,* **25,** 475.

Derjaguin, B.V. and Landau, L.D. (1941), "Theory of the stability of strongly charged lyophobic sols and the adhesion of strongly charged particles in solutions of electrolytes," *Acta Physicochimica USSR,* **14**, 633-662.

Derjaguin, B.V. and Landau, L.D. (1993), "Theory of the stability of strongly charged lyophobic sols and of the adhesion of strongly charged particles in solutions of electrolytes," *Progress in Surface Science*, **43**, 30-59.

Elimelech, M., Gregory, J., Jia, X. and Williams, R.A., (1995), "Particle Deposition and Aggregation - Measurement, Modelling and Simulation," Butterworth-Heinemann, Elsevier.

Frens, G. and Overbeek, J.T. (1972), "Repeptization and Theory of Electrocratic Colloids," *Journal of Colloid and Interface Science,* **38**, 376-387.

Gouy, M. (1909), "Sur la constitution de la charge électrique à la surface d'un électrolyte", *Comptes rendus de l'Académie des sciences*, **149,** 654-657

Grahame, D.C., (1953), "Diffuse Double Layer Theory for Electrolytes of Unsymmetrical Valence Types," *The Journal of Chemical Physics*, **21**, 1054-1060.

Gray, D.H. and Rex, R.W. (1966), "Formation Damage in Sandstones caused by Clay Dispersion and Migration," *Clays and Clay Minerals*, **14**, 355-366.

Gregory, J. (1975), "Interaction of unequal double layers at constant charge," *Journal of Colloid and Interface Science,* **51,** 44-51.

Gouy, G. (1909), "Sur la constitution de la charge électrique à la surface d'un électrolyte", *Comptes rendus de l'Académie des sciences*, **149,** 654

Gupta, V. and Miller, J.D. (2010), "Surface force measurements at the basal planes of ordered kaolinite particles," *Journal of Colloid and Interface Science,* **344,** (2), 362-371.

Gupta, V., Hampton, M.A., Stokes, J.R., Nguyen, A.V. and Miller, J.D. (2011), "Particle interactions in kaolinite suspensions and corresponding aggregate structures," *Journal of Colloid and Interface Science*, **359,** (1), 95-103.

Hahn, M.W. and O'Melia, C.R. (2004) "Deposition and Reentrainment of Brownian Particles in Porous Media under Unfavorable Chemical Conditions: Some Concepts and Applications," *Environmental Science and Technology*, **38**, 210-220.

Hogg, R., Healy, T.W. and Fuerstenau, D.W. (1966), "Mutual coagulation of colloidal dispersions," *Transactionsof the Faraday Society*, **62,** 1638-1651.

House, W.A. and Orr, D.R. (1992), "Investigation of the pH-Dependence of the Kinetics of Quartz Dissolution at 25 Degrees C," *Journal of the Chemical Society-Faraday Transactions*, **88,** 233-241.

Israelachvili, J.N. and Adams, G.E. (1978), "Measurement of forces between 2 mica surfaces in aqueous electrolyte solutions in range 0-100 nm," *Journal of the Chemical Society, Faraday Transactions*, ***74***, 975-1001.

Israelachvili, J.N. (2011), "Intermolecular and surface forces," *Elsevier/Academic Press*, 3rd ed. Amsterdam.

Johnson, S.B., Russel, A.S. and Scales, P.J. (1998), "Volume fraction effects in shear rheology and electroacoustic studies of concentrated alumina and kaolin suspensions," *Colloids and Surfaces A: Physicochemical and Engineering Aspects*, **141**, 119-130.

Kia, E.F., Fogler, H.S. and Reed, M.G. (1987) "Effect of Salt Composition on Clay Release in Berea Sandstones," *SPE Production Engineering*, **2,** 277-283.

Khilar, K.C. and Fogler, H.S. (1983) "Water Sensitivity of Sandstones" *SPE Journal*, **23**, 55-64.

Khilar, K.C. and Fogler, H.S. (1984), "The Existence of a Critical Salt Concentration for Particle Release," *Journal of Colloid and Interface Science*, **101**, 214-224.

Kozeny, J. (1927) "Ueber kapillare Leitung des Wassers im Boden," *Sitzungsberichte der Wiener Akademie der Wissenschaften*, **136,** 271-306.

Lyklema, J.J., de Keizer, A., Bijsterbosch, B.H., Fleer, G.J. and Cohen Stuart, M.A. (1995), Electric Double Layers. *Chap 3* In *Volume II: Solid-Liquid interfaces. Fundamentals of Interface and Colloid Science*, ed. J.J. Lyklema, A. de Keizer, B.H. Bijsterbosch, Fleer, G.J. and Cohen Stuart, M.A.C., 1-232. Academic Press.

McDowell-Boyer, L., Hunt, J.R., and Sittar, N. (1986), "Particle Transport Through Porous Media," *Water Resources Research*, **22,** 1901-1921.

Michelsen, M.L. and Mollerup, J.M. (2007), "Thermodynamic Models: Fundamentals & Computational Aspects," *Tie-Line Publications*, Holte (Denmark).

Milsch, H., Seibt, A. and Spangenberg, E. (2009), "Long-term Petrophysical Investigations on Geothermal Reservoir Rocks at Simulated In Situ Conditions," *Transport in Porous Media*, **77,** 59-78.

Mortensen , J., Engstrøm, F. and Lind, I. (1998), "The Relation Among Porosity Permeability And Specific Surface Of Chalk From The Gorm Field Danish North Sea," *SPE Reservoir Evaluation and Engineering*, **1**, 245-251.

Mugan, N. (1965), "Permeability Reduction Through Changes in pH and Salinity," *Journal of Petroleum Technology*, **17,** 1449-1453.

Rodríguez, K. and Araujo, M. (2006), " Temperature and pressure effects on zeta potential values of reservoir minerals," *Journal of Colloid and Interface Science*, **300,** (2), 788-794.

Rosenbrand, E., Fabricius, I.L., Kjøller, C. Haugwitz, C.E. and Jacobsen, P.S. (under review) "The Effect of Hot Water Injection on Sandstone Permeability," *Geothermics.*

Rosenbrand, E., Kjøller, C. Riis, J.F., Kets, F. And Fabricius, I.L., (submitted) "Mechanisms of permeability reduction by kaolinite: filtration versus suspension," *Transport in Porous Media.*

Sen, T.K. and Khilar, K.C. (2006), "Review on subsurface colloids and colloid-associated contaminant transport in saturated porous media," *Advances in Colloid and Interface Science*, 119, **(2-3)**, 71-96.

Schembre, J.M. and Kovscek, A.R. (2005), "Mechanism of Formation Damage at Elevated Temperature," *Journal of Energy Resources Technology* **127,** (3), 171-180.

Schofield, R.K. and Samson, H.R. (1954), "Flocculation of Kaolinite due to the Attraction of Oppositely Charged Crystal Faces," *Discussions of the Faraday Society*, **18**, 135-145.

Shaw, C.J., Churcher, L.P. and Blaine, H.F. (1991), "The Effect of Firing on Berea Sandstone", *SPE Formation Evaluation*, **6,** 72-78.

Stern, O. (1924), "Theory of the electrolytic double shift," *Zeitschrift fuer Electrochemie,* **30**, 508-518.

Verwey, E.J.W and Overbeek, J.T.G (1948), "Theory of the stability of lyophobic colloids," *Elsevier*.

Wang, Y.-H. and Siu, W.-K. (2006), "Structure characteristics and mechanical properties of kaolinite soils. I. Surface charges and structural characterizations," *Canadian Geotechnical Journal*, **43,** 587-600.

Zbik, M. and Frost, R.L. (2009). "Micro-structure differences in kaolinite suspensions," *Journal of Colloid and Interface Science*, **339,** 110-116.

Hot water injection in geothermal sandstone aquifers is considered for seasonal energy storage in Denmark. However, an increase in the aquifer temperature might reduce permeability and increase production costs. An understanding of the factors that control permeability is required in order to address the effects of temperature on permeability. Therefore, different aspects of sandstone permeability are investigated in this research project. Mineral fluid interaction and clay mineral content affect permeability to different fluids and the effect of temperature on permeability. Hot water injection might induce clay particle mobilisation and mineral dissolution.

DTU Civil Engineering
Department of Civil Engineering
Technical University of Denmark

Brovej, Building 118
2800 Kgs. Lyngby
Telephone 45 25 17 00

www.byg.dtu.dk

ISBN: 9788778774019
ISSN: 1601-2917